AD_____

Award Number: DAMD17-00-1-0217

TITLE: Breast Cancer Diagnosis Using Ultrasound and Diffusive Light

PRINCIPAL INVESTIGATOR: Quing Zhu, Ph.D.

CONTRACTING ORGANIZATION: University of Connecticut
Storrs, Connecticut 06269-1113

REPORT DATE: August 2004

TYPE OF REPORT: Final

PREPARED FOR: U.S. Army Medical Research and Materiel Command
Fort Detrick, Maryland 21702-5012

REPORT DOCUMENTATION PAGE

Form Approved
OMB No. 074-0188

1. AGENCY USE ONLY (Leave blank)	2. REPORT DATE	3. REPORT TYPE AND DATES COVERED
	August 2004	Final (15 Aug 2000 - 14 Jul 2004)

4. TITLE AND SUBTITLE
Breast Cancer Diagnosis Using Ultrasound and Diffusive Light

5. FUNDING NUMBERS
DAMD17-00-1-0217

6. AUTHOR(S)
Quing Zhu, Ph.D.

7. PERFORMING ORGANIZATION NAME(S) AND ADDRESS(ES)
University of Connecticut
Storrs, Connecticut 06269-1113

E-Mail: zhu@engr.uconn.edu

8. PERFORMING ORGANIZATION REPORT NUMBER

9. SPONSORING / MONITORING AGENCY NAME(S) AND ADDRESS(ES)
U.S. Army Medical Research and Materiel Command
Fort Detrick, Maryland 21702-5012

10. SPONSORING / MONITORING AGENCY REPORT NUMBER

11. SUPPLEMENTARY NOTES
Original contains color plates: All DTIC reproductions will be in black and white.

12a. DISTRIBUTION / AVAILABILITY STATEMENT
Approved for Public Release; Distribution Unlimited

12b. DISTRIBUTION CODE

13. ABSTRACT (Maximum 200 Words)

We have developed a novel near-infrared optical technique with ultrasound localization. We have made significant progress on using our technique to improve breast cancer diagnosis. Initial results with a group of more than 90 biopsied patients have shown that early stage invasive cancers present two-fold greater total hemoglobin concentration than fibroadenomas and benign lesions. Initial results of advanced cancers have shown that the angiogenesis distributions of larger cancers are highly distorted and heterogeneous and the distributions correlate with histological microvessel density counts.

We believe that our unique technique has a great potential to improve current practice on breast cancer diagnosis and to monitor tumor vascular changes of advanced cancers during the chemotherapy treatment.

14. SUBJECT TERMS
Breast cancer diagnosis

15. NUMBER OF PAGES
160

16. PRICE CODE

17. SECURITY CLASSIFICATION OF REPORT	18. SECURITY CLASSIFICATION OF THIS PAGE	19. SECURITY CLASSIFICATION OF ABSTRACT	20. LIMITATION OF ABSTRACT
Unclassified	Unclassified	Unclassified	Unlimited

Table of Contents

Introduction.....

Diffuse optical tomography in the near infrared (NIR) is an emerging modality with potential applications in radiology and oncology [1-8]. Optical tomography with NIR light is made possible in a spectrum window that exists within tissues in the 700-900 nm NIR region, in which photon transport is dominated by scattering rather than absorption. Optical tomography offers insight into functional parameters, such as tumor angiogenesis, required for tumor growth and metastasis, tumor hypoxia, indicator of tumor response to various forms of therapy, and tumor metabolism. If a single optical wavelength is used, optical absorption related to tumor angiogenesis and other normal blood vessels can be measured. If two or more optical wavelengths are used, both oxy-hemoglobin and deoxy-hemoglobin concentrations can be measured simultaneously. However, optical tomography alone has not been widely used in clinical studies. The fundamental problem remains the intense light scattering in tissue, which makes the lesion localization difficult.

In general, localization or imaging based on tomographic inverse scattering approaches suffers from low spatial resolution and location uncertainty, and the inversion problem is, in general, underdetermined and ill-posed. The image reconstruction results depend on many parameters, such as the system signal-to-noise ratio, measurement geometry, regularization schemes used in inversion, etc. Thus to date, optical tomography has been limited to laboratory tests and case reports [2-7].

More recently, many research groups have investigated the use of *a priori* lesion structure information provided by other imaging modalities, such as ultrasound (US) [9-16,39], MRI [6], and X-ray mammography [44] to improve the localization of optical tomography. A flexible light guide using optical fibers makes optical imaging compatible with many other imaging modalities and allows for simultaneous imaging under identical geometric conditions. Furthermore, the lesion structure information provided by other modalities can be used to assist optical imaging reconstruction and therefore to reduce the location uncertainty and to improve the quantification accuracy of light. Our group has pioneered the hybrid optical tomography assisted with US to improve tomographic reconstruction [9-16,39,42,43]. Our unique approach employs a commercial ultrasound transducer and NIR optical imaging sensors mounted on a hand-held probe. The co-registered ultrasound is used for lesion localization and optical sensors are used for imaging tumor angiogenesis and tumor hypoxia. With the US localization, the entire imaging volume is thus segmented into lesion regions of a finer imaging grid and non-lesion regions of a coarse grid. As a result, the total number of imaging voxels with unknown optical properties is significantly reduced, and the inversion is well determined. In addition, since the lesion absorption coefficient is higher than that of background tissue, in general, the total absorption of the lesion over a smaller voxel is on the same scale as the total absorption of the background over a bigger voxel. Thus, our dual-mesh scheme further conditions the inversion by reconstructing total absorption distribution instead of absorption per se. The absorption distribution is obtained by dividing the total distribution with different voxel sizes in lesion and background regions, respectively. The dual-mesh algorithm has been tested in phantoms [80] and in a group of biopsy patients [15, 42]. Initial results with a group of biopsy patients have shown that early stage invasive cancers may be distinguished by a two-fold greater total hemoglobin concentration compared to fibroadenomas and other benign lesions [15, 42]. Preliminary results of advanced cancers have shown that the angiogenesis distribution is highly distorted and heterogeneous and the distorted distributions correlate with histological microvessel density counts [43].

Our unique approach uses ultrasound localization to overcome the poor localization problem that the diffused light has and thus significantly improves the sensitivity and specificity of optical tomography. Our

unique approach may have significant clinical applications on 1) breast cancer diagnosis; and 2) assessing treatment response and estimating treatment efficacy.

Beast cancer diagnosis and reduction in number of benign biopsies: The large number of biopsies performed for benign breast abnormalities has long been recognized as a serious problem [17]. In the 1970s, use of US as an adjunct to x-ray mammography decreased the number of biopsies for benign masses 25% - 35% by enabling reliable identification of simple cysts [18,19]) from solid lesions. In the 1980s, investigators reported US features that occurred more frequently in benign solid breast masses and other features that occurred more frequently in malignant masses [54-56]. However, in subsequent studies, US results were not yet reliable enough to determine whether biopsy should be performed on a solid US features that would be typical of either benign or malignant lesions [57]. This insufficient predictive value of ultrasound has prompted radiologists to recommend biopsies on most solid nodules, which result in a large number of biopsies yielding benign breast lesions. Currently 70 to 80 percent of such biopsies yield benign findings [58]. In addition, the diagnostic accuracy of ultrasound depends largely on the experience of physicians.

Optical tomography offers complementary functional parameters, such as tumor angiogenesis and hypoxia, when compared to conventional x-ray and ultrasound imaging techniques, and therefore has a great potential to assist the characterization of benign and malignant processes and reduce unnecessary normal biopsies.

Monitoring and assessing treatment response of neoadjuvant chemotherapy: Primary Systemic Therapy (PST) previously known as neo-adjuvant chemotherapy, is a valid form of therapy for women with breast cancer. Although to date there has been no survival advantage, it clearly improves the rate of breast conservation without compromising survival. It enables definition of tumor sensitivity in vivo thus allowing for potentially more effective treatments to be given to an individual if effective ways of monitoring response exist. Since complete pathologic response has been associated with improved survival, this endpoint is an important outcome measure. Because of these advantages, more groups are turning to this form of therapy as initial treatment even for earlier stage respectable breast cancer including the American College of Surgeons who are proposing three such trials.

However, factors that influence the response of cancers to presurgical chemotherapy are not completely understood [20]. Although recent trials reported clinical response rates >70%, only a small fraction of patients achieves a complete microscopic response to therapy, defined as an absence of gross viable tumor at definitive surgery after therapy [21-22]. Patients who achieve a microscopic complete response have a significantly better prognosis than patients left with residual tumor at the end of chemotherapy [22-23]. The evaluation of complete response is not reliably possible with any of the conventional anatomic methods such as palpation, mammography, and ultrasound [46,47,48,49]. Histologic findings of complete response correlate with palpation, ultrasound, or mammography in only 13-25% of cases [*46,48,49]*. In a study by Mumtaz et al., all patients in whom clinical criteria indicated complete response were found at histology to have residual tumor up to 6.5 cm in diameter [*93]*. In addition, the literature reveals contradictory statements regarding the individual techniques [46,50,48,51,52,49]. All three methods may over- or underestimate residual tumor size and the findings of the individual methods may not correlate with one another [46,50,48,51,53,52,49].

Despite the development of new techniques to characterize the biologic features of breast tumors, the factors influencing the quality of response to therapy remain obscure. Biological makers have shown an ability to

predict breast cancer response to only particular forms of therapy [24-26]. One of the factors that may influence response to systemic chemotherapy is tumor perfusion [27-28]. Tumors with relatively poor perfusion may not receive adequate delivery of systemic therapy. This lack of blood flow to the tumor may be a factor in poor response to intravenous chemotherapy [29]. Furthermore, underperfused tumors may be hypoxic [29-30]. Hypoxia has been implicated in the induction of biologic features associated with aggressive behavior and poor response to various forms of chemotherapy [31]. A recent publication in Nature Medicine using the angiogenesis inhibitor bevacizumab in patients with rectal cancer, has shown this therapy to be associated with improved oxygenation and reduced blood vessel permeability within the tumor [41]. This may result in improved delivery of chemotherapy to the tumor and reduction in metastatic potential. Ideally chemotherapy should be monitored during treatment as this could facilitate modification of the procedure at the time of the therapy to enable the lesion to be adequately treated. In addition, therapeutic agents that are highly molecularly targeted tend to induce arrest of caner cell growth and development but not necessary significant tumor shrinkage, at least in the short term [45]. Therefore, conventional anatomic methods including palpation, diagnostic ultrasound and mammography are not useful early indicators of response to these agents. Thus the demand for functional or molecular imaging methods that would give information about what is happening in the tumor at the molecular level is high [45].

Currently, new imaging techniques that are used to monitor and assess tumor response to chemotherapy include dynamic contrast-enhanced MRI [33,34], ^{15}O-water contrast-enhanced positron emission tomography (PET) [32], 99m Tc-sestamibi contrast-enhanced single-photon emission tomography (SPECT) [35,36], and Doppler sonography [37-38]. MRI, PET and SPECT require rather expensive systems and the Doppler sonography is limited to imaging large blood vessels. In current clinical practice, MRI or PET may only be used at the beginning and the end of chemotherapy leaving the entire treatment period completely unmonitored. Compared with Doppler sonography, which visualizes larger blood vessels, near-infrared diffused light probes tumor micro-vessel density, which is directly related to tumor angiogenesis distributions. In addition, optical tomography can provide tumor hypoxia distribution, which is highly valuable for assessing treatment efficacy. Furthermore, near-infrared systems are cost-effective, portable and can be easily coupled to clinical ultrasound systems for repeated imaging.

Body.....

Key Research Accomplishments.....

A. Developed the unique technique by simultaneously deploying near infrared sensors and an ultrasound transducer on a hand-held probe for breast cancer diagnosis [10,12,16].

B. Invented the unique dual-mesh imaging algorithm by segmenting the imaging medium into lesion region of a smaller voxel size and non-lesion region of a larger voxel size to improve the optical imaging reconstruction [14,39].

C. Demonstrated with more than 90 biopsy patients that early stage invasive cancers present two-fold greater total hemoglobin concentration than fibroadenomas and benign lesions [15],[42].

D. Demonstrated with large cancers that the angiogenesis distributions of larger cancers are highly distorted and heterogeneous and the hemoglobin concentration correlates with histological microvessel density counts [43].

E. **Demonstrated with advanced cancers that our unique technique may have a potential value to assess and monitor angiogenesis development during chemotherapy treatment [43].**

Reportable Outcomes.....

A. **Developed the unique technique by simultaneously deploying near infrared sensors and ultrasound transducer on a hand-held probe for breast cancer diagnosis [10, 12,16].**

Photon density waves launched from a source and detected by a detector travel a "banana" path, which can be visualized by Monte Carlo simulation shown in Fig. 2. In all figures, the horizontal axis is the propagation depth in centimeter and the vertical axis is the lateral dimension in centimeter. Source and detector positions are marked as S and D. The source-detector separations shown in (a), (b) and (c) are 2.8 cm, 4.1 cm and 5.5 cm, respectively. At each source location, 10,000,000 photons were generated. Each photon propagated in the medium, being absorbed or scattered. The color scale is the normalized absorption intensity. The optical properties of the medium used in simulation were absorption coefficient $0.03cm^{-1}$ and reduced scattering coefficient 6.0 cm^{-1}, which were representative values of breast tissue. As one can see, the photon density waves probe the medium over a large region. The high sensitivity region in both spatial and depth dimensions depends on the source-detector separation. For a detector located further from the source (Part (c)), the photon waves propagated wider and deeper can be detected. With many source and detector pairs of different separations shown in Fig. 1(b), the photon density waves can probe the medium underneath and be detected with high sensitivity. Ultrasound is a coherent imaging modality and the sound waves propagate into the medium along a straight path and reflected waves from lesions underneath are used for forming images. Therefore, sensors of two modalities probe the medium underneath although the sensor locations are offset on the probe. Therefore, the two modalities have unique synergy not only in providing complementary structure and function information of the lesion but also in optimization of sensor locations.

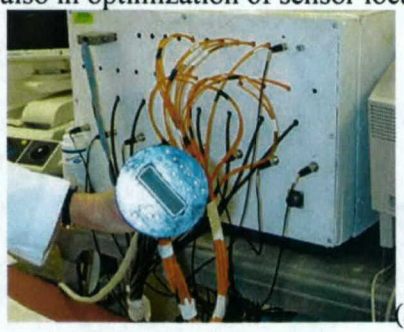

(a)

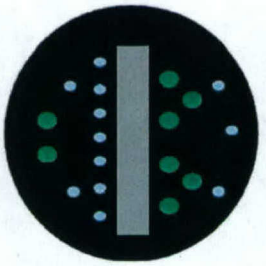

(b)

Fig. 1. (a) First prototype of our hand-held combined probe and a frequency domain NIR optical imager. (b) Sensor distribution of the combined probe. The diameter of the combined probe is 10 cm. Smaller circles are optical source fibers and big circles are detector fibers. A commercial ultrasound probe is located at the center.

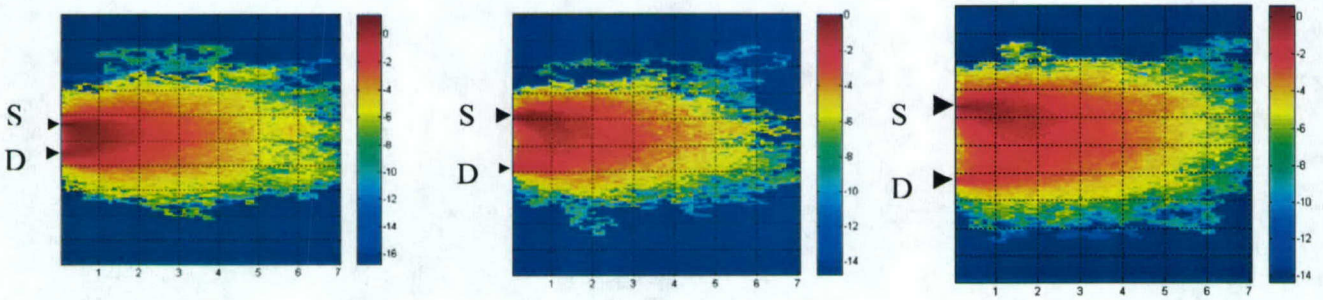

Fig. 2. Monte Carlo simulation demonstrating photon propagation path lunched from a source and detected by a detector. (a) source-detector separation is 2.8 cm. (b) source-detector separation is 4.1 cm. (c) source-detector separation is 5.5 cm.

The technical aspects of our NIR imager have been described in detail in Ref. [10]. Briefly, the imager consisted of 12 pairs of dual wavelength (780nm and 830nm) laser diodes, which were used as light sources, and their outputs were coupled to the probe through optical fibers. On the receiving side, 8 photomultiplier (PMT) tubes were used to detect diffusely scattered light from the tissue and 8 optical fibers were used to couple detected light to the PMTs. The laser diodes' outputs were amplitude modulated at 140 MHz and the detector outputs were demodulated to 20KHz. Eight detection signals and one reference were amplified, sampled and acquired into a PC simultaneously. The entire data acquisition took about 3 to 4 seconds, which was fast enough for acquiring data from patients.

B. Invented the unique dual-mesh imaging algorithm by segmenting the imaging medium into lesion region of smaller voxel size and non-lesion region of larger voxel size to improve the optical imaging reconstruction [14,39].

The details of our dual-mesh optical imaging reconstruction algorithm have been described previously [14,39]. Briefly, the optical tomographic reconstruction takes advantages of US localization of lesions and segments the imaging volume into finer grid in US identified lesion region and coarser grid in non-lesion regions (see Fig.3). To account for possible larger angiogenesis extension of ultrasound-identified lesions, we have used a much larger region of interest (ROI) for finer grid lesion mapping. Therefore, the exact lesion shape is not important and an elliptical ROI is used in imaging reconstruction. In all images, 0.5 cm $\times 0.5$ cm $\times 0.5$ cm imaging grid was used for lesion region and 1.5cm $\times 1.5$cm $\times 1$ cm was used for background region. A modified Born approximation is used to relate the scattered field $U_{sd}(r_{si}, r_{di}, \omega)$ measured at the optical source (s) and detector (d) pair i to light absorption variations $\Delta\mu_a^{\lambda}(r')$ of wavelength λ in each volume element of two regions within the sample. The matrix form of image reconstruction is given by

$$[U_{sd}]_{M\times 1} = [W_L, W_B]_{M\times N}[M_L, M_B]^T{}_{N\times 1} \qquad (1)$$

where W_L and W_B are weight matrices for lesion and background regions, respectively; $[M_L] = [\int_{1_L} \Delta\mu_a^{\lambda}(r')d^3r', \ldots\ldots \int_{N_L} \Delta\mu_a^{\lambda}(r')d^3r']$ and $[M_B] = [\int_{1_B} \Delta\mu_a^{\lambda}(r')d^3r', \ldots\ldots \int_{N_B} \Delta\mu_a^{\lambda}(r')d^3r']$ are total absorption distributions of lesion and background regions, respectively. The weight matrices are calculated based on the background absorption $\overline{\mu}_a^{\lambda}$ and reduced scattering $\overline{\mu}_s'^{\lambda}$ measurements obtained from the normal contralateral breast. Instead of reconstructing $\Delta\mu_a^{\lambda}$ distribution directly, as is done in the standard Born approximation, the total absorption distribution M is reconstructed and the total is divided by different voxel sizes of lesion and background tissue to obtain $\Delta\mu_a^{\lambda}$ distribution. By choosing a finer grid for lesion and a coarse grid for background tissue, we can maintain the total number of voxels with unknown optical absorption on the same scale of the total measurements. As a result, the inverse problem is less underdetermined. In addition, since the lesion absorption coefficient is higher than that of background tissue, in general, the total absorption of the lesion over a smaller voxel is on the same scale as the total absorption of the background over a bigger voxel. Therefore, the matrix $[M_L, M_B]$ is appropriately scaled for inversion. In addition, we have incooperated a scaling factor to correct depth dependence of the weight matrix W and large phantoms can be imaged uniformly in propagation direction or depth [39]. The reconstruction is formulated as a least square problem and the unknown distribution M is iteratively calculated using the standard conjugate gradient method. In general, only three iterations are needed for the algorithm to converge to a stable solution.

Since the major chromophores are deoxygenated (deoxyHb) and oxygenated (oxyHb) hemoglobin in the wavelength range studied, we can estimate deoxyHb and oxyHb concentrations at each imaging voxel by inverting the following equations voxel by voxel as:

$$\begin{bmatrix} \mu_a^{\lambda_1}(r') \\ \mu_a^{\lambda_2}(r') \end{bmatrix} = \begin{bmatrix} \varepsilon_{Hb}^{\lambda_1}, \varepsilon_{HbO_2}^{\lambda_1} \\ \varepsilon_{Hb}^{\lambda_2}, \varepsilon_{HbO_2}^{\lambda_2} \end{bmatrix} \times \begin{bmatrix} deoxyHb(r') \\ oxyHb(r') \end{bmatrix} \tag{2}$$

$$\begin{bmatrix} deoxyHb(r') \\ oxyHb(r') \end{bmatrix} = \frac{1}{\Delta} \begin{bmatrix} \varepsilon_{HbO_2}^{\lambda_2}, -\varepsilon_{HbO_2}^{\lambda_1} \\ -\varepsilon_{Hb}^{\lambda_2}, \varepsilon_{Hb}^{\lambda_1} \end{bmatrix} \times \begin{bmatrix} \mu_a^{\lambda_1}(r') \\ \mu_a^{\lambda_2}(r') \end{bmatrix}. \tag{3}$$

where $\mu_a^{\lambda_1}(r')$ and $\mu_a^{\lambda_2}(r')$ are absorption coefficients obtained at imaging voxel r', where wavelengths λ_1 and λ_2 correspond to 780 nm and 830 nm in our system, respectively. ε s are extinction coefficients given in Ref. [40]. The total hemoglobin concentration $totalHb(r') = deoxyHb(r') + oxyHb(r')$ and oxygenation saturation $Y\% = \dfrac{oxyHb(r')}{oxyHb(r') + deoxy(r')} 100\%$ can be calculated as:

$$totalHb(r') = \frac{1}{\Delta} \left\{ \{\varepsilon_{HbO_2}^{\lambda_2} - \varepsilon_{Hb}^{\lambda_2}\} \mu_a^{\lambda_1}(r') + \{\varepsilon_{Hb}^{\lambda_1} - \varepsilon_{HbO_2}^{\lambda_1}\} \mu_a^{\lambda_2}(r') \right\} \tag{4}$$

and

$$Y\% = \frac{-\varepsilon_{Hb}^{\lambda_2} \dfrac{\mu_a^{\lambda_1}(r')}{\mu_a^{\lambda_2}(r')} + \varepsilon_{Hb}^{\lambda_1}}{(\varepsilon_{HbO_2}^{\lambda_2} - \varepsilon_{Hb}^{\lambda_2}) \dfrac{\mu_a^{\lambda_1}(r')}{\mu_a^{\lambda_2}(r')} - (\varepsilon_{HbO_2}^{\lambda_1} - \varepsilon_{Hb}^{\lambda_1})} 100\% , \tag{5}$$

where $\Delta = \varepsilon_{Hb}^{\lambda_1} \varepsilon_{HbO_2}^{\lambda_2} - \varepsilon_{HbO_2}^{\lambda_1} \varepsilon_{Hb}^{\lambda_2}$. The maximum lesion total hemoglobin concentration was measured and the background total hemoglobin concentration was computed outside the finer-grid imaging region. To quantify the spatial extension of the angiogenesis distribution, we have measured the full width at half maximum (FWHM) in x and y spatial dimensions and computed the geometric mean, referred as FWHM in the proposal.

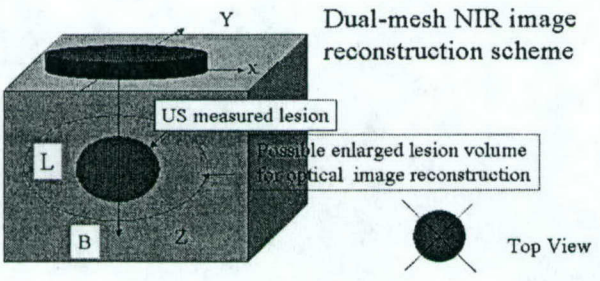

FIG.3. Illustration of the dual-mesh optical imaging reconstruction with the assistant of ultrasound lesion mapping. the entire imaging volume is segmented into lesion (L) and background regions (B) and the finer imaging grid is used for lesion region and coarse grid is used for background. To account for possible larger angiogenesis extension of the ultrasound-identified lesions, we have used a much larger region of interest (ROI) than US identified one for finer grid lesion mapping. In general, an elliptical ROI is used in optical imaging reconstruction.

C. Demonstrated with more than 90 biopsy patients that early stage invasive cancers present two-fold greater total hemoglobin concentration than fibroadenomas and benign lesions [15],[42].

The first example is obtained from a 55-year-old woman. Figure 4 (a) shows a gray scale ultrasound image of a non-palpable lesion. The lesion was located at the 4 o'clock position of the right breast. The ultrasound showed a nodular mass with internal echoes and the lesion was considered suspicious. The estimated lesion diameters measured from two orthogonal ultrasound images was 8 mm. An ultrasound-guided core needle biopsy was recommended and biopsy result revealed that the lesion was intraductal and infiltrating ductal carcinoma (nuclear grade II, histological grade III). The cancer once removed from the breast measured 1 cm in greatest diameter and was composed predominantly of invasive carcinoma (>95%), extending to surgical margins. Negative margins were achieved upon re-excision.

The optical absorption maps at 780nm and 830 nm are shown in Fig. 4(b) and (c), respectively. In both (b) and (c), the first slice is 0.7 cm deep into the breast tissue from the skin surface and the last slice is closer to the chest wall. The spacing of the slices is 0.5 cm. The horizontal and vertical axes of each slice are spatial x and y dimensions of 9 cm in size. The lesion is well resolved in slice #5 and has shown much larger spatial extension at 830 nm than that at 780 nm. The measured maximum absorption coefficients are μ_a^{780}=0.24 cm^{-1} and μ_a^{830}=0.28 cm^{-1}, respectively, and the absorption maximums at both wavelengths are located at (0, 1.0, 2.25) cm, which is close to the lesion center measured by ultrasound. The total hemoglobin distribution of the lesion is shown in Fig.4 (d). The measured maximum total hemoglobin concentration for lesion is 122.03 μmoles, and the measured average background hemoglobin concentration is 13.73 μmoles. The spatial extension of lesion's angiogenesis is measured from the FWHM of the total hemoglobin map and it is estimated to be 2 cm. This number is about two times larger than the 8 mm diameter measured by ultrasound and indicates that optical contrasts extend well beyond the cancer periphery because of angiogenesis.

Another example was obtained from a 56-year-old woman who had a non-palpable lesion located at the 10 o'clock position of the left breast. Ultrasound showed a solid mass with internal echoes measuring 9 mm in size and the lesion was considered suspicious (see Fig.5 (a)). An ultrasound guided core needle biopsy was recommended and biopsy results revealed that the lesion was in-situ and invasive ductal carcinoma with ductal and lobular features (nuclear grade II, histological grade II). The tumor once removed from the breast measured 1.5 cm in greatest diameter and was composed predominantly of invasive carcinoma (>80%), extending to inferior/anterior surgical margin. Negative inferior margin was achieved upon re-excision.

The total hemoglobin concentration map is shown in Fig.5 (b). In (b), the first slice is 0.4 cm deep into the breast tissue from the skin surface and the last slice is closer to the chest wall. The spacing between the slices is 0.5 cm. This lesion is well resolved in slice #4 with maximums value located at (0 1.0 1.9) cm, which is very close to the lesion center measured by ultrasound. The calculated maximum total hemoglobin concentration of the lesion is 127.60 μmoles, and the background concentration is 24.16 μmoles.

Example of fibroadenoma

Figure 6 (a) shows an ultrasound image of a hypoechoic mass of a 37-year-old woman. The diagnosis was that the lesion likely was a fibroadenoma; however, there was concern that the lesion could be a carcinoma because of the irregular shape and the posterior shadowing seen by ultrasound. An ultrasound guided core breast biopsy revealed that the lesion was simply a fibroadenoma. Total hemoglobin distribution maps are shown in (b). Compared with the invasive cancer cases, the spatial distribution of total hemoglobin is quite

diffused and the calculated maximum total hemoglobin concentration is 52 μmoles and the background hemoglobin concentration is 14 μmoles.

The initial statistics of maximum total hemoglobin concentration of three groups obtained from 19 cases are given in Ref 15 and shown in Fig. 7(a). The invasive cancer group of 2 cases has shown a mean maximum of 119 μmoles (± 1.6 μmoles), while the benign group of fibroadenoma (15 cases) and hyperplasia (1 case) has a mean maximum of 67 μmoles (± 17.0 μmoles). One combined fibroadenoma and fibrocystic change with non-invasive neoplasia/carcinoma in situ case has a maximum of 48 μmoles. The malignant group presents about two-fold greater hemoglobin concentration than that of the benign group. Recently, we have completed a large-scale clinical study at Hartford Hospital [42]. New results obtained from 8 earlier stage invasive carcinomas and 73 benign lesions of 6 groups have further demonstrated that on average malignant cancers present more than two-fold greater total hemoglobin concentration than benign lesions (see Fig.7 (b)). The mean maximum values of total hemoglobin concentration of the malignant and benign groups are 123 μmoles (± 26.8) and 58 μmoles (± 24.5), respectively. The sensitivity, specificity, positive predictive value, and negative predictive value of this group of patients are 100%, 96%, 73%, and 100%. We have also shown that optical tomography provides much higher sensitivity and specificity than Doppler US because it probes tumor microvessel density.

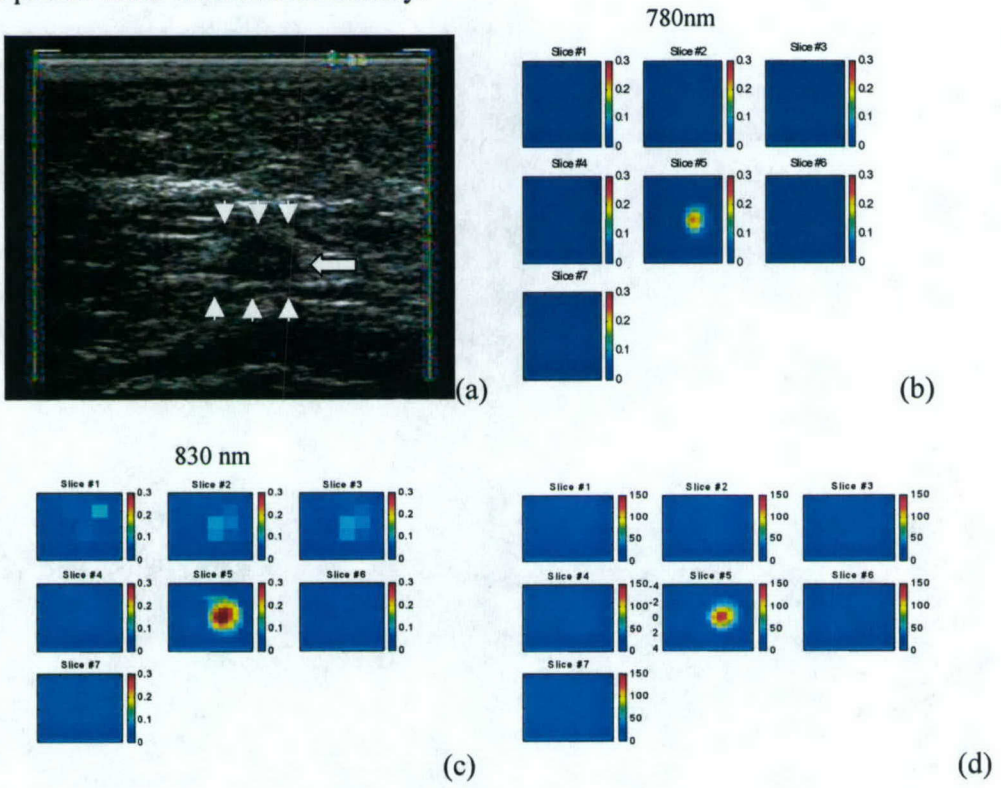

Fig. 4. (a) shows a gray scale ultrasound image of a non-palpable lesion of a 55-year-old woman. The lesion pointed by the arrow was located at the 4 o'clock position of the right breast measuring 8 mm in diameter. Ultrasound showed nodular mass with internal echoes and the lesion was considered suspicious. (b) and (c) are optical absorption maps at 780 nm and 830 nm, respectively. x and y axes are spatial dimensions of 9 cm by 9 cm. The slices beginning from left to right correspond to absorption maps from 0.7 cm underneath skin surface to chest wall in 0.5 cm spacing. (d) is the total hemoglobin concentration and the vertical scale is in micro moles ranging from 0 to 150 [from Ref. 15].

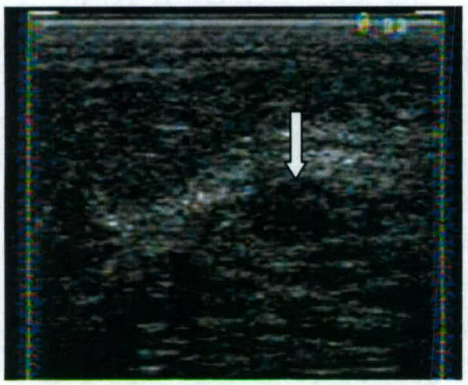

(a)

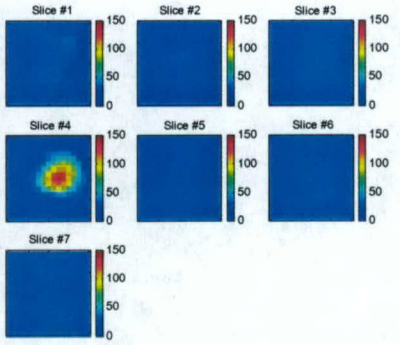

(b)

Fig. 5. This example was obtained from a 56-year-old woman who had non-palpable 9 mm lesion located at the 10 o'clock position of the left breast. An ultrasound guided core needle biopsy revealed an in-situ and invasive ductal carcinoma with ductal and lobular features (nuclear grade II, histological grade II). (b) is the total hemoglobin concentration and the vertical scale is in micro moles ranging from 0 to 150 [from Ref.15].

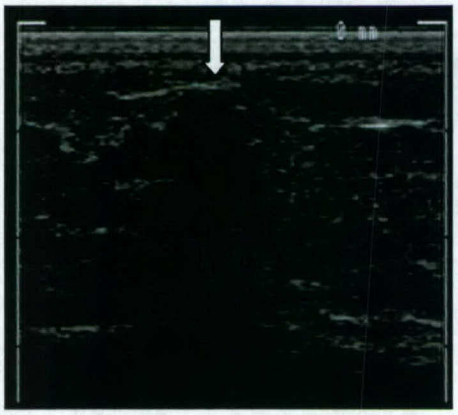

(a)

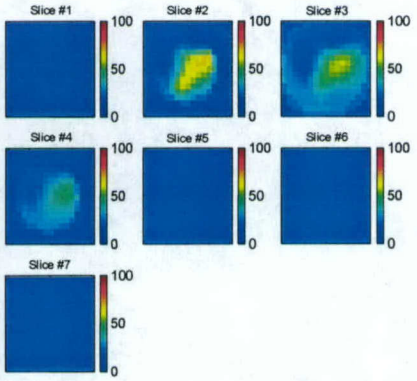

(b)

Fig.6. An ultrasound image of a solid hypoechogenic lesion located at 9 to 10 o'clock position of a 37-year-old woman. The diagnosis was that the lesion could represent fibroadenoma, however, there was a chance that the lesion could be a carcinoma because of the irregular shape and posterior shadow seen by ultrasound. An ultrasound guided core breast biopsy revealed that the lesion was simply a fibroadenoma. (b) is the total hemoglobin concentration and the vertical scale is in micro moles ranging from 0 to 100 [From Ref.15].

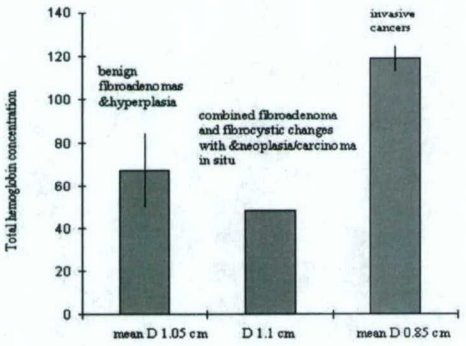

(a)

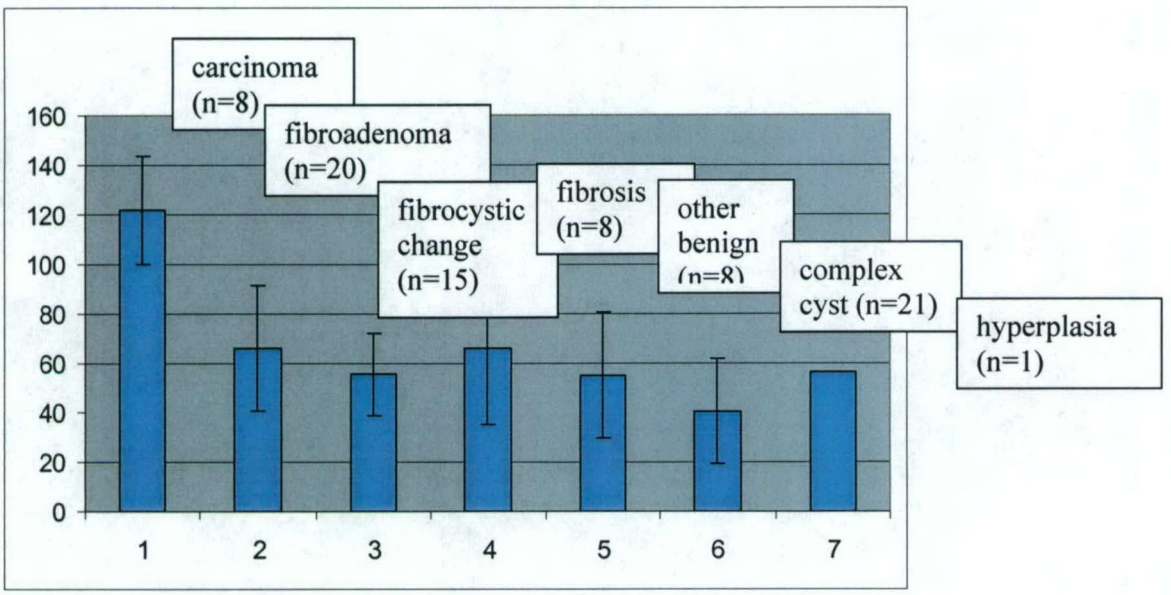

(b)

Fig. 7. (b) Graph indicates mean value of maximum total hemoglobin concentration of each group and standard deviation (bar). Horizontal: group numbers. Vertical: total hemoglobin concentration in μ mol/liter

D. Demonstrated with advanced cancers that the angiogenesis distributions of larger cancers are highly distorted and heterogeneous and the hemoglobin concentration correlates with histological microvessel density counts [43].

During the diagnostic imaging study, we imaged a patient who was undergoing chemotherapy. This 44-year-old woman had a large 4 cm x 4 cm x 1.5 cm palpable mass (Fig.8(a)) located at the 6 to 8 o'clock position of the left breast. The lesion center was approximately 1.5 cm in depth relative to the skin. The lesion was considered as highly suspicious for malignancy and an ultrasound guided needle biopsy revealed that the lesion was a high-grade invasive carcinoma with necrosis. The total hemoglobin concentration map is shown in Fig.8 (b) and the distribution is highly heterogeneous with high concentration distributed at the cancer periphery. Slice 1 is the spatial x-y image of 9 cm x 9 cm obtained at 0.5 cm deep from the skin surface. Slice 7 is 3.5 cm deep toward the chest wall and the spacing between slices is 0.5 cm. The maximum and average, measured within finer lesion mesh region, hemoglobin concentrations are 92.1 μ moles and 26.2 μ moles. Since this cancer was too large for breast conserving surgery, the patient was treated with chemotherapy in the neo-adjuvant setting for three months. At the time the patient completed the chemotherapy, we imaged her tumor again with the combined probe. Fig.8 (c) is the ultrasound image of the cancer three month later and the cancer contrast was poor and cancer boundaries were completely unclear probably due to treatment. Fig.8 (d) is the total hemoglobin distribution. The maximum and average hemoglobin concentrations of the lesion are 79.03 μ moles and 24.9 μ moles, respectively. Compared with the images acquired before treatment, the spatial extension of the angiogenesis pattern is much smaller and more confined to the core area. The maximum total hemoglobin concentration is reduced by about 10 μ moles and the average is about the same as before. This example clearly demonstrates the feasibility of monitoring the treatment using the combined technique.

To correlate the optical tomography images with vessel densities, we have performed micro-vessel density counts. Three sections from tissue obtained at breast-conservation surgery marked with lateral, anterior,

posterior positions were used for counting. Sections 3 to 5 micrometer thick were stained on an immunohistochemistry slide staining system (DAKO autostainer) with factor 8/86 mouse monoclonal antibody (anti-human von Willebrand factor, DAKO Corp, Carpinteria, Calif) at 1:100 dilution digested by proteinase K for 3 minutes, by labeled polymers (DAKO EnVision plus) immunoperoxidase method. The microvessel density counts were performed in ten consecutive fields with the use of an ocular grid at X200 magnification. The first field chosen was a hotspot (area of maximum vascular density either within the infiltrating tumor mass or at the tumor-stromal interface). The total number of microvessels were 196 (lateral), 114 (anterior) and 48 (posterior) per 10 consecutive fields, respectively. These high counts obtained from lateral and anterior positions correlate well with the high total hemoglobin concentration distributions shown in slices 3 in Fig. 8(d), and low counts obtained from posterior sample correlates with lower distributions seen in slices 4 and 5 in Fig. 8 (d). A representative section demonstrating high micro-vessel density is shown in Fig.8 (e).

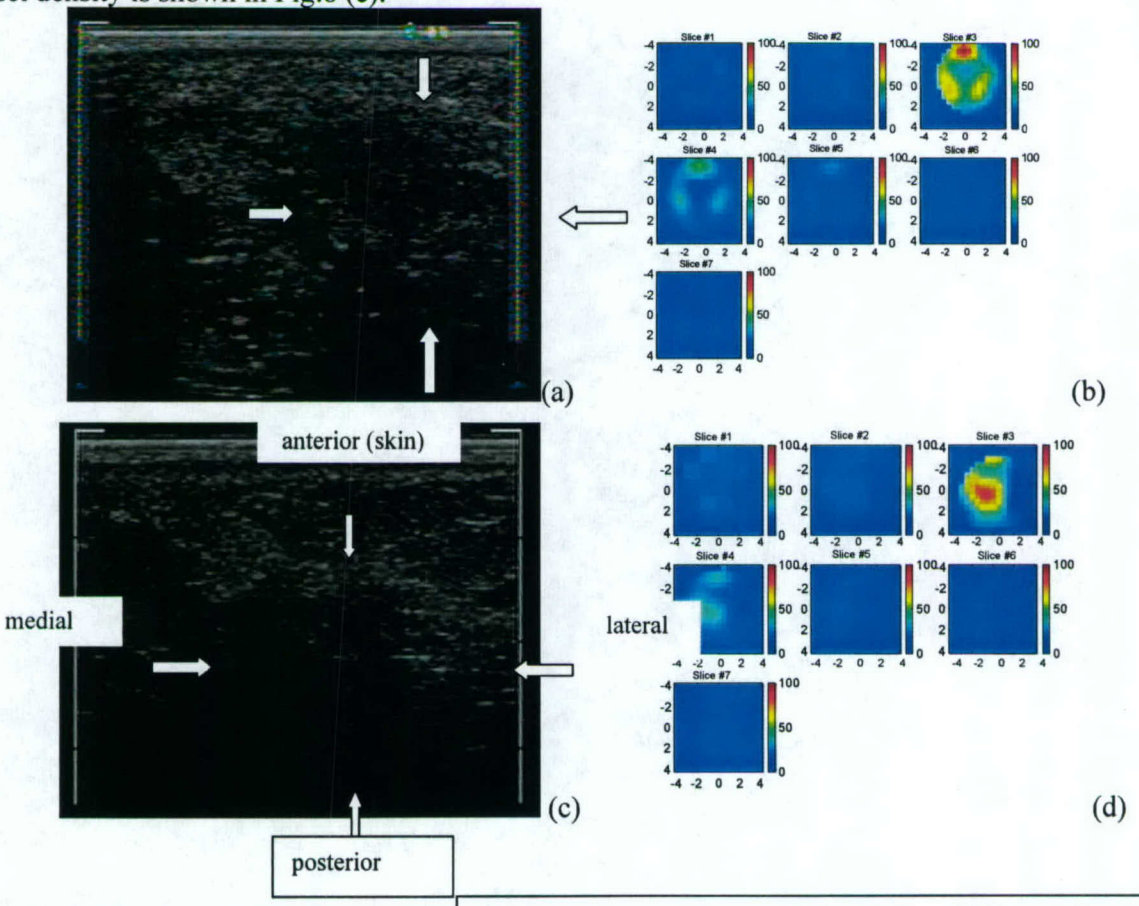

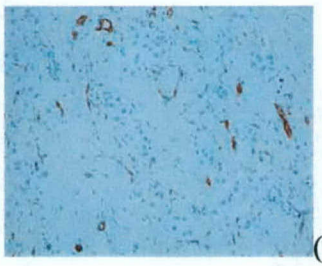
(e)

Fig.8. (a) Ultrasound image of a 4 cm by 4 cm high-grade invasive carcinoma with necrosis. (b) Total hemoglobin concentration of the lesion. Slice 1 is x-y image of 9 cm by 9 cm obtained at 0.5 cm depth from the skin surface and slice 7 is 3.5 cm deep toward the chest wall. The spacing between the slices is 0.5 cm. **Slices are from left to right and top to bottom.** (c) Ultrasound image of the same cancer treated with chemotherapy for three months. (d) Total hemoglobin concentration of the lesion (e) Representative section of the carcinoma demonstrating high microvessel density .

The second imaging example was obtained from a 47-year-old woman who had a 3 cm x 3 cm x 2 cm dominant mass at the 2 o'clock position in her left breast. The lesion center was about 2.3 cm in depth relative to the skin. Ultrasound showed hypoechoic mass with irregular margins (see Fig. 9(a)) and the lesion was considered as highly suspicious for malignancy. Figure 9(b) is the total hemoglobin concentration distribution which is highly heterogeneous. The measured maximum total hemoglobin concentration of the tumor and average are 40.6 μ moles and 17.2 μ moles, respectively. Surgical pathology report revealed that the mass was infiltrating carcinoma (histological grade II, nuclear grade II) with low mitotic activity. The total counts of microvessels obtained from anterior and posterior core biopsy samples were 61 and 40 per 10 consecutive fields, respectively. The total counts measured from anterior and posterior surgical samples were 52 and 29, respectively. These low counts correlate well with the low optical absorption shown in Fig. 9 (b) and indicate that the tumor was poorly perfused. Representative histological sections of these two examples are shown in Fig.9(c). **These two examples clearly demonstrate that angiogenesis distributions non-invasively obtained from optical tomography/US correlate with microscopic angiogenesis distributions and our technique has a great potential for assessing tumor perfusion and therefore predicting treatment responses.**

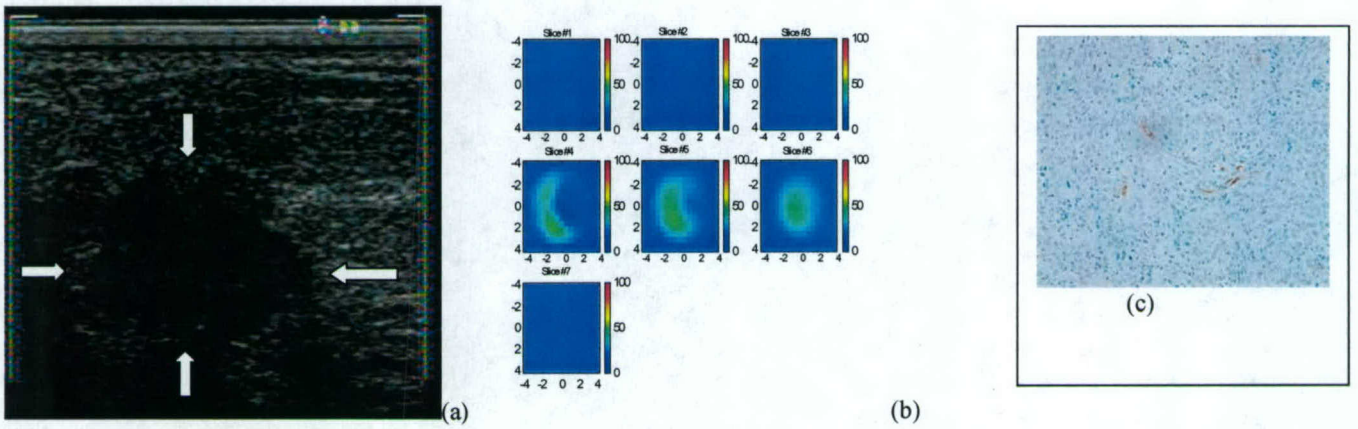

Figure 9 (ID5P4 data). (a) Ultrasound image of a 47-year-old woman with a highly suspicious lesion located at 2'oclock position of her left breast. (b) Total hemoglobin concentration of the lesion. (c) Representative section of infiltrating ductal carcinoma of breast demonstrating low microvessel density (original magnification X200; anti-human von Willebrand factor, DAKO EnVision plus).

E. **Demonstrated with advanced cancers that our unique technique may have a potential value to assess and monitor angiogenesis development during chemotherapy treatment [43].**

This example was obtained from a 46 year-old woman who had a swollen left breast of two months duration with mild erythema of the skin overlying the lower inner quadrant. No discrete mass was palpable. An incisional biopsy from the lower inner quadrant showed a poorly differentiated infiltrating ductal carcinoma. PET imaging (see Fig. 10) obtained before her chemotherapy treatment (Fig.10 (a)) revealed that the cancer had metastasized to lymph nodes and spinal code. The cancer was quite diffuse occupying the entire breast. The patient was treated with adriamycin-based chemotherapy. We identified the upper quadrant mass from ultrasound and monitored the angiogenesis and oxygen saturation changes with the hybrid technique during her chemotherapy treatment. Figure 11(a), (b) and (c) are ultrasound images acquired at the beginning,

during the fourth cycle of chemotherapy, and before definitive surgery, (d), (e) and (f) are corresponding total hemoglobin changes, and (g), (h) (i) are corresponding oxygen saturation maps. The oxygen saturation is represented as per cent oxyHb/totalHb with 100% as the maximal value. The peak hemoglobin concentration has significantly reduced from 255.3, 147.5 to 76.9 in unit of μ mol/liter and also in spatial extension. The measured FWHM at the depth closer to the chest wall (slice #6 in figure 11) has dropped from 2.7 cm, 2.6 cm to the size, which is not measurable. High oxygen saturation was noted in the tumor initially near chest-wall region (slice 6 &7) and rapidly fell to deoxygenated levels (blue color). Microvessel count obtained from core biopsy sample was 190 which correlates with high hemoglobin concentration seen in Fig. 11(d). Microvessel counts of surgical samples obtained from anterior and posterior were 111 and 68 which correlate with higher and lower hemoglobin images seen in slice 4 and 6 of Fig.11(f). PET imaging showed a complete response to chemotherapy (see Fig.10(b)). Upon completion of neoadjuvant chemotherapy, the patient underwent left modified radical mastectomy. The pathology report indicated no viable malignant cells in the upper quadrant region that we imaged.

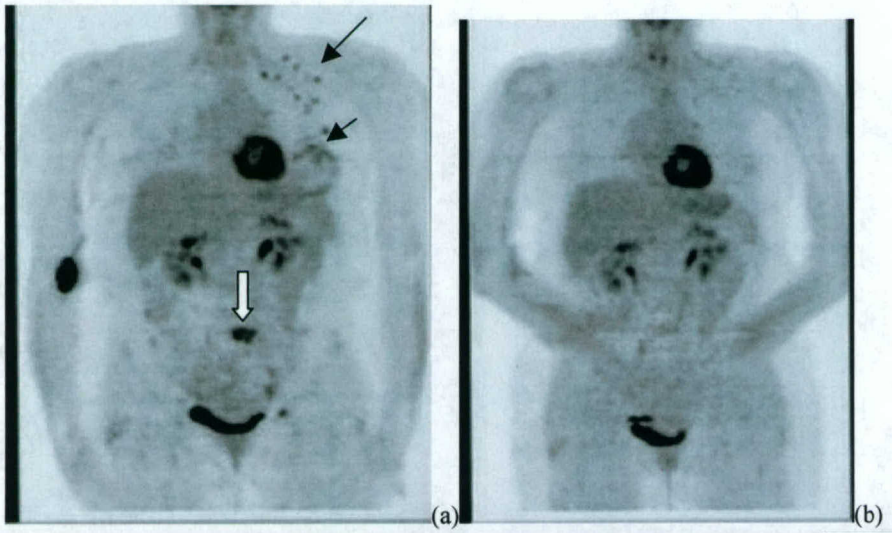

Fig 10. PET images. (a) Image acquired before chemotherapy. The ductal carcinoma in the left breast is pointed by the small black arrow and positive lymph notes (black dots) are pointed by the longer black arrow. The positive spinal code is pointed by the white arrow. (b) Image acquired after 6 cycles of chemotherapy before the definitive surgery. The activities of carcinoma in the left breast, positive lymph notes, and positive spinal code are no-longer visible.

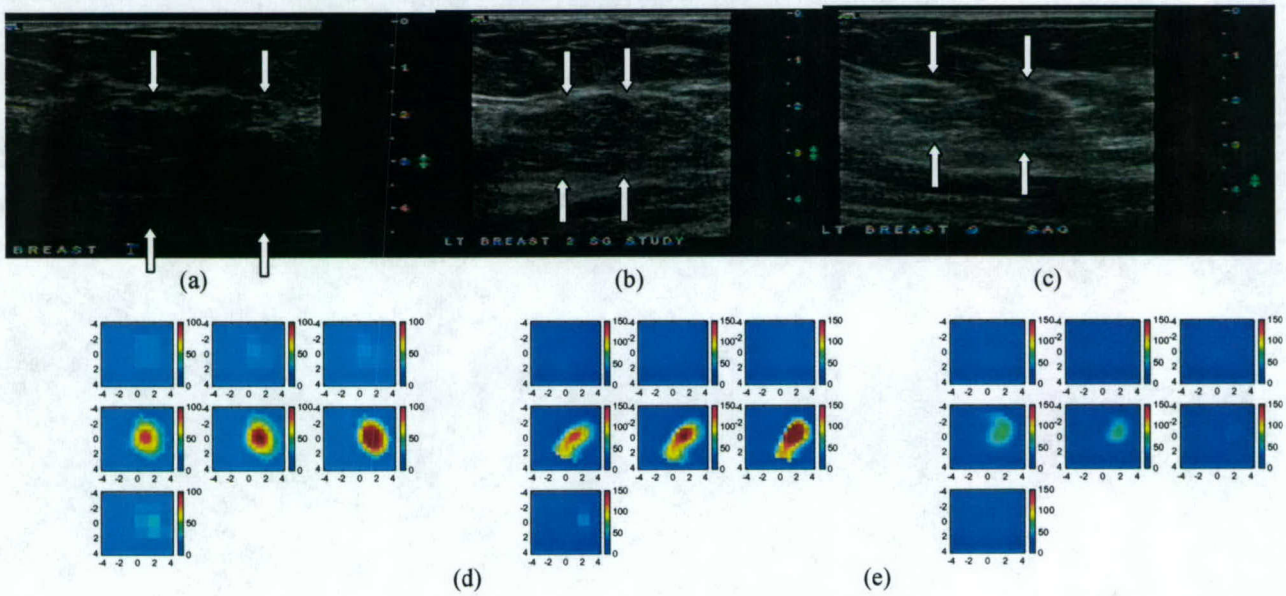

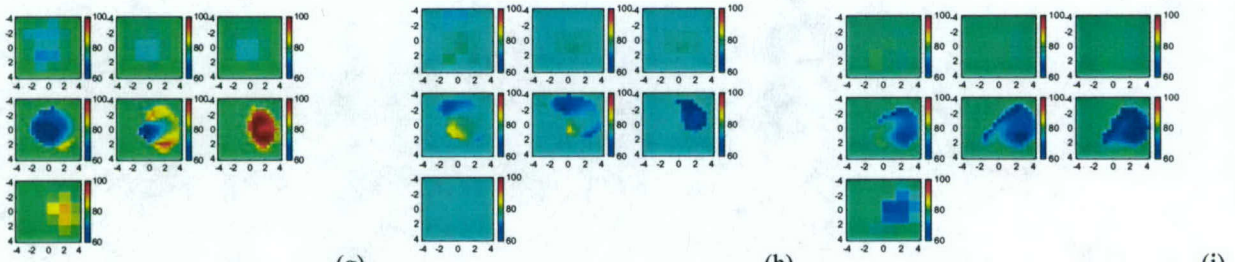

(g) (h) (i)

Fig.11. US images acquired at the beginning (a), 4th cycle (b) and end (c) of chemotherapy. (d), (e) and (f) are corresponding NIR hemoglobin concentrations, while (g), (h) and (i) are oxygen saturation maps. The slices in (d)-(i) are numbered from left to right and top to bottom.

Conclusions.....

Optical tomography with ultrasound localization demonstrated its great potential in distinguishing benign from smaller malignant tumors [15,42]. The invasive cancer cases reveal about twofold greater total hemoglobin concentration than benign cases, and suggest that discrimination of benign and malignant breast lesions might be enhanced by this type of achievable optical quantification with ultasound localization. Furthermore, the small invasive cancers are well localized and have wavelength-dependent appearance in optical absorption maps, while the benign lesions appear diffused and relatively wavelength independent.

The technique has additional benefits when studying larger tumors and it maps tumor vascularity and tumor hypoxia [43]. These indices can be followed before and during theraputic interventions. It has been shown that tumor hypoxia is related to the growth rate and chemotherapeutic responsiveness of tumors [41]. The ability to demonstrate and follow these parameters before and during therapy non-invasively could prove invaluable in choosing tailored treatments especially in the era of new drugs targeting angiogenesis.

References.....

1. Yodh A and Chance B (1995). Spectroscopy and imaging with diffusing light. Phys. Today. **48**, 34-40.
2. Tromberg B, Shah N, Lanning R, Cerussi A, Espinoza J, Pham T, Svaasand L, and Butler J (2000). Non-Invasive in vivo characterization of breast tumors using photon migration spectroscopy. Neoplasia vol.2, No 1:2: 26-40.
3. Franceschini MA, Moesta KT, Fantini S, Gaida G, Gratton E, Jess H, Seeber M, Schlag PM, Kashke M (1997). Frequency-domain techniques enhance optical mammography: initial clinical results. Proc. of Nat. Ac. of Sci., 94: 6468-6473.
4. Pogue B, Poplack SP, McBride TO, Wells WA, Osterman K, Osterberg U, and Paulsen KD (2001). Quantitative hemoglobin tomography with diffuse near-infrared spectroscopy: pilot results in the breast. Radiology, 218: 261-266, 2001.
5. Dehghani H, Pogue B, Poplack SP, and Paulsen KD (2003). Multiwavelength three-dimensional near-infrared tomography of the breast: initial simulation, phantom, and clinical results. Applied Optics, 42 (1), 135-145.

6. Ntziachristos V, Yodh A, Schnall M., and Chance B (2000). Concurrent MRI and diffuse optical tomography of breast after indocyanine green enhancement. Proc. of Nat. Ac. of Sci., 97 (6), 2267-2772.
7. Jiang H, Xu Y, Iftimia N, Eggert J, Klove K, Baron L and Fajardo L (2001). Three-dimensional optical tomographic imaging of breast in a human subject. IEEE Trans on Medical Imaging, 20(12), 1334-1340.
8. Jholboke M, Tromberg B, Li X, Shah N, Fishkin J, Kidney D, Butler J, Chance B, and Yodh A (2000). Three-dimentional diffuse optical mammography with ultrasound localization in a human subject. Journal of Biomedical Optics 5(2), 237-247.
9. Zhu Q, Dunduran T, Holboke M, Ntziachristos V and Yodh A(1999). Imager that combines near infrared diffusive light and ultrasound. Optics Letters, **24**(15), 1050-1052.
10. Chen NG, Guo PY, Yan SK, Piao DQ, and Zhu Q (2001). Simultaneous near infrared diffusive light and ultrasound imaging. Applied Optics, **40** (34), 6367-6380.
11. Zhu Q, Conant E, and Chance B (2000). Optical imaging as an adjunct to sonograph in differentiating benign from malignant breast lesions. Journal of Biomedical Optics, **5** (2), 229-236.
12. Zhu Q, Chen NG, Piao DQ, Guo PY and Ding XH (2001). Design of near infrared imaging probe with the assistance of ultrasound localization. Applied Optics, **40**(19), 3288-3303.
13. Chen NG and Zhu, Q "Characterization of small absorbers inside turbid media," Optics Letters, Vol 27, No. 4, pp 252-254 (2002).
14. Zhu Q, Chen NG, Kurtzman HS (2003). Imaging tumor angiogenesis by the use of combined near infrared diffusive light and ultrasound. Optics Letters, **28** (5), 337-339.
15. Zhu Q, Huang MM, Chen NG, Zarfos K, Jagjivan B, Kane M, Kurtzman SH, "Optical imaging combined with sonography can differentiate early stage invasive breast cancers from benign lesions," Neoplasia, 5(5): 379-388, 2003.
16. Chen NG, Huang MM, Xia HJ, Piao DQ, Cronin E, and Zhu Q, "portable near infrared diffusive light imager for breast cancer detection," Journal of Biomedical Optics, May/June, 9(3):504:510 , 2004.
17. Howard J. Using mammography for cancer control: an unrealized potential. Cancer 1987; 33:33-48.
18. Hilton SW, Leopold GR, Olson LK, Willson SA. Real-time breast sonography: application in 300 consecutive patients. AJR 1986; 147:479-486.
19. Rubin E, Miller VE, Berland LL, Han SY, Koehler RE, Stanley RJ. Hand-held real-time breast sonography. AJR 1985; 144:623-627.
20. Mankoff DA, Dunnwald LK, Gralow JR, Ellis GK, Charlop A, Lawton TJ, Schubert EK, Tseng J, Livington RB, "Blood Flow and Metabolism in Locally Advanced Breast Cancer: Relationship to Response to Therapy," Journal of Nuclear Medicine, 2002, Vol. 43 No. 4: 500-509.
21. Booser DJ, Hortobagyi GN. , "Treatment of locally advanced breast cancer," Semin Oncol. 1992, 19: 278-285.
22. Feldman LD, Hortobagyi GN, Buzdar AU, Ames FC, Blumenschein GR, "Pathological assessment of response to induction chemotherapy in breast cancer," Cancer Res. 1986; 46: 2578-2581.
23. Machiavelli M, Romero A, Perez J. et al, " Prognostic significance of pathological response of primary tumor and metastatic axillary lymph nodes after neoadjuvant chemotherapy for locally advanced breast carcinoma," Cancer J. Sci Am. 1998; 4:125-131.
24. Pinder SE, Wencyk P, Sibbering DM, et al. Assessment of the new proliferation marker MIB1 in breast carcinoma using image analysis: associations with other prognostic factors and survival. Br J Cancer. 1995; 71:146–149.
25. Pertschuk LP, Feldman JG, Kim YD, et al. Estrogen receptor immunocytochemistry in paraffin embedded tissues with ER1D5 predicts breast cancer endocrine response more accurately than H222Sp gamma in frozen sections or cytosol-based ligand-binding assays. Cancer. 1996; 77:2514–2519.

26. Thor AD, Moore DHI, Edgerton SM, et al. Accumulation of p53 tumor suppressor gene protein: an independent marker of prognosis in breast cancers. J Natl Cancer Inst. 1992; 84:845–855.

27. Sagar SM, Klassen GA, Barclay KD, Aldrich JE. Antitumor treatment: tumor blood flow—measurement and manipulation for therapeutic gain. Cancer Treat Rev. 1993; 19:299–349.

28. Jain RK. Haemodynamic and transport barriers to the treatment of solid tumors. Int J Radiat Biol. 1991; 60:85–100.

29. Kedar RP, Cosgrove DO, Smith IE, Mansi JL, Bamber JC. Breast carcinoma: measurement of tumor response to primary medical therapy with color flow Doppler imaging. Radiology. 1994; 190:825–830.

30. Vaupel P, Kallinowski F, Okunieff P. Blood flow, oxygen and nutrient supply, and metabolic microenvironment of human tumors: a review. Cancer Res. 1989; 1:6449–6465.

31. Teicher BA. Hypoxia and drug resistance. Cancer Metastasis Rev. 1994; 13:139–168.

32. Wilson CBJH, Lammertsma AA, McKenzie CG, Sikora K, Jones T. Measurements of blood flow and exchanging water space in breast tumors using positron emission tomography: a rapid and non-invasive dynamic method. Cancer Res. 1992; 52:1592–1597.

33. Gilles R, Guinebretiere JM, Toussaint C, Spielman M, Rietjens M, Petit JY, Contesso G, Masselot J, Vanel D (1994) Locally advanced breast cancer: contrast-enhanced subtraction MR imaging of response to preoperative chemotherapy. Radiology 191:633-638

34. Abraham DC, Jones RC, Jones SE, et al. Evaluation of neoadjuvant chemotherapeutic response of locally advanced breast cancer by magnetic resonance imaging. Cancer. 1996; 78:91–100.

35. Maini CL, Tofani A, Sciuto R, et al. Technetium-99m-MIBI scintigraphy in the assessment of neoadjuvant chemotherapy in breast carcinoma. J Nucl Med. 1997; 38:1546–1550.

36. Mankoff DA, Dunnwald LK, Gralow JR, Ellis GK, Drucker MJ, Livingston RB. Monitoring the response of patients with locally advanced breast carcinoma to neoadjuvant chemotherapy using [technetium-99m]-sestamibi scintimammography. Cancer. 1999; 85:2410–2423.

37. Kedar RP, Cosgrove DO, Smith IE, Mansi JL, Bamber JC. Breast carcinoma: measurement of tumor response to primary medical therapy with color flow Doppler imaging. Radiology. 1994; 190:825–830.

38. Huber S, Medl M, Vesely M, Czembirek H. Zuna I. Delorme S, "Ultrasonographic Tissue Characterization in Monitoring Tumor Response to Neoadjuvant Chemotherapy in Locally Advanced Breast Cancer (Work in Progress), J. Ultrasound in Med. 19:677:686, 2000.

39. Huang, MM and Zhu, Q, "A Dual-mesh optical tomography reconstruction method with depth correction using a priori ultrasound information," Applied Optics, 43(8), 1648:1653, 2004.

40. Cope M, Ph.D Dissertation, University of College London, 1991.

41. Willett C, Boucher Y, Tomaso E et al., Direct evidence that the VEGF-specific antibody bevacizumab has antivascular effects in human rectal cancer, Nature Medicine, Vol 10 (2), February 2004.

42. Zhu, Q, Cronin, E, Currier, A, Vine, H, Huang, MM, Chen, NG, Chen Xu, C, "Benign versus Malignant Breast Masses: Optical Differentiation using US to Guide Optical Imaging Reconstruction," submitted to Radiology on Nov. 2003 and revision was submitted on June 2004.

43. Zhu, Q, Kurtzman, S, Hegde, P, Tannenbaum, S, Kane, M, Huang, MM, Chen, NG, Jagjivan, B, Zarfos, K, "Utilizing optical tomography with ultrasound localization to image heterogeneous hemoglobin distribution in large breast cancers," submitted to Neoplasia on July 2004.

44. Li A., Miller E., Kilmer M, Brukilacchio T, Chaves T , Scott J, Zhang Q, Wu T., Chorlton M, Moore R, Kopans D and Boas D, "Tomographic optical breast imaging guided by three-dimensional mammography," Appl. Opt., 42(25), 5181-5190 (2003)

45. Sullivan D, " Challenges and opportunities for in vivo imaging in oncology," Technology in Cancer Researcch and treatments, December 2002.
46. Minckwitz G von, Costa SD, Eiermann W, Blohmer JU, Tulusan AH, Jackisch C. Kaufmann M (1999) Maximized reduction of primary breast tumor size using preoperative chemotherapy with doxorubicin and Docetaxel. J. Clin Oncol 7:1999-2005.
47. Junkermann H, Founier D. von 91997) Imaging procedures for assessment of the response of mammary carcinoma to preoperative chemotherapy. Radiology 37: 726:732.
48. Vinnicombe SJ, Mac Vicar AD, Guy RL, Sloane JP, Powles TJ, Kenn G, Husband JE (1996) Primary breast cancer: mammographic changes after neo-adjuvant chemotherapy, with pathologic correlation. Radiology 198:333-340.
49. Herrada J, Iyer RB, Atkinson EN, Sneige N, Buzdar AU, Hortobabyi GN(1997) Relative value of physical examination, mammography, and breast sonography in evaluating the size of the primary tumor and regional lymph node metastases in women receiving neo-adjuvant chemotherapy for locally advanced breast carcinoma. Cli Cancer Res 3:1565;1569.
50. Segel MC, Paulus DD, Hortobagyi GN(1988) Advanced primary breast cancer: assessment at mammography response to induction chemotherapy. Radiology 169:49-54.
51. Fornage BD, Toubas O, Morel M (1987) Clinical, Mammographic and sonographic determination of pre-operative breast cancer size. Cancer 60:765:771.
52. Anderson EDC, Forrest APM, Hawkins RA, Anderson TJ, Leonard RFC, Chetty U(1991) Primary systemic chemotherapy for operable breast cancer. Br J Cancer 63:561-566.
53. Feldman LD, Hortobagyi GN, Buzdar AU, Ames FC, Blumenschein GR(1986) Pathological assessment of response to induction chemotherapy in breast cancer. Cancer Res. 46:2578:2581.
54. Cole-Beuglet C, Soriano RZ, Kurth AB, Goldberg BB. Ultrasound mammography. Radiol Clin North Am 1980; 18:133-143.
55. Cole-Beuglet C, Soriano RZ, Kurth AB, Goldberg BB. Fibroadenoma of the breast: sonomammography correlated with pathology in 122 patients. AJR 1983; 140:369-375.
56. Egan RL, Egan KL. Automated water-path full-breast sonography: correlation with histology of 176 solid lesions. AJR 1984; 143:499-507.
57. Fornage BD, Lorigan JG, Andry E. Fibroadenoma of the breast: US appearance. Radiology 1989; 172:671-675.
58. Hall, FM, Storella, JM, Silverstone, DZ et al., "Non-palpable breast lesions: recommendations for biopsy based on suspicious carcinoma of mammography," Radiology 167, pp.353-358 (1988).

Appendices.....

1. Chen, NG, Guo, PY, Yan, SK, Piao DQ, and Zhu, Q, "Simultaneous near infrared diffusive light and ultrasound imaging," Applied Optics, December, 40(34): 6367-6380, 2001.

2. Chen, NG , Huang, MM, Xia, HJ, Piao, DQ, Cronin, E, and Zhu, Q, "portable near infrared diffusive light imager for breast cancer detection," Journal of Biomedical Optics, May/June issue, 504-510, 2004.

3. Zhu, Q, Chen, NG, Ding, XH, Piao DQ, and Guo, PY, "Design of near infrared imaging probe with the assistance of ultrasound localization," Applied Optics, 40(19): 3288-3303, 2001.

4. Chen, NG and Zhu, Q, "Characterization of small absorbers inside the turbid medium," Optics Letters, 27(4): 252-254, 2002

5. Huang, M., Xie, TQ, Chen, NG, and Zhu Q, "Simultaneous reconstruction of absorption and scattering maps with ultrasound localization: feasibility study using transmission geometry," Applied Optics, 42(19): 4102-4114, 2003

6. Zhu, **Q**, Chen NG, Kurtzman, S, "Imaging tumor angiogenesis using combined near infrared diffusive light and ultrasound," Optics Letters, 28(5): 337-339, 2003

7. Huang, MM and Zhu, Q, "A Dual-mesh optical tomography reconstruction method with depth correction using a priori ultrasound information," Applied Optics, March 15 issue 2004.

8. Zhu, Q, Huang, MM, Chen, NG, Zarfos, K, Jagjivan, B, Kane, M, Hedge, P, Kurtzman, SH, "Ultrasound-guided optical tomographic imaging of malignant and benign breast lesions: initial clinical results of 19 cases," Neoplasia, 5(5), 379-388, 2003

9. Zhu, Q, Cronin, E, Currier, A, Vine, H, Huang, MM, Chen, NG, Chen Xu, C, "Benign versus Malignant Breast Masses: Optical Differentiation using US to Guide Optical Imaging Reconstruction," submitted to Radiology on Nov. 2003 and revision was submitted on June 2004.

10. Zhu, Q, Kurtzman, S, Hegde, P, Tannenbaum, S, Kane, M, Huang, MM, Chen, NG, Jagjivan, B, Zarfos, K, "Utilizing optical tomography with ultrasound localization to image heterogeneous hemoglobin distribution in large breast cancers," submitted to Neoplasia on July 2004.

Simultaneous near-infrared diffusive light and ultrasound imaging

Nan Guang Chen, Puyun Guo, Shikui Yan, Daqing Piao, and Quing Zhu

We have constructed a near-real-time combined imager suitable for simultaneous ultrasound and near-infrared diffusive light imaging and coregistration. The imager consists of a combined hand-held probe and the associated electronics for data acquisition. A two-dimensional ultrasound array is deployed at the center of the combined probe, and 12 dual-wavelength laser source fibers (780 and 830 nm) and 8 optical detector fibers are deployed at the periphery. We have experimentally evaluated the effects of missing optical sources in the middle of the combined probe on the accuracy of the reconstructed optical absorption coefficient and assessed the improvements of a reconstructed absorption coefficient with the guidance of the coregistered ultrasound. The results have shown that, when the central ultrasound array area is in the neighborhood of 2 cm × 2 cm, which corresponds to the size of most commercial ultrasound transducers, the optical imaging is not affected. The results have also shown that the iterative inversion algorithm converges quickly with the guidance of *a priori* three-dimensional target distribution, and only one iteration is needed to reconstruct an accurate optical absorption coefficient.

OCIS codes: 170.0170, 170.3010, 170.5270, 170.7170, 170.3830.

1. Introduction

Ultrasound is used extensively for differentiation of cysts from solid lesions in breast examinations, and it is routinely used in conjunction with mammography. Ultrasound can detect breast lesions a few millimeters in size.[1] However, its specificity in breast cancer diagnosis is not considered to be high enough as a result of overlapping characteristics of benign and malignant lesions.[2,3] Optical imaging based on diffusive near-infrared (NIR) light has the great potential to differentiate tumors from normal breast tissues through determination of tissue parameters, such as blood volume, blood O_2 saturation, tissue light scattering, water concentration, and the concentration and lifetime of exogenous contrast agents.[4–12] As a potential diagnostic tool, however, NIR diffusive light imaging suffers from low spatial resolution and lesion location uncertainties because of intense light scattering in tissue.

The authors are with the Department of Electrical and Computer Engineering, University of Connecticut, Storrs, Connecticut 06269. N. G. Chen's e-mail address is chenng@engr.uconn.edu, and Q. Zhu's e-mail address is zhu@engr.uconn.edu.

Received 27 November 2000; revised manuscript received 24 July 2001.

0003-6935/01/346367-14$15.00/0

Most NIR imaging reconstruction algorithms are based on tomographic inversion techniques.[13–20] Reconstruction of tissue optical properties in general is underdetermined and ill-posed because the total number of unknown optical properties always exceeds the number of measurements, and the perturbations produced by the heterogeneities are much smaller than the background signals. In addition, the inversion reconstruction algorithms are sensitive to measurement noise and model errors.

Our group and others have introduced a novel hybrid imaging method that combines the complementary features of ultrasound and NIR diffusive light imaging.[21–25] The hybrid imaging obtains coregistered ultrasound and NIR diffusive light images through simultaneous deployment of an ultrasound array and NIR source–detector fibers on the same probe.[21,22,24] Coregistration permits joint evaluation of acoustic and optical properties of breast lesions and enables use of lesion morphology provided by high-resolution ultrasound to improve the lesion optical property estimate. With the *a priori* knowledge of lesion location and shape provided by coregistered ultrasound, NIR imaging reconstruction can be localized within specified three-dimensional (3-D) regions. As a result, the reconstruction is overdetermined because the total number of unknown optical properties is reduced significantly. In addition, the reconstruction is less sensitive to noise because the

convergence can be achieved with a small number of iterations.

The clinical use of the combined diagnosis relies on the coregistration of both ultrasound and NIR sensors at the probe level. Conventional ultrasound pulse-echo imaging requires that an imaging transducer be located on top of the target, whereas NIR diffusive light imaging is feasible when the optical source and detector fibers are distributed at the periphery of the ultrasound transducer. However, the effects of missing optical sources in the middle of the combined probe on the accuracy of the reconstructed optical properties have to be evaluated. In addition, the improvements of reconstructed optical properties with the guidance of the coregistered ultrasound need to be quantitatively assessed. Furthermore, real-time data acquisition is necessary to avoid errors in coregistration caused by patient motion during the clinical experiments. In this paper we report our experimental results on the optimal probe configuration, and we quantify the improvements on reconstructed optical properties using a combined probe. We also demonstrate simultaneous combined imaging with a near-real-time imager.

2. Near-Infrared Diffusive Wave Imaging

We used the Born approximation to relate the scattered field $U_{sc}'(\mathbf{r}, \omega)$ measured at the probe surface to absorption variations in each volume element within the sample. In the Born approximation, the scattered wave originated from a source at $\mathbf{r}_{si}$, and measured at $\mathbf{r}_{di}$ it can be related to the medium absorption heterogeneity $\Delta\mu_a(\mathbf{r}_{vj})$ at $\mathbf{r}_{vj}$ by

$$[U_{sd}]_{MX1} = [W]_{MXN}\{\Delta\mu_a\}_{NX1} \tag{1}$$

where M is the total number of source–detector pairs, N is the total number of imaging voxels, and $W_{ij} = G(\mathbf{r}_{vj}, \mathbf{r}_{di}, \omega)U_{inc}(\mathbf{r}_{vj}, \mathbf{r}_{si}, \omega)\nu\Delta\mathbf{r}_v^3/\bar{D}$ is the weight matrix given in Ref. 19. $G(\mathbf{r}_{vj}, \mathbf{r}_{di}, \omega)$ and $U_{inc}(\mathbf{r}_{vj}, \mathbf{r}_{si}, \omega)$ are a Green's function and incident wave, respectively. ω is the modulation frequency and $\bar{D}$ is the average or background diffusion coefficient, which is the average value over the background or whole tissue.

With M measurements obtained from all possible source–detector pairs in the planar array, we can solve N unknowns of μ_a by inverting the above matrix equation. In general, the perturbation Eq. (1) is underdetermined ($M < N$) and ill-posed.

NIR imaging by itself generally has poor depth discrimination. However, ultrasound is excellent in providing accurate target depth. Once the target depth is available from coregistered ultrasound, we can set $\Delta\mu_a$ of a nontarget depth equal to zero. This implies that all the measured perturbations originate from the particular depth that contains the target. Because the number of unknowns is reduced significantly, the reconstruction converges very fast. In Ref. 23 we reported that, with *a priori* target depth provided by ultrasound, the accuracy of the reconstructed μ_a has been improved by 15–30% on average, and the speed of reconstruction has been improved by an order of magnitude. In this paper we furthermore demonstrate that, with the 3-D target distribution provided by coregistered ultrasound, the accuracy of reconstructed μ_a and the reconstruction speed can be further improved.

To solve the unknown optical properties of Eq. (1), we used the total least-squares (TLS) method[26,27] to iteratively invert Eq. (1). The TLS method performs better than other least-squares when the measurement data are subject to noise and the linear operator W contains errors. We found that the TLS method provides more accurate reconstructed optical properties than other least-squares methods, and we adopted TLS in solving inverse problems. It has been shown in Ref. 28 that the TLS minimization is equivalent to the following minimization problem:

$$\min \frac{\|U_{sd} - WX\|^2}{\|X\|^2 + 1}, \tag{2}$$

where X represents unknown optical properties. The conjugate gradient technique was employed to iteratively solve Eq. (2).

3. Methods

A. Combined Probe and Imaging Geometry

There are four basic requirements to guide the design of the combined probe. First, reflection geometry is preferred because a conventional ultrasound scan is performed with this geometry. Second, an ultrasound array needs to occupy the center of the combined probe for coherent imaging. Third, NIR sources and detectors have to be distributed at the periphery. Because photon propagation distribution exhibits a banana shape, imaging of the tissue volume underneath the probe is feasible even through there are no sources and detectors deployed in the central portion of the probe. Fourth, the minimum source–detector separation should be larger than 1 cm for the diffusion approximation to be valid, and the maximum separation should be ~8–9 cm to effectively probe depths of 3–4 cm.

On the basis of these requirements we deployed 12 dual-wavelength optical source fibers and 8 detector fibers over a 9 cm × 9 cm probe area (see Fig. 1). The minimum and maximum source–detector separations in the configuration are 1.4 and 8 cm, respectively. To study the effect of the central optical hole on the accuracy of the reconstructed optical properties, we compared the reconstruction results with an extra center source and without the center source. The configuration without the center source corresponds to a 2 cm × 2 cm hole area. We further moved the noncenter 12 sources and 8 detectors toward periphery by leaving a 3 cm × 3 cm hole area in the middle. Figure 2 shows the picture of a combined probe with the 3 cm × 3 cm central area occupied by an ultrasound array. The ultrasound array consists of 64 elements made of 1.5-mm-diameter piezoelectric transducers (Valpey Fisher Inc). The

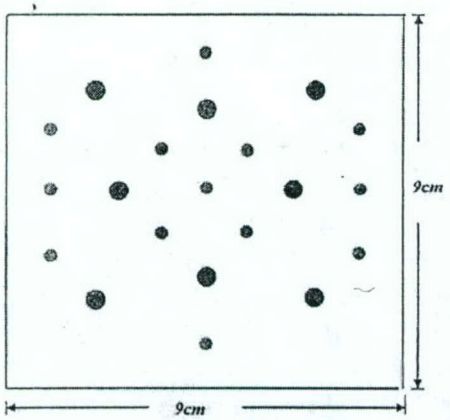

Fig. 1. Schematic arrangement of NIR source and detector fibers on the probe. Small solid circles are the source fibers and larger solid cycles are the detector fibers.

transducers are deployed in a rectangular matrix with 4-mm spacing in both x and y directions. The center frequency of the transducer is 6 MHz and the bandwidth is 40%. The transducers are made from the same piece of piezoelectric transducer material. Therefore the gain difference among different transducers is less than 3 dB. The 12 dual-wavelength optical laser diode sources (760 and 830 nm) and 8 photomultiplier tube (PMT) detectors are coupled to the probe through optical fibers, which are deployed at the periphery of the two-dimensional (2-D) ultrasound array. This hybrid array deployment compromises ultrasound coherent imaging and NIR diffusive light imaging characteristics.

The 9 cm × 9 cm × 4 cm image volume underneath the probe is discretized into voxels of size 0.4 cm × 0.4 cm × 1 cm. There is a trade-off between the accurate estimation of the weight matrix W and the voxel size. Because W_{ij} is a discrete approximation of the integral

$$\int_v G(\mathbf{r}_v, \mathbf{r}_d, \omega) U_{\text{inc}}(\mathbf{r}_v, \mathbf{r}_s, \omega) \frac{\nu}{D} \, \mathrm{d}\mathbf{r}_v^3,$$

it is more accurate when the voxel size is smaller. However, the total number of reconstructed unknowns will increase dramatically with the decreasing voxel size. Furthermore, the rank of W does not increase in the same order as the total number of voxels when the voxel size decreases. This suggests that neighboring W_{ij}'s are correlated when the voxel size is smaller, and a further decrease in voxel size will not add more independent information to the weight matrix. We found that a 0.4 cm × 0.4 cm × 1 cm voxel size is a good compromise. Therefore we used this voxel size in image reconstructions reported in this paper.

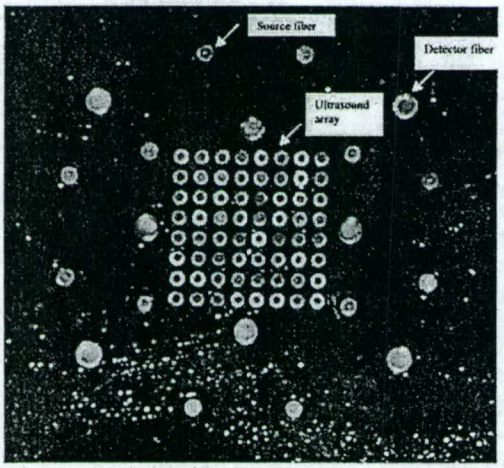

Fig. 2. Picture of an experimental probe. An ultrasound array of 8 × 8 = 64 transducers occupies the central 3 cm × 3 cm area, and 12 dual-wavelength source fibers and 8 detector fibers are deployed at the periphery.

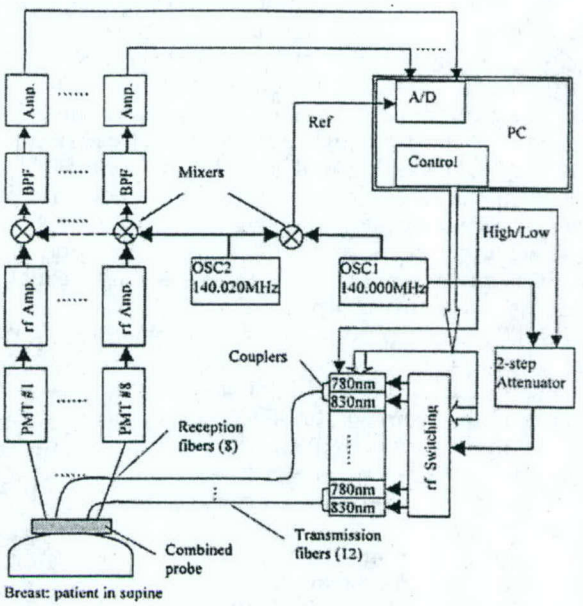

Fig. 3. Schematic of the NIR frequency-domain imaging system. The modulation frequency is 140 MHz. The 12 dual-wavelength source channels are switched on sequentially by a PC, and 8 detector channels receive signals in parallel. BPF, bandpass filter; OSC, oscillator.

B. Experimental Systems

1. *Near-Infrared Imaging System*

We constructed a NIR frequency-domain imaging system. The block diagram of the system is shown in Fig. 3. This system has 12 dual-wavelength source channels and 8 parallel receiving channels. On the transmission part, 12 pairs of dual-wavelength (780 and 830 nm) laser diodes are used as light sources, and their outputs are amplitude modulated at 140.000 MHz. Each one of the 12 optical combiners (OZ Optics Inc.) looks like a Y adapter, guiding the emission of two diodes of different wave-

lengths through the same thin optical fiber (approximately 0.2 mm in diameter). To reduce noise and interference, an individual driving circuit is built for each diode. As a laser diode works in series, a control board that interprets instructions from a PC is used to coordinate operations of associated components. When a single transmission channel is selected, it turns on the corresponding driving circuit so that a dc driving current can be set up for the diode. At the same time, a selected signal is sent to a rf switching unit, which distributes a rf signal to the right channel to modulate the optical output. On the reception part, eight PMTs are employed to detect diffusely reflected light from turbid media. Each PMT is housed in a sealed aluminum box, shielding both environment lights and electromagnetic fields, and an optical fiber (3 mm in diameter) couples NIR light from the detection point to the reception window of the PMT. The electrical signal converted from the optical input is generally weak and rather high in frequency, so high-gain amplification and frequency transform are necessary before it can be sampled by an analog-to-digital (A/D) board inside the PC. We built eight parallel heterodyne amplification channels to measure the response of all detectors simultaneously, which reduces the data-acquisition time. Each amplification channel consists of a rf amplifier (40 dB), a mixer in which the rf signal (OSC1, 140.000 MHz) is mixed with a local oscillator (OSC2, 140.020 MHz), a bandpass filter centered at 20 kHz, and a low-frequency amplifier of 30 dB. The heterodyned two-stage amplification scheme helps suppress wideband noises efficiently. We also generated a reference signal of 20 kHz by directly mixing OSC1 and OSC2, which is necessary for retrieving phase shifts. Eight detection signals and one reference are sampled, converted, and acquired into the PC simultaneously, in which the Hilbert transform is used to compute the amplitude and phase of each channel. The entire data acquisition takes less than 1 min, which is fast enough to acquire data from patients.

One of the challenges encountered in the design of a NIR imaging system is the huge dynamic range of signals received at various source–detector distances. For example, for a semi-infinite phantom made of 0.5% Intralipid solution, the amplitude measured at 1 cm away from a source is approximately 5000 times larger than that at 8-cm separation. In addition, the perturbation that is due to an embedded heterogeneity with optical properties similar to a tumor is normally a few percent of the background signal. As a result, a reflection-mode NIR imaging system should have at least a 120-dB dynamic range to probe a target up to 4 cm in depth. It is hard to build amplifiers that work linearly over such a wide dynamic range. We overcome this difficulty by implementing two-level source outputs. The dc output of a laser diode is controlled when its feedback loop is adjusted, whereas the rf signal is switched simultaneously by a two-step attenuator (no attenuation or 30-dB attenuation). When the source and detector are close to each other, the source is controlled to yield a low-level output. When the separation becomes larger, a 30-dB higher output level should be used. With this two-level source scheme, our system achieved fairly good linearity over a wide range of source–detector separations (from 1.5 to 8 cm).

Because the parameters of an individual laser diode or a PMT vary considerably from one to another, we have to calibrate the gain and phase shift for each channel. A set of measurements obtained from all source–detector pairs placed on the boundary of a homogeneous medium is

$$\bar{A}_{\alpha\beta},\ \bar{\phi}_{\alpha\beta}, \qquad \alpha = 1, 2, \ldots, m; \qquad \beta = 1, 2, \ldots, n.$$

Here, amplitude $\bar{A}_{\alpha\beta}$ and phase $\bar{\phi}_{\alpha\beta}$ are related to source α and detector β, and m and n are the total number of sources and detectors, respectively. From the diffusion theory, we can obtain the following set of equations[7]:

$$\bar{A}_{\alpha\beta} = I_s(\alpha) I_d(\beta) \frac{\exp(-k_i \rho_{\alpha\beta})}{\rho_{\alpha\beta}^2},$$

$$\bar{\phi}_{\alpha\beta} = \varphi_s(\alpha) + \varphi_d(\beta) + k_r \rho_{\alpha\beta},$$

in which $I_s(\alpha)$ and $\varphi_s(\alpha)$ are the relative gain and phase delay associated with source channel α, $I_d(\beta)$ and $\varphi_d(\beta)$ are similar quantities associated with detector channel β, $\rho_{\alpha\beta}$ is the corresponding separation, and $k_r + jk_i$ is the complex wave number. We obtain the following set of linear equations by taking a logarithm of the above equations related to amplitude:

$$\log(\rho_{\alpha\beta}^2 \bar{A}_{\alpha\beta}) = \log[I_s(\alpha)] + \log[I_d(\beta)] - k_i \rho_{\alpha\beta},$$

$$\bar{\phi}_{\alpha\beta} = \varphi_s(\alpha) + \varphi_d(\beta) + k_r \rho_{\alpha\beta}. \qquad (3)$$

Although the optical properties of the calibration medium are known in advance, we leave the wave number as a variable and use fitted k_r and k_i to calculate the background scattering and absorption coefficients. We verified our calibration method by comparing the best fitted k's with real values. The results of our using 0.5–0.8% Intralipid solutions always yielded scattering and absorption coefficients with a rather good accuracy. With the two unknown wave numbers included, the total number of unknowns is $2(m + n + 2)$, which is generally far smaller than the number of measurements $m \times n$. Consequently, Eq. (3) is overdetermined. We can solve all $I_s(\alpha)$, $I_d(\beta)$, $\varphi_s(\alpha)$, and $\varphi_d(\beta)$ terms as well as two unknown wave numbers in a least-squares sense. Then all measurements can be calibrated accordingly. The results of amplitude $A_{\alpha\beta} = \exp(-k_i \rho_{\alpha\beta})/\rho_{\alpha\beta}^2$ and phase $\phi_{\alpha\beta} = k_r \rho_{\alpha\beta}$ after calibration are shown in Fig. 4. As one can see, the calibrated amplitude ($\log \rho_{\alpha\beta}^2 A_{\alpha\beta}$) and the phase from various source–detector pairs change linearly with distance.

2. *Ultrasound System*

The ultrasound system diagram is shown in Fig. 5, and the system consists of 64 parallel transmission and receiving channels. Each transmission circuit can generate a high-voltage pulse of 200-ns duration (6 MHz) with 125 V peak to peak to the connected

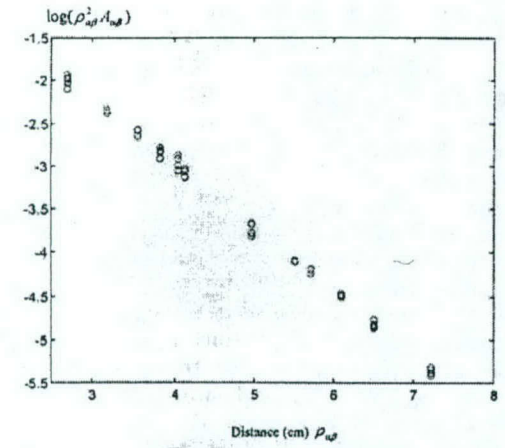

(a)

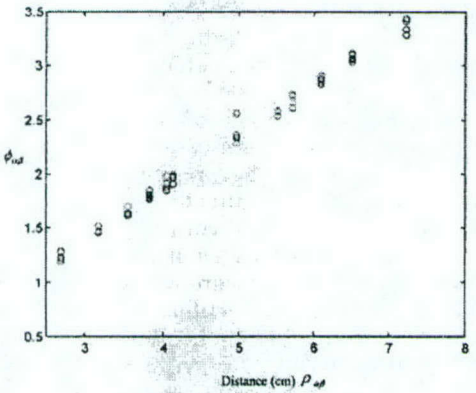

(b)

Fig. 4. (a) Log($\rho_{\alpha\beta}{}^2 A_{\alpha\beta}$) versus distancev $\rho_{\alpha\beta}$ after calibration. (b) Phase $\phi_{\alpha\beta}$ versus distance $\rho_{\alpha\beta}$ after calibration.

transducer. Each receiving circuit has two-stage amplifiers followed by an A/D converter with 40-MHz sampling frequency. The amplifier gain can be controlled based on the target strength. A group of transmission channels can be addressed simultaneously to transmit pulses from neighbor transducers with specified delays and therefore to focus the transmission beam. The retuned signals can be received simultaneously by a group of transducers, and the signals can be summed with specified delays to form a receiving beam.

The data-acquisition procedure is the following. The first 9-element neighbor subarray (dashed rectangle in Fig. 6) from the 64-element transducer array and the corresponding channels are chosen, and then the transmission delay profiles are generated in the computer according to the prespecified focal depth. The delay profile data are transferred to the 64-channel delay profile generator, which triggers the 64 high-voltage pulsers as well as the receiving channels. The returned ultrasound signals are amplified

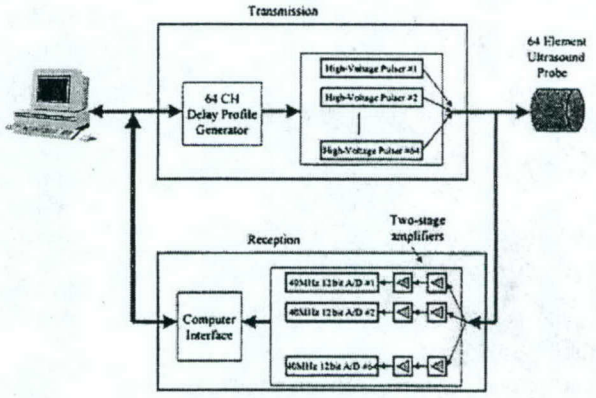

Fig. 5. Schematic of our ultrasound scanner. We connected 64 ultrasound transducers to 64 parallel transmission and reception channels. The transmission part consists of 64 high-voltage pulsers, which can be controlled by computer-generated delay profiles. The reception part consists of 64 two-stage amplifiers and A/D converters. CH, channel.

by two-stage amplifiers and sampled by A/D converters. The data are buffered in the memories and are read by the computer after the entire data acquisition is completed. The second subarray (solid rectangle in Fig. 6) is chosen and the same data-acquisition process is repeated. A total of 64 subarrays is used in the data acquisition. After the 64-subarray data acquisition is completed, the data stored in the memories are read by the computer for image formation. The entire data acquisition and imaging display are performed in approximately 5 s, which is fast enough for clinical experiments. To ensure good signal-to-noise ratio, we perform all the electronics using printed circuit boards.

Figure 7 shows the picture of the entire system and the combined probe. Both the NIR system (top) and the ultrasound system (bottom) are mounted on a hospital cart. The combined probe, which houses the ultrasound array and the NIR source–detector fibers, is designed to be hand held to scan patients.

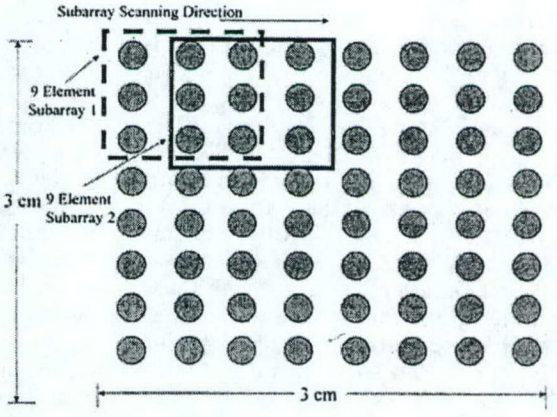

Fig. 6. Ultrasound subarray scanning configuration.

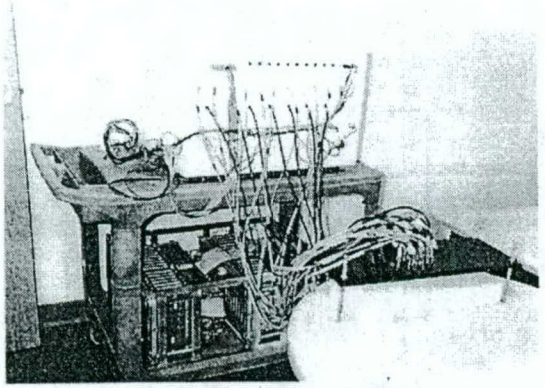

Fig. 7. Picture of our combined system. NIR system (top) and ultrasound system (bottom) are mounted on a hospital cart.

C. Phantoms

We used 0.5–0.6% Intralipid solutions to mimic normal human breast tissues in all experiments, and the corresponding reduced scattering coefficient μ_s' ranges from 5 to 6 cm^{-1}. The Intralipid is contained in a large fish tank to set up approximately a semi-infinite homogeneous phantom. Small semispherical balls (1 cm in diameter), made of acrylamide gel,[22] are inserted into Intralipid to emulate lesions embedded in a breast. The reduced scattering coefficients of the gel phantoms are similar to that of the background medium ($\mu_s' \approx 6$ cm^{-1}), and we changed the absorption coefficients to different values by adding different concentrations of India ink to emulate high-contrast ($\mu_a = 0.25$-cm^{-1}) and low-contrast ($\mu_a = 0.1$-cm^{-1}) lesions. Ultrasound scattering particles of 200 μm in diameter are added to the gel phantom before the gel is formed.

4. Experimental Results

A. Effects of Missing Optical Sources in the Combined Probe

A series of experiments was conducted to estimate the optimal hole size. Three probe configurations were investigated: (a) no-hole, (b) 2 cm × 2 cm central hole, and (c) 3 cm × 3 cm hole probes. The no-hole probe was essentially the same as case (b) except that an additional light source was added in the middle. Figure 8 shows reconstructed NIR images for on-center targets of high ($\mu_a = 0.25$ cm^{-1}, left column) and low contrast ($\mu_a = 0.1$ cm^{-1}, right column) located 2.5 cm deep inside the Intralipid. The fitted background μ_a and μ_s are 0.015 and 5.36 cm^{-1}, respectively. With the target depth provided by ultrasound, we performed reconstruction in the target layer. The centers of the voxels in this layer were (x, y, 2.5 cm), where x and y were discrete spatial x–y coordinates, and the thickness of the layer was 1 cm. For the high-contrast target case, there are no important differences in image quality associated with different probes [Figs. 8(a) and 8(c)] except that with a 3 cm × 3 cm hole. The first row of Table 1 provides measured maximum μ_a values from the corresponding images. Because of the low spatial resolution of diffusive imaging, the boundaries of the targets are not well defined. The maximum value is a better estimation of reconstructed target μ_a. From no hole to 2 cm × 2 cm, the reconstructed maximum μ_a decreases slowly. But for 3 cm × 3 cm, the maximum μ_a drops suddenly to 0.104 cm^{-1}, which is less than half of the original value. Another imaging parameter we measured is the full width at half-maximum (FWHM) of the corresponding images. Because the image lobes were elliptical in general, we measured the widths of longer and shorter axes and used the geometric mean to estimate the FWHM. The results are shown in Table 1, and the FWHM almost increases with the hole size. We also measured the image artifact level, which was defined as the ratio of the peak artifact to the maximum strength of the image lobe and is given in decibels. The results are shown in Table 1. No artifacts were observed in the images of no-hole and 2 cm × 2 cm hole probes. However, the peak artifact level at the −14.3-dB level was measured in the image of the 3 cm × 3 cm hole probe. When the contrast was low, the reconstructed maximum absorption coefficients and measured FWHMs were essentially the same for the no-hole and 2 cm × 2 cm hole probes. However, the reconstructed maximum value dropped to 60% of the true value for the 3 cm × 3 cm probe. The artifact levels measured in the images of three probe configurations were similar and were worse than the high-contrast case. The image artifacts are related to the reconstruction algorithm. When the target contrast is weak or the signal-to-noise ratio is low, the inversion algorithm produces artifacts around the edges of the images.

For shallow targets (here we set the target depth to be 1.5 cm) the NIR system has a relatively poorer performance. This is due to less source–detector pairs experiencing the existence of a shallow absorber. As shown in Fig. 9, image artifacts are obviously worse compared with Fig. 8. However, the conclusion about the hole size of the probe remains true. Table 2 lists all the measured imaging parameters obtained from three probe configurations. Although a 3 cm × 3 cm hole is somewhat too big to obtain good enough results, the optimal hole size is in the neighborhood of 2 cm × 2 cm. This optimal size is approximately the size of commercial ultrasound transducers.

In the above studies, we used the iteration number obtained from the no-hole configuration for the rest of the configurations. Ideally, the iteration should stop when the object function [see Eq. (2)] or the error performance surface reaches the noise floor. However, system noise, particularly coherent noise, was difficult to estimate from experimental data. In general, we found that the reconstructed values were closer to true values when the object function reached approximately 5–15% of the initial value (total energy in the measurements). Therefore we used this criterion (~10% of the initial value) for the no-hole configuration. Because the signal-to-noise ratio of

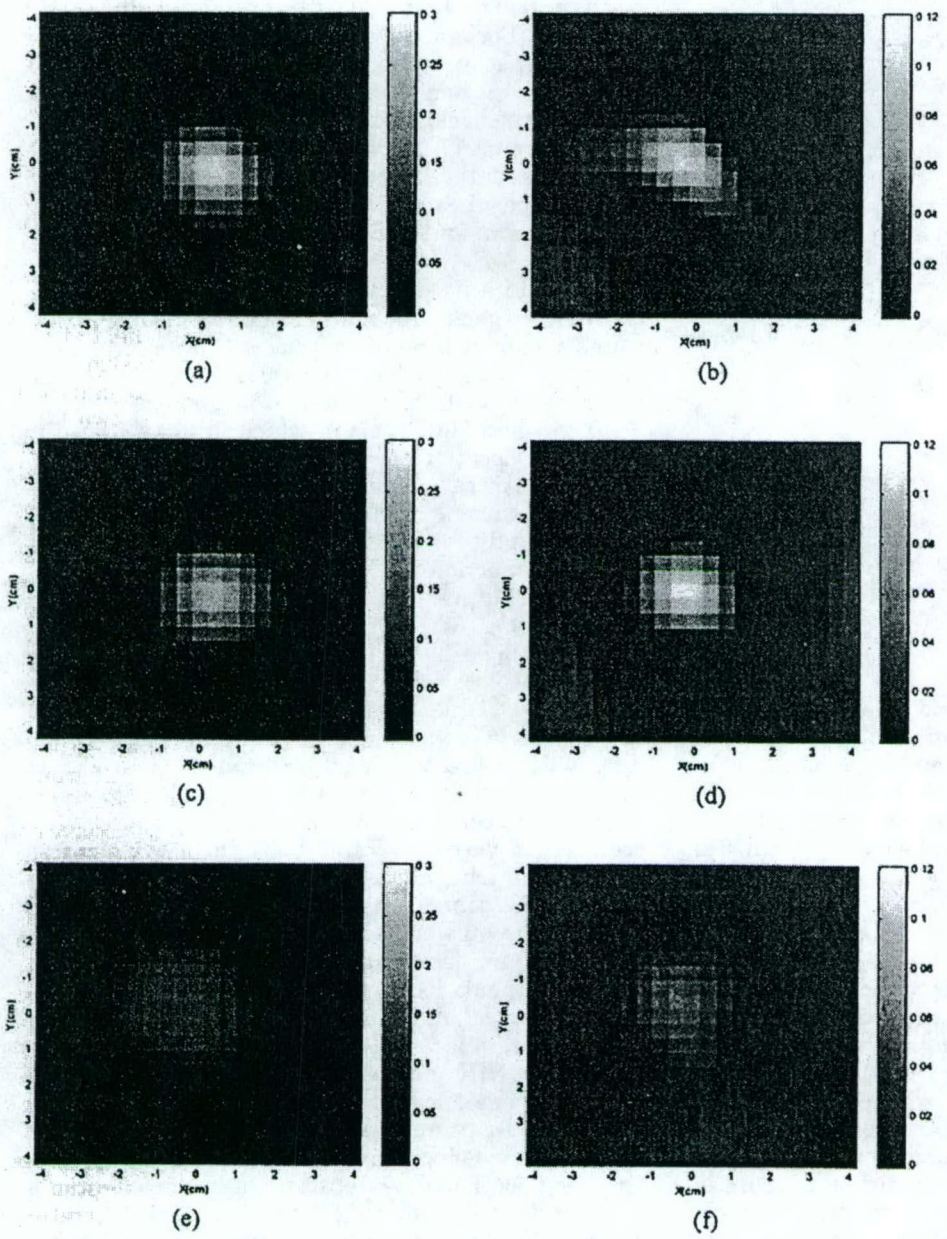

Fig. 8. Reconstructed NIR images of deeper targets (2.5 cm in depth, 1 cm in diameter, and the fitted background μ_a and μ_s' are 0.015 and 5.36 cm^{-1}, respectively). The left column corresponds to images of a high-contrast target (μ_a = 0.25 cm^{-1}) obtained from different probe configurations, and the right column corresponds to images of a low-contrast target (μ_a = 0.1 cm^{-1}). Each row is related to a specific hole size: (a) and (b) no hole, (c) and (d) 2 cm × 2 cm, (e) and (f) 3 cm × 3 cm.

the data decreased with the increase in hole size, we could not find consistent criterion for both no-hole and hole data. Therefore we used the same iteration number obtained from the no-hole case for the hole configurations, and the comparison was based on the same iteration number.

B. Ultrasound-Guided Near-Infrared Imaging

Three-dimensional ultrasound images can provide 3-D distributions of targets. With the *a priori* target depth information, the optical reconstruction can be improved significantly. An example is given in Fig. 10. The target again was a 1-cm-diameter gel ball of low (μ_a = 0.1-cm^{-1}) optical contrast and was embedded at approximately (0, 0, 2.5 cm) inside the Intralipid medium. The fitted background μ_a and μ_s' are 0.02 and 5.08 cm^{-1}, respectively. The combined probe shown in Fig. 2 was used to obtain the ultrasound and NIR data simultaneously. Figure 10(a) shows an A-scan line of a returned ultrasound echo

Table 1. Parameters of Reconstructed Images for Deep High-Contrast (μ_s = 0.25-cm^{-1}) and Low-Contrast (μ_s = 0.1-cm^{-1}) Targets[a]

Parameter	Probe Type		
	No Hole	2 cm × 2 cm	3 cm × 3 cm
High contrast			
$\hat{\mu}_{a(max)}$[b] (cm^{-1})	0.251	0.234	0.104
FWHM[c] (cm)	1.85	1.91	2.44
Artifacts (dB)	Background (−22)	Background	−14.3
Low contrast			
$\hat{\mu}_{a(max)}$ (cm^{-1})	0.105	0.111	0.064
FWHM (cm)	2.02	1.83	2.16
Artifacts (dB)	−6.90	−8.10	−5.65

[a]The fitted background μ_a and μ_s' are 0.015 and 5.36 cm^{-1}, respectively.

[b]$\hat{\mu}_{a(max)}$ is the measured maximum value of the reconstructed absorption coefficient map.

[c]FWHM is defined as the geometric mean of the widths measured at longer and shorter axes of the elliptical image lobe.

signal received by one ultrasound transducer located on top of the target. As acoustic scatters were uniformly distributed in the target, signals were reflected from inside the target as well as from the surfaces. The reflected signals from the front and back surfaces of the gel ball can be clearly identified in the echo signal. On the basis of the target depth, we reconstructed the optical absorption coefficient at the target depth only (1 cm in thickness) by setting the purturbations from the other depths equal to zero. We also performed 3-D optical-only reconstruction. Figure 10(b) shows the reconstructed absorption image from a 3-D optical-only reconstruction [layer three of voxel coordinates (x, y, 2.5 cm) and 1 cm thick], whereas Fig. 10(c) shows the reconstructed image of the corresponding target from ultrasound-guided reconstruction. For optical-only reconstruction, the algorithm did not converge to a localized spatial region, and the image contrast was poor. The measured maximum absorption coefficient was 0.088 cm^{-1}, which was close to the true value. However, the measured spatial location of the maximum value was (−1.6, −1.2 cm), which was too far from the true target location. With the *a priori* target depth, the reconstruction performed at the target layer can localize the target to the correct spatial position. The measured maximum absorption coefficient was 0.12 cm^{-1} and its location was (0, 0.4 cm), which was very close to the true target location. This example demonstrates that *a priori* target depth can significantly improve the reconstruction accuracy and target localization.

In addition to use of *a priori* target depth information, we can also use the target spatial distribution provided by ultrasound to guide the reconstruction. We performed a set of experiments with two targets located at 2.5 cm in depth inside the Intralipid. Each target is a 1-cm^3 gel cube containing ultrasound scatters. For optical properties, they both could be high contrast (μ_a = 0.25 cm^{-1}) or low contrast (μ_a = 0.1 cm^{-1}), but had the same reduced scattering coefficient as the background. The fitted background μ_a and μ_s' are 0.017 and 4.90 cm^{-1}, respectively. One target was centered approximately at (−1.0, −1.0, 2.5 cm), whereas the other was at (1.0, 1.0, 2.5 cm). The distance between the centers of the two targets was 2.8 cm.

Figure 11(a) is the ultrasound image of two high-contrast targets. As the field of view of the ultrasound system was nearly a 3 cm × 3 cm square, these two targets appeared at diagonal corners. The measured peak positions of the two targets were (−0.6, −1.0 cm) and (1.0, 1.0 cm), which differed from the true target locations by only one voxel. The low contrast of the ultrasound image is related to the speckle noise. Because our ultrasound array is sparse, the imaging quality is not state of the art (see more discussion in Section 5). The NIR image of these targets was obtained simultaneously and is shown in Figure 11(b). We performed the reconstruction at the target layer by taking advantage of target depth information. A total of 123 iterations was used to obtain Fig. 11(b). The measured peak positions of the two targets were (−1.4, −1.0 cm) and (0.6, 0.6 cm), which were one voxel off from the true target locations (−1.0, −1.0 cm) and (1.0, 1.0 cm), respectively. The corresponding reconstructed absorption coefficients were 0.242 and 0.251 cm^{-1}, which were close to the true values. However, the two targets were almost connected to each other, and their spatial localization was poor. For low-contrast targets, the ultrasound image is shown in Fig. 11(c), and the measured peak locations of the two targets were (−1.0, −0.6 cm) and (0.6, 1.0 cm), which differed from the true target locations by only one voxel. The corresponding NIR image is shown in Fig. 11(d), and the measured peak locations of the two targets were (−2.2, −1.0 cm) and (0.6, 1.0 cm). The left target was off the true location by three voxels. The corresponding reconstructed absorption coefficients were 0.063 and 0.1004 cm^{-1} at 87 iteration steps. As one can see, the target shape and localization were poorer than those in the high-contrast case. In addition, an artifact appeared at the edge of the image.

From the coregistered ultrasound images, we obtained spatial distributions of the two targets and specified target regions. Figures 12(a) and 12(c) show the −6-dB contour plots of Figs. 11(a) and 11(c). Applying the same reconstruction scheme to these specific regions, we obtained Figs. 12(b) and 12(c) in one iteration. The reconstructed absorption coefficients were 0.2357 and 0.219 cm^{-1} for the two high-contrast target cases and 0.123 and 0.131 cm^{-1} for the low-contrast case. We can see much better improvement in the low-contrast target case when we compare Fig. 12(d) with Fig. 11(d). This example demonstrates that, when the targets are visible in ultrasound images, their morphology information

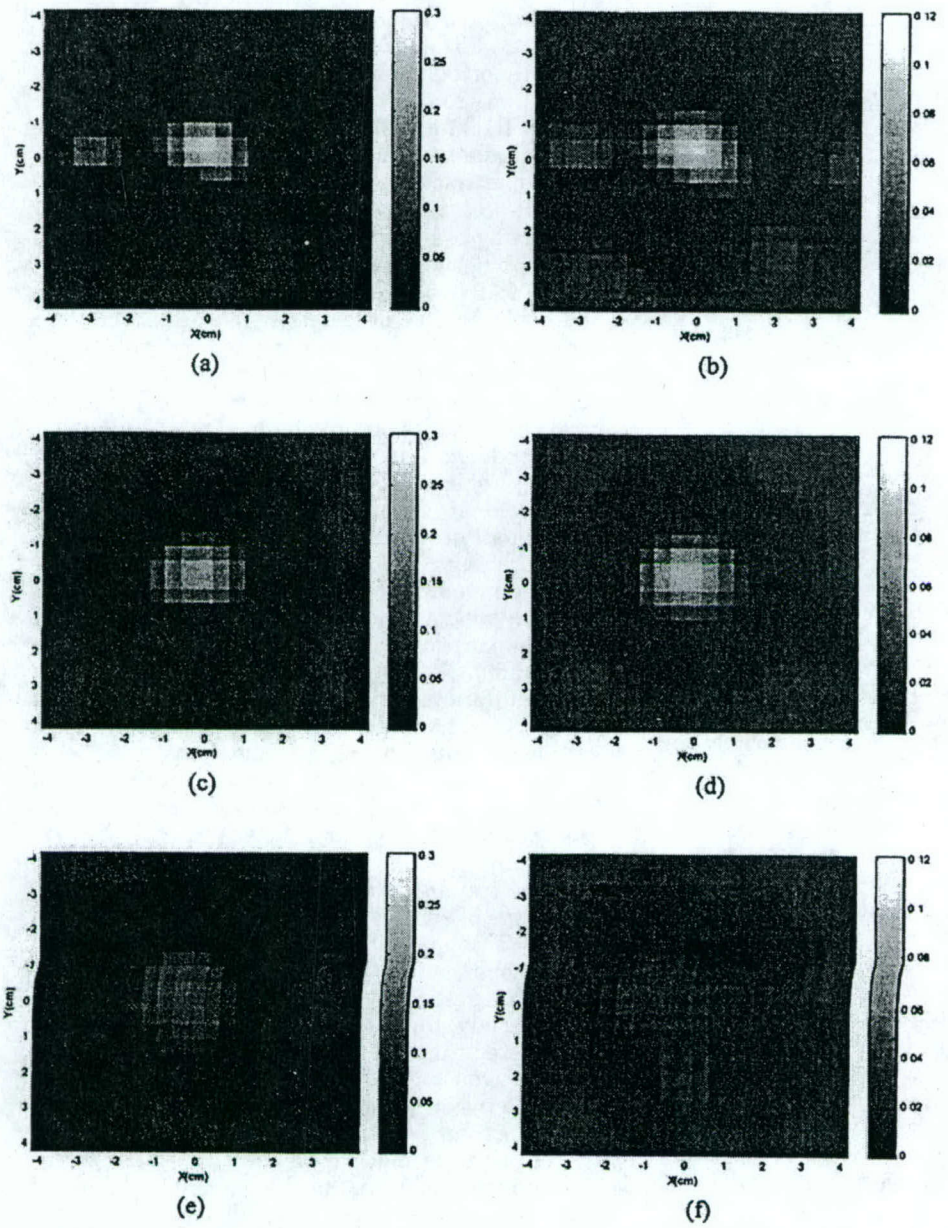

Fig. 9. Reconstructed NIR images for shallow targets (1.5 cm in depth, 1 cm in diameter, and the fitted background μ_a and μ_s' are 0.015 and 5.36 cm^{-1}, respectively). The left column corresponds to images of a high-contrast target (μ_a = 0.25 cm^{-1}), and the right column corresponds to images of a low-contrast target (μ_a = 0.1 cm^{-1}). Each row is related to a specific hole size: (a) and (b) no hole, (c) and (d) 2 cm × 2 cm, (e) and (f) 3 cm × 3 cm.

provided by ultrasound can be used to guide the optical reconstruction in the specified regions.

The result regarding the iteration step is significant. As we discussed above, there is no known stopping criterion to terminate the iteration because it is difficult to estimate the noise level in the measurements. With the *a priori* target depth and spatial distribution provided by coregistered ultrasound, we can obtain an accurate optical absorption coefficient in one iteration. Therefore no stopping criterion is needed for the inversion algorithms. However, this result will need to be further evaluated with more samples of different contrasts.

5. Discussion

Commercial ultrasound scanners use one-dimensional probes that provide 2-D images of x–z views of the targets, where x and z are the spatial and propagation dimensions, respectively. Such x–z images cannot coregister with NIR images, which are

Table 2. Parameters of Reconstructed Images for Shallow High-Contrast (μ_a = 0.25-cm^{-1}) and Low-Contrast (μ_a = 0.1-cm^{-1}) Targets[a]

Parameter	Probe Type		
	No Hole	2 cm × 2 cm	3 cm × 3 cm
High contrast			
$\hat{\mu}_{a(\max)}$ (cm^{-1})	0.250	0.194	0.118
FWHM (cm)	1.32	1.61	2.08
Artifacts (dB)	−7.98	−12.7	−9.76
Low contrast			
$\hat{\mu}_{a(\max)}$ (cm^{-1})	0.100	0.091	0.042
FWHM (cm)	1.88	2.11	3.17
Artifacts (dB)	−6.25	−7.44	−0.65

[a]The fitted background μ_a and μ_s' are 0.015 and 5.35 cm^{-1}, respectively.

obtained from x–y views of the targets. Our current 2-D ultrasound array is capable of providing x–y views of the targets, which can be used to coregister with NIR images. However, the array is sparse and therefore the image resolution is not state of the art. Nevertheless, its spatial resolution is comparable to NIR imaging and can be used to guide NIR image reconstruction. With 3-D ultrasound guidance, only one iteration is needed to obtain accurate absorption coefficients. This result is significant because no stopping criterion is necessary. More studies with a variety of target contrasts and locations will be performed to verify this result.

We purchased a 2-D state-of-the-art ultrasound array of 1280 transducer elements and we are building a multiplexing unit for our 64-channel electronics. In addition, the new 2-D transducer size is approximately 2 cm × 3 cm, which is in the neighborhood of the optimal hole size we found through this study. With the new 2-D ultrasound transducer, we will be able to obtain high-resolution ultrasound images and delineate the target boundaries with finer details for optical reconstruction.

Ultrasound contrast depends on lesion acoustic properties, and NIR optical contrast is related to lesion optical properties. Both contrasts exist in tumors, but the sensitivities of these two modalities may be different. It is possible that some early-stage cancers have NIR contrast but are not detectable by ultrasound. It would be desirable if we could obtain sensitivity of optical imaging alone. However, light scattering is a main problem that prevents the accurate and reliable localization of lesions. It is also possible that some lesions have acoustic contrast but no NIR contrast or low NIR contrast. Currently, ultrasound is routinely used as an adjunct tool to x-ray mammography; the combined sensitivity of these two modalities in breast cancer detection is more than 90%.[29] Recently, ultrasound has also been advocated to screen dense breasts.[30] We anticipate that our combined imaging will add more specificity to the ultrasonically detected lesions.

In the reported phantom studies, we assigned zero perturbations to the regions where no targets were present. In clinical studies, we plan to segment the ultrasound images and specify different tissue types as well as suspicious regions in the segmented images. We will then reduce the reconstructed optical unknowns by assigning unknown optical properties to different tissue types as well as to suspicious regions. Finally, we will reconstruct the reduced sets of unknown optical properties. We expect a more accurate estimation of reconstructed optical properties and fast convergence speed, as reported in this paper. However, it is still too early to judge the clinical performance of the combined method; further clinical studies are needed.

Probing regions of the banana-shaped diffusive photons depend on source–detector separations and measurement geometry. For a semi-infinite geometry, the probing regions extend further into the medium when source–detector separation increases. This is why we have multiple source–detector pairs of various separations to detect targets at variable depths from 0.5 to 4 cm. Of course it is hard to achieve uniform sensitivity in the entire region of interest. For example, a superficial target (~1 cm deep) would cause strong perturbations when it is close to a source or a detector, but will result in much weaker signals when it is located deeper. Normalization of scattering photon density waves with respect to the incident waves makes it possible for reconstruction algorithms to handle the huge dynamic range of signals and to detect a target as deep as 4 cm. This normalization procedure was applied to the reconstruction algorithm used to obtain the reported images.

In this study, the target absorption coefficient was reconstructed from the measurements. Because the target μ_s' was similar to the background μ_s', the coupling between μ_a and μ_s' in our measurements was negligible. We also performed experiments with gel phantom made with Intralipid with a concentration similar to that of the background and did not observe perturbation beyond the noise level. Similar reconstruction studies can be performed for scattering coefficients as well. Simultaneous reconstruction of both absorption and scattering coefficients is also possible. Because the eigenvalues of the absorption and scattering weight matrices are significantly different, good regulation schemes are needed for simultaneous reconstruction. This subject is one of our topics for further study.

6. Summary

We have constructed a near-real-time imager that can provide coregistered ultrasound and NIR images simultaneously. This new technique is designed to improve the specificity of breast cancer diagnosis. Because the ultrasound transducer needs to occupy

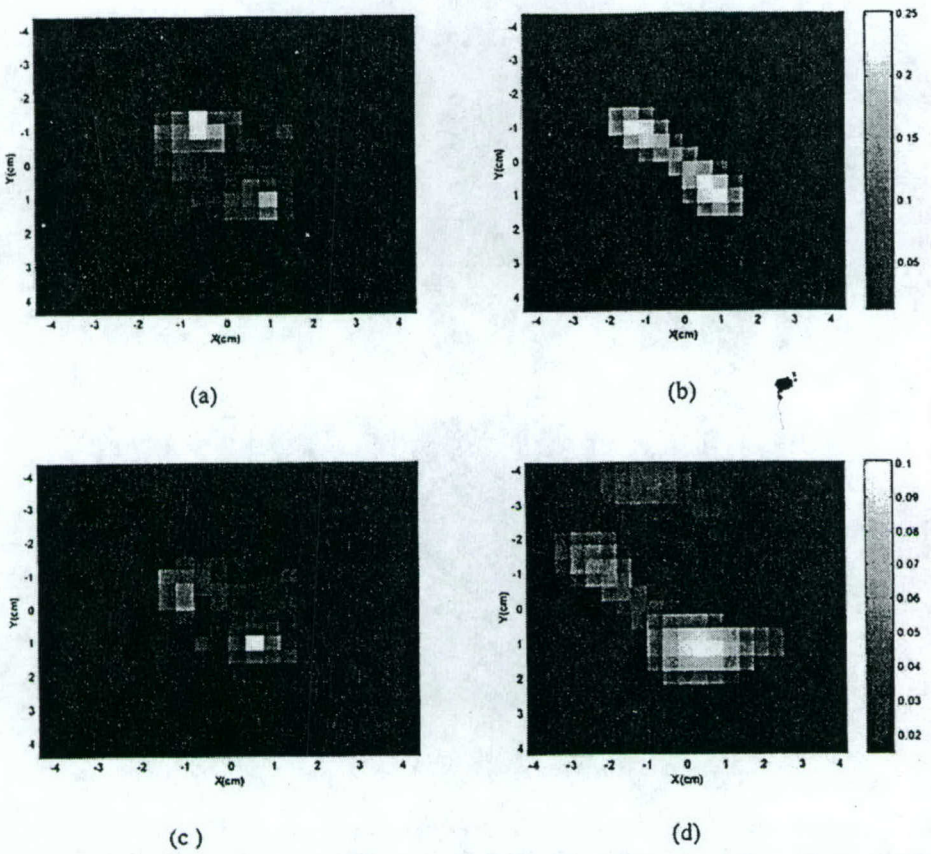

Fig. 11. Simultaneously obtained ultrasound and NIR absorption images. The fitted background μ_a and μ_s' are 0.017 and 4.90 cm^{-1}, respectively. (a) Ultrasound and (b) NIR absorption image of two high-contrast targets (target μ_a = 0.25 cm^{-1}). (c) Ultrasound and (d) NIR image of two low-contrast targets (target μ_a = 0.10 cm^{-1}). In both high- and low-contrast cases, the two targets were located at 2.5 cm in depth.

creased to 3 cm × 3 cm, however, the reconstructed values are obviously lower than real values. If we increase the iteration steps, artifacts in the reconstructed images would soon become dominant.

With the target 3-D distribution provided by coregistered ultrasound, significant improvements in algorithm convergence and reconstruction speed were achieved. In general, *a priori* target depth information guides the inversion algorithm to reconstruct the heterogeneities at the correct spatial locations and improves the reconstruction speed by an order of magnitude. In addition, the *a priori* target spatial distribution can further reduce the iteration to one step and also obtain accurate optical absorption coefficients. Given the fact that no known stopping criterion is available, this result is significant because no iteration is needed. However, this result will need to be evaluated with more samples of different contrasts.

We acknowledge the following for their funding support: the state of Connecticut (99CT21), U.S. Department of Defense Army Breast Cancer Program (DAMD17-00-1-0217, DAMD17-01-1-0216), and Multiple-Dimensional Technology, Inc.

References

1. T. A. Stavros, D. Thickman, and C. Rapp, "Solid breast nodules: use of sonography to distinguish between benign and malignant lesions," Radiology **196,** 123–134 (1995).
2. G. Rahbar, A. C. Sie, G. C. Hansen, J. S. Prince, M. L. Melany, H. Reynolds, V. P. Jackson, J. W. Sayre, and L. W. Bassett, "Benign versus malignant solid breast masses: US differentiation," Radiology **213,** 889–894 (1999).
3. V. P. Jackson, "The current role of ultrasonography in breast imaging," Radiol. Clin. North Am. **33,** 1161–1170 (1995).
4. B. Tromberg, N. Shah, R. Lanning, A. Cerussi, J. Espinoza, T. Pham, L. Svaasand, and J. Butler, "Non-invasive in vivo characterization of breast tumors using photon migration spectroscopy," Neoplasia **2,** 26–40 (2000).
5. S. Fantini, S. Walker, M. Franceschini, M. Kaschke, P. Schlag, and K. Moesta, "Assessment of the size, position, and optical properties of breast tumors *in vivo* by noninvasive optical methods," Appl. Opt. **37,** 1982–1989 (1998).
6. S. M. Nioka, M. Shnall, M. Miwa, S. Orel, M. Haida, S. Zhao, and B. Chance, "Photon imaging of human breast cancer," Adv. Exp. Med. Biol. **16,** 171–179 (1994).
7. R. M. Danen, Y. Wang, X. D. Li, W. S. Thayer, and A. G. Yodh,

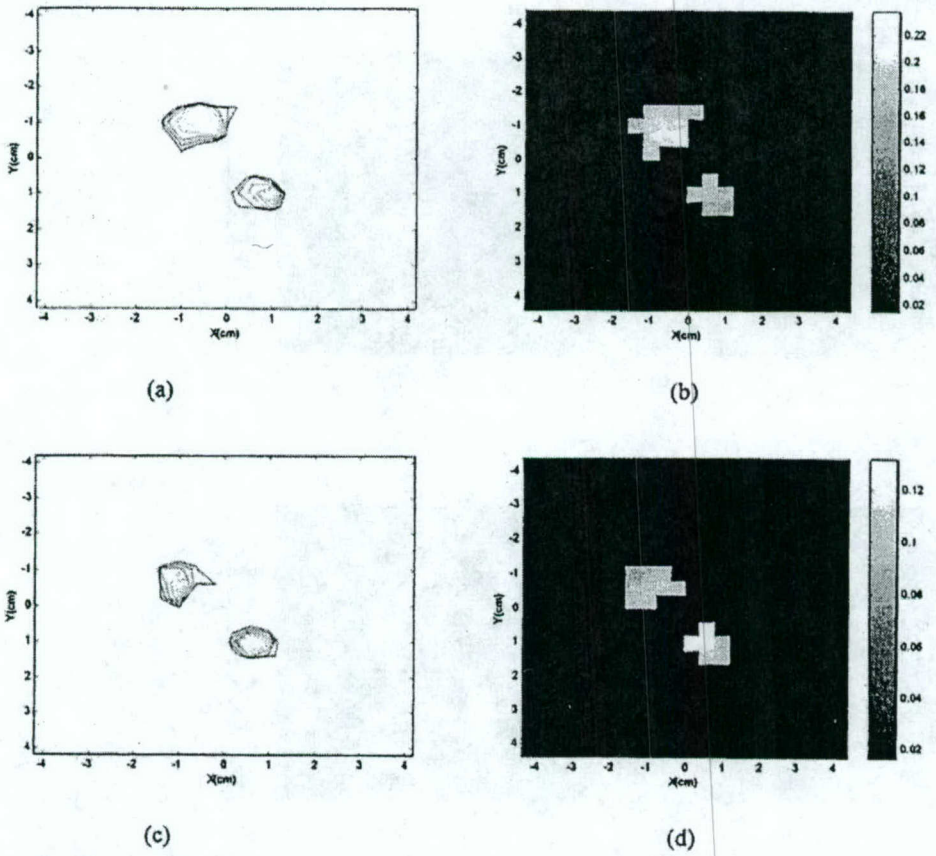

Fig. 12. (a) and (c) −6-dB contour plots of ultrasound images shown in Figs. 11(a) and 11(c). The outer contour is −6 dB from the peak, and the contour spacing is 1 dB. (b) and (d) Corresponding NIR absorption maps reconstructed in target regions specified by ultrasound.

"Regional imager for low resolution functional imaging of the brain with diffusing near-infrared light," Photochem. Photobiol. **67,** 33–40 (1998).

8. T. McBride, B. W. Pogue, E. Gerety, S. Poplack, U. Osterberg, B. Pogue, and K. Paulsen, "Spectroscopic diffuse optical tomography for the quantitative assessment of hemoglobin concentration and oxygen saturation in breast tissue," Appl. Opt. **38,** 5480–5490 (1999).
9. M. A. Franceschini, K. T. Moesta, S. Fantini, G. Gaida, E. Gratton, H. Jess, M. Seeber, P. M. Schlag, and M. Kashke, "Frequency-domain techniques enhance optical mammography: initial clinical results," Proc. Natl. Acad. Sci. USA **94,** 6468–6473 (1997).
10. J. B. Fishkin, O. Coquoz, E. R. Anderson, M. Brenner, and B. J. Tromberg, "Frequency-domain photon migration measurements of normal and malignant tissue optical properties in a human subject," Appl. Opt. **36,** 10–20 (1997).
11. T. L. Troy, D. L. Page, and E. M. Sevick-Muraca, "Optical properties of normal and diseased breast tissues: prognosis for optical mammography," J. Biomed. Opt. **1,** 342–355 (1996).
12. R. J. Grable, D. P. Rohler, and S. Kla, "Optical tomography breast imaging," in *Optical Tomography and Spectroscopy of Tissue: Theory, Instrumentation, Model, and Human Studies II*, B. Chance and R. Alfano, eds., Proc. SPIE **2979,** 197–210 (1997).
13. Y. Yao, Y. Wang, Y. Pei, W. Zhu, and R. L. Barbour, "Frequency-domain optical imaging of absorption and scattering distributions by a Born iterative method," J. Opt. Soc. Am. A **14,** 325–341 (1997).
14. H. Jiang, K. Paulsen, U. Osterberg, B. Pogue, and M. Patterson, "Optical image reconstruction using frequency-domain data: simulations and experiments," J. Opt. Soc. Am. A. **12,** 253–266 (1995).
15. X. Li, T. Durduran, A. Yodh, B. Chance, and D. N. Pattanayak, "Diffraction tomography for biomedical imaging with diffuse-photon density waves," Opt. Lett. **22,** 573–575 (1997).
16. C. Matson and H. Liu, "Backpropagation in turbid media," J. Opt. Soc. Am. A **16,** 1254–1265 (1999).
17. M. A. O'Leary, "Imaging with diffuse photon density waves," Ph.D. dissertation (University of Pennsylvania, Philadelphia, Pa., 1996).
18. K. Paulsen, P. Meaney, M. Moskowitz, and J. Sullivan, Jr., "A dual mesh scheme for finite element based reconstruction algorithms," IEEE Trans. Med. Imaging **14,** 504–514 (1995).
19. S. Arridge and M. Schweiger, "Photon-measurement density functions. Part I: Analytical forms," Appl. Opt. **34,** 7395–7409 (1995).
20. S. Arridge and M. Schweiger, "Photon-measurement density functions. II. Finite-element-method calculations," Appl. Opt. **34,** 8026–8037 (1995).
21. Q. Zhu, T. Dunrana, M. Holboke, V. Ntziachristos, and A. Yodh, "Imager that combines near-infrared diffusive light and ultrasound," Opt. Lett. **24,** 1050–1052 (1999).
22. Q. Zhu, D. Sullivan, B. Chance, and T. Dambro, "Combined

ultrasound and near infrared diffusive light imaging," IEEE Trans. Ultrason. Ferroelectr. Freq. Control **46,** 665–678 (1999).
23. Q. Zhu, E. Conant, and B. Chance, "Optical imaging as an adjunct to sonograph in differentiating benign from malignant breast lesions," J. Biomed. Opt. **5**(2), 229–236 (2000).
24. Q. Zhu, N. G. Chen, D. Q. Piao, P. Y. Guo, and X. H. Ding, "Design of near-infrared imaging probe with the assistance of ultrasound localization," Appl. Opt. **40,** 3288–3303 (2001).
25. M. Jholboke, B. J. Tromberg, X. Li, N. Shah, J. Fishkin, D. Kidney, J. Butler, B. Chance, and A. G. Yodh, "Three-dimensional diffuse optical mammography with ultrasound localization in human subject," J. Biomed. Opt. **5**(2), 237–247 (2000).
26. W. Zhu, Y. Wang, and J. Zhang, "Total least-squares reconstruction with wavelets for optical tomography," J. Opt. Soc. Am. A **15,** 2639–2650 (1998).
27. P. C. Li, W. Flax, E. S. Ebbini, and M. O'Donnell, "Blocked element compensation in phased array imaging," IEEE Trans. Ultrason. Ferroelectr. Freq. Control **40**(4), 283–292 (1993).
28. G. H. Golub, "Some modified matrix eigenvalue problems," SIAM (Soc. Ind. Appl. Math.) Rev. **15,** 318–334 (1973).
29. H. Zonderland, E. G. Coerkamp, J. Hermans, M. J. van de Vijver, and A. E. van Voorthuisen, "Diagnosis of breast cancer: contribution of US as an adjunct to mammography," Radiology **213,** 413–422 (1999).
30. T. M. Kolb, J. Lichy, and J. H. Newhouse, "Occult cancer in women with dense breast: detection with screening US-diagnostic yield and tumor characteristics," Radiology **207,** 191–199 (1998).

Journal of Biomedical Optics 9(3), 504–510 (May/June 2004)

Portable near-infrared diffusive light imager for breast cancer detection

Nan Guang Chen
Minming Huang
Hongjun Xia
Daqing Piao
University of Connecticut
Department of Electrical & Computer Engineering
Storrs, Connecticut 06269

Edward Cronin
Hartford Hospital
Radiology Department
Hartford, Connecticut 06102

Quing Zhu
University of Connecticut
Department of Electrical & Computer Engineering
Storrs, Connecticut 06269

Abstract. We present a frequency-domain near-infrared optical tomography system designed for breast cancer detection, in conjunction with conventional ultrasound. It features fast optical switching, three-wavelength excitations, and avalanche photodiode as detectors. Laser diodes at 660, 780, and 830 nm are used as light sources and their outputs are distributed sequentially to one of nine source fibers. An equivalent 130-dB isolation between electrical signals from different source channels is achieved with the optical switches of very low crosstalk. Ten detection channels, each of which includes a silicon avalanche photodiode, detect diffusive photon density waves simultaneously. The dynamic range of an avalanche photodiode is about 20 to 30 dB higher than that of a photomultiplier tube, thus eliminating the need for multistep system gain control. The entire system is compact in size (<0.051 m^3) and fast in data acquisition (less than 2 sec for a complete scan). Calibration and the clinical experiment results are presented in the paper. [DOI: 10.1117/1.1695410]

Keywords: diffusive imaging; optical switches; avalanche photodiodes; dynamic range; breast cancer.

Paper 44011 received Jul. 11, 2003; revised manuscript received Jan. 19, 2004; accepted for publication Feb. 3, 2004.

1 Introduction

Frequency-domain near-infrared optical tomography systems have been widely used to study optical properties of breast cancers *in vivo*.[1–3] In the Optical and Ultrasound Imaging Laboratory at the University of Connecticut, we are developing a hybrid imager that combines optical tomography and conventional ultrasound for breast cancer detection.[4,5] The ultimate goal of our studies is to establish a method that is more accurate and efficient than conventional x-ray mammography for breast cancer detection and diagnosis, for assessing cancer treatment, and for monitoring cancer recurrence. The combination of ultrasound with optical imaging provides complementary diagnostic information. The acoustic property of a simple cyst can be well distinguished from that of a tumor, while the local blood volume and blood oxygenation can be related to tumor malignance. In addition, using high-resolution ultrasound images to guide optical imaging reconstruction can partly solve the ill-posed problem and lead to more accurate reconstructed values.[6,7] As a similar idea, combination of optical imaging with MRI for small animal imaging has been reported recently.[8,9] Our clinical experiments at the University of Connecticut Health Center and Hartford Hospital have been successful, but we do feel the need to update the optical imager we built two years ago. First of all, it is heavy and bulky, which makes the transportation to multiple clinical locations difficult. Second, we used electronic switching for the light sources. Because the laser diodes need a certain time period to stabilize after switching, the data acquisition time was about 8 sec for one scan. In general, three scans at lesion locations and at reference locations are necessary for checking patient motion and for calculating averages. To reduce the size, weight, and data acquisition time, we designed and built a completely new optical imager.

There are two major changes in our new frequency-domain optical imager. Instead of using paired dual-wavelength laser diodes and electronic switching, only three laser diodes (660, 780, and 830 nm) are used in the new system. So the total number of laser diodes is reduced from 24 (would be 36 if three wavelengths are needed) to three. Optical switching is employed to distribute outputs of laser diodes to different source channels. Such architecture helps simplify the light source driving circuitry, reduce the size and weight, and increase the switching speed. For the detection subsystem, photomultiplier tubes (PMTs) were replaced by much lighter and smaller silicon avalanche photodiodes (APDs). Semiconductor photodetectors generally have higher quantum efficiency and dynamic range than PMTs, and cover a fairly wide spectral range (400 to 1100 nm for silicon photodiodes). Two important types of high-speed semiconductor photodetectors are PIN photodiodes and APDs. Nonetheless, a typical PMT has an internal gain ranging from 10^5 to 10^7. Consequently, its optoelectrical current level is much higher than those of PIN and APD detectors. This is the main reason that PMTs are so popular in weak light detection, and that we used them in our previous system. Normal photodiodes usually have a noise level about two orders lower than that of a high-speed preamplifier. Consequently, the signal-to-noise ratio of the detec-

Address all correspondence to Nanguang Chen, Electrical & Computer Engineering Department, University of Connecticut, 371 Fairfield Road, Unit 1157, Storrs, Connecticut 06269. Tel: 860-486-1818; FAX: 860-486-1273; E-mail: chenng@engr.uconn.edu

1083-3668/2004/$15.00

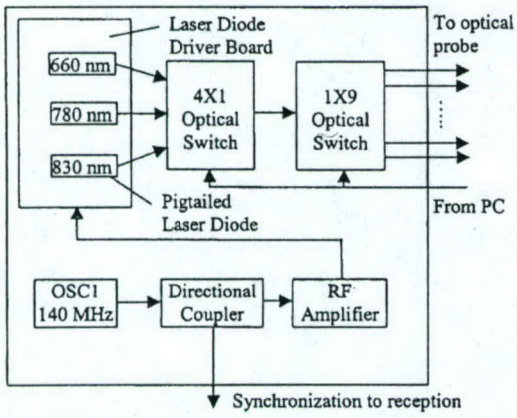

Fig. 1 Schematic of the transmission part.

tion system is dominated by the preamplifier noise. A silicon APD can have an internal gain of 100 to 1000. Such an internal gain makes it possible to match the noise level of optoelectrical signals with the input noises of available preamplifiers. While the noise level remains almost the same, the signal strength is increased by 40 to 60 dB and so is the signal-to-noise ratio. Since the output signals from APD detectors are much weaker than the output from a PMT, cautions have been taken to reduce the impact of environmental noises and, especially, feed-through interferences. We have employed a careful radio-frequency (RF) design to achieve the minimal feed-through interference level from the transmission part to the reception part.

2 System Design

To suppress interferences as much as possible, the new diffusive light imager is separated into a transmission part and a reception part. Each part is enclosed in an aluminum chassis measuring $17\times13\times7$ cubic inches. The transmission part is responsible for generating amplitude-modulated light output at three wavelengths of 660, 780, and 830 nm. It also contains optical switches that distribute light power to nine source channels. In the reception part, there are 10 detection channels that simultaneously measure intensities of diffusive light collected by light guides. The connection between the transmission and the reception parts is a coaxial cable, which transmits a synchronization signal from the transmission part to the reception part. The synchronization signal is used to generate a reference signal, which is necessary for retrieving phase shifts related to photon density waves at different locations. A negative effect of the synchronization signal is the unwanted interferences that it brings into the detection channels. However, the synchronization signal has to be strong enough to overcome zero-cross point shifting caused by noises. So determination of the synchronization signal level is a tradeoff between the interference level and phase accuracy. We gradually lowered the synchronization signal to the point beyond which the measured phase noise increased suddenly.

Shown in Fig. 1 is the schematic of the transmission part. Pigtailed laser diodes from Thorlabs are used as light sources. Three wavelengths (660, 780, and 830 nm) pertinent to imaging hemoglobin concentrations and tumor hypoxia are available at an $\approx$10-mW fiber output power. A 10-dBm oscillator generates 140-MHz sine waves for modulation. Most of its output goes through a directional coupler to a RF amplifier, while a small portion is directed to the reception part as the synchronization signal. An attenuator (not shown in Fig. 1) is used to further reduce the power level of the synchronization signal. The amplified 140-MHz signal is connected to a laser diode driver board, at which it is combined with dc bias currents to feed laser diodes. Modulated light outputs are coupled to three input ports of a 4×1 optical switch. A remaining input port is reserved for an additional wavelength, which we may add in the future. The output of the 4×1 optical switch is directly connected to the input of a 1×9 optical switch, each of whose output fibers corresponds to one source position.

Table 1 Specifications of piezosystem jena 4×1 and 1×9 optical switches.

Insertion loss	2 dB (max)	1.6 dB (typical)
Cross talk	60 dB (max)	65 dB (typical)
Repeatability (>1500 cycles over 1 h)	0.02 dB (max)	0.01 dB (typical)
Operating voltage	5 V (500 mA)	
Operating temperature range	0° to 50°C	

Both optical switches were purchased from piezosystem jena GmbH. They are compact in size ($168\times113\times30$ mm^3) and can be controlled by BCD codes via a D-sub 25 connector. Input and output optical fibers (62.5-μm core diameter) are terminated with standard ST connectors. Other specifications (for both 4×1 and 1×9) are listed in Table 1. Their switching time is about 2 ms, much faster than other similar products on the market, and warrants near-real-time image acquisition. Crosstalk and repeatability of these switches are also reasonably good. For example, the crosstalk between different optical channels is better than 65 dB. Since the optical power is converted proportionally to voltage or current at a photodetector, the resulting isolation in electrical signals from different sources channels is 130 dB. A National Instruments multifunction data acquisition card (DAQ) installed in a PC provides 4-digit control signals for each optical switch.

The reception part consists of 10 identical detection channels, which are sealed in 10 small aluminum boxes for RF shielding. Figure 2(a) shows the overall structure of the reception part, while Fig. 2(b) shows the schematic of each detection channel. In each detection channel, a light guide collecting diffusive lights from an optical imaging probe is coupled to an APD (S3884, Hamamatsu) by the use of an adaptor. As a result of modulated light sources, the optoelectrical current of the APD detector has an ac component at the same frequency, i.e., 140 MHz. A high-speed low-noise transimpendence amplifier (SA5212A, Philips Semiconductors) converts the opto-electrical current to a voltage signal, which is then mixed with a 140.020-MHz signal (generated by a local oscillator OSC2) at a frequency mixer (SBL-1, Mini-Circuits). The heterodyne signal passes through a bandpass (BP) filter with a center frequency at 20 KHz, and is further amplified by

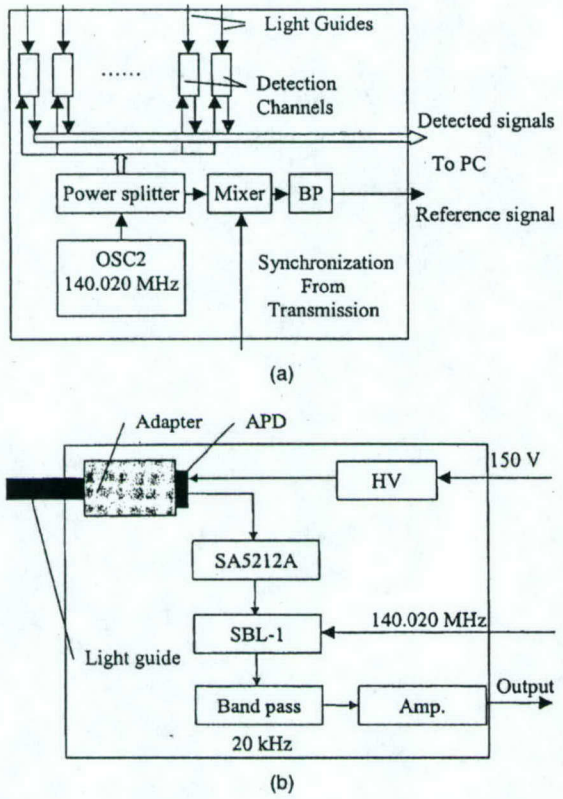

Fig. 2 Schematic of the reception part.

another low-frequency amplifier by about 40 dB. The resulting signal contains both amplitude and phase information related to the original RF signal. However, a reference signal is necessary for accurate retrieval of the phase. The synchronization signal from the transmission part is mixed with the local oscillation of 140.020 MHz to generate the reference signal, which serves as a trigger signal for data acquisition. Outputs from all detection channels and the reference signal are digitized with two DAQ cards (PCI-6070E, National Instruments) working synchronously. Hilbert transform is performed on a PC to compute the amplitude and phase of each acquired waveform. The amplitude A_{ij} for the source i and detector j is simply the mean magnitude of the Hilbert transform of corresponding waveform $u_{ij}(n)$,

$$A_{ij} = mean(abs\{hilbert[u_{ij}(n)]\}), \quad (1)$$

where n denotes the discrete time point. The phase ϕ_{ij} is given by

$$\varphi_{ij} = mean(angle\{hilbert[u_{ij}(n)]\} - angle\{hilbert[u_r(n)]\}), \quad (2)$$

where $u_r(n)$ is the reference sequence.

A high voltage (HV) adjustment circuit is used to provide an appropriate voltage for each individual APD. Shown in Fig. 3(a) is a typical way to connect the HV power supply (CA02P, EMCO High Voltage Corporation) with an APD and a transimpedance amplifier.[10] A resistor of 10 to 100 k limits

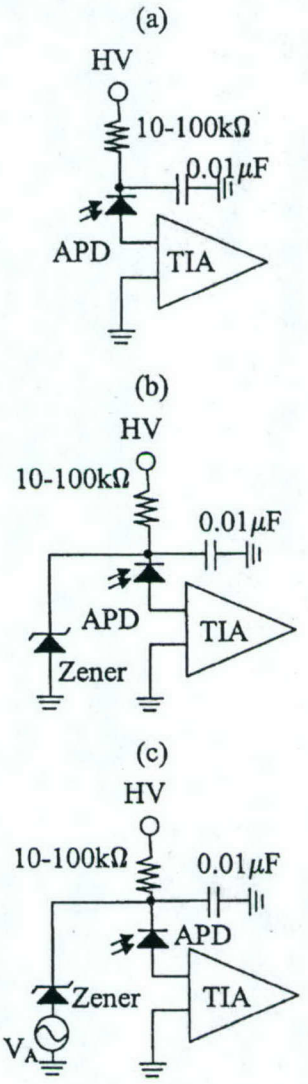

Fig. 3 High-voltage power supply circuitry.

the optoelectrical current, while the HV is set to the operational voltage. This circuit is good for digital applications such as in optical communication. However, the optoelectrical response becomes nonlinear when the optical input power causes a substantial increase in the voltage across the resistor and a decrease in the APD bias. By parallel connecting a Zener diode to clamp the voltage across the APD, as shown in Fig. 3(b), we can significantly improve the linear input range. Of course, the breaking voltage of the Zener diode should match the operational voltage of the APD, and the HV should be set at a higher value. But there is still another problem. The avalanche photodiodes came with operational voltages ranging from 127 to 139 V (for internal gain $M = 100$). It is very difficult to do exact and homogeneous matching for all the 10 channels. We add a variable voltage source in series with the Zener diode to facilitate the adjustment [Fig. 3(c)]. The variable voltage source is comprised of a transistor and a potentiometer, which provides continuously adjustable voltage

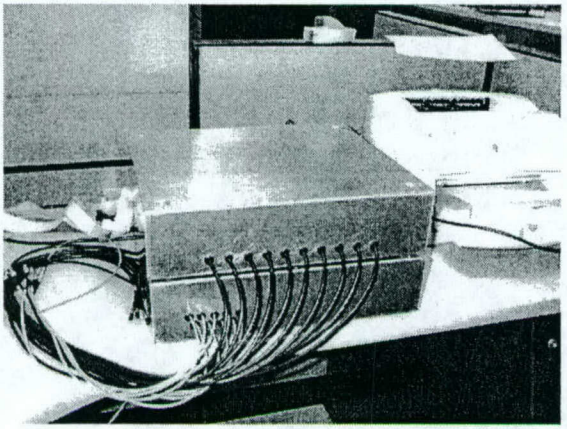

(a)

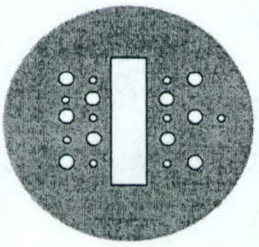

(b)

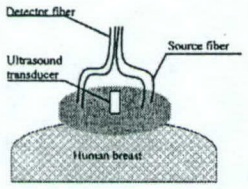

(c)

Fig. 4 (a) Picture of the new imager. Its size is compared with a portable printer. (b) Configuration of the combined probe. Smaller circles indicate locations of light sources, and larger circles correspond to detection light guide positions. The central rectangular hole is used to hold an ultrasound transducer. (c) Geometry for detection breast cancers with the combined probe.

from 0.5 to 12 V. The breaking voltage of the Zener diode is around 126 V.

A special procedure in the data acquisition program is needed to overcome the limited dynamic range of the DAQ card. The analog-to-digital conversion has a 12-bit resolution, which corresponds to about a 72-dB dynamic range. However, the analog part of the reception system is capable of providing an 80- to 90-dB dynamic range. We used the programmable input range of the DAQ card to solve this problem. For each source-detector pair, the waveform related to the photon density wave is digitized twice. In the first period we use an input range of the DAQ card of -1 to 1 V, while in the second period we use -10 to 10 V. The amplitudes and phases are retrieved for both the smaller range and the larger range. If the amplitude associated with the bigger range is greater than 1 V, it will be taken as the measured value, and so will the corresponding phase. Otherwise, the values associated with the

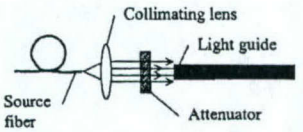

(a)

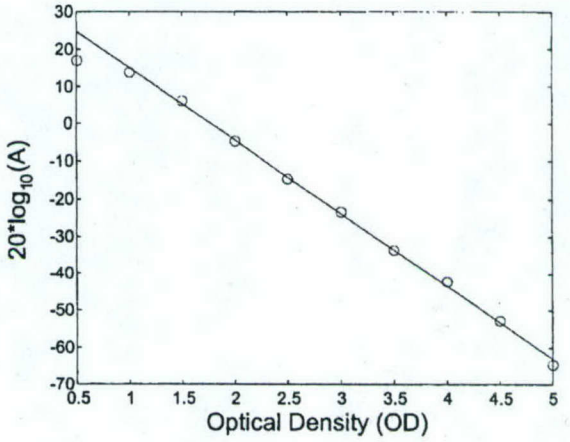

(b)

Fig. 5 (a) Setup for testing the system linearity. (b) The amplitudes (A) in logarithm versus total optical density of inserted attenuators. Circles: measured values; solid line: linear fitting.

smaller range will be adopted. This procedure effectively increases the dynamic range by 20 dB.

The overall weight of the system is about 12 kilograms, while our previous PMT-based system weighs more than 60 kilograms. Shown in Fig. 4(a) is a picture of our new imager. The transmission and reception parts are stacked together, while a portable printer is put aside for comparison of the sizes. For the sake of mobility, an LCD monitor is used together with a desktop computer for data acquisition. Source fibers and detection light guides are connected to a combined probe [Fig. 4(b)]. In clinical studies, a commercial ultrasound transducer is inserted in the middle of the combined probe, which is placed on the top of a breast with the patient in a supine position.

3 Testing and Calibration

The system linearity was tested with neutral density filters and the setup shown in Fig. 5(a). The source fiber was connected to one source channel through an inline attenuator of 20 dB. Output light from the source fiber was collimated with a lens, and a small portion of it (about 1%) is directed to the light guide connected to a detection channel. Neutral density filters were inserted into the path of the collimated light to adjust the light intensity coupled to the detector. The optical density (OD) values of the neutral density filter set were 0.5, 1, and 3. By stacking them together, an attenuation range from $10^{-0.5}$ ($OD=0.5$) to 10^{-5} ($OD=5$) was achieved. The detected signal amplitude in logarithm scale versus optical density is plotted in Fig. 5(b). It is obvious that the linearity of the detection system is very good in the range $1 \leq OD \leq 5$, which is equivalent to 80 dB. At the point of $OD=0.5$, saturation of the detector occurred and the amplitude was suppressed by

approximately 7 dB. The dynamic range of system was estimated around 85 dB. This is achieved without two-stage light source control, which is necessary for a PMT system of similar dynamic range. The measured phases remain essential constant, as a result of very small amplitude-phase cross talk.

Uniformity of source and detection channels was calibrated with following procedures. To test the source channel uniformity, different source channels were sequentially coupled to one detection channel via an inline attenuator of 70 dB. To test the detection channel uniformity, different detection channels were switched to one source channel. The variations in amplitude and phase of source channels were 0.27 dB and 0.19 rad respectively. For the detection channels, the variations were 0.9 dB for amplitudes and 0.23 rad for phases. The relative gain and phase shift of each source or detection channel were included in image reconstruction algorithms to cancel channel heterogeneity.

4 Image Reconstruction Method

A dual-mesh image reconstruction algorithm, proposed in our previous publication,[7] has been implemented in our new imager. Briefly, the total imaging volume is segmented into two regions L and B, where the lesion region L contains suspected structures found on co-registered ultrasound images and the nonlesion region B is the background. Then the target and background regions are discretized with different voxel sizes, resulting in a finer grid in the lesion region and a coarse grid in nonlesion region. We consider only absorption changes in the medium on the assumption that the contribution of scattering heterogeneities to the measurement is negligible, although similar procedures can be applied to reconstructing scattering coefficients. When the Born approximation is valid, the scattered diffusive light intensity can be approximated by

$$U'_{sc}(\mathbf{r}_{si},\mathbf{r}_{di},\omega)\approx -\frac{1}{D}\Bigg(\sum_{Lj} G(\mathbf{r}_{vj},\mathbf{r}_{di})U_{inc}(\mathbf{r}_{vj},\mathbf{r}_{si}) \times \int_j \Delta\mu_a(\mathbf{r}')d^3r' + \sum_{B_k} G(\mathbf{r}_{vk},\mathbf{r}_{di})U_{inc}(\mathbf{r}_{vk},\mathbf{r}_{si}) \times \int_k \Delta\mu_a(\mathbf{r}')d^3\mathbf{r}'\Bigg), \quad (3)$$

where $G(\mathbf{r}_1,\mathbf{r}_2)$ and $U_{inc}(\mathbf{r}_1,\mathbf{r}_2)$ are the Green's function and incident diffusive light intensity connecting location $\mathbf{r}_1$ and $\mathbf{r}_2$, r_{vj} is the center of voxel j in lesion region L, r_{vk} is the center of voxel k in the background region B, and r_{si} and r_{di} are source and detector positions, respectively. Equation (1) can be written in the following matrix form:

$$[U_{sd}]_{M\times 1}=[W_L,W_B]_{M\times N}[M_L,M_B]^T_{N\times 1}, \quad (4)$$

where

$$W_L=\left[-\frac{1}{D}G(r_{vj},r_{di})U_{inc}(r_{vj},r_{si})\right]_{M\times N_L},$$

$$W_B=\left[-\frac{1}{D}G(r_{vk},r_{di})U_{inc}(r_{vk},r_{si})\right]_{M\times N_B},$$

$$[M_L]=\left[\int_{1_L}\Delta\mu_a(r')d^3r',\cdots,\int_{N_L}\Delta\mu_a(r')d^3r'\right],$$

and

$$[M_B]=\left[\int_{1_B}\Delta\mu_a(r')d^3r',\cdots,\int_{N_B}\Delta\mu_a(r')d^3r'\right].$$

Instead of reconstructing $\Delta\mu_a$ distribution directly, we reconstruct the total absorption distribution M and then divide it by different voxel sizes of target and background regions to obtain the $\Delta\mu_a$ distribution. In general, the target region is more absorbing than the background, and the total absorption distribution M, which is approximately the product of $\Delta\mu_a$ and the corresponding voxel size, is well scaled between lesion region and nonlesion region for inversion. In the following clincal case studies, we have used a finer grid of $0.5\times0.5\times0.5$ (cm^3) in the target region and a coarse grid of $1.5\times1.5\times1.0$ (cm^3) in the background region. As a result, the weight matrix $[W']=[W_L,W_B]$ expands to several discrete layers in depth and the weight matrix W_L of larger tumors also expands to two to three layers. The total least square method is employed to formulize the inverse problem, and the conjugate gradient method is used to minimize the object function.[4,5] The iterative search converges quickly in two to three iterations, and thus no regularization scheme is used in the inversion.

5 Clinical Case Study

Clinical studies were performed at Hartford Hospital with the protocol approved by the IRB committee of the Hartford Hospital. The first example was obtained from a 45-year-old patient who had a suspicious lesion at the 3 o'clock position of the left breast. The combined probe was centered approximately above the lesion for acquisition of ultrasound and optical images. The ultrasound gray-scale image with Doppler superimposed is shown in Fig. 6. The lesion has an irregular shape and posterior shadowing. Ultrasound Doppler reveals blood flow at the lesion periphery. The diagnosis based on ultrasound was highly suspicious and biopsy was recommended.

Optical data at three wavelengths were taken before the biopsy procedure. The data acquisition time for each scan was less than 2 sec, much faster than our previous system (about 8 sec for two source levels). Multiple data sets at the lesion location as well as at the contralateral normal breast were acquired. It took about 5 min for the entire experiment. Figures 7–9 show the reconstructed optical absorption maps at three wavelengths. For each slice, the spatial dimensions are 9 by 9 cm. The first slice is 0.7 cm from the skin surface and the last slice is close to the chest wall. The spacing between slices is 0.5 cm. The optical absorption distributions appear diffused, and absorption maximums at the three wavelengths are 0.1420, 0.1499, and 0.1450 cm^{-1}, respectively. The total hemoglobin concentration calculated from 780 and 830 nm is shown in Fig. 10. The extinction coefficients used are ob-

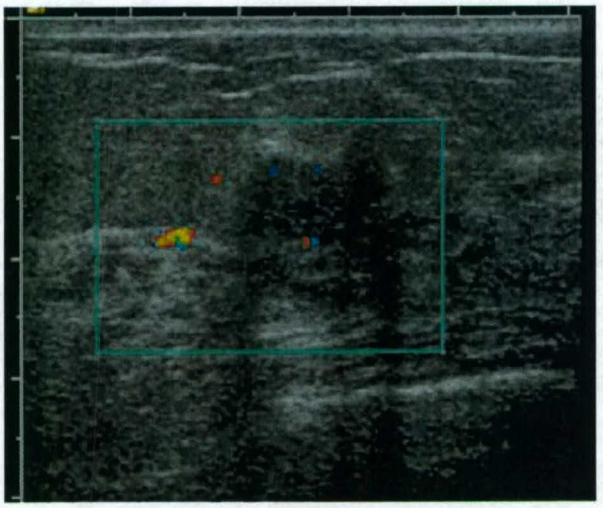

Fig. 6 Ultrasound gray-scale image with Doppler superimposed. The lesion was located at the 3 o'clock position of the left breast of a 45-year-old patient and was considered as highly suspicious. The ultrasound revealed irregular shape and posterior shadowing with blood flow seen at several periphery sites of the lesion.

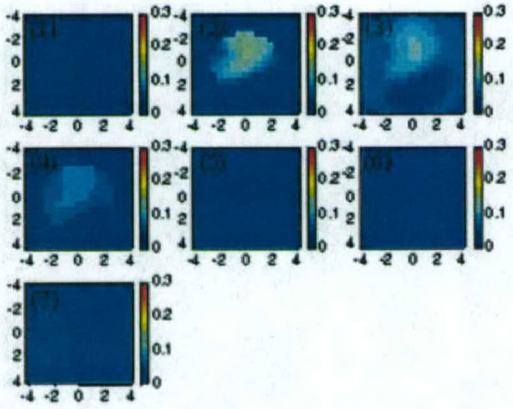

Fig. 7 Reconstructed optical absorption map at 660 nm. The slices were from 0.7 cm underneath the skin to the chest wall with 0.5-cm spacing. For each slice, the horizontal and vertical axes are X and Y, respectively, with the spatial dimensions of 9×9 cm. The lesion appears in slice 2, 3, and 4.

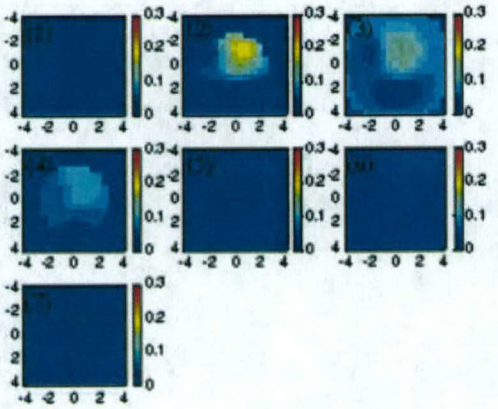

Fig. 8 Reconstructed optical absorption map at 780 nm. Similar distribution at 660 nm was observed.

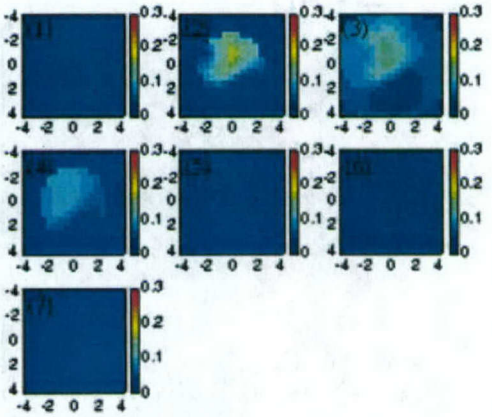

Fig. 9 Reconstructed optical absorption map at 830 nm. Similar distributions at 660 and 780 nm were observed.

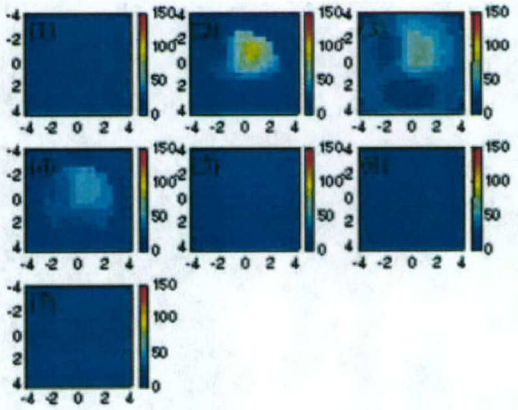

Fig. 10 Total hemoglobin concentration calculated from 780 and 830 nm. The color bars are in units of micromoles.

tained from Ref. 11. The maximum concentration is 68.90 μmol. Earlier results obtained from two invasive early stage cancers and 17 benign lesions have shown that malignant cancers present an average of 119-μmol maximum total hemoglobin concentration while the benign group has an average of 67 μmol.[12] A nearly two-fold higher contrast has been obtained. In addition, the malignant cancers were well resolved while the benign lesions appeared diffused. Based on our experience, the diffused patterns of the absorption distributions and the maximum total hemoglobin concentration level all suggested that the lesion should be benign. Biopsy revealed that the lesion was a benign fibroadenoma with no evidence of malignancy.

6 Discussions and Conclusions

In our original design of the new imager, wavelengths of 780, 808, and 830 nm are picked for light sources. Unfortunately, pigtailing of the 808-nm laser diodes was not successful and the coupling efficiency was too low to provide enough output optical power. So we chose a commercially available 660-nm pigtailed laser diode as the third wavelength besides 780 and 830 nm. However, the 660-nm light is much more strongly absorbed by human tissues than 780 and 830 nm. As a result, the signal strength of distant source-detector pairs is generally too weak for 660 nm and leads to inferior image quality compared with the other two wavelengths. This is the reason we just used optical images at 780 and 830 nm to calculate the total hemoglobin concentration. Nonetheless, 660 nm is still useful for shallow lesions, which primarily result in perturbations for short source-detector pairs. We will include more useful wavelengths in the future. In addition, the total hemoglobin is estimated as $Hb_t(r)=0.2002\mu_a^{780}(r)+0.2732\mu_a^{830}(r)$, where $\mu_a^{780}(r)$ and $\mu_a^{830}(r)$ are absorption coefficients obtained at 780 and 830 nm at voxel r. If three wavelengths are used, the total hemoglobin can be estimated as $Hb_t(r)=0.0029\mu_a^{660}(r)+0.18361\mu_a^{780}(r)+0.2838\mu_a^{830}(r)$. The contribution of the 660-nm absorption to total hemoglobin is small, however, the significance of adding 660 nm is on tissue hypoxia estimation. This issue will be addressed in our future publications.

To conclude, a portable multichannel multiwavelength optical tomography system has been developed for breast cancer imaging. The major advantages of this new imager include its compactness and the near-real-time data acquisition speed. In addition, it has a wide dynamic range achieved without multistep system gain control.

Acknowledgments

We would like to thank the following for their funding support: the State of Connecticut (99CT21), DOD ARMY Breast Cancer Program (DAMD17-00-1-0217, DAMD17-01-1-0216), and NIH (8R01EB002136-02).

References

1. M. A. Franceschini, K. T. Moesta, S. Fantini, G. Gaida, E. Gratton, H. Jess, M. Seeber, P. M. Schlag, and M. Kashke, "Frequency-domain techniques enhance optical mammography: initial clinical results," *Proc. Natl. Acad. Sci. U.S.A.* **94**, 6468–6473 (1997).
2. H. Jiang, K. Paulsen, Ulf Osterberg, B. Pogue, and M. Patterson, "Optical image reconstruction using frequency-domain data: simulations and experiments," *J. Opt. Soc. Am. A* **13**, 253–266 (1996).
3. J. B. Fishkin, O. Coquoz, E. R. Anderson, M. Brenner, and B. J. Tromberg, "Frequency-domain photon migration measurements of normal and malignant tissue optical properties in human subject," *Appl. Opt.* **36**, 10–20 (1997).
4. Q. Zhu, N. G. Chen, X. Ding, D. Piao, and P. Guo, "Design of near infrared imaging probe with the assistance of ultrasound localization," *Appl. Opt.* **40**, 3288–3303 (2001).
5. N. G. Chen, P. Guo, S. Yan, D. Piao, and Q. Zhu, "Simultaneous near infrared diffusive light and ultrasound imaging," *Appl. Opt.* **40**, 6367–6280 (2001).
6. N. G. Chen and Q. Zhu, "Characterization of small absorbers inside turbid media," *Opt. Lett.* **27**, 252–254 (2002).
7. Q. Zhu, N. G. Chen, and S. Kurtzman, "Imaging tumor angiogenesis using combined near infrared diffusive light and ultrasound," *Opt. Lett.* **28**, 337–339 (2003).
8. H. Xu, H. Dehghani, B. W. Pogue, R. Springett, K. D. Paulsen, and J. F. Dunn, "Near infrared imaging in the small animal brain: optimization of fiber positions," *J. Biomed. Opt.* **8**, 102–110 (2003).
9. V. Ntziachristos, A. G. Yodh, M. D. Schnall, and B. Chance, "MRI-guided diffuse optical spectroscopy of malignant and benign breast lesions," *Neoplasia* **4**, 347–354 (2002).
10. "Characteristics and use of Si APD (avalanche photodiodes)," Technical information SD-28, Hamamatsu Corporation.
11. M. Cope, "The development of a near infrared spectroscopy system and its application for noninvasive monitoring of cerebral blood and tissue oxygenation in the newborn infant," PhD thesis, Department of Medical Physics and Bioengineering, University College London, 1991.
12. Q. Zhu, M. Huang, N. G. Chen, K. Zarfos, B. Jagjivan, M. Kane, and S. H. Kurtzman, "Ultrasound-guided optical tomographic imaging of malignant and benign breast lesions: initial clinical results of 19 cases," *Neoplasia* **5**(5), 379–389 (2003).

Design of near-infrared imaging probe with the assistance of ultrasound localization

Quing Zhu, Nan Guang Chen, Daqing Piao, Puyun Guo, and XiaoHui Ding

A total of 364 optical source–detector pairs were deployed uniformly over a 9 cm × 9 cm probe area initially, and then the total pairs were reduced gradually to 60 in experimental and simulation studies. For each source–detector configuration, three-dimensional (3-D) images of a 1-cm-diameter absorber of different contrasts were reconstructed from the measurements made with a frequency-domain system. The results have shown that more than 160 source–detector pairs are needed to reconstruct the absorption coefficient to within 60% of the true value and appropriate spatial and contrast resolution. However, the error in target depth estimated from 3-D images was more than 1 cm in all source–detector configurations. With the *a priori* target depth information provided by ultrasound, the accuracy of the reconstructed absorption coefficient was improved by 15% and 30% on average, and the beam width was improved by 24% and 41% on average for high- and low-contrast cases, respectively. The speed of reconstruction was improved by ten times on average.

OCIS codes: 170.0170, 170.3010, 170.5270, 170.7170, 170.3830.

1. Introduction

Recently, optical imaging techniques based on diffusive near-infrared (NIR) light have been employed to obtain interior optical properties of human tissues.[1–8] Functional imaging with NIR light has the potential to detect and diagnose diseases or cancers through the determination of hemoglobin concentration, blood O_2 saturation, tissue light scattering, water concentration, and the concentration and lifetime of exogenous contrast agents. Optical imaging requires that an array of sources and detectors be distributed directly or coupled through optical fibers on a boundary surface. Measurements made at all source–detector positions can be used in tomographic image reconstruction schemes to determine optical properties of the medium. The frequently used geometric configurations of sources and detectors are ring arrays[4,9–11] and planar arrays.[3,12–15] A ring array consists of multiple sources and detectors that can be distributed uniformly on a ring. Optical properties of the thin tissue slice (two-dimensional slice) enclosed by the ring can be determined from all measurements. A planar array can be configured with either transmission or reflection geometries. In transmission geometry, multiple detectors can be deployed on a planar array, and multiple sources or a single source can be deployed on an opposite plane parallel to the detector plane. Optical properties of the three-dimensional (3-D) tissue volume between the source and the detector planes can be determined from all measurements. In reflection geometry, multiple sources and detectors can be distributed on a planar probe that can be hand-held.[3,15] Optical properties of the 3-D tissue volume at slice depths below the probe can be determined from all measurements. The reflection probe configuration is desirable for the imaging of brain and breast tissues.

Although many researchers in the field have constructed imaging probes using reflection geometry,[2,3,15] to our knowledge the required total number of source–detector pairs over a given probe area needed to accurately reconstruct optical properties and localized spatial and depth distributions has not been addressed before. In this paper we study the relationship between the total number of source-detector pairs and the reconstructed imaging quality through experimental measurements. Computer simulations are performed to assist in understanding the experimental results.

Because the target localization from diffusive waves is difficult, our group and others have introduced use of *a priori* target location information pro-

The authors are with the Department of Electrical and Computer Engineering, University of Connecticut, 260 Glenbrook Road, U157, Storrs, Connecticut 06269. Q. Zhu's e-mail address is zhu@engr.uconn.edu.

Received 20 September 2000; revised manuscript received 21 March 2001.

0003-6935/01/193288-16$15.00/0

vided by ultrasound to improve optical imaging.[15–18] In this paper we demonstrate experimentally that the accurate target depth information can significantly improve the accuracy of the reconstructed absorption coefficient and the reconstruction speed for any optical array configuration.

The required total number of source–detector pairs is also related to the image reconstruction algorithms used. In this paper we obtained experimental measurements using a frequency-domain system with the source amplitude modulated at 140 MHz. In simulations, forward measurements were generated by use of the analytic solution of a photon density wave scattered by a spherical inhomogeneity embedded in a semi-infinite scattering medium.[19] In both experiments and simulations, linear perturbation theory within the Born approximation was used to relate optical signals at the probe surface to absorption variations in each volume element within the sample. The total least-squares (TLS) method[20–22] was used to formulate the inverse problem. The conjugate gradient technique was employed to iteratively solve the inverse problem. Therefore the results we obtained are directly relevant to the probe design with reconstruction algorithms based on the linear perturbation theory and can be used as a first-order approximation if high-order perturbations are employed in image reconstructions.

This paper is organized as follows. In Section 2 we describe an analytic solution used to generate simulated forward data, the Born approximation, and the TLS method for image reconstruction. In Section 3 we discuss the probe geometry, a frequency-domain NIR system used to acquire the experimental measurements, and an ultrasound subsystem used to acquire the target depth information, computation procedures used to obtain both simulated and experimental absorption images. In Sections 4 and 5 we report experimental results obtained from the dense and sparse arrays with and without *a priori* target depth information. A high-contrast example is given in Section 4, and a low-contrast case is given in Section 5. Simulations are performed to assist in understanding the noise on the image reconstruction. Imaging parameters evaluated are a −6-dB width of the image lobe, the reconstructed maximum value of the absorption coefficient and its spatial location, and the image artifact level. In Sections 6 and 7 we provide a discussion and summary, respectively.

2. Basic Principles

A. Forward Model

In our experiments, forward measurements were made with a frequency-domain system operating at a 140-MHz modulation frequency. In computer simulations, forward measurements were generated from an analytic solution of a photon density wave scattered by a spherical inhomogeneity.[19] When the center of the sphere coincides with the origin of spherical coordinates, the solution for the scattered

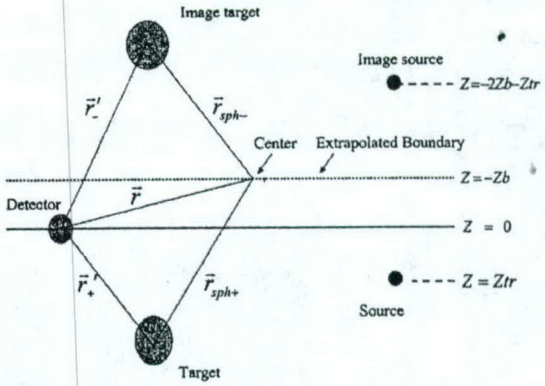

Fig. 1. Target, source, and detector configurations for a semi-infinite medium.

photon density wave U_{sc} outside the sphere at a detector position $\mathbf{r} = (r,\theta,\phi)$ is of the form

$$U_{sc}(\mathbf{r},\omega) = \sum_{l,m} \{A_{l,m}[j_l(k^{out}r) + jn_l(k^{out}r)]Y_{l,m}(\theta,\phi)\}, \quad (1)$$

where j_l and n_l are spherical Bessel and Neuman functions, respectively; $Y_{l,m}(\theta,\phi)$ are the spherical harmonics, and $k^{out} = [(-v\mu_a{}^{out} + j\omega)/D^{out}]^{1/2}$ is the complex wave number outside the sphere. ω is the angular modulation frequency of the light source, $\mu_a{}^{out}$ is the absorption coefficient outside the sphere, and D^{out} is the photon diffusion coefficient outside the sphere given by $D^{out} = 1/(3\mu_s')$, where μ_s' is the reduced scattering coefficient outside the sphere. The coefficients $A_{l,m}$, determined by the boundary conditions, are

$$A_{l,m} = -(jvSk^{out}/D^{out})h_l^{(1)}(k^{out}r_s)Y_{l,m}{}^*(\theta_s,\phi_s) \times \frac{D^{out}xj_l(y)j_l'(x) - D^{in}yj_l'(y)j_l(x)}{D^{out}xh_l^{(1)'}(x)j_l(y) - D^{in}yh_l^{(1)}(x)j_l'(y)}, \quad (2)$$

where $x = k^{out}a$, $y = k^{in}a$, $\mathbf{r}_s = (r_s,\theta_s,\phi_s)$ is the source position, $h_l^{(1)}$ are the Hankel functions of the first kind, and j_l' and $h_l^{(1)'}$ are the first derivatives of j_l and $h_l^{(1)}$. The analytic solution has the important advantage in that it is exact to all orders of perturbation theory and thus can represent accurate measurements.

We generalized the above analytic solution to a semi-infinite geometry by using a method of images with extrapolated boundary conditions (see Fig. 1). A type I boundary condition (zero light energy density at the extrapolated boundary) is used to derive the scattered wave U_{sc}'. To calculate the U_{sc}' in semi-infinite geometry, we use $\mathbf{r}_{sph+} = (r_{0+},\theta_{0+},\phi_{0+})$ and $\mathbf{r}_{sph-} = (r_{0-},\theta_{0-},\phi_{0-})$ to represent the centers of the sphere and the image sphere, respectively. The vectors $\mathbf{r}_+' = \mathbf{r} - \mathbf{r}_{sph+} = (r_+',\theta_+',\phi_+')$ and $\mathbf{r}_-' = \mathbf{r} - \mathbf{r}_{sph-} = (r_-',\theta_-',\phi_-')$ are therefore pointing to the detector position $\mathbf{r} = (r,\theta,\phi)$ from the sphere and the

image sphere, respectively. The semi-infinite solution of U_{sc}' can be approximated as

$$\begin{aligned} U_{sc}'(\mathbf{r},\omega) = &\sum_{l,m} \{A_{l,m}^{+}[j_l(k^{out}r_+') \\ &+ jn_l(k^{out}r_+')]Y_{l,m}(\theta_+',\phi_+')\} \\ &- \sum_{l,m} \{A_{l,m}^{-}[j_l(k^{out}r_+') \\ &+ jn_l(k^{out}r_+')]Y_{l,m}(\theta_+',\phi_+')\} \\ &+ \sum_{l,m} \{A_{l,m}^{+}[j_l(k^{out}r_-') \\ &+ jn_l(k^{out}r_-')]Y_{l,m}(\theta_-', \phi_-')\} \\ &- \sum_{l,m} \{A_{l,m}^{-}[j_l(k^{out}r_-') \\ &+ jn_l(k^{out}r_-')]Y_{l,m}(\theta_-',\phi_-')\}, \end{aligned} \tag{3}$$

where

$$A_{l,m}^{+} = -(jvSK^{out}/D^{out})h_l^{(1)}(k^{out}r_s^{+})Y_{l,m}^{*}(\theta_s^{+},\phi_s^{+}) \times \left[\frac{D^{out}xj_l(y)j_l'(x) - D^{in}yj_l'(y)j_l(x)}{D^{out}xh_l^{(1)'}(x)j_l(y) - D^{in}yh_l^{(1)}(x)j_l'(y)}\right], \tag{4}$$

$$A_{l,m}^{-} = -(jvSk^{out}/D^{out})h_l^{(1)}(k^{out}r_s^{-})Y_{l,m}^{*}(\theta_s^{-},\phi_s^{-}) \times \frac{D^{out}xj_l(y)j_l'(x) - D^{in}yj_l'(y)j_l(x)}{D^{out}xh_l^{(1)'}(x)j_l(y) - D^{in}yh_l^{(1)}(x)j_l'(y)}. \tag{5}$$

$\mathbf{r}_s^{+} = (r_s^{+},\theta_s^{+},\phi_s^{+})$ and $\mathbf{r}_s^{-} = (r_s^{-},\theta_s^{-},\phi_s^{-})$ are the positions of the source and the image source, respectively.

The incident photon density wave at the detector position $\mathbf{r}$ has the following form[3]:

$$U_{inc}(\mathbf{r},\omega) = \frac{S}{4\pi D^{out}}\left[\frac{\exp(jk^{out}|\mathbf{r}-\mathbf{r}_s^{+}|)}{|\mathbf{r}-\mathbf{r}_s^{+}|} - \frac{\exp(jk^{out}|\mathbf{r}-\mathbf{r}_s^{-}|)}{|\mathbf{r}-\mathbf{r}_s^{-}|}\right]. \tag{6}$$

The total photon density at detector $\mathbf{r}$ is a superposition of its incident (homogeneous) and scattered (heterogeneous) waves:

$$U(\mathbf{r},\omega) = U_{inc}(\mathbf{r},\omega) + U_{sc}'(\mathbf{r},\omega). \tag{7}$$

B. Born Approximation for Reconstruction

The Born approximation was used to relate $U_{sc}'(\mathbf{r},\omega)$ measured at the probe surface to absorption variations in each volume element within the sample. In the Born approximation, the scattered wave that originated from a source at $\mathbf{r}_s$ and measured at detector $\mathbf{r}_d$ can be related to the medium heterogeneity $\Delta\mu_a(\mathbf{r}_v)$ by

$$U_{sc}'(\mathbf{r}_d,\mathbf{r}_s,\omega) = \int G(\mathbf{r}_v,\mathbf{r}_d,\omega)U_{inc}(\mathbf{r}_v,\mathbf{r}_s,\omega) \times [v\Delta\mu_a(\mathbf{r}_v)/\bar{D}]dr_v^{3}, \tag{8}$$

where $G(\mathbf{r}_v,\mathbf{r}_d,\omega)$ is the Green function and $\Delta\mu_a(\mathbf{r}_v) = \mu_a(\mathbf{r}_v) - \bar{\mu}_a$ is the medium absorption variation.[11] $\bar{\mu}_a$ is the average value of the medium absorption coefficient. By breaking the medium into discrete voxels, we obtain the following linear equations:

$$U_{sc}'(\mathbf{r}_{di},\mathbf{r}_{si},\omega) = \sum_{j}^{N} G(\mathbf{r}_{vj},\mathbf{r}_{di},\omega)U_{inc}(\mathbf{r}_{vj},\mathbf{r}_{si},\omega) \times [v\Delta\mu_a(\mathbf{r}_{vj})/\bar{D}]\Delta r_v^{3}. \tag{9}$$

When $W_{ij} = G(\mathbf{r}_{vj},\mathbf{r}_{di},\omega)U_{inc}(\mathbf{r}_{vj},\mathbf{r}_{si},\omega)v\Delta r_v^{3}/\bar{D}$, we obtain the matrix equation of Eq. (9):

$$[W]_{MXN}\{\Delta\mu_a\}_{NX1} = [U_{sd}]_{MX1}. \tag{10}$$

The realistic constrains on $\Delta\mu_a$ are $(-\alpha \times$ background $\mu_a) = < \Delta\mu_a < 1$, where $0 < \alpha < 1$.

The above constrains ensure that the reconstructed absorption coefficient $\hat{\mu}_a$ = background $\mu_a + \Delta\mu_a$ is positive and not unrealistically higher than unity. With M measurements obtained from all possible source–detector pairs in the planar array, we can solve N unknowns of $\Delta\mu_a$ by inverting the matrix Eq. (10). In general, the perturbation in Eq. (10) is underdetermined ($M < N$) and ill-posed.

When the target depth is available from ultrasound, we can set $\Delta\mu_a$ of a nontarget depth equal to zero. This implies that all the measured perturbations were originated from the particular depth that contained the target. Because the number of unknowns was reduced significantly, the reconstruction converged fast.

C. Total Least-Squares Solution

To solve the unknown optical properties of Eq. (10), several iterative algorithms have been used in the literature including the regularized least-squares method[10] and the TLS method.[20,21] The TLS performs better than the regularized least-squares method when the measurement data are subject to noise and the linear operator W contains errors. The operator errors can result from both the approximations used to derive the linear model and the numerical errors in the computation of the operator. We found that the TLS method provides more accurate reconstructed optical properties than the regularized least-squares method, so we adapted the TLS method to solve the inverse problems. It has been shown by Golub[22] that the TLS minimization is equivalent to the following minimization problem:

$$\min \frac{\|U_{sd} - WX\|^2}{\|X\|^2 + 1}, \tag{11}$$

where X represents unknown optical properties. The conjugate gradient technique was employed to iteratively solve Eq. (11).

3. Methods

A. Probe Design and Imaging Geometry

There are two basic requirements to guide the design of the NIR probe. First, all source–detector separa-

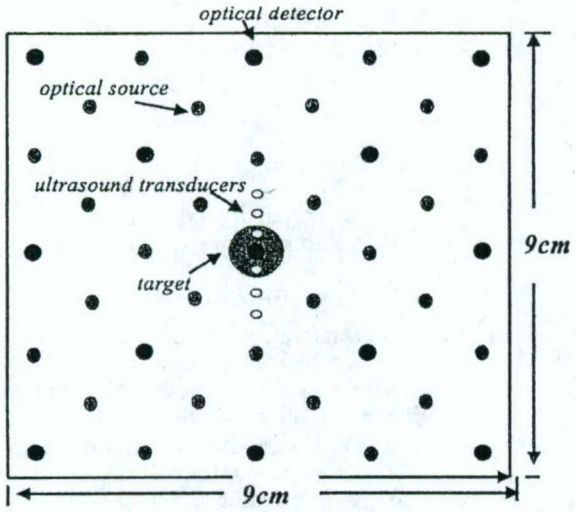

Fig. 2. Configuration of a dense array with 28 optical sources and 13 detectors as well as six ultrasound transducers. Large black circles are optical detectors, gray circles are optical sources, and small white circles are ultrasound transducers. A 1-cm-diameter spherical target was located at various depths in simulations and experiments.

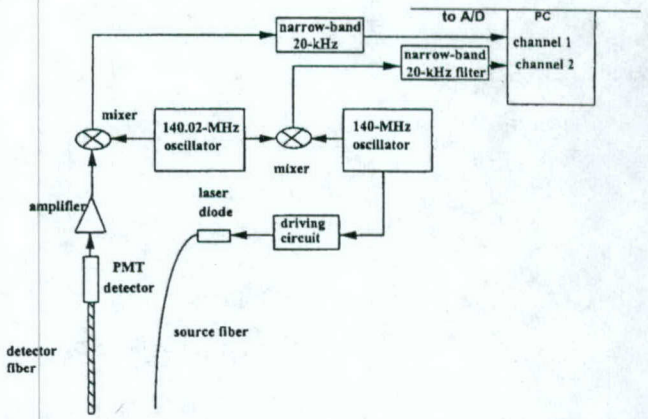

Fig. 3. Schematic of a single-channel optical data-acquisition system. A 140.02-MHz oscillator is used to drive the laser diode (780 nm) that delivers the light to the medium through the fiber. The detected signals are amplified and mixed with signals from a 140-MHz oscillator. The heterodyned 20-kHz signals are amplified, filtered, and digitized. The signals from two oscillators are also directly mixed to provide reference signals. The amplitude and phase of the waveform received through the medium are calculated from signals measured through the medium and the reference. PMT, photomultiplier tube.

tions have to be as large as 1 cm so that diffusion theory is a valid approximation for image reconstruction. Second, because the depth of a photon path is measured approximately one third to one half the source–detector separation, the distribution of source-detector distances should be from approximately 1 to 10 cm to effectively probe the depth from approximately 0.5 to 4 cm. On the basis of these requirements, we deployed a total of 28 sources and 13 detectors over a probe area of 9 cm × 9 cm (see Fig. 2). The minimum source–detector separation in the configuration is 1.4 cm and the maximum is 10.0 cm. We call this array a filled or dense array (a term adapted from ultrasound array design). The 9 cm × 9 cm × 4 cm imaging volume was discretized into voxels of size 0.5 cm × 0.5 cm × 1 cm; therefore a total of four layers in depth was obtained. The target was a 1-cm-diameter sphere located at different locations. Because one of the objectives of this study was to evaluate the target depth distribution, the centers of the four layers in depth were adapted to the target depth. For example, if the target depth was $z = 3$ cm, the centers of the four layers were chosen as 1, 2, 3, and 4 cm, respectively.

The ultrasound transducers shown in Fig. 2 were deployed simultaneously on the same probe. The diameter of each ultrasound transducer is 1.5 mm and the spacing between the transducers is 4 mm, except the two located closer to the optical detector in the middle. The spacing between these two transducers is 8 mm. Because this study requires accurate target location as a reference to compare with the reconstructed absorption image location, six transducers are used to guide the spatial positioning of a target. The target is centered when the two middle ultrasound transducers receive the strongest signals. The target depth is determined from returned pulse-echo signals. In this study we do not intend to provide ultrasound images of the target with such a sparse ultrasound array, but we demonstrate the feasibility of using *a priori* depth information to improve optical reconstruction.

In regard to the image voxel size, there is a tradeoff between the accurate estimation of the weight matrix W and the voxel size. Because W_{ij} is a discrete approximation of the integral

$$\int_{v} G(\mathbf{r}_v,\mathbf{r}_d,\omega)U_{inc}(\mathbf{r}_v,\mathbf{r}_s,\omega)(\nu/\bar{D})d\mathbf{r}_v^3,$$

it is more accurate when the voxel size is smaller. However, the total number of reconstructed unknowns will increase dramatically with the decreasing voxel size. Because the rank of the matrix W is less than or equal to the total number of measurements [Eq. (10)], a further decrease in voxel size will not add more independent information to the weight matrix. We found that a 0.5 cm × 0.5 cm × 1 cm voxel size is a good compromise. Therefore we used this voxel size in image reconstructions reported in this paper.

B. Experimental System

We constructed a NIR frequency-domain system, and the block diagram of the system is shown in Fig. 3. On the source side, a 140.000-MHz sine-wave oscillator was used to modulate the output of a 780-nm diode laser that was housed in an optical coupler (OZ Optics Inc.). The output of the diode was coupled to the turbid medium through a single 200-μm multimode

optic fiber. On the reception side, an optical fiber of 3 mm in diameter was used to couple the detected light to a photomultiplier tube detector. The output of the photomultiplier tube was amplified and then mixed with a local oscillator at a frequency of 140.020 MHz. The heterodyned signal at 20 kHz after the mixer was further amplified and filtered by a band-pass filter. The outputs of two oscillators (140.000- and 140.020-MHz signals) were directly mixed to produce 20-kHz reference signals. Both signals were sampled simultaneously by a dual-channel 1.25-MHz analog-to-digital converter (A/D) board. The Hilbert transform was performed on both sampled and reference waveforms. The amplitude of the Hilbert transform of the sampled waveform corresponds to the measured amplitude, and the phase difference between the phases of the Hilbert transforms of the sampled and reference waveforms corresponds to the measured phase.

A black probe with holes shown in Fig. 2 was used to emulate the semi-infinite boundary condition. Two 3-D positioners were moved independently to position the source and detector fibers at the desired spatial locations within the 9 cm × 9 cm area.

A challenge in the reflection NIR probe design is to preserve a huge dynamic range in received signals. For example, the amplitude at a 1-cm source–detector separation measured from 0.6% Intralipid in reflection mode is approximately 84 dB larger than that at a 9-cm separation. So the signals can be saturated when they are measured from closer source–detector pairs, but they may be too low at more distant source-detector pairs. The problem can be overcome by means of controlling the light illumination. At least two illumination conditions need to be used: a low source level for closer source–detector pairs and a high level for distance source–detector pairs. In our system, a 30-dB attenuator connected to the 140-MHz oscillator was switched on and off to provide two different source levels and thus to preserve the dynamic range. Figure 4(a) shows a plot of the measured log $[\rho^2 U_{sd}(\rho)]$ versus the source–detector separation ρ, and Fig. 4(b) shows the plot of the measured phase versus the source–detector separation. The Intralipid concentration was 0.6%, which corresponded to $\mu_s' = 6\ \text{cm}^{-1}$. Theoretically both log $[\rho^2 U_{sd}(\rho)]$ and phase are linearly related to the source–detector separation because of the semi-infinite boundary condition used,[3] and experimental measurements shown in Fig. 4 validate that they are linearly related to the source–detector separation.

The ultrasound system consists of six transducers (see Fig. 5), a pulser (Panametrics Inc.), an A/D converter, and a multiplexer. The pulser provided a high-voltage pulse of 6-MHz central frequency to drive each selected transducer. The returned signals were received by the same transducer, amplified by the receiving circuit inside the pulser, and sampled by the A/D converter with a 100-MHz sampling frequency.

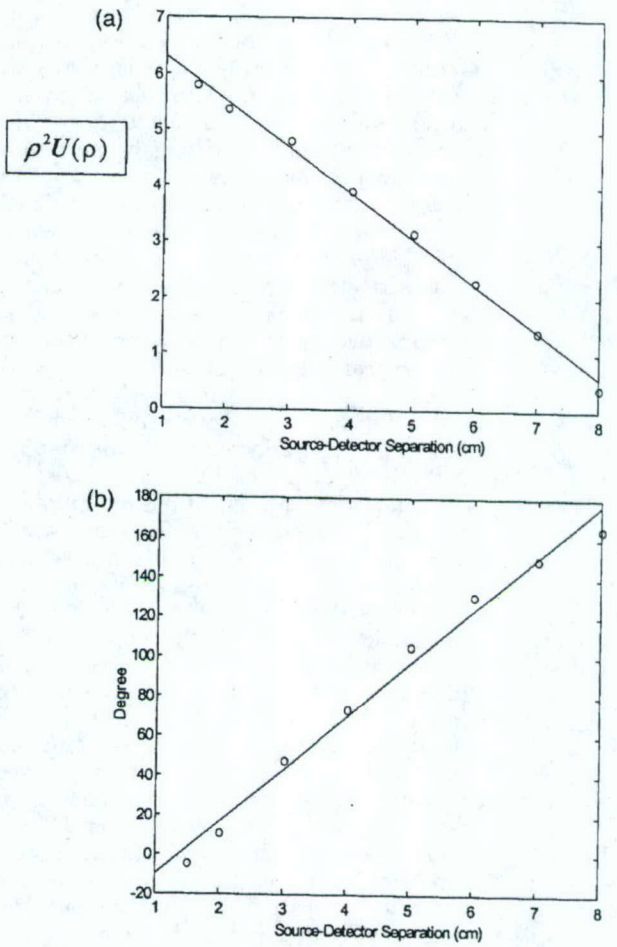

Fig. 4. Calibration curves. (a) log $[\rho^2 U(\rho)]$ versus source-detector separation. (b) Phase versus source–detector separation.

C. Computation Procedures

1. *Computation Procedures of Experimental Data*

To study the relationship between the total number of source–detector pairs and distributions of reconstructed optical absorption coefficients, we started from the dense array with a total of 28 sources and 13 detectors (see Fig. 2) and gradually reduced this number to generate sparse arrays with 24 × 13 (24 sources and 13 detectors), 20 × 13, 28 × 9, 24 × 9, 16 × 13, 20 × 9, 12 × 13, 16 × 9, 28 × 5, 24 × 5, 12 × 9, 20 × 5, 16 × 5, and 12 × 5 source–detector pairs, respectively. Each sparse array was a subset of the

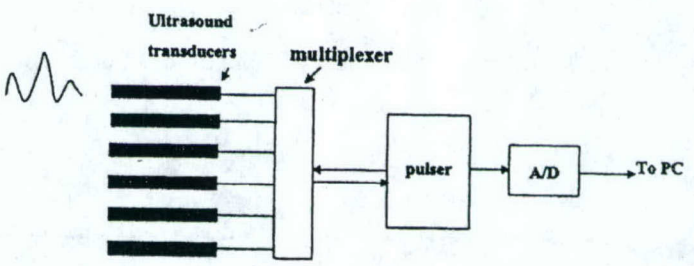

Fig. 5. Ultrasound data-acquisition system. The pulser is used to generate high-voltage pulses that are used to excite the selected ultrasound transducer. The returned signals are received by the selected transducer and are sampled by the A/D converter.

dense array, and its probe area was the same as the dense array. For each sparse array configuration, we compared the reconstructed optical imaging parameters measured from the dense array with those from the sparse arrays. The parameters include the maximum values of reconstructed $\hat{\mu}_a$ at different layers and their spatial locations, spatial resolution and artifact level of the $\hat{\mu}_a$ image, and target depth distribution. Targets of different absorption contrasts were located at different positions inside the Intralipid. For each target case, one set of measurements with the dense array was obtained, and subsets of the measurements were used as sparse array measurements. In all experiments, the background Intralipid concentration was approximately 0.6%, and μ_s' was experimentally determined from curve fitting results. Currently, we did not reconstruct target μ_s', and we used the common μ_s' for both the background and the target.

The total number of iterations or stopping criterion was difficult to determine for experimental data. Ideally, the iteration should stop when the object function [see Eq. (11)] or the error performance surface reaches the noise floor. However, the system noise, particularly coherent noise, was difficult to estimate. In general, we found that the reconstructed values were closer to true values when the object function reached approximately 5–15% of the initial value (total energy in the measurements). However, this criterion was applicable only to reconstructions with total source–detector pairs closer to the dense array case. Therefore we used this criterion for the dense array reconstruction and used the same iteration number obtained from the dense array for the sparse arrays. Thus the iteration number is normalized to the dense array case.

2. *Computation Procedures of Simulation*

Simulations were performed to assist the understanding of the random noise on the reconstructed absorption coefficient. In simulations, Gaussian noise with different standard deviations proportional to the average value of each forward data set was added to the forward measurements. Typically, 0.5%, 1.5%, and 2.0% of the average value of each forward data set were used as standard deviations to generate noise. In simulations, the target μ_a was changed to different contrast values, and target μ_s' was kept the same as the background. The background μ_a and μ_s' were 0.02 and 6 cm^{-1}, respectively.

The stopping criterion used in the simulations was based on the noise level of the object function. Considering that the object function fluctuates within one standard deviation σ around the mean E when the iteration number is large, we can use $E + \sigma$ as a stopping criterion, i.e., the iteration will stop if the object function is less than $E + \sigma$. When the linear perturbation is assumed, E can be approximated as $\Sigma_j^N n(j)^2$ and σ as $\Sigma_j^N[2n(j)^4]^{1/2}$, where N is the total number of source–detector pairs and $n(j)$ is the generated random noise with a standard deviation proportional to the specified percentage of the mean of the forward data set.

D. Testing Targets

Spherical testing targets of ~1 cm in diameter were made of acrylamide gel.[16] The acrylamide powder was dissolved in distilled water, and 20% concentration of Intralipid was added to the acrylamide solution to dilute the solution to a 0.6% Intralipid concentration ($\mu_s' = 6$ cm^{-1}). India ink was added to the solution to produce target μ_a of different values. Acoustic scattering particles of 200 μm in diameter were added to the solution before polymerization. Components of ammonium persulfate and tetramethylethylenediamine (known as TEMED) were added to the solution to produce polymerization.

4. Results of a High-Contrast Target Case

A. Experimental Results of a Dense Array

Figure 6(a) is an experimental image of a high-contrast target ($\mu_a = 0.25$ cm^{-1}) located in the Intralipid background ($\mu_s' = 6$ cm^{-1}). The target was a 1-cm-diameter sphere and its center was located at ($x = 0$, $y = 0$, $z = 3.0$ cm), where x and y were the spatial coordinates and z was the propagation depth. The target depth was well controlled by use of ultrasound pulse-echo signals, and the error was less than 1 mm. The 3-D images were reconstructed from the measurements made with the dense array, and the image shown was obtained at target layer 3. The centers of the imaging voxels in z are 1, 2, 3, and 4 cm for layers 1, 2, 3, and 4, respectively. The measured maximum value of the image lobe [$\hat{\mu}_{a(\max)}$] was 0.233 cm^{-1}, which was a close estimate of the target μ_a. The measured spatial location of $\hat{\mu}_{a(\max)}$ was ($x = 0.5$ cm, $y = 0.0$ cm), which agreed reasonably well with the true target location. The spatial resolution can be estimated from the −6-dB contour plot of Fig. 6(a), which is shown in Fig. 6(b). The outer contour is −6 dB from the $\hat{\mu}_{a(\max)}$, and the contour spacing is 1 dB. The width of the image lobe measured at the −6 dB-level corresponds to a full width at half-maximum (FWHM), which is commonly used to estimate resolution. The measured widths of longer and shorter axes were 1.01 and 1.60 cm, respectively, and the geometric mean was 1.27 cm, which was used to represent the −6-dB beam width. The contrast resolution can be estimated from the peak artifact level, and no artifact was observed in the image. The target depth can be assessed from the images obtained from other nontarget layers. Figure 6(c) is the image obtained at nontarget layer 4, and an image lobe of $\hat{\mu}_{a(\max)} = 0.138$ cm^{-1} was observed. The spatial location of $\hat{\mu}_{a(\max)}$ was ($x = 0.0$, $y = 0.0$), which agreed well with the true target location. No distinct lobes were observed at nontarget layers 1 and 2, which indicates that the error in the target depth estimated from 3-D images was approximately 1 cm. Because the error in the true target depth was less

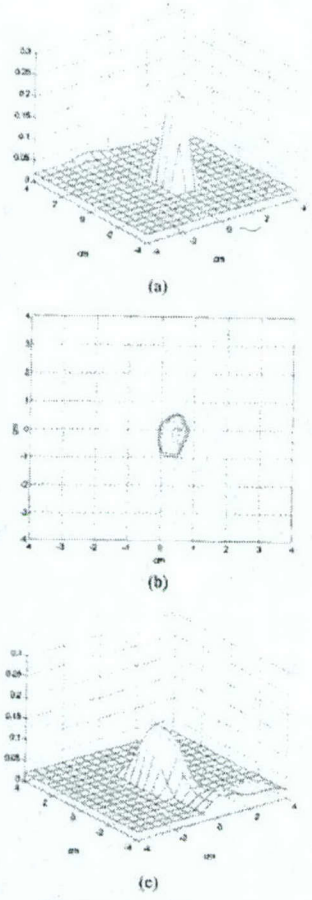

Fig. 6. Experimental 3-D images of $\hat{\mu}_a$ reconstructed with a total of $28 \times 13 = 364$ source–detector pairs at 2437 iterations. The target ($\mu_a = 0.25\ \mathrm{cm}^{-1}$) was located at ($x = 0, y = 0, z = 3.0$ cm) inside the Intralipid background. (a) Reconstructed $\hat{\mu}_a$ at target layer 3. The horizontal axes represent spatial x and y coordinates in centimeters, and the vertical axis is the $\hat{\mu}_a$. The measured maximum value of the image lobe [$\hat{\mu}_{a(\max)}$] was $0.233\ \mathrm{cm}^{-1}$, and its location was ($x = 0.5, y = 0.0$). No image artifacts were observed. (b) −6-dB contour plot of (a). The outer contour is −6 dB from the $\hat{\mu}_{a(\max)}$, and the contour spacing is 1 dB. The measured −6-dB beam width was 1.27 cm. (c) Reconstructed $\hat{\mu}_a$ at nontarget layer 4. An image lobe of strength $0.138\ \mathrm{cm}^{-1}$ and spatial location of ($x = 0.0, y = 0.0$) was observed.

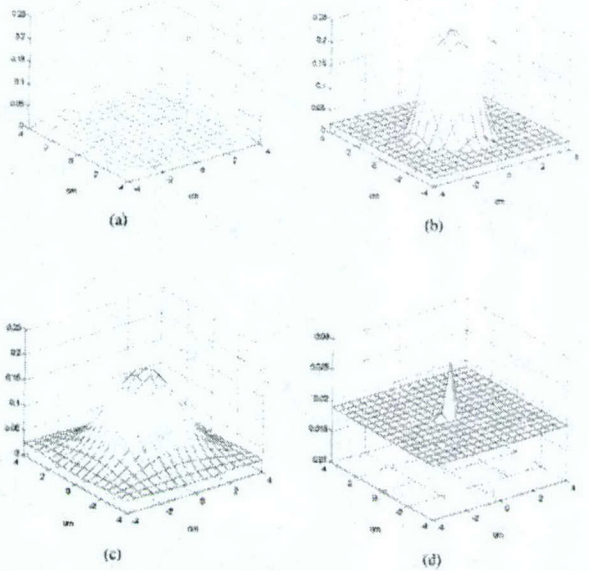

Fig. 7. Simulated 3-D images of $\hat{\mu}_a$ reconstructed with a total of $28 \times 13 = 364$ source–detector pairs. The target ($\mu_a = 0.25\ \mathrm{cm}^{-1}$) was located at ($x = 0, y = 0, z = 3.0$ cm) inside the Intralipid background. (a) Reconstructed $\hat{\mu}_a$ at nontarget layer 2 (simulation, 0.5% noise). No image lobe was observed. (b) Reconstructed $\hat{\mu}_a$ at target layer 3 (simulation, 0.5% noise). The target of strength $\hat{\mu}_{a(\max)} = 0.248\ \mathrm{cm}^{-1}$ and the spatial location (0.0, 0.0) was observed. (c) Reconstructed $\hat{\mu}_a$ at nontarget layer 4 (simulation, 0.5% noise). The target of strength $0.190\ \mathrm{cm}^{-1}$ and location ($x = 0.0, y = 0.0$) was observed. (d). Reconstructed $\hat{\mu}_a$ at nontarget layer 2 with 1.0% noise. The target of $0.028\ \mathrm{cm}^{-1}$ was observed. Note that the scale of (d) is different from (a)–(c).

than 1 mm, this 1-cm error was due largely to the depth uncertainty of diffusive waves.

B. Simulation Results of a Dense Array

Our simulations support the experimental results. Figure 7 shows simulation results obtained with the dense array. A simulated 1-cm-diameter absorber ($\mu_a = 0.25\ \mathrm{cm}^{-1}$) was located at ($x = 0, y = 0, z = 3$ cm) inside a homogeneous scattering background ($\mu_s' = 6\ \mathrm{cm}^{-1}$). We added 0.5% Gaussian noise to the forward data generated from the analytic solution. Images obtained at nontarget layer 2, target layer 3, and nontarget layer 4 are shown in Fig. 7(a), Fig. (b), and 7(c), respectively. No target was found at layer 2, and the target of strengths 0.248 and $0.190\ \mathrm{cm}^{-1}$ appeared at layers 3 and 4, respectively. However, when the noise level in the forward data was increased to 1.0%, the target of strength $\hat{\mu}_{a(\max)} = 0.028\ \mathrm{cm}^{-1}$ appeared at nontarget layer 2 [Fig. 7(d)] as well as target layer 3 [$\hat{\mu}_{a(\max)} = 0.163\ \mathrm{cm}^{-1}$] and nontarget layer 4 [$\hat{\mu}_{a(\max)} = 0.111\ \mathrm{cm}^{-1}$]. This suggests that measurement noise is an important parameter to affect the target depth estimate.

C. Experimental Results of a Dense Array with Ultrasound Assistance

From ultrasound we obtained the target depth as well as the target boundary information. Figure 8(a) shows the received pulse-echo signals (from a depth of 2.3–3.5 cm) obtained from the six ultrasound transducers (see Fig. 2). The spatial dimension covered by the six transducers is 2.4 cm. The front surface of the target was indicated clearly by the returned pulses shown by two arrows, and the back surface was seen through the reflection of a soft plastic plate. The reflected signals of the back surface are also shown by arrows. The plate was used to hold the target and was transparent to light. The measured depth of the target front surface was 2.44 cm and the back surface was 3.43 cm. The distance

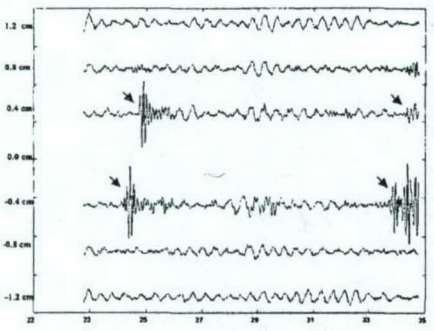

(a)

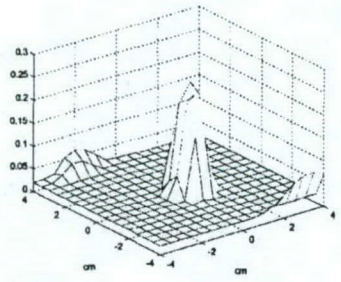

(b)

Fig. 8. (a) Ultrasound pulse-echo signals or *A*-scan lines obtained from six transducers. The abscissa is the propagation depth in millimeters. From reflected signals, the measured depth of the target front surface is 2.44 cm, and the back surface is 3.43 cm. The center of the target is ~3 cm. The total length of the signal corresponds to 1.2 cm in depth, and the measured distance between the front and the back surfaces is 0.993 cm. The spatial dimension covered by the transducers is 2.4 cm. (b) An image of the high-contrast target reconstructed at a target layer when we used only *a priori* target depth information provided by ultrasound. The reconstructed $\hat{\mu}_{a(\max)}$ reached 0.245 cm^{-1} at 216 iterations.

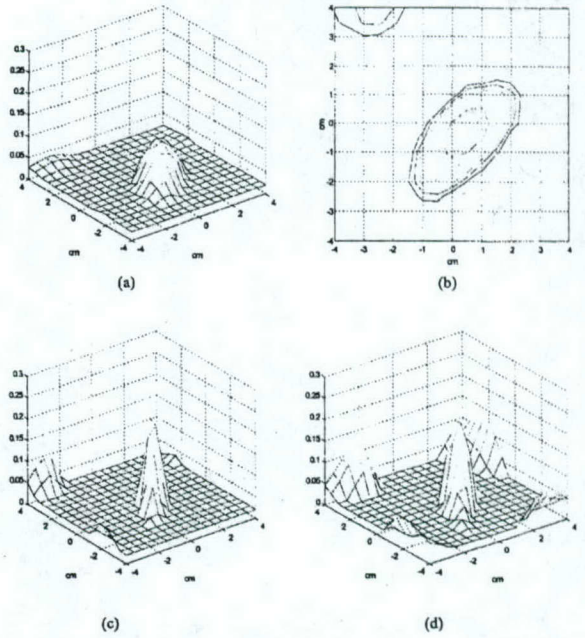

(a) (b) (c) (d)

Fig. 9. Experimental images at target layer 3 reconstructed with a total of $16 \times 5 = 80$ source–detector pairs. (a) Reconstructed $\hat{\mu}_a$ at target layer 3 with 2478 iterations. The measured $\hat{\mu}_{a(\max)}$ was 0.107 cm^{-1}, which was 43% of the true value, and the spatial location of $\hat{\mu}_{a(\max)}$ was $(x = 0.5, y = -0.5)$. The measured peak image artifact level was −10 dB below the peak of the main image lobe. (b) −12-dB contour plot of (a). The outer contour is −12 dB, and the contour spacing is 2 dB. The measured −6-dB beam width was 2.55 cm, which was 200% broader than that of the dense array. (c) Reconstructed $\hat{\mu}_a$ at target layer 3 with 10,000 iterations. The measured $\hat{\mu}_{a(\max)}$ reached 0.264 cm^{-1}, and the peak artifact level was increased by 2 dB as well. (d) Reconstructed $\hat{\mu}_a$ at the target layer with only *a priori* target depth information provided by ultrasound. $\hat{\mu}_{a(\max)} = 0.173$ cm^{-1} at 216 iterations.

between the peaks of front reflection and backreflection was 0.993 cm, which corresponded to the target size. With the assistance of target depth, we reconstructed the absorption image at the target layer only. Figure 8(b) is the reconstructed $\hat{\mu}_a$ obtained from the dense array measurements. A total of 216 iterations were used to obtain $\hat{\mu}_{a(\max)} = 0.245$ cm^{-1}, and the reconstruction was approximately ten times faster than that without the depth information. The spatial resolution was approximately the same as Fig. 6(a), and the −6-dB beam width was 1.31 cm. The contrast resolution was 5 dB poorer because the measurement noise was lumped to single-layer reconstruction instead of being distributed to four layers.

D. Experimental Results of a Sparse Array

The imaging quality of sparse arrays decreased. Figure 9(a) is an experimental image at target layer 3 obtained from the 16×5 sparse array. The sparse array measurements used were a subset of the dense array measurements. The measured $\hat{\mu}_{a(\max)}$ was 0.107 cm^{-1}, which was 43% of the true value. The −6-dB beam width was 2.55 cm, which was 200% broader than that of the dense array. Edge artifacts were observed and are best seen from Fig. 9(b), which is the −12-dB contour plot of Fig. 9(a). The outer contour is −12 dB, and the spacing is 2 dB. The peak artifact level is −10 dB from the $\hat{\mu}_{a(\max)}$. The reconstructed $\hat{\mu}_a$ can be increased if the iteration is significantly increased. The iteration number used to obtain Fig. 9(a) was 2478, which was the same as that used to obtain Fig. 6. When the iteration number was increased to 10,000 for the sparse array case, the reconstructed $\hat{\mu}_{a(\max)}$ reached 0.264 cm^{-1}, which was close to the true target μ_a. However, the image artifact level was increased too [see Fig. 9(c)], and the ratio of the peak artifact to $\hat{\mu}_{a(\max)}$ was 2 dB higher than that shown in Fig. 9(a). In addition, the background noise fluctuation of nontarget layers 1 and 2 was increased. The noise fluctuation can be estimated from the standard deviations of reconstructed $\hat{\mu}_a$ at nontar-

get layers 1 and 2. At 2478 iterations, the averages and the standard deviations of $\hat{\mu}_a$ were 0.0233 ($\pm$0.0028) and 0.0202 cm^{-1} ($\pm$0.0022 cm^{-1}) for nontarget layers 1 and 2, respectively, and these values were 0.0244 ($\pm$0.0078) and 0.0208 cm^{-1} ($\pm$0.0073 cm^{-1}) at 10,000 iterations.

The measured maximum values of the image lobes or target strengths at the target layer and nontarget layer 4 continuously grew with each iteration, even though the reconstructed values at the target layer were close to the true value. This problem was mentioned in the literature,[11] but was not explained well. It is largely related to use of nonlinear constrains on $\Delta\mu_a$ in Eq. (10), particularly the choice of α. When α is close to 1, the reconstruction converges fast, and the target strength increases little after a certain number of iterations. When α is close to 0, the reconstruction converges slowly, and the target strength grows continuously. However, when the measurement signal-to-noise ratio (SNR) is not high, for example, in sparse array or low-contrast cases, the choice of $\alpha \approx 1$ can cause unstable reconstruction. In some cases, the reconstructed images can jump from one set of $\hat{\mu}_a$ to another, which causes the object function to increase suddenly and reduce again. This is related to the underdetermined nature of Eq. (10), i.e., the unknowns are far more than the measurements. In some cases the reconstructed images have multiple lobes of similar strengths, which indicate that the reconstruction does not converge at all. In all cases, the image background fluctuations were large compared with the fluctuations when a smaller α was used. We found that α between 0.1 and 0.4 can provide stable reconstruction, and we used $\alpha \approx 0.1$ for all experiments.

Another factor that accounts for the slow increase in the reconstructed value is use of linear perturbation to approximate the measurements that contain all higher-order perturbations. The minimization procedure [Eq. (11)] blindly minimizes the difference between the measurements and their linear approximation $W\Delta\mu_a$ and therefore reconstructs higher and higher $\Delta\mu_a$ if the iteration continues.

The target depth estimate was poorer than that of the dense array because of the lower SNR of the sparse array measurements. Similar to the dense array case, a target of strength $\hat{\mu}_{a(\max)} = 0.072$ cm^{-1} and location ($x = 0.5$, $y = 0.0$) was observed at nontarget layer 4. In addition, a target of strength $\hat{\mu}_{a(\max)} = 0.0348$ cm^{-1} and location ($x = 0.5$, $y = -0.5$) was observed at nontarget layer 2. However, the target mass, which was approximately the volume underneath the image lobe, was much smaller than that obtained at layers 3 and 4, and the target at layer 2 was buried in the background noise.

Figure 9(d) is the reconstructed $\hat{\mu}_a$ at the target layer from only the sparse array measurements. A total of 216 iteration steps were used to obtain $\hat{\mu}_{a(\max)} = 0.173$ cm^{-1}, and the reconstruction was approximately 50 times faster than that without the depth information. The measured -6-dB beam width was 1.49 cm, which was approximately the same as Fig. 9(c) but was improved 42% from Fig. 9(a). The contrast resolution was 2 dB worse for the same reason discussed above.

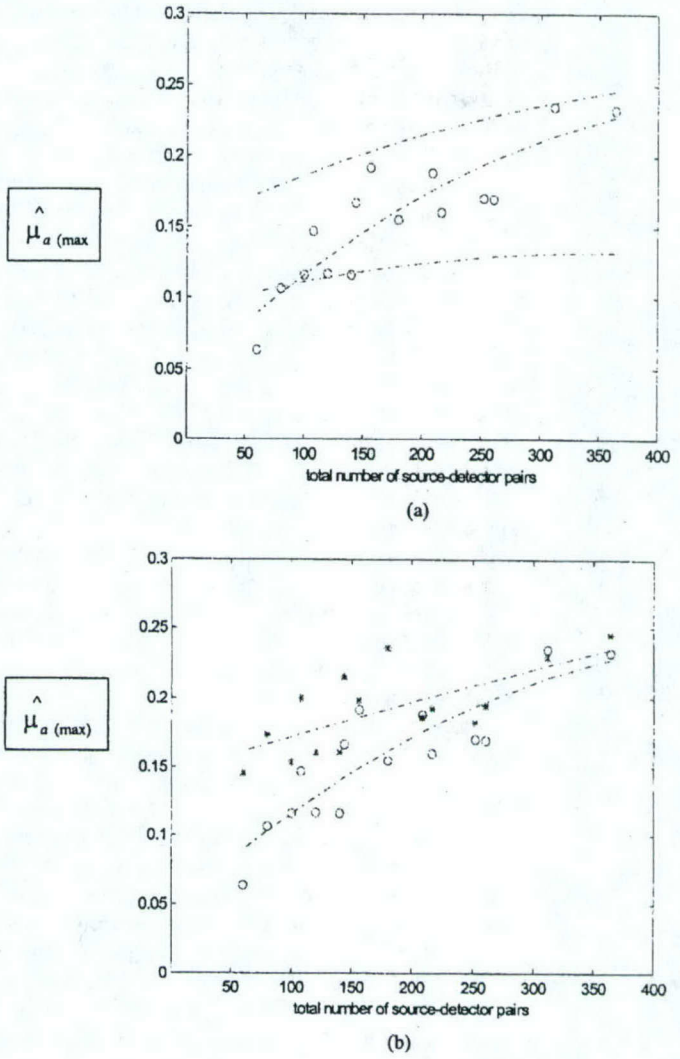

Fig. 10. $\hat{\mu}_{a(\max)}$ versus the total number of source–detector pairs. The center of the target ($\mu_a = 0.25$ cm^{-1}) was located at ($x = 0.0$, $y = 0.0$, $z = 3.0$ cm) in computer simulations and experiments. (a) Curves were obtained at the target layer. Two dashed curves (upper and lower) are the curve-fitting results of simulation data points obtained with 0.5% and 2.0% noise added to the forward data, respectively. The experimental data are plotted with circles, and the dashed curve in the middle is the fitting result of the experimental points. (b) The measured target strength (circles) and the curve-fitting result (lower curve). The measured target strength (stars) was reconstructed at the target layer only by use of *a priori* depth information and the curve fitting result (upper curve).

E. Simulation and Experimental Results of Reconstructed $\hat{\mu}_{a(\max)}$ versus Total Number of Source–Detector Pairs

To understand the effects of random noise on the performance of the reconstruction, we performed simulations for each array configuration. Gaussian noise of 0.5%, 1.0%, 1.5%, and 2.0% were added to each forward data set generated from the analytic solution [see Eq. (3)]. The center of a simulated 1-cm-diameter spherical target ($\mu_a = 0.25$

cm^{-1}) was located at ($x = 0$, $y = 0$, $z = 3.0$ cm). Reconstructed images at different noise levels were obtained for each array configuration, and the peak values of image lobes [$\hat{\mu}_{a(\max)}$] at target layer 3 were measured. Figure 10(a) shows simulation and experimental results of reconstructed $\hat{\mu}_{a(\max)}$ versus the total number of source–detector pairs. Two dashed curves are the fitting results of simulated data points with 0.5% (upper) and 2.0% (lower) noise. The dashed curve in the middle is the fitting result of experimental points plotted with circles. Second-order polynomials were used for all curve fittings. The reduction of the reconstructed $\hat{\mu}_{a(\max)}$ was significant when the noise level went up in the simulated data. Because the SNR of experimental data was decreased when the total number of source–detector pairs was reduced, the data were scattered around the 0.5% noise curve when the total pairs were large and were distributed around the 2.0% noise curve (values were 60% less than that obtained from the dense array) when the total pairs were reduced to less than 140. However, because our experimental system has both coherent and random noise, simulations based on random noise can only qualitatively explain the noise effect on the experimental data.

Figure 10(b) shows the experimental results of reconstructed $\hat{\mu}_{a(\max)}$ versus the total number of source–detector pairs obtained from 3-D imaging (circles) and ultrasound-assisted imaging (stars). The upper curve is the fitting result of the circles, and the lower curve is the result of the stars. In both cases, the reconstructed values were decreased when the total number of pairs was reduced. However, the reconstructed values were more accurate when the target depth information was available, and the improvement on average was 15%. The improvement was more dramatic when the total pairs were less.

For sparse arrays with total source–detector pairs less than 140, the reconstructed $\hat{\mu}_{a(\max)}$ could be increased if the iterations were significantly increased. However, the image artifact level of the target layer and the noise level of the nontarget layers were increased too. With the assistance of simulations, we offer the following explanations to the increased image artifact and noise level problem. In simulations, the iteration was stopped when the TLS error between the measurement and the linear approximation reached the noise floor, which was

$$E + \sigma = \sum_{j}^{N} n(j)^2 + \sum_{j}^{N} [2n(j)^4]^{1/2},$$

where $n(j)$ was the generated random noise with the standard deviation proportional to a certain percent of the mean of the forward data set for each array configuration. When the object function reached the noise floor, the gradient

$$\nabla g = \frac{-2(U_{sd} - W\Delta\mu_a)^T(W)}{\Delta\mu_a{}^T\,\Delta\mu_a + 1} - \frac{-2(U_{sc} - W\Delta\mu_a)^T(U_{sd} - W\Delta\mu_a)(\Delta\mu_a)}{(\Delta\mu_a{}^T\,\Delta\mu_a + 1)^2}$$

can be approximated as

$$\nabla g \approx \frac{-2(N)^T(W)}{\Delta\mu_a{}^T\Delta\mu_a + 1} - \frac{-2(N)^T(N)(\Delta\mu_a)}{(\Delta\mu_a{}^T\Delta\mu_a + 1)^2},$$

where N is the noise vector. Therefore the search procedure of Eq. (11) is more random and noisy. Because $\Delta\mu_{a_{(new)}} = \Delta\mu_{a_{(old)}} + \beta\nabla g$, the $\Delta\mu_a$ updating is more random and noisy. β is proportional to the square of the gradient. Continuous iteration when the object function has reached the noise floor may destroy the convergence of the reconstruction. We found that when the SNR of the data is high, for example, high-contrast cases, continuous iteration in general increases reconstructed μ_a and sidelobes. However, when the SNR of the data is low, for example, low-contrast cases, continuous iteration does not increase the reconstructed μ_a, but destroys the convergence of the reconstruction [see Fig. 12(c) below].

F. Experimental Results of Imaging Parameters Versus Total Number of Source–Detector Pairs

The imaging parameters measured from different array configurations are listed in Table 1. Listed first are the measured parameters at target layer 3. These parameters are a −6-dB beam width of the image lobe, the peak sidelobe level, $\hat{\mu}_{a(\max)}$, and the distance in the x–y plane between the location of $\hat{\mu}_{a(\max)}$ and the true target location. Next are the same parameters measured at nontarget layer 4. The increase in beam width was negligible for the arrays with more than 140 source–detector pairs and was 100% broader for the sparse arrays with total pairs less than this number. The sidelobe level was progressively increased when the total pairs were reduced. At nontarget layer 4, when the total pairs were reduced to less than 140, the measured image lobes were broad and no sidelobes were seen. The agreement between the measured $\hat{\mu}_{a(\max)}$ location and the true target location is good for all the array configurations, which suggests that this parameter is not sensitive to the total number of source–detector pairs in high-contrast cases. Table 1 next lists the strength of the target measured at nontarget layer 2 and its spatial location. Because the SNR of the sparse array measurement was lower, the target appeared at layer 2 when total pairs were less than 180. However, in all cases, the target mass measured at this layer was much smaller than that obtained at the target layer and nontarget layer 4. Finally, Table 1 lists the measured imaging parameters when the target depth was available to optical reconstruction. Compared with parameters obtained from optical im-

Table 1. Imaging Parameters Measured with Different Array Configurations: High-Contrast Target Case ($\mu_a = 0.25\ cm^{-1}$)

Parameter	Total Pairs														
	28 × 13	24 × 13	20 × 13	28 × 9	24 × 9	16 × 13	20 × 9	12 × 13	16 × 9	28 × 5	24 × 5	12 × 9	20 × 5	16 × 5	12 × 5
Target layer 3 (2437 iterations)															
−6-dB beam width (cm)	1.27	1.42	1.65	1.67	1.70	1.44	1.78	1.39	1.55	*2.45*	*2.34*	*1.69*	*2.50*	*2.55*	*3.09*
Peak sidelobe (dB)	−18	−13	−12	−14	−13	−16	−12	−13	−11	−12	−11	−10	−11	−10	−8
$\hat{\mu}_{a(max)}$ (cm^{-1})	0.23	0.23	0.17	0.17	0.16	0.18	0.16	0.19	0.17	0.12	0.12	0.15	0.12	0.11	0.06
$\lvert\hat{\mu}_{a(max)} - (0,0)\rvert$ (cm)	0.5	0.7	0.7	0.5	0.5	0.7	0.5	0.7	0.7	0.5	0.5	0.7	0.5	0.7	0.7
Nontarget layer 4 (2437 iterations)															
−6-dB beam width (cm)	2.10	2.11	2.48	2.40	2.52	2.26	2.59	2.40	2.54	4.35	4.10	2.63	3.93	4.51	5.36
Peak sidelobe (dB)	−8	−9	−17	−14	−13	−19	−12	−13	−12						
$\hat{\mu}_{a(max)}$ (cm^{-1})	0.14	0.14	0.12	0.11	0.11	0.14	0.11	0.14	0.13	0.06	0.07	0.12	0.06	0.07	0.07
$\lvert\hat{\mu}_{a(max)} - (0,0)\rvert$ (cm)	0.0	0.5	0.0	0.7	0.7	0.5	0.7	0.0	0.7	0.5	0.5	0.7	0.5	0.5	0.5
Nontarget layer 2 (2437 iterations)															
$\hat{\mu}_{a(max)}$ (cm^{-1})	0.00	0.00	0.00	0.00	0.00	0.00	0.043	0.024	0.047	0.026	0.043	0.048	0.032	0.035	0.038
$\lvert\hat{\mu}_{a(max)} - (0,0)\rvert$ (cm)							1.12	0.70	1.12	0.70	1.00	1.12	0.70	0.70	0.5
Target layer only (216 iterations)															
−6-dB beam width (cm)	1.31	1.40	1.68	1.61	1.55	1.57	1.50	1.41	1.20	1.71	1.48	1.45	1.77	1.49	1.75
Peak sidelobe (dB)	−12	−12	−12	−9	−8	−12	−7	−9	−7	−8	−8	−6	−8	−8	−8
$\hat{\mu}_{a(max)}$ (cm^{-1})	0.25	0.23	0.19	0.18	0.19	0.19	0.24	0.20	0.22	0.16	0.16	0.20	0.15	0.17	0.15
$\lvert\hat{\mu}_{a(max)} - (0,0)\rvert$ (cm)	0.5	0.5	0.5	0.5	0.5	0.5	0.5	0.5	0.5	0.5	0.5	0.5	0.5	0.5	0.5

Note: Italicized entries are 100% broader than the dense array beam width.

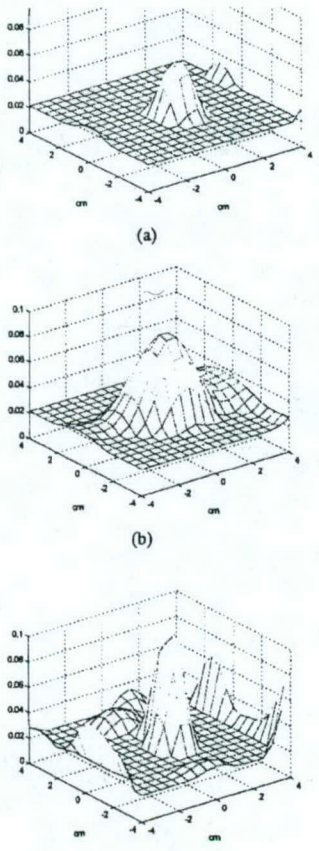

Fig. 11. Experimental images of $\hat{\mu}_a$ reconstructed from a total of $28 \times 13 = 364$ source–detector pairs. The target ($\mu_a = 0.10\ \mathrm{cm}^{-1}$) was located at ($x = 0, y = 0, z = 2.5$ cm) inside the Intralipid background. (a) Reconstructed $\hat{\mu}_a$ at target layer 3. The measured $\hat{\mu}_{a(\max)}$ was $0.063\ \mathrm{cm}^{-1}$ at 510 iterations, and its location was ($x = 0.0, y = -0.5$). Edge artifacts were observed and the peak level was -7 dB from the $\hat{\mu}_{a(\max)}$. (b) Reconstructed $\hat{\mu}_a$ at nontarget layer 4. The measured $\hat{\mu}_{a(\max)}$ was $0.0871\ \mathrm{cm}^{-1}$ at 510 iterations, and its location was ($x = 0, y = 0$). (c) Reconstructed $\hat{\mu}_a$ at the target layer when only the target depth information provided by ultrasound was used. $\hat{\mu}_{a(\max)} = 0.107\ \mathrm{cm}^{-1}$ at 56 iterations.

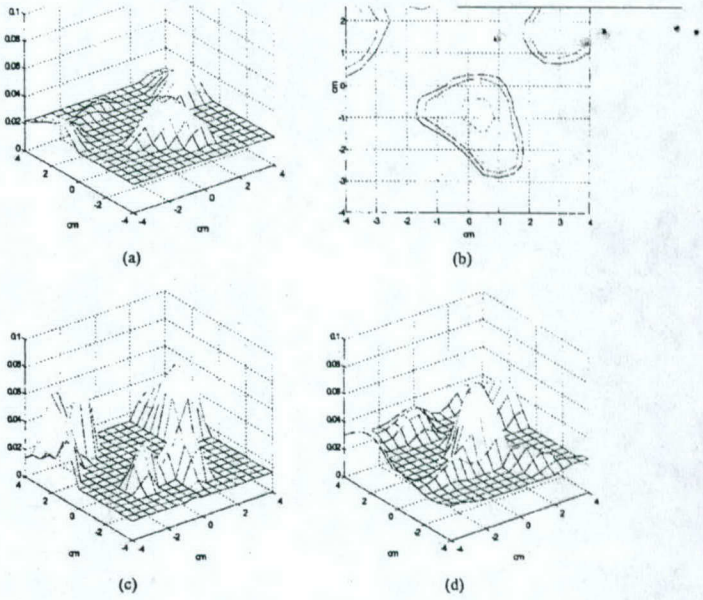

Fig. 12. Experimental images of $\hat{\mu}_a$ at target layer 3 reconstructed from a total of $24 \times 5 = 120$ source–detector pairs. (a) Reconstructed $\hat{\mu}_a$ at target layer 3 with 510 iterations. The measured $\hat{\mu}_{a(\max)}$ was $0.049\ \mathrm{cm}^{-1}$, which was 49% of the true target μ_a, and its location was ($x = 0.5, y = -1.0$), which was displaced from the true target location by 1.11 cm. Image artifacts were observed, and the peak was -3 dB from the $\hat{\mu}_{a(\max)}$. (b) -6-dB contour plot of (a). (c) Reconstructed $\hat{\mu}_a$ at target layer 3 with 1500 iterations. The peak artifact was 5 dB higher than the image lobe. (d) Reconstructed $\hat{\mu}_a$ at target layer 3 (56 iterations) with only *a priori* target depth information provided by ultrasound. The measured $\hat{\mu}_{a(\max)}$ was $0.074\ \mathrm{cm}^{-1}$, and its location was ($x = 0.5, y = -0.5$). Image artifacts were observed, and the peak was -5 dB from the $\hat{\mu}_{a(\max)}$.

aging only, the -6-dB beam width was improved by 24% on average, and the reconstruction speed was approximately 10 times faster; however, the sidelobe was 3 dB worse.

5. Results of a Lower-Contrast Target Case

A. Experimental Results of a Dense Array

To study the effects of target contrast on the quality of the reconstructed image for each array configuration, we conducted a set of experiments with a lower-contrast target ($\mu_a = 0.10\ \mathrm{cm}^{-1}$) embedded in the Intralipid. The center of the target was located at ($x = 0, y = 0, z = 2.5$ cm). The centers of the imaging voxels in z were 0.5, 1.5, 2.5, and 3.5 cm for layers 1, 2, 3, and 4, respectively. Figure 11 shows the images of the lower-contrast target obtained at target layer 3 [Fig. 11(a)] and deeper nontarget layer 4 [Fig. 11(b)]. The images were reconstructed from the measurements made with the dense array. At target layer 3, the measured $\hat{\mu}_{a(\max)}$ was $0.063\ \mathrm{cm}^{-1}$, which was approximately 63% of the target μ_a. The measured spatial location of $\hat{\mu}_{a(\max)}$ was ($x = 0.0, y = -0.5$), which agreed reasonably well with the true target location. The measured -6-dB beam width was 1.83 cm, which was 144% times broader than the beam width of the high-contrast case. Edge artifacts were observed, and the peak level was -7 dB from the $\hat{\mu}_{a(\max)}$. At nontarget layer 4, the measured $\hat{\mu}_{a(\max)}$ was $0.0871\ \mathrm{cm}^{-1}$, which was even higher than that measured at the target layer. Because the SNR of the data was lower than the high-contrast case, the target depth estimate was poorer. A target of $\hat{\mu}_{a(\max)} = 0.0543\ \mathrm{cm}^{-1}$ located at ($x = 0, y = -0.5$) was observed at nontarget layer 2, and its mass was much smaller than that obtained at the target layer and nontarget layer 4.

Figure 11(c) is the reconstructed $\hat{\mu}_a$ at the target

layer from only the dense array measurements. A total of 56 iterations were used to obtain $\hat{\mu}_{a(\max)} = 0.107\ \mathrm{cm}^{-1}$, and the reconstruction was approximately ten times faster than that without the depth information. The spatial resolution was 8% better than that obtained from Fig. 11(a), and the −6-dB beam width was 1.67 cm. The contrast resolution was 2 dB worse.

B. Experimental Results of a Sparse Array

The imaging quality of sparse arrays decreased. Figure 12(a) is an image of the same target ($\mu_a = 0.10\ \mathrm{cm}^{-1}$) reconstructed from measurements made with the 24 × 5 sparse array. The measured $\hat{\mu}_{a(\max)}$ was $0.049\ \mathrm{cm}^{-1}$, which was 49% of the true value. The −6-dB contour plot is shown in Fig. 12(b). The measured spatial location of $\hat{\mu}_{a(\max)}$ was ($x = 0.5$, $y = -1.0$), which was displaced from the true target location by 1.11 cm in radius. The measured −6-dB beam width was 2.98 cm, which was 163% broader than that measured from the dense array. Sidelobes were abundant, and the peak value was −3 dB below the peak of the image lobe. These sidelobes would produce false targets in the image if no *a priori* information about the target locations were given.

In this case, continuous iteration did not increase the target strength but increased the sidelobe strength. Figure 12(a) was obtained at 510 iterations, whereas Fig. 12(c) was obtained at 1500 iterations. After approximately three times more iterations, the peak of the artifact was 5 dB higher than the peak of the image lobe. The target depth estimated from 3-D images was worse at 1500 iterations than that at the 510 iterations. The measured target strengths at nontarget layer 2 were 0.064 and $0.1661\ \mathrm{cm}^{-1}$ at 510 and 1500 iterations, respectively, and the strengths at nontarget layer 4 were 0.0597 and $0.1087\ \mathrm{cm}^{-1}$, respectively. In addition, the background noise fluctuation or standard deviation measured at nontarget layer 1 was increased with the iterations. The mean and the standard deviation at 510 iterations were 0.024 and $0.0041\ \mathrm{cm}^{-1}$, whereas these values at 1500 iterations were 0.0267 and $0.0104\ \mathrm{cm}^{-1}$.

As shown in Fig. 12(d), the reconstructed image improved a lot when the target depth was given. The maximum strength was $0.074\ \mathrm{cm}^{-1}$, and its location was (0.5, −0.5). The −6-dB beam width was 2.63 cm, which was 12% better than that obtained from Fig. 12(a). The sidelobe was −6 dB from the peak, which was improved by 3 dB compared with Fig. 12(a).

C. Experimental Results of Reconstructed $\hat{\mu}_{a(\max)}$ versus Total Number of Source–Detector Pairs

With the iteration number normalized to the dense array case, we measured target strengths at target layer 3 and nontarget layer 4 for all sparse array configurations. Figure 13 shows the experimental data points (circles) of measured $\hat{\mu}_{a(\max)}$ versus the total number of source–detector pairs obtained at target layer 3 [Fig. 13(a)] and nontarget layer 4 [Fig. 13(b)]. The two curves were the fitting results of experimental points when we used second-order polynomials. In both layers, the $\hat{\mu}_{a(\max)}$ values were decreased when the total number of source–detector pairs was reduced. The reconstructed target strengths were reduced to less than 60% when the total pairs were less than 156 and 140 for target layer 3 and nontarget layer 4, respectively. The ultrasound-assisted reconstruction results are shown in Fig. 13(a) (stars), and the average reconstructed $\hat{\mu}_{a(\max)}$ for all array configurations was $0.085\ \mathrm{cm}^{-1}$. Compared with the average of $0.055\ \mathrm{cm}^{-1}$ obtained from optical imaging only at the target layer, a 30% improvement was achieved.

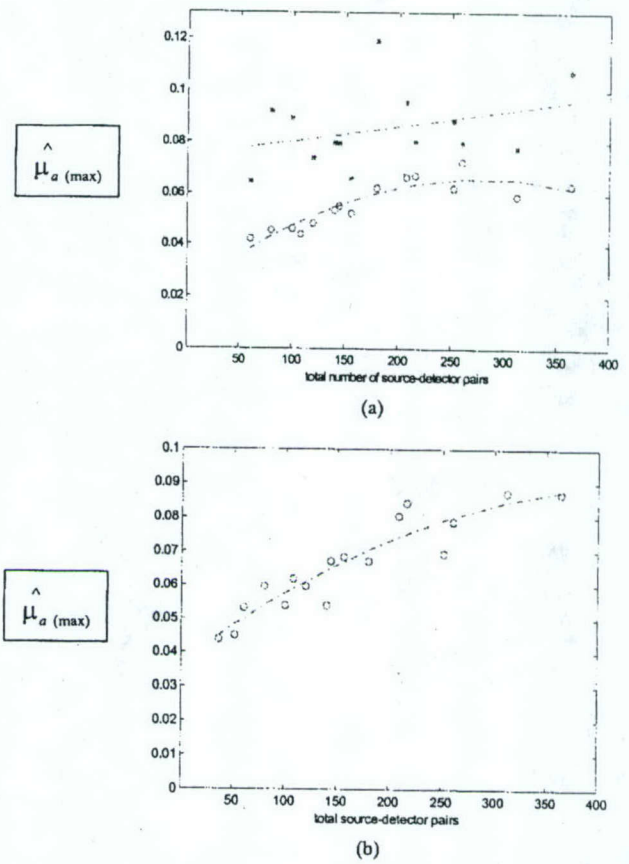

Fig. 13. Low-contrast target case. (a) Reconstructed $\hat{\mu}_{a(\max)}$ versus total source–detector pairs with the target depth available (stars) and the curve-fitting results (upper curve). Reconstructed $\hat{\mu}_{a(\max)}$ versus total source–detector pairs measured at target layer (circles) and the curve-fitting results (lower curve) and (b) at deeper nontarget layer 4.

D. Experimental Results of Imaging Parameters versus Total Number of Source–Detector Pairs

The measured imaging parameters obtained from different array configurations are listed in Table 2. Similar to Table 1, listed are the measured parameters at target layer 3 and nontarget layer 4. The increase in beam width at the target layer was negligible for the arrays with more than 156 source-detector pairs and was more than 50% for the sparse arrays with total pairs less than this number. The sidelobes were progressively worse when the total

Table 2. Imaging Parameters Measured with Different Array Configurations: Lower-Contrast Target Case (μ_a = 0.10 cm^{-1})

Parameter	Total Pairs														
	28 × 13	24 × 13	20 × 13	28 × 9	24 × 9	16 × 13	20 × 9	12 × 13	16 × 9	28 × 5	24 × 5	12 × 9	20 × 5	16 × 5	12 × 5
Target layer 3 (510 iterations)															
−6-dB beam width (cm)	1.83	1.98	2.02	2.24	1.86	2.09	2.42	*2.73*	*3.07*	*3.07*	*2.98*	*4.10*	*3.57*	*4.23*	*3.07*
Peak sidelobe (dB)	−6	−6	−7	−4	−3	−5	−2	−6	−3	−4	−3	−1	−3	−2	−2
$\hat{\mu}_{a(max)}$ (cm^{-1})	0.06	0.06	0.07	0.06	0.07	0.07	0.06	0.05	0.06	0.05	0.05	0.04	0.05	0.05	0.04
$\lvert\hat{\mu}_{a(max)} - (0,0)\rvert$ (cm)	0.5	0.5	0.7	1.0	0.7	0.7	0.7	0.7	0.7	1.11	1.11	1.11	1.0	1.0	1.58
Nontarget layer 4 (510 iterations)															
−6-dB beam width (cm)	3.36	3.42	3.31	4.81	3.08	3.28	4.69	4.20	5.49	5.57	5.15	4.88	6.62	8.49	8.81
Peak sidelobe (dB)	−8	−9	−8	−6	−7	−7	−5								
$\hat{\mu}_{a(max)}$ (cm^{-1})	0.09	0.09	0.08	0.07	0.08	0.08	0.07	0.07	0.07	0.05	0.06	0.06	0.05	0.06	0.05
$\lvert\hat{\mu}_{a(max)} - (0,0)\rvert$ (cm)	0.0	0.0	0.5	0.7	0.5	0.5	0.5	0.5	0.5	0.5	0.5	1.11	0.5	0.5	0.5
Nontarget layer 2 (510 iterations)															
$\hat{\mu}_{a(max)}$ (cm^{-1})	0.062	0.058	0.054	0.048	0.051	0.049	0.047	0.046	0.047	0.054	0.064	0.034	0.060	0.064	0.049
$\lvert\hat{\mu}_{a(max)} - (0,0)\rvert$ (cm)	0.70	0.70	0.70	0.5	0.70	1.12	0.5	1.12	0.0	0.70	0.0	0.50	0.0	0.0	0.70
Target layer only (56 iterations)															
−6-dB beam width (cm)	1.67	2.43	2.35	1.72	2.10	1.93	1.56	3.12	2.37	2.12	2.63	1.12	1.84	1.86	3.30
Peak sidelobe (dB)	−4	−5	−6	−3	−3	−6	−2	−6	−4	−4	−5	+5	−4	−3	−2
$\hat{\mu}_{a(max)}$ (cm^{-1})	0.11	0.08	0.08	0.09	0.08	0.10	0.12	0.07	0.08	0.08	0.07	0.09	0.09	0.06	0.06
$\lvert\hat{\mu}_{a(max)} - (0,0)\rvert$ (cm)	0.7	0.0	0.0	0.5	0.0	0.7	0.0	0.7	0.0	0.7	0.7	1.11	0.7	0.5	0.7

Note: Italicized entries are 50% broader than the dense array beam width.

pairs were reduced. At the target layer, the distance between the $\hat{\mu}_{a(\max)}$ location and the true target location was more than 1 cm for the arrays with total pairs less than 140. Table 2 then lists the measured peak image lobe at nontarget layer 2 and its location. The target appeared at nontarget layer 2 in all array configurations because of the lower SNR of the data. However, the target mass observed at this layer was much smaller than that at layers 3 and 4 in all cases. The last row in Table 2 shows the measured imaging parameters when the target depth was available to optical reconstruction. Compared with parameters obtained from optical imaging only, the −6-dB beam width was improved by 41% on average, and the reconstruction speed was approximately ten times faster; however, the sidelobe was 1 dB worse.

6. Discussion

In addition to the total number of source–detector pairs, the measured imaging parameters are also related to other system parameters, for example, modulation frequency and system noise. The 140-MHz modulation frequency chosen in this study is a typical frequency used by many research groups. Our system noise level, including both coherent and incoherent, is less than 10 mV peak to peak, which is sufficiently low. Therefore the results we obtained are pertinent to 3-D imaging using similar system parameters and reflection geometry.

In this study the target absorption coefficient was reconstructed from measurements. Similar studies can be done for the scattering coefficient as well. To reconstruct the scattering coefficient, we can use the scattering weight matrix derived by O'Leary[11] to relate the medium scattering variations with the measurements. Simultaneous reconstruction of both absorption and scattering coefficients in reflection geometry is also possible, provided that the absorption and scattering weight matrices are regulated carefully. Because the eigenvalues of the two matrices are significantly different, good regulation schemes are needed to balance the reconstructed absorption and scattering coefficients at each iteration. This subject is one of our topics for further study.

In this study the ultrasound-assisted optical reconstruction was demonstrated at a particular target layer. Similar studies can be done with multiple targets located at different layers. In the multiple target case, we can attribute measured perturbations to more layers instead of a single layer. However, the improvements in reconstructed optical properties and reconstruction speed may be less than that of the single-layer case.

Ultrasound has good imaging capability, and it can detect small lesions of a few millimeters in size. However, its specificity in cancer detection is not high as a result of overlapping characteristics of benign and malignant lesions. NIR imaging has high specificity in cancer detection; however, it suffers low resolution and lesion location uncertainty because of the diffused nature of the NIR light. The hybrid imaging that combines ultrasound imaging capability and NIR contrast has a great potential to overcome deficiencies of either method. As we reported in the paper, the target depth information can significantly improve the accuracy of the reconstructed optical absorption coefficient and reconstruction speed. In addition to use of *a priori* target depth information, the target spatial distribution provided by ultrasound can be used in optical reconstruction as well.[15] With the localized spatial and temporal target information, the accuracy of the reconstructed optical properties and the reconstruction speed can be improved further. To demonstrate this, we need an ultrasound imaging transducer located at the middle portion of the probe. We are currently pursuing this study.[23,24]

In this study the targets of different contrasts were located at the center position. We have also done studies with targets of different contrasts located at off-center positions. For an off-center target case, the effective number of source–detector pairs is less than that of the on-center target case because measurements from certain source–detector pairs do not contain much information about the target. For example, if a target is placed at ($x = 2, y = 2, z = 3.0$ cm), the measurements of source–detector pairs at the opposite corner of the probe contribute little to the image reconstruction. In one study, targets of high and low contrast were located at ($x = 2, y = 2, z = 3.0$ cm). The reconstructed maximum absorption coefficient at the target layer was related more to the total neighbor source–detector pairs. However, the maximum value at a deeper nontarget layer was related more to the total source–detector pairs and was decreased with the reduction of total pairs. Because the photons originated from distant sources and detected by distant detectors experience longer and more diffused scattering paths, they are likely to interact with the off-center target and contribute to the absorption estimate at the deeper layer. In the same study, the measured sidelobe levels were 4.5 and 2.0 dB poorer on average compared with the on-center high- and low-target cases, respectively. The beam widths were comparable to those measured from on-center cases.

7. Summary

The relationship between the total number of source-detector pairs and the imaging parameters of a reconstructed absorption coefficient was evaluated experimentally. A frequency-domain system of a 140-MHz modulation frequency was used in the experiments. Reconstruction at a selected target depth with *a priori* depth information provided by ultrasound was demonstrated. The results have shown that the reconstructed absorption coefficient and the spatial resolution of the absorption image were decreased when the total number of source-detector pairs was reduced. More than 160 source-detector pairs were needed to reconstruct the absorption coefficient within 60% of the true value and spatial resolution comparable to that obtained with the dense array. The contrast resolution was

poorer in general because of edge artifacts and could be worse if significant larger iteration numbers are used for reconstruction. The error in target depth estimated from 3-D optical images was approximately 1 cm. With the *a priori* target depth information provided by ultrasound, the reconstruction can be done at a selected depth. Because the unknowns were reduced significantly, the reconstruction speed was approximately ten times faster than that without depth information. In addition, the accuracy of the reconstructed absorption coefficient was improved by 15% and 30% on average for high- and low-contrast cases, respectively. Furthermore, the measured −6-dB beam width was improved by 24% and 41% for high- and low-contrast cases, respectively. The sidelobe was 3 and 1 dB poorer for high- and low-contrast cases because the measurement noise was lumped to single-layer reconstruction instead of multiple layers.

In conclusion, ultrasound-assisted 3-D optical imaging has shown promising results to overcome the problems associated with the reconstruction by use of diffusive waves. With the target depth information provided by ultrasound, the reconstructed absorption coefficient was more accurate and the reconstruction speed was much faster.

We acknowledge the funding support of the Connecticut Innovation Program, the U.S. Department of Defense Army Breast Cancer Program (DAMD17-00-1-0217), the Windy Will Cancer Fund, Multidimensional Technology Inc., and the Research Foundation of the University of Connecticut.

References

1. S. Fantini, S. Walker, M. Franceschini, M. Kaschke, P. Schlag, and K. Moesta, "Assessment of the size, position, and optical properties of breast tumors *in vivo* by noninvasive optical methods," Appl. Opt. **37,** 1982–1989 (1998).
2. S. Zhou, Y. Chen, Q. Nioka, X. Li, L. Pfaff, C. M. Cowan, and B. Chance, "Portable dual-wavelength amplitude cancellation image system for the determination of human breast tumor," in *Optical Tomography and Spectroscopy of Tissue III*, B. Chance, R. Alfano, and B. Tromberg, eds., Proc. SPIE **3597,** 571–579 (1999).
3. R. M. Danen, Y. Wang, X. D. Li, W. S. Thayer, and A. G. Yodh, "Regional imager for low resolution functional imaging of the brain with diffusing near-infrared light," Photochem. Photobiol. **67,** 33–40 (1998).
4. T. McBride, B. W. Pogue, E. Gerety, S. Poplack, U. Osterberg, B. Pogue, and K. Paulsen, "Spectroscopic diffuse optical tomography for the quantitative assessment of hemoglobin concentration and oxygen saturation in breast tissue," Appl. Opt. **38,** 5480–5490 (1999).
5. M. A. Franceschini, K. T. Moesta, S. Fantini, G. Gaida, E. Gratton, H. Jess, M. Seeber, P. M. Schlag, and M. Kashke, "Frequency-domain techniques enhance optical mammography: initial clinical results," Proc. Natl. Acad. Sci. USA **94,** 6468–6473 (1997).
6. J. B. Fishkin, O. Coquoz, E. R. Anderson, M. Brenner, and B. J. Tromberg, "Frequency-domain photon migration measurements of normal and malignant tissue optical properties in human subject," Appl. Opt. **36,** 10–20 (1997).
7. T. L. Troy, D. L. Page, and E. M. Sevick-Muraca, "Optical properties of normal and diseased breast tissues: prognosis for optical mammography," J. Biomed. Opt. **1**(3), 342–355 (1996).
8. R. J. Grable, D. P. Rohler, and S. Kla, "Optical tomography breast imaging," in *Optical Tomography and Spectroscopy of Tissue: Theory, Instrumentation, Model, and Human Studies II*, B. Chance and R. Alfano, eds., Proc. SPIE **2979,** 197–210 (1997).
9. H. Jiang, K. Paulsen, U. Osterberg, B. Pogue, and M. Patterson, "Optical image reconstruction using frequency-domain data: simulations and experiments," J. Opt. Soc. Am. A **12,** 253–266 (1995).
10. W. Zhu, Y. Wang, Y. Deng, Y. Yao, and R. Barbour, "A wavelet-based multiresolution regularized least squares reconstruction approach for optical tomography," IEEE Trans. Med. Imaging **16**(2), 210–217 (1997).
11. M. A. O'Leary, "Imaging with diffuse photon density waves," Ph.D. dissertation (University of Pennsylvania, Philadelphia, Pa., 1996).
12. X. Li, T. Durduran, A. Yodh, B. Chance, and D. N. Pattanayak, "Diffraction tomography for biomedical imaging with diffuse-photon density waves," Opt. Lett. **22,** 573–575 (1997).
13. C. Matson and H. Liu, "Analysis of the forward problem with diffuse photon density waves in turbid media by use of a diffraction tomography model," J. Opt. Soc. Am. A **16,** 455–466 (1999).
14. C. Matson and H. Liu, "Backpropagation in turbid media," J. Opt. Soc. Am. A **16,** 1254–1265 (1999).
15. Q. Zhu, T. Dunrana, M. Holboke, V. Ntziachristos, and A. Yodh, "Imager that combines near-infrared diffusive light and ultrasound," Opt. Lett. **24,** 1050–1052 (1999).
16. Q. Zhu, D. Sullivan, B. Chance, and T. Dambro, "Combined ultrasound and near infrared diffusive light imaging," IEEE Trans. Ultrason. Ferroelectr. Freq. Control **46,** 665–678 (1999).
17. Q. Zhu, E. Conant, and B. Chance, "Optical imaging as an adjunct to sonograph in differentiating benign from malignant breast lesions," J. Biomed. Opt. **5**(2), 229–236 (2000).
18. M. Jholboke, B. J. Tromberg, X. Li, N. Shah, J. Fishkin, D. Kidney, J. Butler, B. Chance, and A. G. Yodh, "Three-dimentional diffuse optical mammography with ultrasound localization in human subject," J. Biomed. Opt. **5**(2), 237–247 (2000).
19. D. A. Boas, M. A. O'Leary, B. Chance, and A. G. Arjun, "Scattering of diffuse photon density waves by spherical inhomogeneities within turbid media: analytic solution and applications," Proc. Natl. Acad. Sci. USA **91,** 4887–4891 (1994).
20. W. Zhu, Y. Wang, and J. Zhang, "Total least-squares reconstruction with wavelets for optical tomography," J. Opt. Soc. Am. A **15,** 2639–2650 (1998).
21. P. C. Li, W. Flax, E. S. Ebbini, and M. O'Donnell, "Blocked element compensation in phased array imaging," IEEE Trans. Ultrason. Ferroelectr. Freq. Control **40,** 283–292 (1993).
22. G. H. Golub, "Some modified matrix eigenvalue problems," SIAM (Soc. Ind. Appl. Math.) Rev. **15,** 318–334 (1973).
23. D. Piao, X.-H. Ding, P. Guo, and Q. Zhu "Optimal distribution of near infrared sensors for simultaneous ultrasound and NIR imaging," in *Biomedical Topical Meetings*, Postconference Digest, Vol. 38 of OSA Trends in Optics and Photonics Series (Optical Society of America, Washington, D.C., 2000), pp. 472–474.
24. P. Guo, Q. Zhu, D. Piao, and J. Fikiet, "Combined ultrasound and NIR imager," in *Biomedical Topical Meetings*, Postconference Digest, Vol. 38 of OSA Trends in Optics and Photonics Series (Optical Society of America, Washington, D.C., 2000), pp. 97–99.

252 OPTICS LETTERS / Vol. 27, No. 4 / February 15, 2002

Characterization of small absorbers inside turbid media

Nan Guang Chen and Quing Zhu

Department of Electrical & Computer Engineering, University of Connecticut, Storrs, Connecticut 06269

Received October 29, 2001

We propose a novel noniterative near-infrared diffusive image reconstruction method that uses minimal *a priori* co-registered ultrasound information. Small absorbing targets embedded in a homogeneous background are described approximately in terms of their monopole, dipole, and quadrupole moments. With an approximate estimation of the center locations of these absorbers from ultrasound images, we show in simulations that the reconstruction accuracy of the absorption coefficient exceeds 80% if the noise level is less than 0.2%. We also demonstrate experimentally that the accuracy can be improved by use of additional ultrasound volume information even for a noise level as high as 1.5%. © 2002 Optical Society of America

OCIS codes: 100.3190, 170.3010, 170.3880, 290.1990.

Functional imaging with near-infrared (NIR) light has found potential applications in many areas, such as breast and brain lesion detection and diagnosis.[1,2] Recently, a combination of NIR imaging with other imaging modalities, such as ultrasound or magnetic resonance imaging, has shown promising results[3–5] in providing complementary contrasts and overcoming NIR reconstruction problems related to intensive light scattering.

In this Letter we introduce a novel reconstruction algorithm for NIR diffusive imaging that uses approximate target center locations estimated from co-registered ultrasound. Our new method is based on estimation of major characteristics of isolated small absorbers. These characteristics are monopole, dipole, and quadrupole moments. Higher-order moments have negligible effects in characterizing the absorbers and are ignored. It is shown in this Letter that measurements of diffusive photon density waves cannot readily achieve a signal-to-noise ratio that is good enough for reconstructing the detailed shape information of targets. However, the quadrupole moment can provide an approximate extension of the target, which is necessary for distributing the integral absorption (the monopole) to an appropriate target region. In situations in which the measurement system suffers from unexpected noise, accurate estimation of the quadrupole moment might not be possible. The target volume estimated from co-registered ultrasound images can be used for distributing the integral absorption inside the target volume. We have conducted a series of simulations at different noise levels to evaluate the performance of this new method. We have also conducted experiments using our combined NIR–ultrasound imager[5] to test the algorithm.

If it is assumed that there are only a few small inhomogeneous targets embedded in a homogeneous background, the distribution of the absorption coefficient can be expressed as

$$\mu_a(\mathbf{r}) = \mu_a{}^0 + \Delta\mu_a(\mathbf{r}). \tag{1}$$

The background absorption coefficient, $\mu_a{}^0$, can be as small as 0.02 cm^{-1} for normal breast tissues, whereas $\Delta\mu_a$ can be well beyond 0.1 cm^{-1} for tumors because of the blood. In the Born approximation, the photon density wave is decomposed into an incident wave and a scattering wave:

$$\Phi(\omega,\mathbf{r}) = \Phi_{\mathrm{inc}}(\omega,\mathbf{r}) + \Phi_{\mathrm{sct}}(\omega,\mathbf{r}). \tag{2}$$

The incident wave is the solution of a homogeneous diffusion equation, and the scattering wave can be given approximately by the linear perturbation theory:

$$\Phi_{\mathrm{sct}}(\omega,\mathbf{r}) \approx -\int_V \frac{\Delta\mu_a(\mathbf{r}')}{D}\,\Phi_{\mathrm{inc}}(\omega,\mathbf{r}')G(\mathbf{r},\mathbf{r}')d^3\mathbf{r}'. \tag{3}$$

In this equation, $G(\mathbf{r},\mathbf{r}')$ is the Green's function, and $D = 1/3\mu_s'$ is inversely proportional to the reduced scattering coefficient, μ_s'. In the context of early stage breast cancer detection, we can further assume that those heterogeneities are confined to a few insolated regions. Then, the scattering wave can be expanded around each of N target centers as

$$\Phi_{\mathrm{sct}}(\omega,\mathbf{r}) = -\frac{1}{D}\sum_{\nu=1}^{N}[\mathrm{M}^\nu W(\mathbf{r}_0{}^\nu) + \mathrm{D}^\nu\cdot\nabla W(\mathbf{r}_0{}^\nu) + \mathrm{Q}^\nu\cdot\nabla\nabla W(\mathbf{r}_0{}^\nu)/2 + O(a^3)]. \tag{4}$$

Here $\mathbf{r}_0{}^\nu$ is the center of the νth target, and $W(\mathbf{r}_0{}^\nu) = \Phi_{\mathrm{inc}}(\omega,\mathbf{r}_0{}^\nu)G(\mathbf{r},\mathbf{r}_0{}^\nu)$ is the weight function. For the νth target, M^ν, D^ν, and Q^ν are its monopole, dipole, and quadrupole moments, respectively. Terms beyond the second order of target dimension a have negligible effects in characterizing the absorbers and are neglected in our model. For the νth target, its monopole, dipole, and quadrupole moments are scalar, vector, and second-order tensor, respectively, and they are given as

$$\mathrm{M}^\nu = \int_{V_\nu}\Delta\mu_a(\mathbf{r}')d^3\mathbf{r}', \qquad \mathrm{D}^\nu = \int_{V_\nu}\Delta\mu_a(\mathbf{r}')\mathbf{r}'d^3\mathbf{r}',$$

$$\mathrm{Q}^\nu = \int_{V_\nu}\Delta\mu_a(\mathbf{r}')\mathbf{r}'\mathbf{r}'d^3\mathbf{r}'. \tag{5}$$

The integrations are over a small isolated region V_ν.

A multiple-source, multiple-detector configuration is typical for frequency-domain diffusive imaging systems. We are using 12 sources (780 nm) that are amplitude modulated at 140 MHz and eight detectors

0146-9592/02/040252-03$15.00/0

in our simulations as well as in the experiments. These sources and detectors are deployed on an absorbing plane, which simplifies boundary conditions. The reflection mode with a semi-infinite geometry is used for both simulation and experiment. The measured scattering wave is related to the target moments by the following equation:

$$[\hat{\phi}_1 \cdots \hat{\phi}_m]^T \approx \Omega[\mathrm{M}^1 \quad \mathrm{D}^1 \quad \mathrm{Q}^1 \quad \cdots \quad \mathrm{Q}^N]^T. \qquad (6)$$

An element of Ω is either the weight function for one target or its derivatives up to the second order.

The inverse problem is to retrieve the characteristics of those embedded absorbers from measured photon density waves on the surface. Based on our simplified forward model, it is necessary to have certain information about absorbers, such as the number of targets and their center positions, in advance. The ultrasound system of our combined imager can provide such information. Once the initial center locations have been specified, the weight function, together with its first and second derivatives, can be calculated immediately. Since the inverse problem has only a few unknowns, reconstruction of target moments is overdetermined and least-squares solutions can be adopted. For each target, the monopole moment represents the integral absorption, the dipole moments result in correction of the center position, and the quadrupole moments lead to estimation of the target volume, in which the integral absorption can be redistributed. The target volume is estimated by simple matching of the quadrupole moments with those of an ellipsoid, which has the freedom to rotate about the center in any direction to any angle.

Figure 1 shows a schematic of the combined probe for experiments, which is a circular plate made of rigid absorbing material. One or two cuboid absorbers were placed 2.5 cm deep in a homogeneous medium. For phantom experiments, raw data were acquired with our combined imaging system. The ultrasound array was translated in the x direction to yield target volume estimates. We used 0.6% Intralipid as a homogeneous background, which yielded a reduced scattering coefficient of 6 cm^{-1} and an absorption coefficient of 0.015 cm^{-1}. The embedded targets were as scattering as the background but were more absorbing. For simulations, the simulated measurement data were the sum of forward model prediction and random noises ranging from 0.1% to 1% (with respect to the amplitudes of the incident waves). The optical properties of homogeneous media and targets are similar to those used in phantom experiments.

Shown in Fig. 2 are simulation results for a single target. The target was a cuboid of (1.2, 0.8, 1) cm in the x, y, and z directions, respectively, and was centered at (0.2, 0, 2.5) cm. The volume of the target was 0.96 cm^3. The absorption coefficient above the background was 0.25 cm^{-1}. Here we provide the results for one dipole moment (D_x) and one quadruple moment (Q_{xx}), but similar results were obtained for other components. The initial target position that was input into the reconstruction algorithm was (0, 0, 2.5) cm, which deviated slightly from the true position. This initial location error resulted in a negligible effect on the reconstructed monopole values, as shown in Fig. 2(a). The offset of center position can be corrected by the estimated dipole moment, D_x [see Fig. 2(c)], which is slightly lower than the true value. However, the inaccuracy of the initial center position obviously affects the reconstructed quadrupole moment. The circles in Fig. 2(e) represent values greater than the true values. After we correct the center position according to the estimated dipole moments, the reconstructed values of Q_{xx}, plotted as asterisks in the same figure, are much closer to the true values. Although the mean values of reconstructed moments are essentially independent of noise

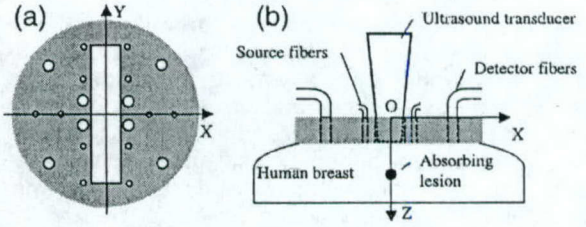

Fig. 1. (a) Bottom view of the combined probe. The central rectangular slot gives the ultrasound array access to tissues underneath the probe. The circular holes are used to hold optical fibers. The small holes are for light sources, and the larger ones are for detectors. The diameter of the probe is 10 cm. (b) Side view of the probe.

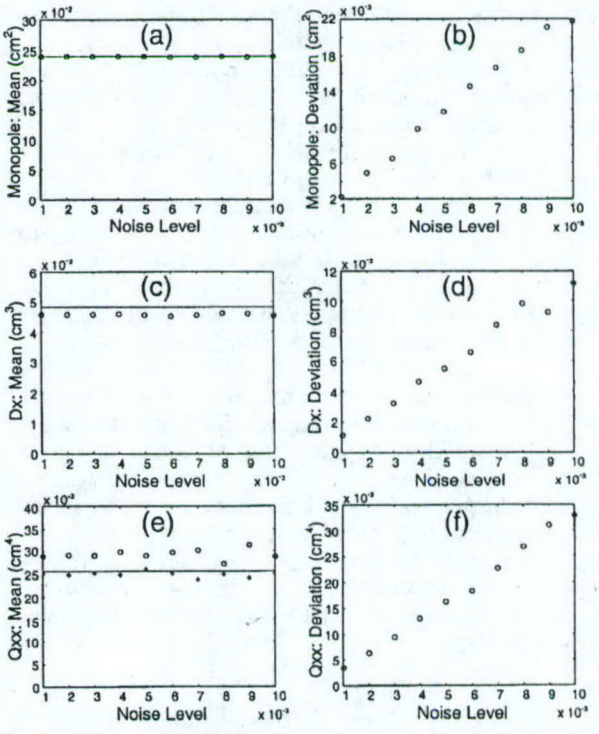

Fig. 2. Simulation results for a single target. (a), (c), and (e) mean values of monopole, dipole, and quadrupole moments, respectively. (b), (d), and (f) standard deviations of the corresponding quantities. The solid lines in (a), (c), and (e) are true values.

Table 1. Reconstructed Absorption Coefficients from Phantom Experiments[a]

	Combination 1		Combination 2	
Value (cm^{-1})	Target 1	Target 2	Target 1	Target 2
True	0.065	0.065	0.102	0.065
Reconstructed	0.064 ± 0.028	0.064 ± 0.027	0.106 ± 0.026	0.064 ± 0.017

[a]The average values and standard deviations are estimated from six sets of experimental data.

level, the standard deviations of all moments increase linearly with increasing noise level. Higher-order moments suffer more from noise, as expected intuitively. For the quadrupole moments, as small as a 0.2% noise level could lead to a relative error of ~20%. This is the main reason that we did not attempt to reconstruct moments beyond the second order.

To test the capability of our algorithm to characterize multiple targets, we performed simulations with two absorbers of different absorption coefficients. The absorbers were the same size as the single target. One absorber was located at $(-1.2, 0, 2.5)$ cm, with an absorption coefficient 0.25 cm^{-1} beyond the background. The other absorber was located at (1.2, 0, 2.5) cm, with an absorption coefficient 0.1 cm^{-1} beyond the background. The main effect of adding one target was that the relative error in the reconstructed monopole moments increased to ~2.5 times. Less of an effect on the dipole moments was observed, although an even more trivial difference for the quadrupole could be seen. It was also found that the noise-induced deviation was independent of target optical properties.

Our current NIR imaging system has a noise level near 1.5%. According to the simulation results, the system cannot readily retrieve the accurate quadrupole moments from measured photon density waves. Thus we have to use the volume information obtained from co-registered ultrasound images in target characterization. We used two geometrically identical targets that were approximately 1-cm^3 cubes. They were gel phantoms made from 0.6% Intralipid solution, ink, and ultrasound scatterers. The boundaries of these targets can clearly be seen in ultrasound images, and target centers and volumes can be estimated accurately. For example, a 1.07-cm^3 target was measured as 1.05 cm^3 by ultrasound. For co-registered NIR imaging, two different combinations of targets were adopted. The first was a pair of equally absorbing cubes with an absorption coefficient of 0.065 cm^{-1}. The second was a pair of absorbing cubes with absorption coefficients of 0.065 and 0.1 cm^{-1}, respectively. We simply distribute the estimated monopole evenly over the target volume. So the reconstructed absorption coefficient was an average value within each target. The true and the reconstructed values are compared in Table 1. The mean values and standard deviations were based on six sets of measurements.

Since target monopole moments can be estimated with sufficient accuracy, the reconstructed absorption coefficient depends more on the estimation of target volume, which can be obtained from the reconstructed quadrupole moment or co-registered ultrasound images. It is possible that the extent of the optical volume of a lesion is larger than the volume estimated from the acoustic images. This is one of our motivations for estimating the optical volume from the quadrupole moments. Further improvements are needed for an accurate estimate of quadrupole moments. In the moment-based method we assume that the lesions are isolated and are embedded in a homogeneous background. This assumption is quite true for more-homogeneous fatty breasts and may not hold for dense breasts that consist of both glandular tissue and fat. In the latter case, we could segment ultrasound images, identify tissue types, and estimate background optical properties of different tissues in the reconstruction as well. Both acoustic and optical contrasts exist in tumors but the sensitivities of these two modalities may be different. Therefore, the correlation between acoustic and optical heterogeneities remains unknown at the current stage and will be determined in our future clinical studies.

In comparison with current sophisticated NIR image reconstruction algorithms, our method is very simple in terms of computation. Once an ultrasound image has been taken and targets have been identified, it is possible to monitor the local change of absorption continuously and in real time. Averaging over a large number of samples will help suppress the effect of random noise.

In this Letter an algorithm for characterizing absorbers has been demonstrated. Theoretically, a similar algorithm is possible for characterizing scattering targets as well. However, since the weights of monopole, dipole, and quadrupole moments of scattering targets are related to spatial derivatives, which are two order higher than those of absorbers, the quadrupole moments will be even harder to reconstruct.

We thank the following for their funding support: the State of Connecticut (99CT21) and the U.S. Department of Defense Army Breast Cancer Program (DAMD17-00-1-0217, DAMD17-01-1-0216). N. G. Chen's e-mail address is chenng@engr.uconn.edu.

References

1. B. Tromberg, N. Shah, R. Lanning, A. Cerussi, J. Espinoza, T. Pham, L. Svaasand, and J. Butler, Neoplasia **2,** 26 (2000).
2. R. M. Danen, Y. Wang, X. D. Li, W. S. Thayer, and A. G. Yodh, Photochem Photobiol. **67,** 33 (1998).
3. B. Pogue and K. Paulsen, Opt. Lett. **23,** 1716 (1998).
4. Q. Zhu, N. G. Chen, D. Q. Piao, P. Y. Guo, and X. H. Ding, Appl. Opt. **40,** 3288 (2001).
5. N. G. Chen, P. Y. Guo, S. K. Yan, D. Q. Piao, and Q. Zhu, Appl. Opt. **40,** 6367 (2001).

Simultaneous reconstruction of absorption and scattering maps with ultrasound localization: feasibility study using transmission geometry

Minming Huang, Tuqiang Xie, Nan Guang Chen, and Quing Zhu

We report the experimental results of the simultaneous reconstruction of absorption and scattering coefficient maps with ultrasound localization. Near-infrared (NIR) data were obtained from frequency domain and dc systems with source and detector fibers configured in transmission geometry. High- or low-contrast targets located close to either the boundary or the center of the turbid medium were reconstructed by using NIR data only and NIR data with ultrasound localization. Results show that the mean reconstructed absorption coefficient and the spatial distribution of the absorption map have been improved significantly with ultrasound localization. The improvements in the mean scattering coefficient and the spatial distribution of the scattering coefficient are moderate. When both the absorption and the scattering coefficients are reconstructed the performance of the frequency-domain system is much better than that of the dc system. © 2003 Optical Society of America

OCIS codes: 170.0170, 170.3010, 170.5270, 170.7170, 170.3830.

1. Introduction

Functional imaging with near-infrared (NIR) diffused light has found potential applications in many areas.[1–9] However, one fundamental problem that we have to overcome is the intense scattering of light. As a result, diffused light probes a widespread region instead of providing information along a straight line. Multiple measurements are always correlated as a result of the overlapping of probed regions. Therefore increasing the total number of measurements does not necessarily provide more independent information for image reconstruction. In general the inverse image reconstruction is underdetermined and ill-posed. The behavior of reconstruction algorithms is affected by many factors, such as the system signal-to-noise ratio, the probe configuration, and regulation schemes used in image reconstructions.

The current approaches to image-reconstruction algorithms are (1) simple backprojection methods,[3,4] (2) perturbation methods,[10–12] and (3) finite-element methods (FEMs).[13–15] The backprojection method provides a real-time estimation of the coarse optical properties of lesions. However, the reconstructed-image resolution is low and the lesions that appear in the images are often displaced from true locations. Perturbation methods are in general based on linear approximations to the heterogeneous functions. Born and Rytov approximations are examples. Measurements between the background and the heterogeneous medium are used to relate the optical signals at the measurement surface to absorption and scattering variations in each volume element within the sample. The least-squares method is in general used to formulate the inverse problem. Iterative search methods, such as conjugate-gradient techniques, are employed to iteratively solve the inverse problem. However, an accurate estimation of the target optical properties depends on an accurate estimation of the background optical properties, which are in general not easy to obtain in breast tissues. In addition, when the absorption or the scattering coefficients of the lesions are significantly higher than the background, the linear perturbation methods cannot give accurate optical properties. Reconstructions based on FEMs provide higher-order estimations to heterogeneous functions. However, as the scattering and absorption coefficients are expanded over local basis functions, the number of unknowns is increased considerably. Nonetheless the

The authors are with the Department of Electrical and Computer Engineering, University of Connecticut, Storrs, Connecticut 06269.

Received 2 July 2002; revised manuscript received 16 December 2002.

0003-6935/03/194102-13$15.00/0

independent information from diffused light is limited, and it essentially stops increasing when the source–detector pairs reach a certain number. In this case the inverse problem becomes more ill-posed and the behavior of the reconstruction algorithm may be unpredictable.

Reconstructions with the aid of *a priori* target geometry information provided by coregistered ultrasound have shown promising results in improving the accuracy of reconstructed optical properties and the localization of targets.[16–20] In this method an ultrasound probe and NIR source and detector fibers have been deployed on a handheld probe and configured in the reflection geometry. The *a priori* tissue type and lesion location as well as shape provided by coregistered ultrasound can guide the NIR image reconstruction to localized target regions. Therefore the total number of voxels with unknown optical properties can be reduced significantly and the inversion becomes well defined. In general the solution is unique and the iterative search algorithms converge very fast.

In this paper we explore experimentally the utility of the combined imaging with NIR sources and detectors configured in transmission geometry. The standard pulse-echo technique is used to obtain coregistered ultrasound images. Compared with NIR reflection geometry, transmission geometry may have the advantages of a lower requirement on the system dynamic range and higher sensitivities. In the reported experiments the FEM forward solver is used to generate a Jacobian weight matrix for simultaneous reconstruction of the absorption and the scattering coefficient maps, and the inversion is performed by using NIR data only and NIR data with *a priori* target geometry provided by coregistered ultrasound.

Frequency-domain and dc systems are widely used by many research groups. The advantage of using a frequency-domain system is that both amplitude and phase information can be obtained, and therefore simultaneous reconstruction of absorption and scattering coefficients is feasible. The disadvantage is the complexity in constructing high-frequency transmission and reception circuitries, particularly when many parallel channels are needed for fast data acquisition. This situation is more pronounced when nearly 100 source and detector positions are needed for three-dimensional (3D) imaging in transmission geometry. In addition the system cost is high. Direct-current systems have the advantages of simplicity in circuit construction and low cost. The drawbacks are that the phase information is not available and cross talk between the reconstructed absorption and scattering coefficients may be unavoidable. In this paper we compare the performance of both systems in simultaneously constructing absorption and diffusion coefficient maps in conditions of NIR reconstruction only and ultrasound guided NIR reconstruction.

2. Forward Model

A commercial FEM package FEMLAB has been used as a forward solver to generate the Jacobian weight matrix. This software has an interactive environment for modeling and simulating scientific and engineering problems based on partial differential equations. Users can utilize various existing models by defining relevant parameters and can also design specific models based on equations under consideration.

In FEMLAB the scalar-governing equation and boundary condition are given as

$$d_a \frac{\partial U(\bar{r})}{\partial t} - \nabla \cdot [c \cdot \nabla U(\bar{r}) + \alpha U(\bar{r})\gamma] + aU(\bar{r}) + \beta \nabla U(\bar{r}) = f(\bar{r}) \text{ in } \Omega, \quad (1)$$

$$\hat{n} \cdot [c \nabla U(\bar{r}) + \alpha U(\bar{r})\gamma] + qU(\bar{r}) = g(\bar{r}) \text{ on boundary } \partial\Omega. \quad (2)$$

Ω is the domain of interest where Eq. (1) is satisfied, and $\partial\Omega$ is the boundary of Ω where Eq. (2), representing a generalized Neumann boundary condition, is satisfied. $U(\bar{r})$ is the unknown scalar to be solved, f is the source term in Ω, c is the diffusion coefficient, a is the absorption coefficient, α is the conservative flux convection coefficient, d_a is the mass coefficient, β is the convection coefficient, γ is the conservative flux source term, $g(r)$ is the source at the boundary, $\hat{n}$ is the outward unit normal vector on $\partial\Omega$, and q is a positive number related to the internal reflection at the boundary. The time-domain photon-diffusion equation can be obtained from Eq. (1) as

$$\frac{1}{v} \frac{\partial \phi(\bar{r}, t)}{\partial t} - \nabla \cdot D(\bar{r}) \cdot \nabla \phi(\bar{r}, t) + \mu_a \phi(\bar{r}, t) = S_0(\bar{r}, t), \quad (3)$$

where U is replaced with $\phi(\bar{r}, t)$, the photon density at location $\bar{r}$; f with $S_0(\bar{r}, t)$, the point source term; a with μ_a, the optical absorption coefficient; c with D, the diffusion coefficient [$D = 1/(3\mu_s')$, where μ_s' is the reduced scattering coefficient]; and d_a with $1/v$, where v is the speed of light in the medium. All other coefficients are chosen to be zero.

By letting $g(r)$ equal zero, we can obtain the Neumann-type boundary condition as

$$\hat{n} \cdot D(\bar{r}) \cdot \nabla \phi(\bar{r}, t) + q\phi(\bar{r}, t) = 0. \quad (4)$$

By setting d_a to zero, we can obtain the steady-state diffusion equation as

$$\nabla \cdot D(\bar{r}) \cdot \nabla \phi(\bar{r}) - \mu_a \phi(\bar{r}) = -S_0(\bar{r}). \quad (5)$$

Furthermore, by replacing μ_a with $\mu_a - i\omega/v$, where ω is the modulation frequency, we can obtain a frequency-domain diffusion equation as

$$\nabla \cdot D(\bar{r}) \cdot \nabla \phi(\bar{r}, \omega) - \left(\mu_a - \frac{i\omega}{v}\right)\phi(\bar{r}, \omega) = -S_0(\bar{r}, \omega). \quad (6)$$

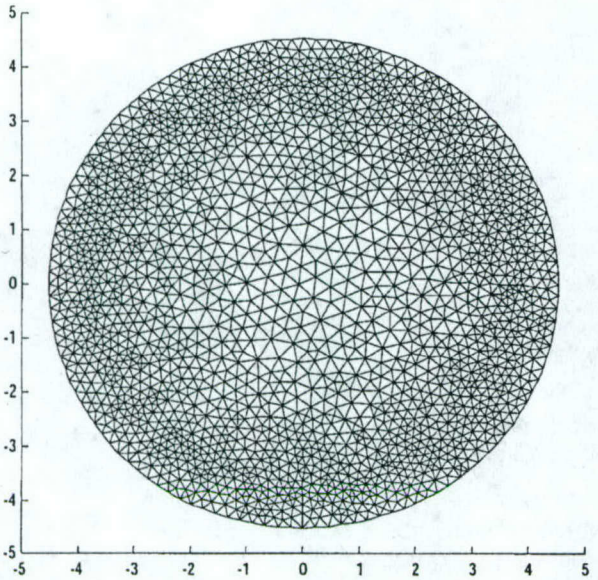

Fig. 1. Two-dimensional mesh used for NIR image geometry.

Assume that the changes due to the absorption and the scattering inhomogeneities are small. The Jacobian matrix

$$\mathbf{W}_{ij} = \left[\frac{\Delta\phi_{ij}}{\Delta\mu_{aj}}, \frac{\Delta\phi_{ij}}{\Delta D_j}\right],$$

that relates the photon-density perturbation at boundary cell i and imaging voxel j with absorption coefficient change $\Delta\mu_{aj}$ and diffusion coefficient change ΔD_j, is given as

$$[\mathbf{W}_{ij}] = \begin{bmatrix} \frac{\Delta\phi_{11}}{\Delta\mu_{a1}} & \cdots & \frac{\Delta\phi_{1L}}{\Delta\mu_{aL}} & \frac{\Delta\phi_{11}}{\Delta D_1} & \cdots & \frac{\Delta\phi_{1L}}{\Delta D_L} \\ \frac{\Delta\phi_{21}}{\Delta\mu_{a1}} & \cdots & \frac{\Delta\phi_{2L}}{\Delta\mu_{aL}} & \frac{\Delta\phi_{21}}{\Delta D_1} & \cdots & \frac{\Delta\phi_{2L}}{\Delta D_L} \\ \vdots & \ddots & \vdots & \vdots & \ddots & \vdots \\ \frac{\Delta\phi_{M1}}{\Delta\mu_{a1}} & \cdots & \frac{\Delta\phi_{ML}}{\Delta\mu_{aL}} & \frac{\Delta\phi_{M1}}{\Delta D_1} & \cdots & \frac{\Delta\phi_{ML}}{\Delta D_L} \end{bmatrix}, \quad (7)$$

where M is the total number of boundary cells and L is the total number of imaging voxels.

3. Computation Procedures

We have generated a two-dimensional (2D) mesh with 4050 triangle elements and 2088 nodes (Fig. 1). The radius of the physical boundary is chosen to be 45.26 cm and the extrapolation distance $Z_b = 0.7 \cdot 1_{tr}$ $[1_{tr} = 1/(\mu_s' + \mu_a)]$ is calculated to be 0.1169 cm,[21] where $\mu_s' + \mu_a$ is the background value and is chosen to be 6 cm^{-1} (a typical value for normal breast tissue). To speed up the Jacobian matrix calculation, we chose a coarse mesh of 5 cm × 5 cm in the middle of the 2D mesh by assuming that there are no perturbations outside this area. The imaging pixel size is chosen to be 0.25 cm × 0.25 cm inside the coarse mesh. As a result the total number of unknown voxels is 400, which is comparable with the total number of measurements.

In the Jacobian matrix calculation we evaluated the linearity of $\Delta\phi_{ij}/\Delta\mu_{aj}$ versus $\Delta\mu_{aj}$ with μ_{aj} changing from 0.02 to 0.3 cm^{-1} (the typical range of the absorption coefficient for breast lesions) at many cell locations. For dc component calculations the error due to the linear approximation is always less than 0.4%. For frequency-domain calculations the real and imaginary parts of ϕ_{ij} of several cells are 1 or 2 orders smaller, and they are very sensitive to small perturbations. However, even for the worst case, the error due to the use of the linear approximation is also less than 0.5% for 24 out of 28 detector locations. Therefore we can simplify the Jacobian matrix calculation by computing $\Delta\phi_{ij}/\Delta\mu_{aj}$ at two points (μ_{aL}, μ_{aH}) that are between 0.02 and 0.3 cm^{-1}. The selection of these two points is based on the following considerations. The linear slope $\Delta\phi_{ij}/\Delta\mu_{aj}$ is best estimated when a smaller perturbation $\Delta\mu_{aj}$ is used. However, a $\Delta\mu_{aj}$ that is too small is not suitable for computing $\Delta\phi_{ij}$. As a good compromise we chose $\mu_{aL} = 0.02$ cm^{-1} and $\mu_{aH} = 0.06$ cm^{-1} for all the calculations. We also evaluated the linearity of $\Delta\phi_{ij}/\Delta D_j$ versus ΔD_j with D_j changing from 0.0556 (the corresponding μ_s' is 6 cm^{-1}) to 0.0306 cm (the corresponding μ_s' is 10.9 cm^{-1}) (the typical diffusion coefficient range for breast lesions) at many cell locations. For both the dc component and frequency-domain calculations the error due to the use of a linear approximation is always less than 0.2%. Therefore we compute $\Delta\phi_{ij}/\Delta D_j$ by using two points at 0.0556 and 0.0356 cm.

The experimental data included many unknown systematic factors (unknown source, detector gains, etc.). To remove those unknown factors, we used the normalized difference method in Ref. 22 as

$$\left[\frac{\phi_{m(i)} - \phi_{mr(i)}}{\phi_{mr(i)}}\phi_{cr(i)}\right] = [W_{ij}] \cdot [\Delta\mu_{a(ji)}, \Delta D_{ji}], \quad (8)$$

where $\phi_{m(i)}$ is the measured heterogeneous data associated with the source–detector pair i with the target in the homogeneous medium, $\phi_{mr(i)}$ is the measured homogeneous data, $\phi_{cr(i)}$ is the calculated forward homogeneous data used for the weight matrix calculation. The ϕ is a complex value in the frequency-domain case. The unknown system factors present in both sets of measured heterogeneous and homogeneous data are canceled by taking the ratio of the perturbation (heterogeneous–homogeneous) to the reference (homogeneous) measurements.

To alleviate the cross talk between the absorption coefficient and the diffusion coefficient, we also normalized each column and row of the weight matrix by

their own mean value to improve the matrix condition. Thus the inverse problem is modified as

$$[F_{ii}] \cdot \left[\frac{\phi_{m(i)} - \phi_{mr(i)}}{\phi_{mr(i)}} \phi_{cr(i)} \right] = [F_{ii}] \cdot [W_{ij}] \cdot [G_{jj}] \cdot [\Delta X_{ji}], \quad (9)$$

where $\lfloor \Delta\mu_{a(ji)}, \Delta D_{ji} \rfloor = \lfloor G_{jj} \rfloor \cdot \lfloor \Delta X_{(ji)} \rfloor$ and

$$F_{ii} = \left(\frac{1}{N} \sum_{k=1}^{N} W_{ik} \right)^{-1}, \quad i = 1, 2, \ldots, M \ (F_{ij} = 0 \text{ when } i \neq j),$$

$$G_{jj} = \left(\frac{1}{M} \sum_{k=1}^{M} W_{kj} \right)^{-1}, \quad j = 1, 2, \ldots, L \ (G_{ij} = 0 \text{ when } i \neq j).$$

Finally the conjugate gradient method is used for solving Eq. (9). Since the error function

$$\left\| F \cdot W \cdot G \cdot \Delta X - F \cdot \frac{\phi_{m(i)} - \phi_{mr(i)}}{\phi_{mr(i)}} \phi_{cr(i)} \right\|^2$$

reduces consistently and becomes flat after certain iterations (around 30 for reconstruction with the NIR data only and 3 for the NIR with ultrasound guidance), the stopping criteria are chosen to be 100 and 3 iterations for the NIR only and the NIR with ultrasound localization, respectively. The corresponding computation time is around 2 min for NIR data only and 30 s for NIR with ultrasound information.

In the experiments, data are obtained from a 3D model (the finite cylindrical medium and the finite length target). However, the Jacobian matrix computation is based on a 2D model (the infinite cylindrical medium and the infinite-length target). According to Refs. 23 and 24 the 2D/3D difference between intensity is reasonably independent of source–detection separation and it is reasonable to correct it by simply multiplying or dividing a constant. Therefore the normalized difference method not only cancels the unknown source–detector gains but also partially eliminates the 2D/3D model mismatch by taking the ratio of the perturbation and the reference measurements.

4. Experimental Systems

To compare the performance of the frequency-domain and the dc systems with and without ultrasound localization, we constructed both systems. Details of our multisource and multidetector frequency-domain system can be found in Ref. 18. Briefly, it consists of 12 pairs of dual-wavelength sources [780 nm (LT024) and 830 nm (LT015), Sharp Corporation] modulated at 140 MHz and 8 parallel detectors (R928, Hamamatsu Corporation). These sources and detectors are coupled to the medium through optical fibers.

Our new dc system consists of six pairs of dual-wavelength laser diodes (780 and 830 nm) amplitude modulated at 20 kHz to avoid dc fluctuations (Fig. 2).

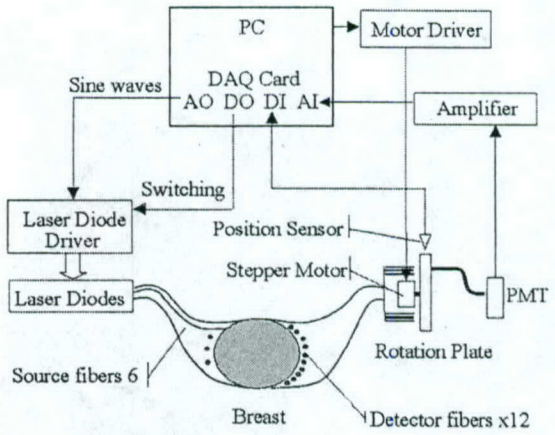

Fig. 2. Schematic of our new dc system: AO, analog output; AI, analog input; DO, digital output; DI, digital input.

Twelve detector fibers are sequentially coupled to a photomultiplier tube (PMT) (R928, Hamamatsu Corporation) through a mechanical multiplexer that uses a stepper motor to collimate accurately a coupling light guide on a rotation plate to one of the detection fibers. Each light source has two output levels of 30 dB in difference to avoid PMT saturation and to improve the system dynamic range. A National Instrumentation data acquisition (DAQ) card is used to generate sinusoidal waveforms on top of a constant current to drive one laser diode at a time. The photon density wave detected by the PMT is amplified and then digitized by the same DAQ card. The corresponding amplitude is retrieved from the acquired waveform on a PC. The digital ports of the DAQ card are used to switch laser diodes sequentially, control the output level, and input a feedback signal for closed-loop stepper motor control. The total DAQ time for a complete data set is around 1 min.

Since our dc system is modulated at 20 kHz, the measured amplitude is an ac signal instead of the dc component that we used for forward Jacobian matrix calculation. We estimated the difference by using a spherical wave of light energy density $[\exp(jk\rho)/D\rho]$ of two wave numbers, $k_1 = (-\mu_a/D)^{1/2}$ and $k_2 = [(-\mu_a + j \times \omega/v)/D]^{1/2}$, where $\omega = (2\pi)2 \times 10^4$ Hz and v and D are the speed of light and the diffusion coefficient, respectively. The normalized difference $[\exp(jk_1\rho) - \exp(jk_2\rho)]/\exp(jk_1\rho)$ can be approximated as

$$-\frac{j\rho\omega}{2v} [1/(D\mu_a)]^{1/2},$$

and it is larger when the wave propagates deeper into the tissue and the background absorption is smaller. For the worst case of $\mu_a = 0.01$ cm^{-1} and $\rho = 10$ cm the difference is less than 3.295^{-5}. Therefore we directly use the Jacobian matrix calculated from the steady-state diffusion equation [Eq. (5)] to relate the measured amplitude data for the inversion.

The experimental setup is shown in Fig. 3. During experiments, source and detector fibers were

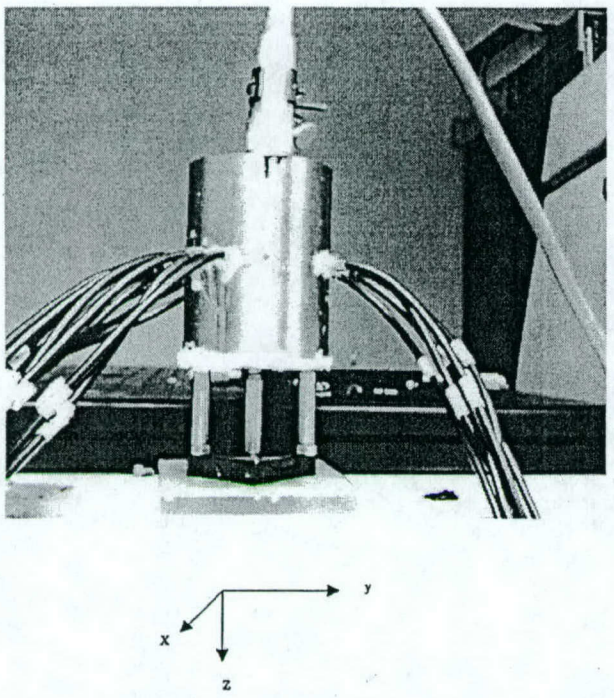

Fig. 3. Experimental setup. A commercial ultrasound probe is located at the top of a water tank, and the NIR source and detector fibers are deployed around the tank and configured in transmission geometry.

placed on a circular plane (Fig. 4). A commercial ultrasound probe of 3.5-MHz central frequency (HP77020A ultrasound imaging system) was placed on top of a water tank filled with Intralipid. This one-dimensional commercial probe provides a cross-section image in the y-z imaging plane (called the B-scan), where y is the lateral direction and z is the propagation direction. By translating the probe mechanically in the x direction, we acquired 3D volumetric image data. Windowing the 3D data in the z direction at a particular depth provides 2D target spatial images at the x-y plane (called the C-scan). C-scans are coregistered with the NIR images. An Intralipid solution of 0.6% was used as a homogeneous background. The fitted μ_a and μ_s' of the Intralipid at 780 nm were 0.02 and 6 cm^{-1}, respectively.

Since we have a limited number of source and detector positions, we placed 8 source fibers instead of 12 on a quarter circle and 8 detector fibers on the opposite quarter for frequency-domain measurements [Fig. 4(a)]. For dc measurements we placed 6 source fibers on a quarter circle and 12 detector fibers on the opposite quarter [see Fig. 4(b)]. After obtaining one set of heterogeneous NIR data with a target in the Intralipid (8 × 8 measurements for the frequency system, 6 × 12 measurements for the dc system), we simply rotated the target by 90° for the frequency-domain system and 77.14° for the dc system to get another set of data. Figure 4(c) shows the rotation scheme used during frequency-domain experiments. Three rotations were performed to obtain one complete data set for reconstruction, which covered 360°. For dc measurements a similar rotation scheme was used and four rotations were performed to obtain one complete data set. Three-dimensional ultrasound data were obtained simultaneously with NIR data acquisition.

5. Results

For NIR reconstruction with transmission geometry the perturbations in ϕ caused by the target are related to the location of the target and the contrast between the target and the background. It is much harder to reconstruct a low-contrast target located in the middle of the medium. In our experiments a cylindrical target (high/low contrast) 1.0 cm in diameter was placed at two typical locations (at the center and close to the boundary). The target was made of polyester resin with calibrated μ_a and μ_s'.[25] Based on the calibration results from Dartmouth College, the absorption coefficient of the target was from 0.20 to 0.3 cm^{-1} for the high-contrast target case and was 0.07 cm^{-1} for the low-contrast target; μ_s' of both targets was 9.6 cm^{-1}. The repeatability of the calibration was within ±5%.

A. Reconstruction when the Frequency-Domain System is Used

For the high-contrast target case, improvements in the reconstructed μ_a are dramatic when ultrasound localization is used. Figures 5(a) and 5(b) show the simultaneously reconstructed absorption and diffu-

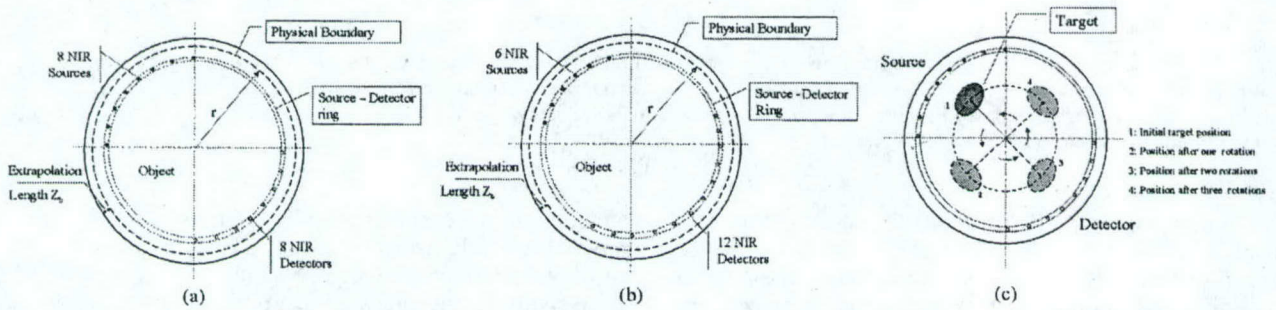

Fig. 4. Configurations of NIR sources and detectors used in the reported experiments: (a) frequency-domain experiments, (b) dc experiments, (c) top view of target rotation scheme used in frequency-domain measurements.

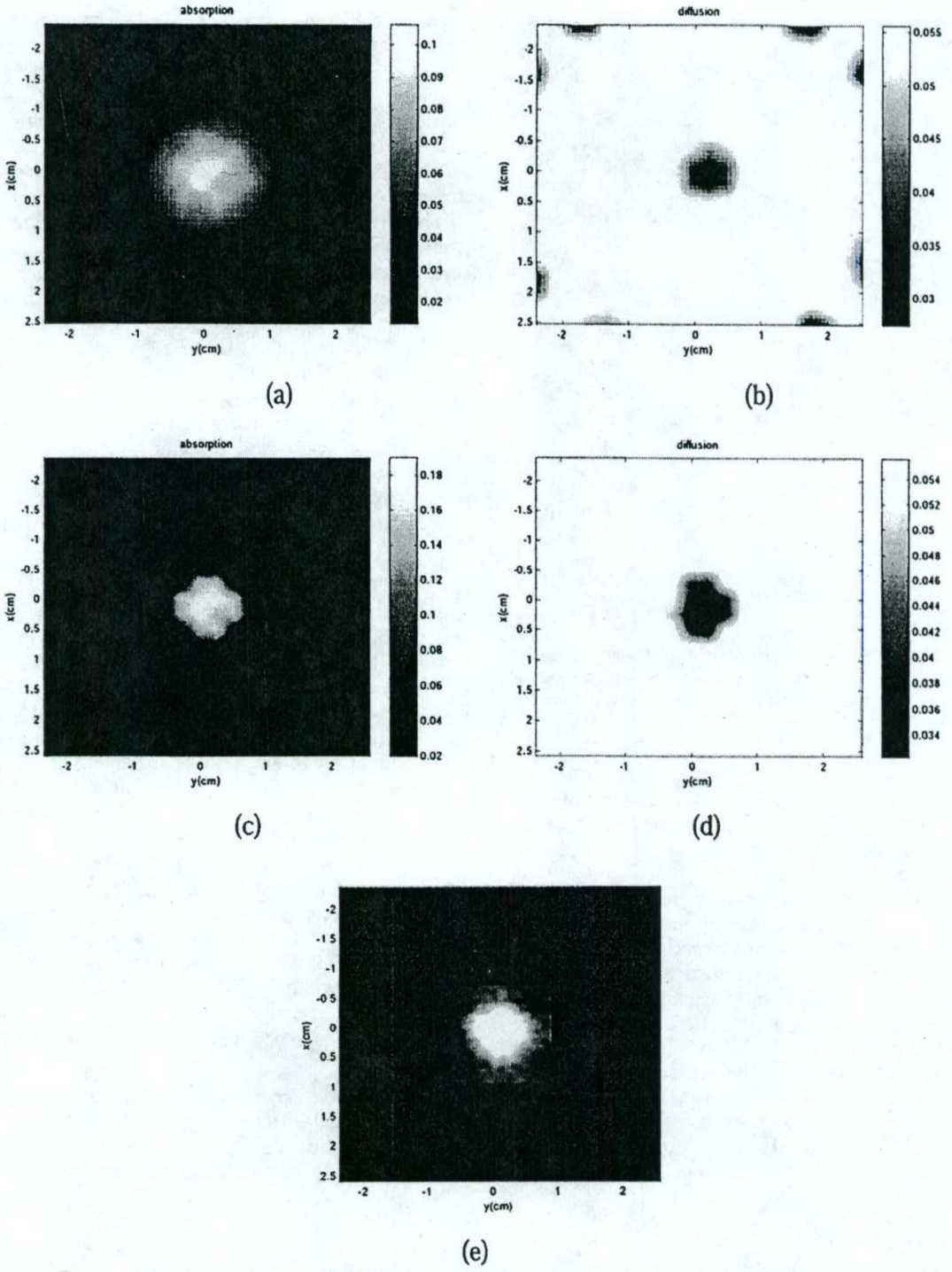

Fig. 5. Comparisons of simultaneously reconstructed absorption and diffusion coefficient maps of a high-contrast target located at the center of the turbid medium: (a), (b) reconstructed μ_a and D distributions when NIR data only are used; (c), (d), reconstructed μ_a and D distributions with ultrasound localization; (e) coregistered ultrasound C-scan image used to guide the NIR reconstruction. X and Y are the spatial dimensions in centemeters.

sion maps where NIR data only is used when the target is located at the center of the medium, while Figs. 5(c) and 5(d) show the reconstructed absorption and diffusion maps with ultrasound localization. Figure 5(e) is the C-scan ultrasound image obtained at the source–detector plane. A threshold was applied to the ultrasound image, which was chosen as the FWHM from the peak value. The pixels with gray-scale values greater than the threshold were mapped out as a target region, while the pixels with

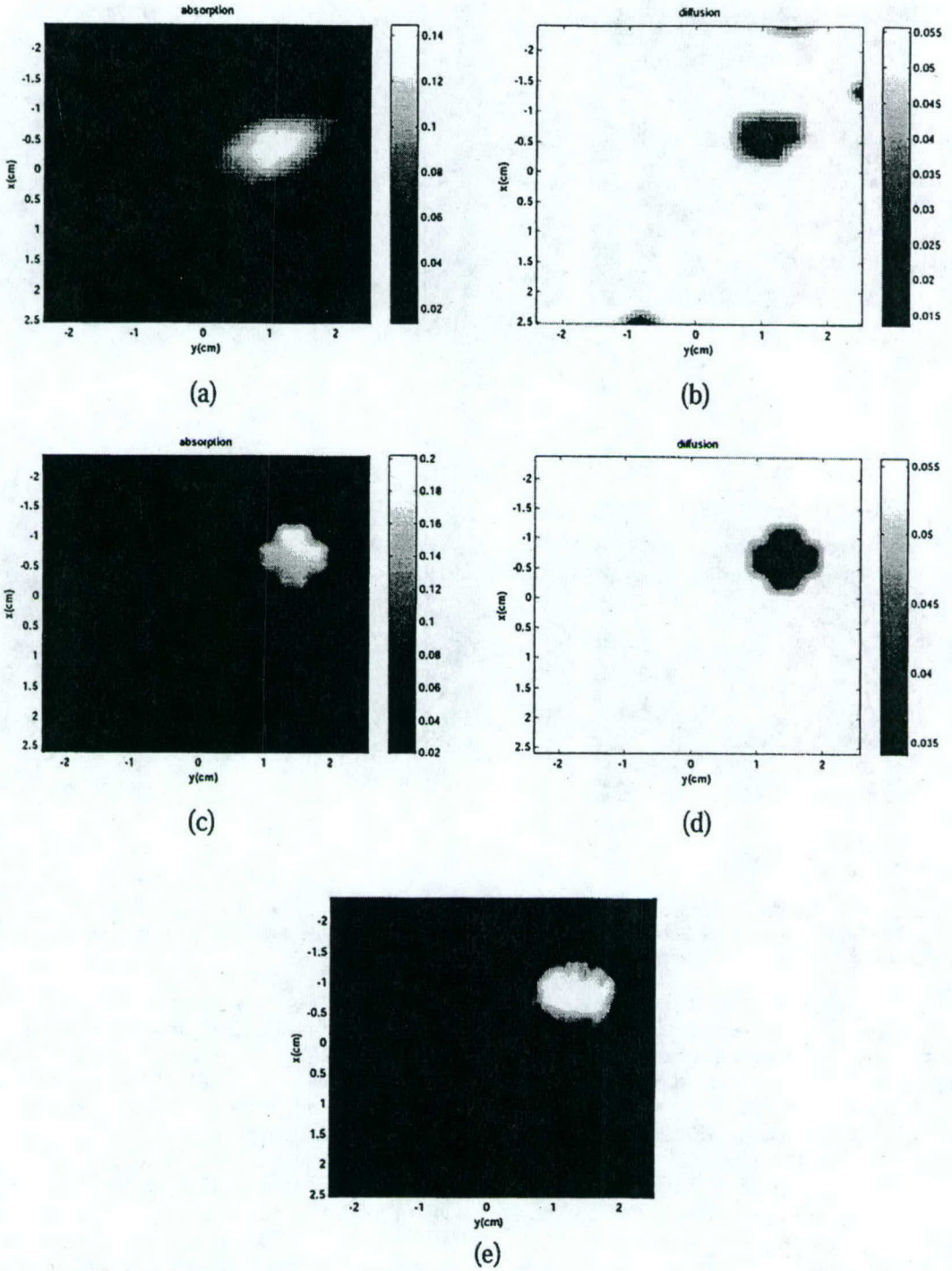

Fig. 6. Comparisons of simultaneously reconstructed absorption and diffusion coefficient maps of a high-contrast target located closer to the boundary of the turbid medium: (a), (b) reconstructed μ_a and D distributions when NIR data only are used; (c), (d), reconstructed μ_a and D distributions with ultrasound localization; (e) coregistered ultrasound C-scan image used to guide the NIR reconstruction.

values less than the threshold were identified as a nontarget region. The inverse reconstruction was localized to the target region. With ultrasound the mean reconstructed absorption coefficient was improved from 32.4% to 64.4% of the calibrated mean value and the FWHM was improved from 140% to 100% of the true target size. The mean value was calculated from the pixels with absorption coefficients greater than the FWHM in the target mass region. As for the diffusion coefficient the mean reconstructed values were within 5% of the calibrated value both with and without ultrasound localization.

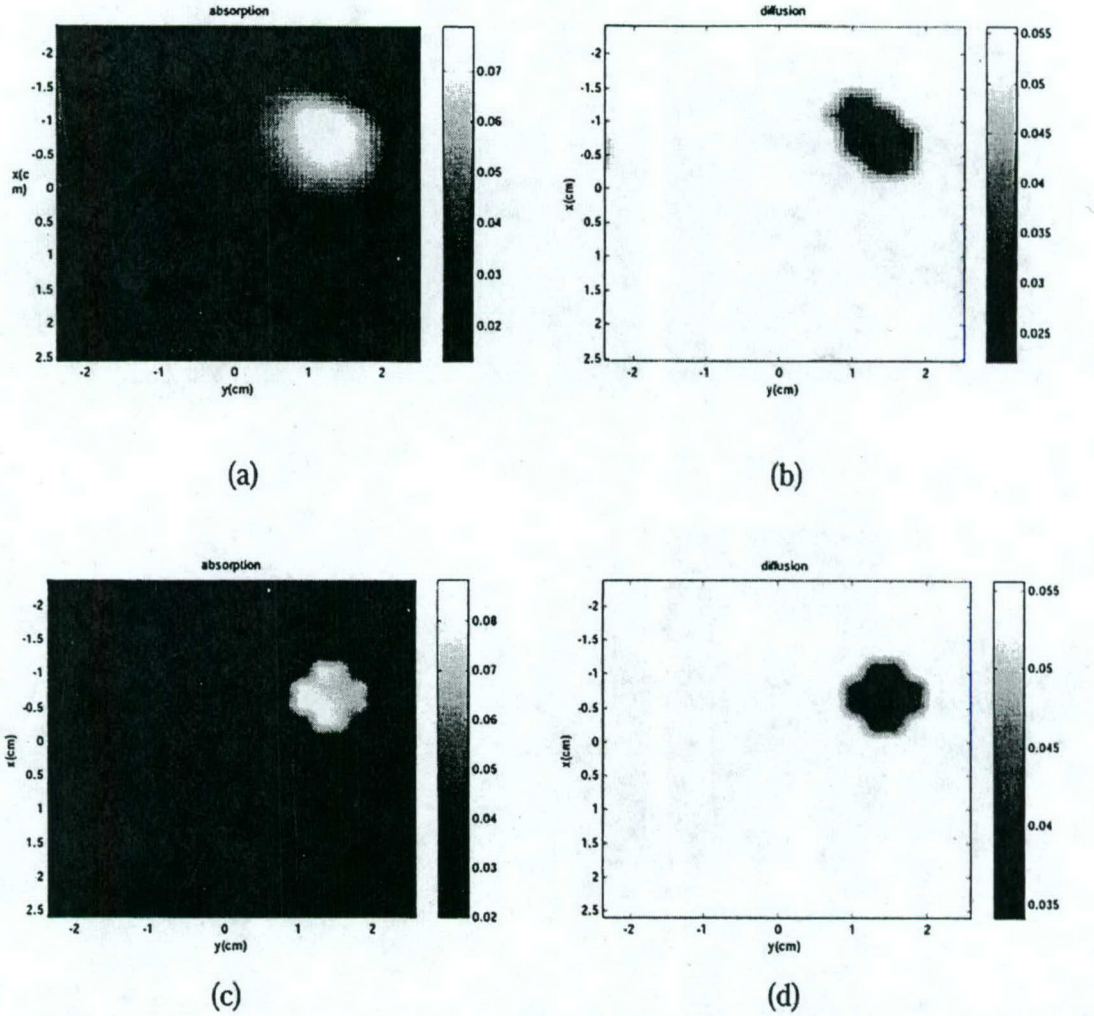

Fig. 7. Comparisons of simultaneously reconstructed absorption and diffusion coefficient maps of a low-contrast target located closer to the boundary: (a), (b) simultaneously reconstructed μ_a and D distributions when NIR data only are used; (c), (d), simultaneously reconstructed μ_a and D distributions with ultrasound localization.

However, the edge artifacts seen in Fig. 5(b) were eliminated by using ultrasound guidance.

Figure 6 shows the experimental results of the same high-contrast target located close to the boundary. Figure 6(a) is the μ_a distribution reconstructed by using NIR data only. The reconstructed mean absorption coefficient was ~45.2% of the calibrated mean value, and the FWHM was around 1.3 cm, which was 130% of the true target size. Figure 6(b) is the D distribution simultaneously reconstructed with the μ_a map by using NIR data only. Artifacts in the boundary of D distribution are visible. The reconstructed mean value was ~65.2% of the calibrated value, and the FWHM was around 1.2 cm. Figures 6(c) and 6(d) are the simultaneously reconstructed μ_a and D distributions with coregistered ultrasound localization. Figure 6(e) is the coregistered C-scan ultrasound image obtained in the source–detector plane. With ultrasound localization the mean μ_a was improved to 65.2% of the calibrated mean value and the FWHM was improved to 1 cm. The mean D was improved to 102% of the calibrated value. Artifacts in the D distribution were eliminated with ultrasound localization.

Figure 7 shows the experimental results of the low-contrast target located close to the boundary. Figure 7(a) is the μ_a distribution reconstructed by using NIR data only. The reconstructed mean absorption coefficient was ~93% of the calibrated value, and the FWHM was around 1.3 cm. Figure 7(b) is the D distribution simultaneously reconstructed with the μ_a map by using NIR data only. The reconstructed mean value was ~81% of the calibrated value, and the FWHM was around 1.2 cm. Figures 7(c) and 7(d) are the simultaneously reconstructed μ_a and D distributions with coregistered ultrasound localization. With ultrasound localization the mean μ_a was within 11% of the calibrated value and the FWHM was improved to 1 cm. The mean D was improved to

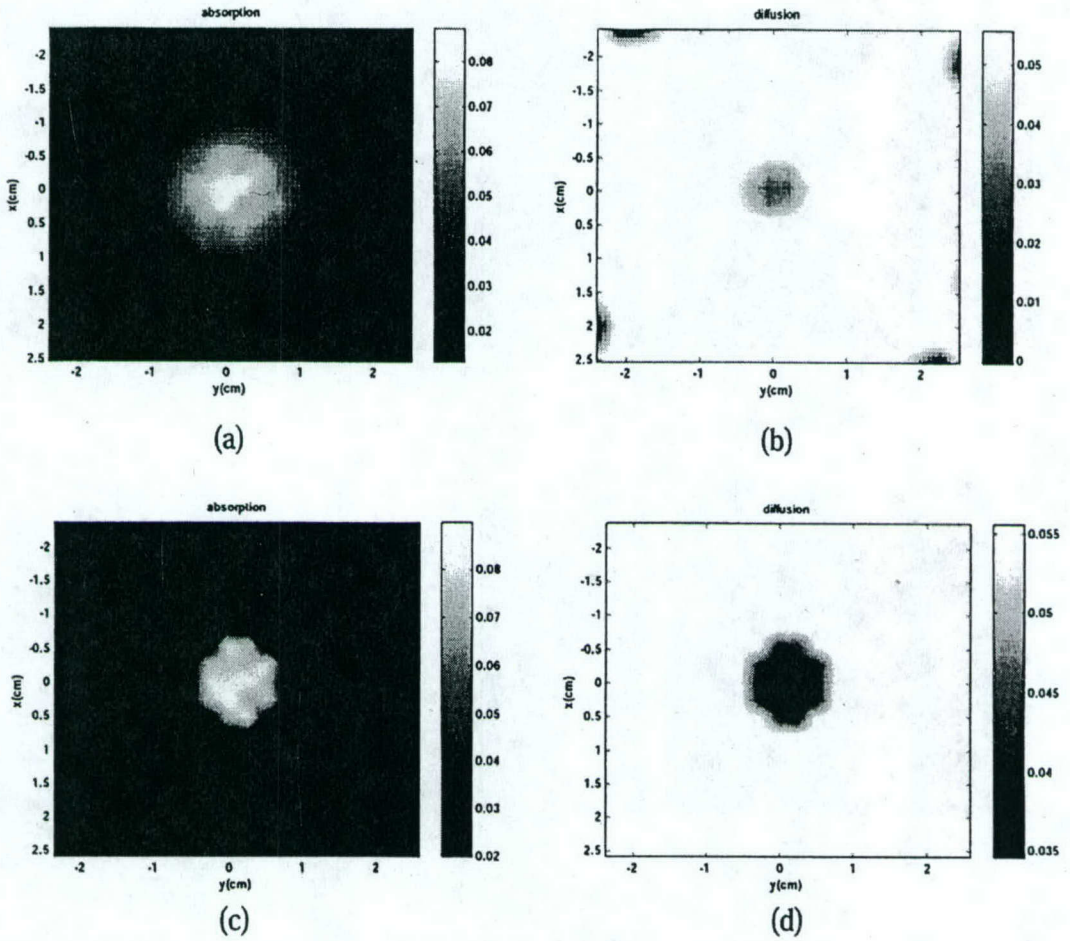

Fig. 8. Comparisons of simultaneously reconstructed absorption and diffusion maps of the same low-contrast target located at the center of the turbid medium: (a), (b), reconstructed μ_a and D distributions when NIR data only are used; (c), (d), reconstructed μ_a and D distributions with ultrasound localization.

102% of the calibrated value. The edge artifacts seen in the D distribution were eliminated with ultrasound localization.

Figure 8(a) and 8(b) show the simultaneously reconstructed μ_a and D distributions of the same low-contrast target located at the center. As one can see the spatial distributions of μ_a and D are worse than those shown in Figs. 7(a) and 7(b). Artifacts in the boundary of the D distribution are visible. The reconstructed mean μ_a was ~94% of the calibrated value, and the reconstructed mean D was ~92% of the calibrated value. Figures 8(c) and 8(d) are the simultaneously reconstructed absorption and diffusion coefficient maps with ultrasound localization. The reconstructed mean μ_a is within 13% of the calibrated value and the reconstructed mean D is within 6% of the calibrated value. The FWHM of the μ_a map has been improved by 30%,

Table 1. Experimental Results from the Frequency-Domain System

		NIR Only		NIR + US		Calibrated Value from Dartmouth College	
Target Location	Target Contrast	Mean μ_a (cm^{-1})	Mean D (cm)	Mean μ_a (cm^{-1})	Mean D (cm)	Mean μ_a (cm^{-1})	Mean D (cm)
Close to the boundary	High contrast	0.113 (45.2%[a])	0.030 (87%)	0.163 (65.2%[a])	0.0355 (102%)	0.2–0.3	0.0347 ± 5%
	Low contrast	0.065 (93%)	0.028 (81%)	0.078 (111%)	0.0355 (102%)	0.07 ± 5%	0.0347 ± 5%
At the center	High contrast	0.081 (32.4%[a])	0.0353 (101%)	0.161 (64.4%[a])	0.0363 (105%)	0.2–0.3	0.0347 ± 5%
	Low contrast	0.067 (94%)	0.032 (92%)	0.0793 (113%)	0.037 (106%)	0.07 ± 5%	0.0347 ± 5%

[a]The percentage is calculated based on the mean value of 0.2–0.3 cm^{-1}.
US, ultrasound

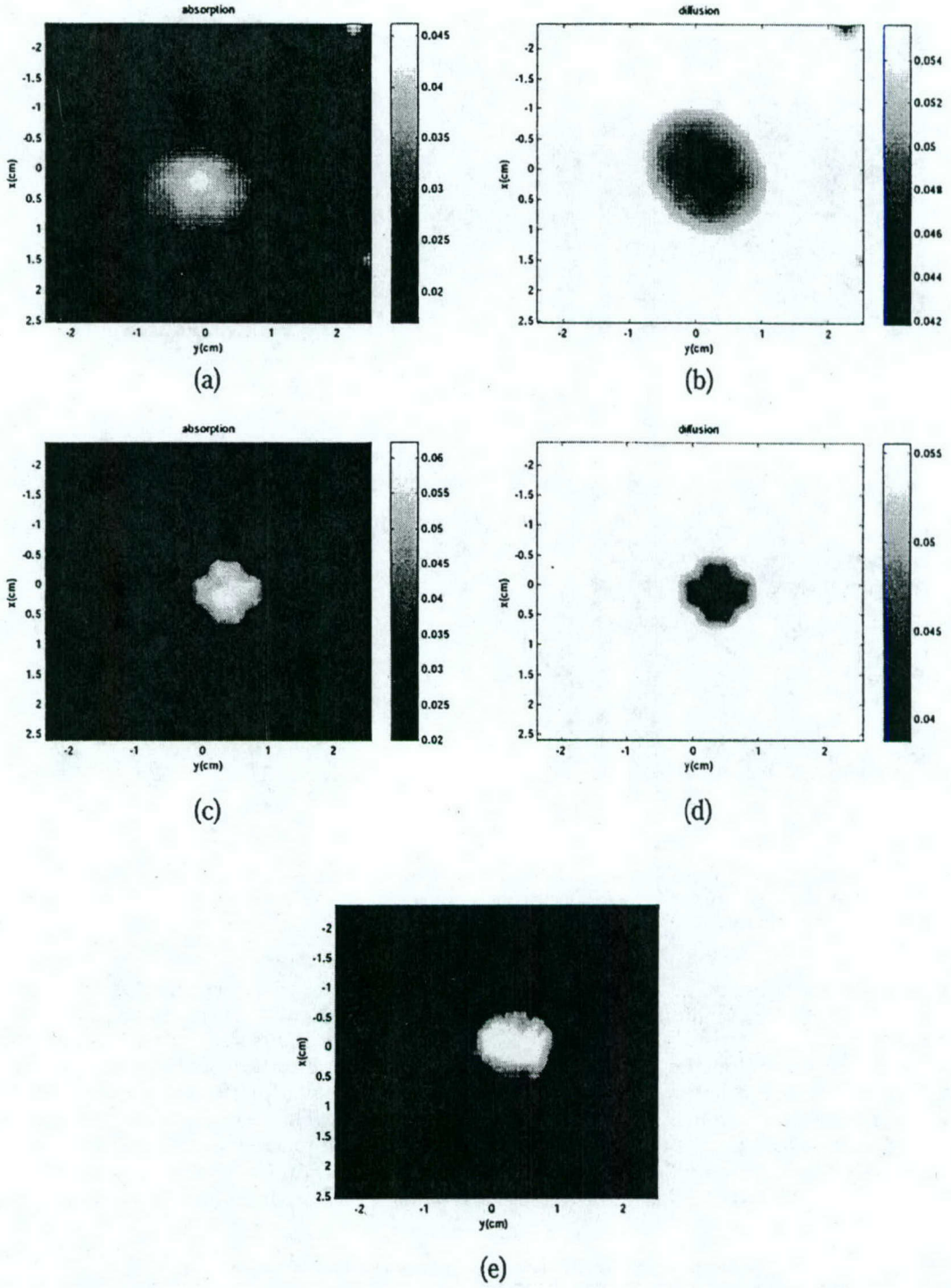

Fig. 9. Comparisons of simultaneously reconstructed absorption and diffusion maps of a high-contrast target located at the center of the medium. The dc system of the configuration in Fig. 4(b) was used for the experiments: (a), (b), reconstructed μ_a and D distributions when NIR data only are used; (c), (d), reconstructed μ_a and D distributions with ultrasound localization; (e) coregistered C-scan ultrasound image used to guide the NIR reconstruction.

and artifacts in the D distribution have been eliminated.

In Table 1 are summaries of the experimental results of the two cases in which the target was located at different positions. In general, when the target was located at the center, the results with NIR data only were poorer than those when the target was located closer to the boundary. With ultrasound lo-

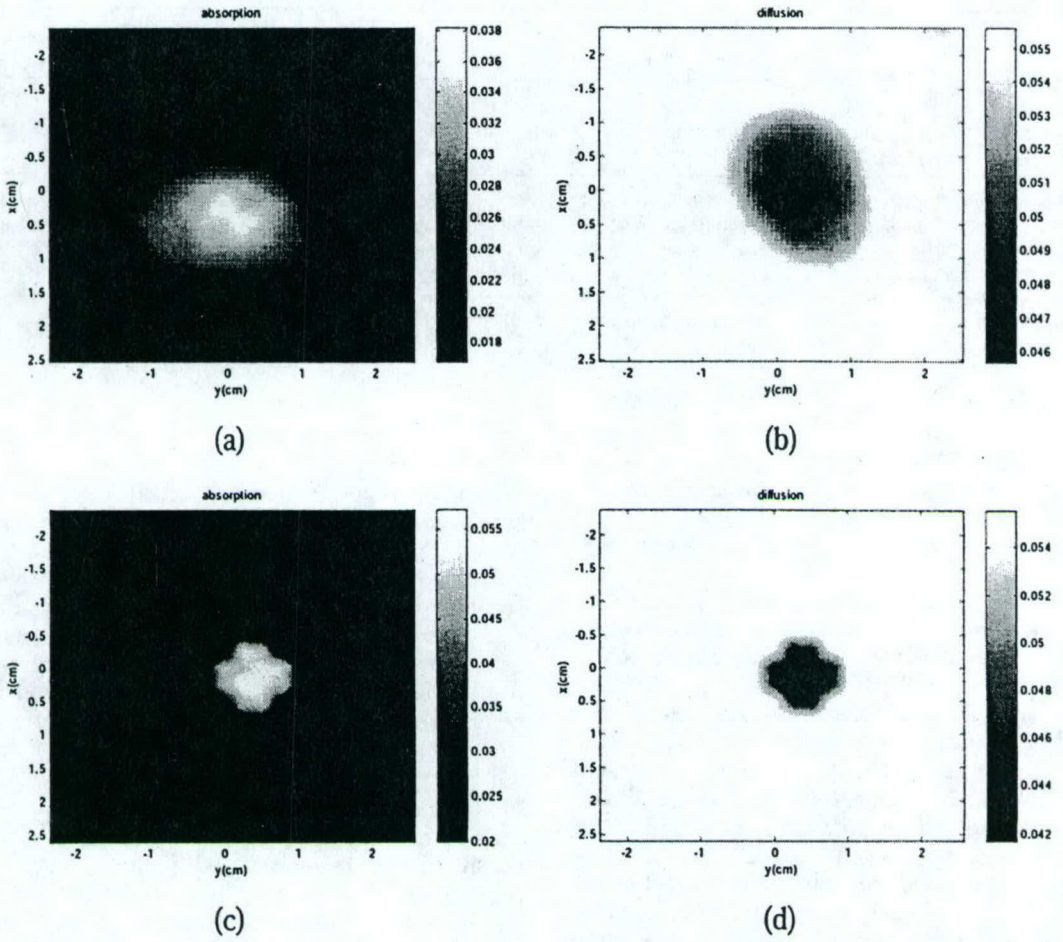

Fig. 10. Comparisons of simultaneously reconstructed absorption and diffusion coefficient maps of a low-contrast target located at the center of the medium: (a), (b), reconstructed μ_a and D distributions, respectively, when NIR data only are used; (c) (d), reconstructed μ_a and D distributions, respectively, with ultrasound localization.

calization, improvements in terms of spatial distributions were higher than those when the target was located at the boundary.

B. Reconstruction when the Direct-Current System is Used

Figures 9(a) and 9(b) show the simultaneously reconstructed μ_a and D distributions of the high-contrast target located at the center. The reconstructed mean μ_a was only 15.6% of the calibrated value, and the reconstructed mean D was ~132% of the calibrated value. Figures 9(c) and 9(d) are the simultaneously reconstructed absorption and diffusion maps with ultrasound localization. Figure 9(e) shows the C-scan ultrasound image obtained at the source–detector plane and used for the localization. The reconstructed mean μ_a has been improved to 22% of the calibrated value and the reconstructed mean D has been improved to 121% of the calibrated value. The FWHM's of μ_a and the D maps have been improved by 50% and 30%, respectively.

Figure 10 shows the experimental results of the low-contrast target located at the center of the medium. Figure 10(a) is the μ_a distribution reconstructed by using NIR data only. The spatial distribution of μ_a is much worse than the high-contrast case. The reconstructed mean absorption coefficient is only 47% of the calibrated value, and the FWHM is around 1.6 cm. Figure 10(b) shows the D distribution simultaneously reconstructed with μ_a by using NIR data only. The reconstructed mean value was ~140% of the calibrated value, and the FWHM was around 1.4 cm. Figures 8(c) and 8(d) are the simultaneously reconstructed μ_a and D distributions with coregistered ultrasound localization. With ultrasound localization the accuracy of reconstructed mean μ_a was improved to 73% of the calibrated value, and the FWHM was improved to 1 cm, while the accuracy of reconstructed mean D was 126% of the calibrated value and the FWHM was improved by 40%.

In Table 2 are summaries of the experimental results of high- and low-contrast cases when the target is located at different positions. Generally the reconstructed absorption coefficients are much lower than those obtained from the frequency-domain sys-

Table 2. Experimental Results from the dc System

Target Location	Target Contrast	NIR Only: Mean Mua (cm^{-1})	NIR Only: Mean D (cm)	NIR + US: Mean Mua (cm^{-1})	NIR + US: Mean D (cm)	Calibrated Value from Dartmouth College: Mean Mua (cm^{-1})	Calibrated Value from Dartmouth College: Mean D (cm)
Close to the boundary	High contrast	0.0485 (19.4%[a])	0.043 (123%)	0.059 (23.6%[a])	0.043 (123%)	0.2–0.3	0.0347 ± 5%
	Low contrast	0.047 (67%)	0.044 (126%)	0.049 (70%)	0.046 (132%)	0.07 ± 5%	0.0347 ± 5%
At the center	High contrast	0.039 (15.6%[a])	0.046 (132%)	0.055 (22%[a])	0.042 (121%)	0.2–0.3	0.0347 ± 5%
	Low contrast	0.0328 (47%)	0.0486 (140%)	0.051 (73%)	0.044 (126%)	0.07 ± 5%	0.0347 ± 5%

[a]The percentage is calculated on the basis of the mean value of 0.2–0.3 cm^{-1}.
US, ultrasound

tem, and the reconstructed diffusion coefficients are much higher than those from the frequency domain. The improvements with ultrasound localization are much less than that obtained from the frequency-domain system.

Comparing the results from frequency-domain and dc systems, we find that the reconstructed results from the frequency-domain system are much better in terms of accuracy. With ultrasound localization the mean absorption coefficients obtained from the frequency-domain data are approximately 111–113% of the calibrated value for the low-contrast target and around 64–65% of the calibrated mean value for the high-contrast target, while they are only 70–73% and 22–23.6% for the same cases in dc. The mean diffusion coefficients obtained from the frequency-domain data are within 102–108% of the calibrated value, while they are approximately 121–132% for the same cases in the dc. The FWHMs obtained from the frequency-domain reconstructions are always within 90–130% of the calibrated value, while the FWHMs are approximately 110–160% for the same cases in the dc.

6. Discussion

The reconstructed absorption and scattering distributions can be partially improved by iteratively updating the Jacobian matrix to account for higher-order terms of the weight matrix. However, this procedure is time-consuming and prohibits near-real-time NIR image processing. The iterative updating of a localized Jacobian matrix within the ultrasound specified region could further improve the accuracy of reconstructed absorption and diffusion coefficients with reduced computation load. Currently we are pursuing this research, and results will be reported in the near future.

In the reported phantom studies we assume that the lesions are isolated and embedded in a homogeneous background. Therefore we localize the image reconstruction by using the target geometry obtained from ultrasound. In the clinical breast-imaging cases the background tissues also scatter and absorb the diffusive light, which are also accounted for in the dual-mesh reconstruction scheme reported in Ref. 20.

7. Summary

We have reported experimental results from the simultaneous reconstruction of absorption and scattering maps with ultrasound localization. Transmission geometry was used for NIR-imaging reconstruction, and standard pulse-echo ultrasound was used for obtaining coregistered ultrasound images. When a frequency-domain system was used the ultrasound localization results showed that the reconstructed mean absorption coefficients of high-contrast phantom targets improved more than 20%, while improvements to the reconstructed mean diffusion coefficients were moderate. For low-contrast targets no significant improvement has been shown in the mean reconstructed values. However, improvements in the target spatial distributions are significant. When a dc system was used, improvements in using ultrasound localization were small in terms of mean reconstructed values. Owing to the lack of phase information and possible cross talk between absorption and scattering coefficients, the dc system performance is much worse than that of the frequency-domain system. With ultrasound localization the reconstruction speed has improved by a factor of 10 and near-real-time optical imaging becomes feasible.

We acknowledge graduate students Shikui Yan and Daqing Piao for continuous help on the software development of the dc system and the mechanical setup of the experimental system. The authors thank Shudong Jiang, Research Associate of Dartmouth College, for help in making the testing phantoms. The authors thank the following for funding support: Donaghue Foundation, U.S. Department of Defense, Army Breast Cancer Program (DAMD17-00-1-0217, DAMD17-01-1-0216), and the National Institutes of Health (1R01CA94044-01A1). The authors greatly appreciate the donation of a prototype dc system by Multi-Dimensional Technology Inc. The dc system used was modified from the prototype.

References

1. B. Tromberg, N. Shah, R. Lanning, A. Cerussi, J. Espinoza, T. Pham, L. Svaasand, and J. Butler, "Noninvasive *in vivo* char-

acterization of breast tumors using photon migration spectroscopy," Neoplasia **2**(1:2), 26–40 (2000).
2. J. B. Fishkin, O. Coquoz, E. R. Anderson, M. Brenner, and B. J. Tromberg, "Frequency-domain photon migration measurements of normal and malignant tissue optical properties in human subject," Appl. Opt. **36,** 10–20 (1997).
3. S. Fantini, S. Walker, M. Franceschini, M. Kaschke, P. Schlag, and K. Moesta, "Assessment of the size, position, and optical properties of breast tumors *in vivo* by noninvasive optical methods," Appl. Opt. **37,** 1982–1989 (1998).
4. R. M. Danen, Y. Wang, X. D. Li, W. S. Thayer, and A. G. Yodh, "Regional imager for low-resolution functional imaging of the brain with diffusing near-infrared light," Photochem. Photobiol. **67,** 33–40 (1998).
5. B. Pogue, S. P. Poplack, T. O. McBride, W. A. Wells, K. S. Osterman, U. Osterberg, and K. D. Paulsen, "Quantitative hemoglobin tomography with diffuse near-infrared spectroscopy: pilot results in the breast," Radiology **218,** 261–266 (2001).
6. B. Chance, J. Glickson, R. Weissleder, C. Tung, D. Blessington, and L. Zhou, "High sensitivity and specificity in human breast cancer detection with near-infrared imaging," in *Digest of Topical Meeting* on *Biomedical Optical Spectroscopy and Diagnostics* (Optical Society of America, Washington, D.C., 2002), pp. 450–455.
7. E. M. Sevick, G. Lopez, J. S. Reynolds, T. L. Troy, and C. L. Hutchinson, "Fluorescence and absorption contrast mechanism for biomedical optical imaging using frequency-domain techniques," Photochem. Photobiol. **66,** 55–64 (1997).
8. H. Liu, Y. Song, K. L. Worden, X. Jiang, A. Constantinescu, and R. P. Mason, "Noninvasive investigation of blood oxygenation dynamics of tumors by near-infrared spectroscopy," Appl. Opt. **39,** 5231–5243 (2000).
9. D. A. Boas, D. H. Brooks, E. L. Miller, C. A. DiMarzio, M. Kilmer, R. J. Gaudette, and Q. Zhang, "Imaging the body with diffuse optical tomography," IEEE Signal Process. Mag. **18,** 57–75 (2001).
10. X. Li, T. Durduran, A. Yodh, B. Chance, and D. N. Pattanayak, "Diffraction tomography for biomedical imaging with diffuse-photon density waves," Opt. Lett. **22,** 573–575 (1998).
11. Y. Yao, Y. Wang, Y. Pei, W. Zhu, and R. L. Barbour, "Frequency-domain optical imaging of absorption and scattering distributions by a Born iterative method," J. Opt. Soc. Am. A **14,** 325–341 (1997).
12. M. A. O'Leary, "Imaging with diffuse photon density waves," Ph.D dissertation (University of Pennsylvania, Philadelphia, Pa., 1996).
13. H. Jiang, "Frequency-domain fluorescent diffusion tomography: a finite-element-based algorithm and simulations," Appl. Opt. **37,** 5337–5343 (1998).
14. K. Paulsen and H. Jiang, "Spatially varying optical property reconstruction using a finite element diffusion equation approximation," Med. Phys. **22,** 691–701 (1995).
15. S. Arridge and M. Schweiger, "Photon-measurement density functions. Part II: Finite-element-method calculations," Appl. Opt. **34,** 8026–8037 (1995).
16. Q. Zhu, T. Dunrana, M. Holboke, V. Ntziachristos, and A. Yodh, "Imager that combines near infrared diffusive light and ultrasound," Opt. Lett. **24,** 1050–1052 (1999).
17. Q. Zhu, E. Conant, and B. Chance, "Optical imaging as an adjunct to sonograph in differentiating benign from malignant breast lesions," J. Biomed. Opt. **5,** 229–236 (2000).
18. N. G. Chen, P. Y. Guo, S. K. Yan, D. Q. Piao, and Q. Zhu, "Simultaneous near-infrared diffusive light and ultrasound imaging," Appl. Opt. **40,** 6367–6380 (2001).
19. N. G. Chen and Q. Zhu, "Characterization of small absorbers inside the turbid medium," Opt. Lett. **27,** 252–254 (2002).
20. Q. Zhu, N. G. Chen, and S. Kurtzman, "Imaging tumor angiogenesis using combined near-infrared diffusive light and ultrasound," Opt. Lett. **38,** 337–339 (2003).
21. N. G. Chen and J. Bai, "Monte Carlo approach to modeling of boundary conditions for the diffusion equation," Phys. Rev. Lett. **80,** 5321–5324 (1998).
22. Y. Pei, H. L. Graber, and R. L. Barbour, "Influence of systematic errors in reference states on image quality and on the stability of derived information for dc optical imaging," Appl. Opt. **40,** 5755–5769 (2001).
23. E. M. C. Hillman, J. C. Hebden, F. E. W. Schmidt, S. R. Arridge, M. Schweiger, H. Dehghani, and D. T. Delpy, "Calibration techniques and data type extraction for time-resolved optical tomography," Rev. Sci. Instrum. **71,** 3415–3427 (2000).
24. M. Schweiger and S. R. Arridge, "Comparison of two- and three-dimensional reconstruction methods in optical tomography," Appl. Opt. **37,** 7419–7428 (1998).
25. M. Firbank, M. Oda, and D. T. Delpy, "An improved design for a stable and reproducible phantom material for use in near-infrared spectroscopy and imaging," Phys. Med. Biol. **40,** 955–961 (1995).

March 1, 2003 / Vol. 28, No. 5 / OPTICS LETTERS 337

Imaging tumor angiogenesis by use of combined near-infrared diffusive light and ultrasound

Quing Zhu and NanGuang Chen

Department of Electrical and Computer Engineering, University of Connecticut, Storrs, Connecticut 06269-2157

Scott H. Kurtzman

University of Connecticut Health Center, Farmington, Connecticut 06030

Received August 15, 2002

A novel two-step reconstruction scheme using a combined near-infrared and ultrasound technique and its utility in imaging distributions of optical absorption and hemoglobin concentration of breast lesions are demonstrated. In the first-step image reconstruction, the entire tissue volume is segmented based on initial coregistered ultrasound measurements into lesion and background regions. Reconstruction is performed by use of a finer grid for lesion region and a coarse grid for the background tissue. As a result, the total number of voxels with unknown absorption can be maintained on the same order of total measurements, and the matrix with unknown total absorption distribution is appropriately scaled for inversion. In the second step, image reconstruction is refined by optimization of lesion parameters measured from ultrasound images. It is shown that detailed distributions of wavelength-dependent absorption and hemoglobin concentration of breast carcinoma can be obtained with the new reconstruction scheme.

OCIS codes: 170.0170, 170.3010, 170.5270, 170.7170, 170.3830.

Tumor blood volume and microvascular density are parameters that are anatomically and functionally associated with tumor angiogenesis. During the past decade, modeling of light propagation in the near-infrared (NIR) region, combined with advancements of light source and detectors, has improved diffused light measurements and made possible the application of tomographic techniques for characterizing and imaging tumor angiogenesis.[1,2] However, the NIR technique has not been widely used in clinics, and the fundamental problem of intense light scattering remains. As a result, diffusive light probes a widespread region instead of providing information along a straight line, and tomographic image reconstruction is, in general, underdetermined and ill-posed. Zhu *et al.*[3] and Chen *et al.*[4] demonstrated a combined imaging technique, using *a priori* lesion structure information provided by coregistered ultrasound images to assist NIR imaging reconstruction in phantom studies.[3,4] As a result, the NIR image reconstruction is well defined and less sensitive to noise. In this Letter we report on our novel two-step image reconstruction scheme that uses the combined approach and demonstrate its utility in imaging tumor absorption and hemoglobin distributions. It is shown that detailed heterogeneous distributions of wavelength-dependent optical absorption and hemoglobin concentration of a breast carcinoma can be obtained. To the best of our knowledge, such detailed distributions have not been reported in the literature.

A picture of our combined hand-held probe used in clinical studies is shown in Fig. 1(a), and the probe dimensions and optical sensor distributions are shown in Fig. 1(b). The combined probe consists of a commercial ultrasound one-dimensional array located at the center of the probe and optical source and detector fibers distributed at the periphery and connected to the NIR imager. The NIR imager consists of 12 dual-wavelength source channels and 8 parallel receiving channels.[4] In the transmission part, 12 pairs of dual-wavelength (780- and 830-nm) laser diodes are amplitude modulated at 140 MHz. In the reception part, 8 photomultiplier tubes detect diffusely reflected light from the tissue. Both the amplitude and phase at each source–detector pair are obtained, and the resulting total number of measurements is $12 \times 8 \times 2 = 192$. The combined probe is made of a black plastic plate 10 cm in diameter; therefore, a semi-infinite boundary condition can be used for the NIR measurement geometry. The amplitude and phase measured from the normal side of the breast are used to calculate the background absorption $\overline{\mu}_a$ and reduced scattering coefficient $\overline{\mu}_s'$.[4] In our two-step image reconstruction, we first segment tissue volume into two regions, L and B, that contain a lesion as measured from coregistered ultrasound images and background tissue, respectively. We use the Born approximation to

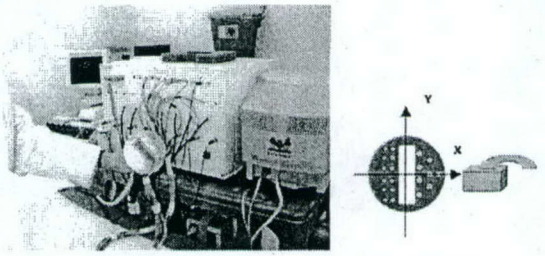

Fig. 1. (a) Hand-held combined probe and a frequency-domain NIR imager. (b) Sensor distribution of the combined probe (diameter, 10 cm). The smaller circles are optical source fibers, and the bigger circles are detector fibers. A commercial ultrasound probe is located at the center and its dimensions are 5.6 cm by 1 cm.

0146-9592/03/050337-03$15.00/0

relate the scattered field $U_{sc}'(r_{si}, r_{di}, \omega)$ measured at source–detector pair i to absorption variations $\Delta\mu_a(r')$ in each volume element of two regions within the sample, where r_{si} and r_{di} are the source and detector positions, respectively. We then discretize the lesion volume and the background volume with different voxel sizes (a finer grid for lesion volume and a coarse grid for background). The scattered field can then be approximated as

$$U_{sc}'(r_{si}, r_{di}, \omega) \approx -\frac{1}{\overline{D}} \times \left[\sum_{Lj} G(r_{vj}, r_{di}) U_{inc}(r_{vj}, r_{si}) \int_j \Delta\mu_a(r')\mathrm{d}^3r' + \sum_{B_k} G(r_{vk}, r_{di}) U_{inc}(r_{vk}, r_{si}) \int_k \Delta\mu_a(r')\mathrm{d}^3r'\right], \quad (1)$$

where r_{vj} and r_{vk} are the centers of voxels j and k in lesion volume L and background volume B, respectively[2], and $U_{inc}(r', r_{si})$ and $G(r', r_{di})$ are the incident wave and the Green function of the semi-infinite geometry, respectively. The matrix form of relation (1) is given as

$$[U_{sd}]_{MX1} = [W_L, W_B]_{MXN}[M_L, M_B]^T, \quad (2)$$

where $W_L = [-1/D G(r_{vj}, r_{di}) U_{inc}(r_{vj}, r_{si})]_{M\times N_L}$ and $W_B = [-1/D G(r_{vk}, r_{di}) U_{inc}(r_{vk}, r_{si})]_{M\times N_B}$ are weight matrices for the lesion volume and the background volume, respectively; $[M_L] = [\int_{1_L} \Delta\mu_a(r')\mathrm{d}^3r, \ldots \int_{N_L} \Delta\mu_a(r')\mathrm{d}^3r']$ and $[M_B] = [\int_{1_B} \Delta\mu_a(r')\mathrm{d}^3r', \ldots \int_{N_B} \Delta\mu_a(r')\mathrm{d}^3r']$ are the total absorption distributions of the lesion volume and the background volume, respectively.

Instead of reconstructing the $\Delta\mu_a$ distribution directly as the standard Born approximation, we reconstruct total absorption distribution M and then divide the total by different voxel sizes of lesion and background tissue to obtain $\Delta\mu_a$ distribution. By choosing a finer grid for the lesion and a coarse grid for the background tissue, we can maintain the total number of voxels with unknown absorption on the same scale of the total measurements. As a result, the inverse problem is less underdetermined and ill-posed. In addition, since the lesion absorption coefficient is higher than that of the background tissue, in general, the total absorption of the lesion over a smaller voxel is on the same scale of total absorption of the background over a bigger voxel, and therefore the matrix $[M_L, M_B]$ is appropriately scaled for inversion. The reconstruction is formulated as a least-squares problem. The unknown distribution M can be iteratively calculated with the conjugate-gradient search method.

The lesion location and volume from coregistered ultrasound is estimated as follows: Since the commercial one-dimensional ultrasound probe that we use acquires two-dimensional ultrasound images in the y–z plane (z is the propagation direction) and the two-dimensional NIR probe provides three-dimensional images, the coregistration is limited to an interception plane. However, if we approximate a lesion as an ellipsoid, we are able to estimate its center and radii from two orthogonal ultrasound images and therefore obtain the lesion volume. Three sources of error may lead to inaccurate estimation of the lesion center and radii and therefore to cause errors in reconstructed optical properties. First, the lesion boundaries may not be well defined in ultrasound images. Second, two separate orthogonal ultrasound images are used to estimate the radii and the center, and these parameters depend on the ultrasound probe position and compression of the hand-held probe. Third, the target volumes or shapes seen by different modalities may be different because of different contrast mechanisms. In the second step, we refine image reconstruction by perturbing the center c_0 and then the radii r_0 and choosing the optimal set of parameters (c_{opt}, r_{opt}).

Clinical studies were performed at the Health Center of the University of Connecticut, and the human subject protocol was approved by the Health Center IRB committee. Patients with palpable and nonpalpable masses that were visible on clinical ultrasound were used as subjects. These subjects were scanned with the combined probe, and ultrasound images and optical measurements were acquired at multiple locations, including the lesion region that was scanned at two orthogonal positions, and a normal region of the contralateral breast scanned at two orthogonal positions.

An example is given in this Letter to demonstrate the use of our reconstruction scheme. Figure 2(a) shows a gray-scale ultrasound image of a palpable lump in a 44-year-old woman. The lesion was located at the 6 to 8 o'clock position of the left breast at approximately 1.5-cm depth. Ultrasound showed an irregular poorly defined hypoechoic mass, and the lesion was considered highly suspicious for malignancy. An ultrasound guided-core needle biopsy was recommended. Biopsy results (after NIR imaging) revealed that the lesion was a high-grade *in situ* ductal carcinoma with necrosis.

Multiple optical measurements at two orthogonal positions were simultaneously made with ultrasound images at the lesion location as well as at approximately the same location of the contralateral normal breast. The fitted average tissue background measured on the normal side of the breast at both wavelengths was $\overline{\mu}_a^{780} = 0.03\ \mathrm{cm}^{-1}$, $\overline{\mu}_a^{830} = 0.05\ \mathrm{cm}^{-1}$, $\overline{\mu}_s'^{780} = 9.22\ \mathrm{cm}^{-1}$, and $\overline{\mu}_s'^{830} = 7.58\ \mathrm{cm}^{-1}$. The perturbations for both wavelengths used to calculate absorption maps were normalized as $U_{sc}'(r_{si}, r_{di}, \omega) = [U_L(r_{si}, r_{di}, \omega) - U_N(r_{si}, r_{di}, \omega)] U_B(r_{si}, r_{di}, \omega)/U_N(r_{si}, r_{di}, \omega)$, where $U_L(r_{si}, r_{di}, \omega)$ and $U_N(r_{si}, r_{di}, \omega)$ were measurements obtained from the lesion region and the contralateral normal region, respectively, and $U_B(r_{si}, r_{di}, \omega)$ was the incident field calculated with fitted background $\overline{\mu}_a$ and $\overline{D} = 1/3\overline{\mu_s'}$. This procedure cancels unknown system gains associated with different sources and detectors as well as electronic channels. The initial estimates of the lesion center and diameter in two orthogonal ultrasound images were $(0, 0.39\ \mathrm{cm}, 1.7\ \mathrm{cm})$ and $3.44\ \mathrm{cm} \times 4.38\ \mathrm{cm} \times 1.76\ \mathrm{cm}$, respectively. A finer grid of $0.5\ \mathrm{cm} \times 0.5\ \mathrm{cm} \times 0.5\ \mathrm{cm}$ and a coarse grid of $1.5\ \mathrm{cm} \times 1.5\ \mathrm{cm} \times 1.0\ \mathrm{cm}$ were chosen for the lesion and background tissue, respectively. The total reconstruction volume was chosen to be $9\ \mathrm{cm} \times 9\ \mathrm{cm} \times 4\ \mathrm{cm}$,

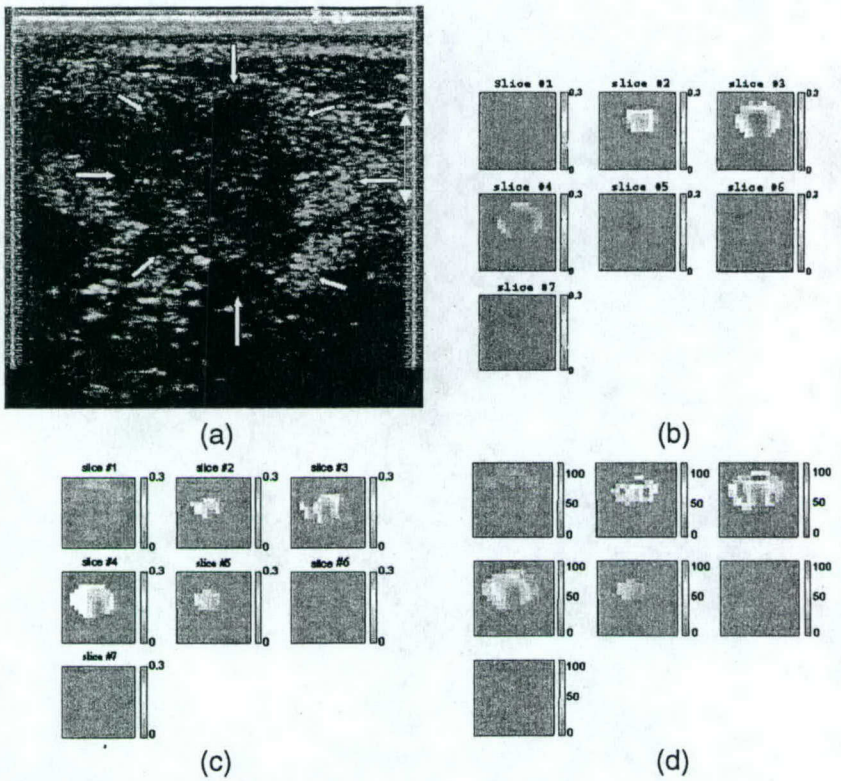

Fig. 2. (a) Gray-scale ultrasound image of a palpable lump of a 44-year-old woman. Ultrasound showed an irregular poorly defined hypoechoic mass, and the lesion was considered as highly suspicious for malignancy. Reconstructed optical absorption maps at (b) 780 nm and (c) 830 nm. The vertical color bars are the absorption coefficient [cm^{-1}]. (d) Total hemoglobin concentration map. The vertical color bars are μmol. The NIR data were simultaneously acquired with the ultrasound image shown in (a). Each image consists of seven slices obtained in 0.5-cm spacing from 0.5 to 3.5 cm in depth. The vertical and horizontal axes correspond to x and y dimensions of 9 cm by 9 cm.

and the total number of voxels with unknown optical absorption was 190, which was of the same order as the 192 total measurements. Image reconstruction was performed with the NIR data simultaneously acquired with the ultrasound image shown in Fig. 2(a). The second-step refined reconstruction revealed optimal lesion centers at approximately (−1.1 cm, 0.3 cm, 1.7 cm) for 780 nm and (−0.9 cm, −0.7 cm, 1.7 cm) for 830 nm and optimal diameters of 4.28 cm × 5.18 cm × 1.96 cm. The detailed absorption maps with high absorption nonuniformly distributed around the lesion boundaries at both wavelengths are shown in Figs. 2(b) and 2(c). By assuming that the major chromophores are oxygenated (oxyHb) and deoxygenated (deoxyHb) hemoglobin molecules in the wavelength range studied, we can estimate the distribution of total hemoglobin concentration as shown in Fig. 2(d). The measured average cancer and background total hemoglobin concentrations were 55.8 μmol and 20.7 μmol, respectively.

It is interesting to note that the absorption distributions at both wavelengths as well as the total hemoglobin concentration were distributed heterogeneously at the cancer periphery. To the best of our knowledge, such fine distributions have not been obtained by use of NIR-only reconstruction techniques. However, this finding agrees with the published literature showing that breast cancers have higher blood volumes than nonmalignant tissue because of angiogenesis, especially at the cancer periphery. In addition, the carcinoma reported here had a necrotic core, which could lead to the low absorption observed at both wavelengths in the center region.

We are grateful to Ellen Oliver, the surgical nurse at the Cancer Center of the University of Connecticut Health Center, for her help in patient scheduling. Graduate students Minming Huang and Daqing Piao are thanked for their help. The authors thank the following for their funding support: the Department of Defense (DAMD17-00-1-0217, DAMD17-01-1-0216) and the Donaghue Foundation. Q. Zhu's e-mail address is zhu@engr.uconn.edu.

References

1. B. Tromberg, N. Shah, R. Lanning, A. Cerussi, J. Espinoza, T. Pham, L. Svaasand, and J. Butler, Neoplasia **2,** 26 (2000).
2. B. Pogue, S. P. Poplack, T. O. McBride, W. A. Wells, K. S. Osterman, U. Osterberg, and K. D. Paulsen, Radiology **218,** 261 (2001).
3. Q. Zhu, T. Durduran, M. Holboke, V. Ntziachristos, and A. Yodh, Opt. Lett. **24,** 1050 (1999).
4. N. G. Chen, P. Y. Guo, S. K. Yan, D. Q. Piao, and Q. Zhu, Appl. Opt. **40,** 6367 (2001).
5. P. Vaupel, F. Kallinowski, and P. Okunieff, Cancer Res. **49,** 6449 (1989).

Dual-mesh optical tomography reconstruction method with a depth correction that uses *a priori* ultrasound information

Minming Huang and Quing Zhu

A dual-mesh reconstruction method with a depth correction for near-infrared diffused wave imaging with ultrasound localization is demonstrated by use of phantoms and clinical cancer cases. Column normalization is applied to the weight matrix obtained from the Born approximation to correct the depth-dependent problem in the reconstructed absorption maps as well as in the total hemoglobin concentration maps. With the depth correction, more uniform absorption maps for target layers at different depths are obtained from the phantoms, and the correlation between the reconstructed hemoglobin concentration maps of deeply located, large cancers and the histological microvessel density counts are dramatically improved. © 2004 Optical Society of America

OCIS codes: 100.3190, 170.3010, 170.3880, 290.1990.

1. Introduction

Optical tomography that uses near-infrared (NIR) diffusive light has huge potential for providing functional parameters for distinguishing between benign and malignant processes.[1–10] However, the intensive light scattering in soft tissues makes it very difficult to obtain accurate optical property maps with an acceptable spatial resolution. Recently, a combination of NIR imaging with other imaging modalities, such as ultrasound or magnetic resonance imaging (MRI), has shown promising results[11–16] in providing complementary contrasts and in overcoming NIR reconstruction problems. In these methods the NIR and the ultrasound or MRI probes have been deployed such that both modalities view the same tissue volume. As a result, the *a priori* lesion information, including tissue type, lesion location, and shape provided by coregistered ultrasound or MRI, can guide the NIR image reconstruction to localized target regions.

The authors are with the Department of Electrical and Computer Engineering, University of Connecticut, Storrs, Connecticut 06269. Q. Zhu's e-mail address is zhu@engr.uconn.edu.

Received 4 September 2003; revised manuscript received 5 December 2003; accepted 15 December 2003.

0003-6935/04/081654-09$15.00/0

However, perturbations of optical properties in nontarget regions could prevent the accurate reconstruction of the optical properties in target regions. Recently, we developed a novel dual-mesh method, which divides the entire imaging volume into target regions and nontarget regions based on the coregistered ultrasound images. The image reconstruction is performed by use of fine voxels for target regions and coarse voxels for nontarget regions. As a result, the total number of voxels with unknown optical properties is significantly reduced and the inversion is well defined. By using the dual-mesh method, we have obtained encouraging results from tissue biopsies taken from a group of patients.[17–19]

However, for deeply located, highly absorbing large tumors, we have found that the reconstructed absorption values and the resulting total hemoglobin concentration are highly dependent on depth (layer).[19] In other words, the reconstructed absorption coefficients of the top layer are higher than those of deeper layers. This depth-dependent reconstruction is related to the weight matrix used for image reconstruction. In our current study[17–20] a handheld probe was used to obtain NIR measurements in the reflection geometry, and the semi-infinite boundary condition was used to compute the weight matrix. The Born approximation was used to relate the unknown optical properties of the medium to the measurements, and an inversion was performed with the conjugate gradient itera-

tive searching method. According to Ref. 21, the resulting weights for the semi-infinite geometry can roughly be described by the so-called "banana function." The banana function causes the reconstructed optical properties[20] to be highly depth dependent owing to the tendency of the iterative searching method to converge along the steepest direction, i.e., the largest weight direction. As a result, even for a homogeneous target, the reconstructed absorption coefficients of the top target layers, which normally have larger weights, are higher than those of the bottom target layers, which normally have smaller weights. Therefore it is essential to scale the weight matrix according to depth before the iterative searching method is applied. In this paper we introduce a simple column normalization scheme, which can dramatically alleviate the depth-dependent problem.

2. Dual-Mesh Method with Depth Correction

The details of our dual-mesh imaging reconstruction algorithm are described in Ref. 17. Briefly, the total imaging volume is segmented into two regions, L and B, where lesion region L contains the heterogeneity measured from coregistered ultrasound images and nonlesion region B is the background. Then the target and background regions are discretized with different voxel sizes, resulting in a fine grid in the lesion region and a coarse grid in the nonlesion region. In the dual-mesh method we consider the absorption changes in the medium with the assumption that the scattering heterogeneities make a negligible contribution to the measurement. Similar procedures can be applied to reconstruct scattering coefficients.[20] From the Born approximation, the scattered field can be approximated as

$$U_{sc}'(r_{si}, r_{di}, \omega) \approx -\frac{1}{D}\left[\sum_{Lj} G(r_{vj}, r_{di})U_{inc}(r_{vj}, r_{si}) \times \int_j \Delta\mu_a(r')\mathrm{d}^3r' + \sum_{B_k} G(r_{vk}, r_{di})U_{inc}(r_{vk}, r_{si}) \times \int_k \Delta\mu_a(r')\mathrm{d}^3r'\right], \quad (1)$$

where $G(r_{vj}, r_{di})U_{inc}(r_{vj}, r_{si})$ and $G(r_{vk}, r_{di})U_{inc}(r_{vk}, r_{si})$ are weight values at the center r_{vj} of voxel j and at the center r_{vk} of voxel k in lesion volume L and in background volume B, and r_{si} and r_{di} are source and detector positions, respectively. Equation (1) can be written into the following matrix form:

$$[U_{sd}]_{M\times 1} = [W_L, W_B]_{M\times N}[M_L, M_B]_{N\times 1}^T, \quad (2)$$

where

$$W_L = \left[-\frac{1}{D} G(r_{vj}, r_{di})U_{inc}(r_{vj}, r_{si})\right]_{M\times N_L},$$

$$W_B = \left[-\frac{1}{D} G(r_{vk}, r_{di})U_{inc}(r_{vk}, r_{si})\right]_{M\times N_B},$$

$$[M_L] = \left[\int_{1_L} \Delta\mu_a(r')\mathrm{d}^3r', \ldots \int_{N_L} \Delta\mu_a(r')\mathrm{d}^3r'\right],$$

$$[M_B] = \left[\int_{1_B} \Delta\mu_a(r')\mathrm{d}^3r', \ldots \int_{N_B} \Delta\mu_a(r')\mathrm{d}^3r'\right],$$

respectively. Instead of reconstructing the $\Delta\mu_a$ distribution, we reconstruct the total absorption distribution M and then divide it by different voxel sizes of the target and the background region to obtain the $\Delta\mu_a$ distribution. In general, the target region is more absorbing than the background is, and the total absorption distribution M, which is approximately the product of $\Delta\mu_a$ times voxel size, is well scaled between the lesion region and the nonlesion region for the inversion. In the reported studies, we have used a fine grid of 0.5 cm × 0.5 cm × 0.5 cm in the target region and a coarse grid of 1.5 cm × 1.5 cm × 1.0 cm in the background region. As a result, the weight matrix $[W] = [W_L, W_B]$ expands to several discrete layers in depth, and the weight matrix W_L of larger tumors also expands to two or three layers.

However, the resulting weight matrix is not well scaled in depth. If the lesion region expands to two or three layers for larger tumors, the weights of the voxels at the top target layer are normally 1–2 times larger than those at the neighboring bottom target layer. To alleviate the depth-dependent problem, we compute a diagonal matrix G to rescale the weight matrix in different layers. For convenience, the weight matrix $W_{L,B}$ is arranged such that small voxels from the target region are followed by big voxels from the background region, and in each region voxels are grouped layer by layer from top to bottom. As a result, we have p_1 target layers and p_2 background layers. To form the diagonal matrix G, the mean absolute values of the columns of the weight matrix $W_{L,B}$ are calculated and grouped into a vector F as

$$F(j) = \frac{1}{N}\sum_j |W_{L,B}(:, j)|, \qquad j = 1, 2, \ldots N. \quad (3)$$

Then the maximum mean absolute values are obtained for each layer, and the ratios between the maximum mean absolute values of the layer p' and that of the reference layer p_0 are used to form the diagonal matrix G:

$$G_{jj} = \max[F(p')]/\max[F(p_0)], \qquad j \in p'$$
$$G_{ij} = 0, \qquad i \neq j, \qquad j = 1, 2, \ldots N, \quad (4)$$

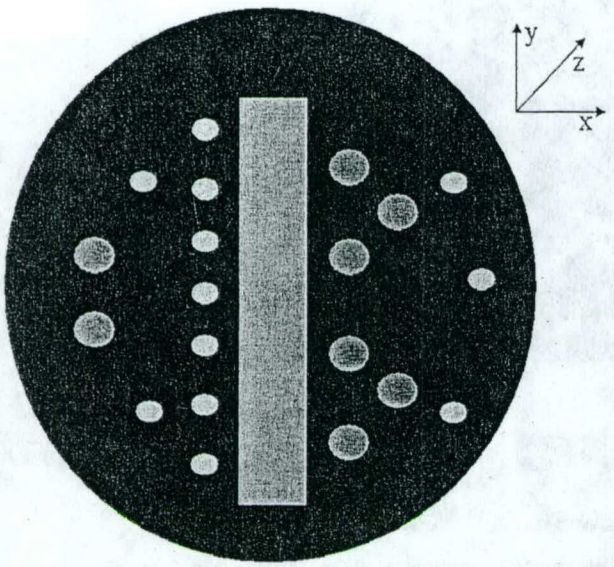

Fig. 1. Sensor distribution of the combined probe. Smaller circles are optical source fiber positions and larger circles are detector fiber positions. An ultrasound probe is located at the center of the combined probe, and the optical source and detector fibers are distributed at the periphery of the ultrasound probe.

where p' is the layer number starting from the top and p_0 is a reference layer number, which is chosen as the bottom target layer in our computation.

The rescaled weight matrix used for reconstruction can be rewritten as

$$[U_{sd}] = [W_L, W_B][G]^{-1}[G][M_L, M_B]^T = [W'][M']^T, \quad (5)$$

where $[W'] = [W_L, W_B][G]^{-1}$ is the rescaled weight matrix and $[M']^T = [G][M_L, M_B]^T$ is the rescaled total absorption distribution. The conjugate gradient method is used to minimize the object function, and the iterative search quickly converges in two or three iterations. No regularization scheme is used in the inversion. The resulting solution $[M']$ is divided by matrix G to obtain the total absorption distribution M. Because the new weight matrix is more uniform across the target layers, the iterative search procedure is less sensitive to the banana function in the target region.

3. Experimental Methods

The details of our NIR imaging system have been documented in Ref. 14. Briefly, it consists of 12 pairs of dual-wavelength sources (780 and 830 nm) and 8 detectors. The light sources are laser diodes with amplitude modulated at 140 MHz, and the detectors are photon multiplier tubes (PMTs). The sources and detectors are coupled to the combined probe through optical fibers. Shown in Fig. 1 is a schematic diagram of the combined probe, a circular plate with smaller circles representing optical source fiber positions and bigger circles denoting detector fiber positions. The rectangular hole in the middle houses the ultrasound transducer, which images the volume underneath. This one-dimensional ultrasound scanner can provide a y–z view of the targets (called a B-scan), where y is the lateral dimension and z is the propagation dimension. In the phantom experiments, the probe was mechanically translated in the x direction to acquire three-dimensional (3D) volumetric image data. Windowing the 3D data in the z direction at a particular depth provides the two-dimensional (2D) target spatial images in the x–y plane (called the C-scan). C-scans are coregistered with NIR images.[22] The probe is made of a black plastic plate and is designed to be handheld. For each source–detector pair, both the amplitude and the phase of the scattered wave at the detector are measured and are used to reconstruct the absorption coefficients of the targets. Therefore both matrices $[U_{sd}]_{M\times 1}$ and $[W_L, W_B]_{M\times N}$ in Eq. (2) are complex numbers.

To evaluate our modified dual-mesh reconstruction method, we performed a series of phantom studies. A 0.6% Intralipid solution was used as the homogeneous background. The calibrated μ_a and μ_s' are 0.0285 and 5.88 cm^{-1}, respectively, at 780 nm. Gel absorbers were suspended inside the Intralipid solution as targets.[23] Six targets with different absorption contrasts and different sizes were chosen. Among these six targets, three were cubic, which were 1 cm^3 in size, and the other three were ellipsoidal, which were approximately 4 cm × 4 cm × 2 cm. The diffusion coefficients of all absorbers were the same as that of the background. Because the reconstruction performances at 780 and 830 nm are similar, we only report the experimental results at the 780-nm wavelength for the phantom studies.

Clinical studies were performed at the University of Connecticut Health Center (UCHC). The UCHC Institutional Review Board committee approved the human subject protocol. Patients with palpable and nonpalpable masses that were visible on clinical ultrasounds and who were scheduled for biopsies were enrolled as research subjects. Two cases of deeply located, advanced cancers were used to demonstrate the improvement in the reconstructed absorption maps as well as in the total hemoglobin concentration maps.

4. Experimental Results

A. Phantom Results

The reconstructed results of a small target without and with the depth correction are compared in Fig. 2. The target is a cube approximately 1 cm in size. The expected absorption coefficient is 0.052 cm^{-1} above the background 0.0285 cm^{-1} (see Table 1, target 1). Figure 2(a) is a B-scan ultrasound image obtained simultaneously with NIR measurements, and the estimated target depth from the B-scan is ~2.0 cm. The ultrasound C-scan image was obtained by mechanical translation of the transducer in the x direction. The resulting C-scan ultrasound images show that the estimated target size is 1.1 cm × 1.1 cm × 1 cm and that its center location is at approximately (0,

(a)

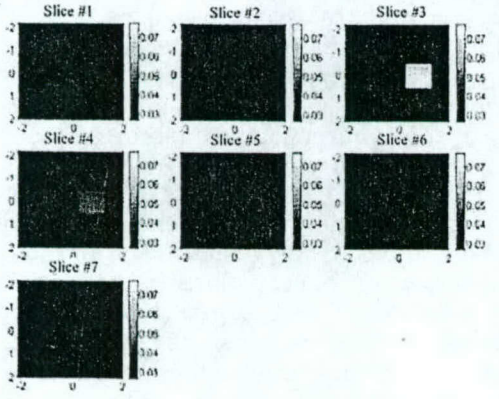

(b)

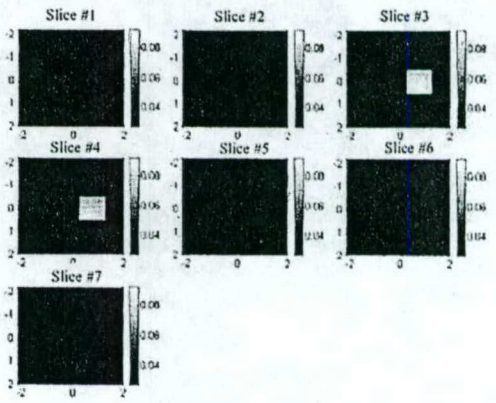

(c)

Fig. 2. Comparison of the reconstruction results of a small 1-cm^3 cubic target located at (0, −1 cm, 2 cm) inside the Intralipid. (a) B-scan ultrasound image. The dotted markers spaced 1 cm apart on the right side of the image indicate the scale in depth. (b) Optical absorption map (780 nm) obtained from the dual-mesh scheme without the depth correction. (c) Optical absorption map (780 nm) obtained from the dual-mesh scheme with the depth correction. The total imaging volume is 4 cm × 4 cm × 3.75 cm. Slice 1 is the spatial x–y image of 4 cm × 4 cm obtained at a depth of 0.75 cm in the Intralipid. Slice 7 is 3.75 cm deep within the Intralipid, and the spacing between slices is 0.5 cm. The unit for the absorption coefficient is cm^{-1}.

−1 cm, 2.0 cm). Figure 2(b) shows the reconstructed absorption maps without the depth correction. The total imaging volume is 4 cm × 4 cm × 3.75 cm. Slice 1 is the spatial x–y image of 4 cm × 4 cm obtained at a 0.75-cm depth in the Intralipid. Slice 7 is at a 3.75-cm depth in the Intralipid, and the spacing between slices is 0.5 cm. For comparison, the mean reconstructed values of different target layers are calculated by averaging the reconstructed values of the voxels within the target regions of corresponding layers, and the mean reconstructed values of the target regions are calculated by averaging the reconstructed values of the voxels within the entire target region of all the layers. The reconstructed absorption values of the top layer are quite reasonable, whereas those of the bottom layer are too small. The mean reconstructed values of two target layers are 0.0713 and 0.0412 cm^{-1} for the top and the bottom layers, respectively, and the mean reconstructed value in the whole target region is 0.0562 cm^{-1}, which is approximately 70% of the expected value. Figure 2(c) shows the reconstructed absorption maps with the depth correction. The mean reconstructed values of layers 1 and 2 in the target region have been improved to 0.085 and 0.077 cm^{-1}, respectively. Moreover, the mean reconstructed value in the whole target region is improved to 0.081 cm^{-1}, which is very close to the expected value of 0.0805 cm^{-1}.

Figure 3 shows the reconstructed results of an ellipsoidal target located at (0, 0, 2.5 cm). The target is homogeneous, and its absorption coefficient is approximately 0.22 cm^{-1} over the background 0.0285 cm^{-1}. From the resulting C-scan ultrasound images, the estimated target size is 4.2 cm × 4.2 cm × 2 cm, and the depth of the target center is ~2.5 cm. Figure 3(a) shows the reconstructed absorption maps without the depth correction. The mean reconstructed values of the four target layers are 0.203, 0.13, 0.085, and 0.062 cm^{-1} (from top to bottom; see Table 2, target 3), respectively, and the mean reconstructed value in the entire target region is 0.116 cm^{-1}, which is ~47% of the expected value of 0.2485 cm^{-1}. Figure 3(b) shows the reconstructed absorp-

Table 1. Comparison of the Reconstructed μ_a Values from Phantom Experiment without and with Depth Correction (Small Phantoms)

Target Contrast	Small Targets (1-cm^3 cube)					
	Target 1 [0, −1 cm, 2 cm]	Target 1 [0, 0, 2 cm]	Target 2 [0, −1 cm, 2 cm]	Target 2 [0, 0, 2 cm]	Target 3 [0, −1 cm, 1 cm]	Target 3 [0, 0, 1 cm]
ROI	1.2 × 1.2 × 1 cm	1.2 × 1.2 × 1 cm	1.2 × 1.2 × 1 cm	1.2 × 1.2 × 1 cm	1.2 × 1.2 × 1 cm	1.2 × 1.2 × 1 cm
Expected μ_a (cm^{-1})	0.0805	0.0805	0.18	0.18	0.103	0.103
Reconstructed* μ_a (cm^{-1})						
Without normalization	0.0713/0.0411 (0.0562)†	0.079/0.0364 (0.0577)†	0.177/0.093 (0.135)†	0.182/0.089 (0.135)†	0.104/0.108 (0.106)†	0.0924/0.0958 (0.0941)†
With normalization	0.0853/0.0771 (0.081)†	0.0773/0.0738 (0.0756)†	0.165/0.143 (0.154)†	0.14/0.134 (0.137)†	0.109/0.1 (0.105)†	0.098/0.089 (0.0935)†

ROI: Region of interest, fine mesh.
*Mean values obtained within the target region for each target layer. The mean values are calculated by averaging the reconstructed values of the voxels within the target region for the corresponding layers.
†Mean values obtained within the entire target region. The mean value is calculated by averaging the reconstructed values of the voxels within the entire target region.

Fig. 3. Comparison of the reconstruction results of a large ellipsoidal phantom target located at (0, 0, 2.5 cm) inside the Intralipid. (a) Optical absorption map (780 nm) obtained from the dual-mesh scheme without the depth correction. (b) Optical absorption map (780 nm) obtained from the modified dual-mesh scheme with the depth correction. The total imaging volume is 8 cm × 8 cm × 3.75 cm. Slice 1 is the spatial x–y image of 8 cm × 8 cm obtained at a depth of 0.75 cm in the Intralipid. Slice 7 is 3.75 cm deep within the Intralipid, and the spacing between slices is 0.5 cm. The unit for the absorption coefficient is cm^{-1}.

tion maps with the depth correction, and the reconstructed image uniformity is dramatically improved. The mean reconstructed values of the four target layers are 0.157, 0.144, 0.169, and 0.235 cm^{-1} (from top to bottom), respectively, and the mean reconstructed value in the whole target region is 0.169 cm^{-1}, which is approximately 68% of the expected value. The mean reconstructed value within the target's full width at half-maximum region is 0.206 cm^{-1}, which is approximately 83% of the expected value.

Table 2. Comparison of the Reconstructed μ_a Values from Phantom Experiment without and with Depth Correction (Big Phantoms)

	Big Targets (4 cm × 4 cm × 2 cm ellipsoidal shape)		
Target Contrast	Target 4 [0, −0.5 cm, 2.7 cm]	Target 5 [0, −0.5 cm, 2.5 cm]	Target 6 [0, 0, 2.5 cm]
ROI	4.2 × 4.2 × 2 cm	4.2 × 4.2 × 2 cm	4.2 × 4.2 × 2 cm
Expected μ_a (cm^{-1})	0.178	0.93	0.2485
Reconstructed* μ_a (cm^{-1})			
Without normalization	0.165/0.107/0.072/0.057 (0.097)†	0.101/0.068/0.0476/0.03 (0.062)†	0.203/0.13/0.085/0.062 (0.116)†
With normalization	0.165/0.130/0.127/0.119 (0.132)†	0.08/0.076/0.079/0.077 (0.079)†	0.157/0.144/0.169/0.235 (0.169)†

ROI: Region of interest, fine mesh.

*Mean values obtained within the target region for each target layer. The mean values are calculated by averaging the reconstructed values of the voxels within the target region for the corresponding layers.

†Mean values obtained within the entire target region. The mean is calculated by averaging the reconstructed values of the voxels within the entire target region.

Tables 1 and 2 summarize the experimental results of the six absorbers, three of which are 1-cm cubes and the rest are ellipsoids. Table 1 shows the comparison of the reconstructed results from three small phantoms without and with the depth correction. For targets located at approximately a 2-cm depth in the Intralipid, the improvement is obvious. Without the correction, the mean value of the top target layer can reach 88%–102% of the expected value, but the mean value of the bottom target layer is approximately 50% of the expected value. With the depth correction, both the mean value of the bottom target layers and the uniformity of the distribution improve dramatically. A comparison of the result without and with the correction shows that the difference between the mean values of the top target layer and the bottom target layer is reduced from approximately 50% to 12.2% of the expected value. For target 3 the difference between the reconstructed values obtained without the correction and those obtained with the correction is negligible due to the layer insensitivity of the banana function at that target depth.

Table 2 shows the comparison of the reconstructed results from three big phantoms without and with the depth correction. All three targets are located approximately 2.5 cm within the Intralipid solution. Without the depth correction, the mean values in the target region decrease quickly from the top layer to the bottom layer. Although the mean value of the top layer is approximately 80%–95% of the expected value, the mean value of the bottom layer reaches only 20%–35% of the expected value. With the depth correction, the mean values of the four target layers are quite uniform. Even for the highest absorber, target 6, the biggest difference between the mean reconstructed values of different layers in the target region is less than 35% of the expected value.

B. Results from Two Advanced Cancers

In Ref. 19 we reported what we believe to be the first heterogeneous hemoglobin distributions of large cancers imaged by optical tomography and also showed that the hemoglobin distributions correlate, to a large extent, with histological microvessel density counts. However, for two deeply located, highly absorbing tumors, we found that the relatively high microvessel counts obtained from posterior samples do not correlate well with the low optical absorption distribution observed in deeper slices during optical imaging. Here we show that the modified dual-mesh method dramatically improves the correlation between the

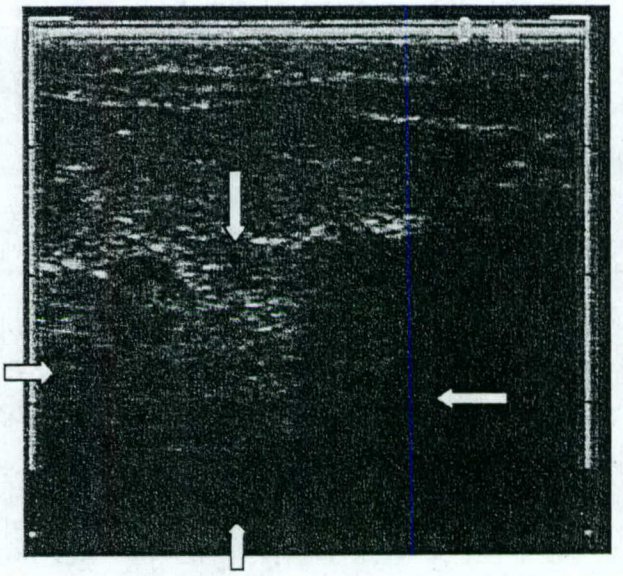

(a)

Fig. 4. (ID 23P7). (a) Ultrasound image of a 33-year-old woman with a highly suspicious breast lesion located at the twelve o'clock position and measuring 3 cm × 3 cm × 1.5 cm. The ultrasound shows the discrete nodularity of the lesion. (b) Optical absorption map (780 nm) obtained from the dual-mesh scheme without the depth correction. (c) Optical absorption map (780 nm) obtained from the modified dual-mesh scheme with the depth correction. (d) Optical absorption map (830 nm) obtained from the dual-mesh scheme without the depth correction. (e) Optical absorption map (830 nm) obtained from the modified dual-mesh scheme. (f) Total hemoglobin concentration of the lesion obtained from the dual-mesh scheme without the depth correction. (g) Total hemoglobin concentration of the lesion obtained from the modified dual-mesh scheme. The total imaging volume is 8 cm × 8 cm × 3.5 cm. Slice 1 is the spatial x–y image of 8 cm × 8 cm obtained at 0.5 cm beneath the skin. Slice 7 is 3.5 cm beneath the skin, toward the chest wall, and the spacing between slices is 0.5 cm. The unit for the absorption coefficient is cm^{-1}, and the unit for the total hemoglobin concentration is μmol/liter.

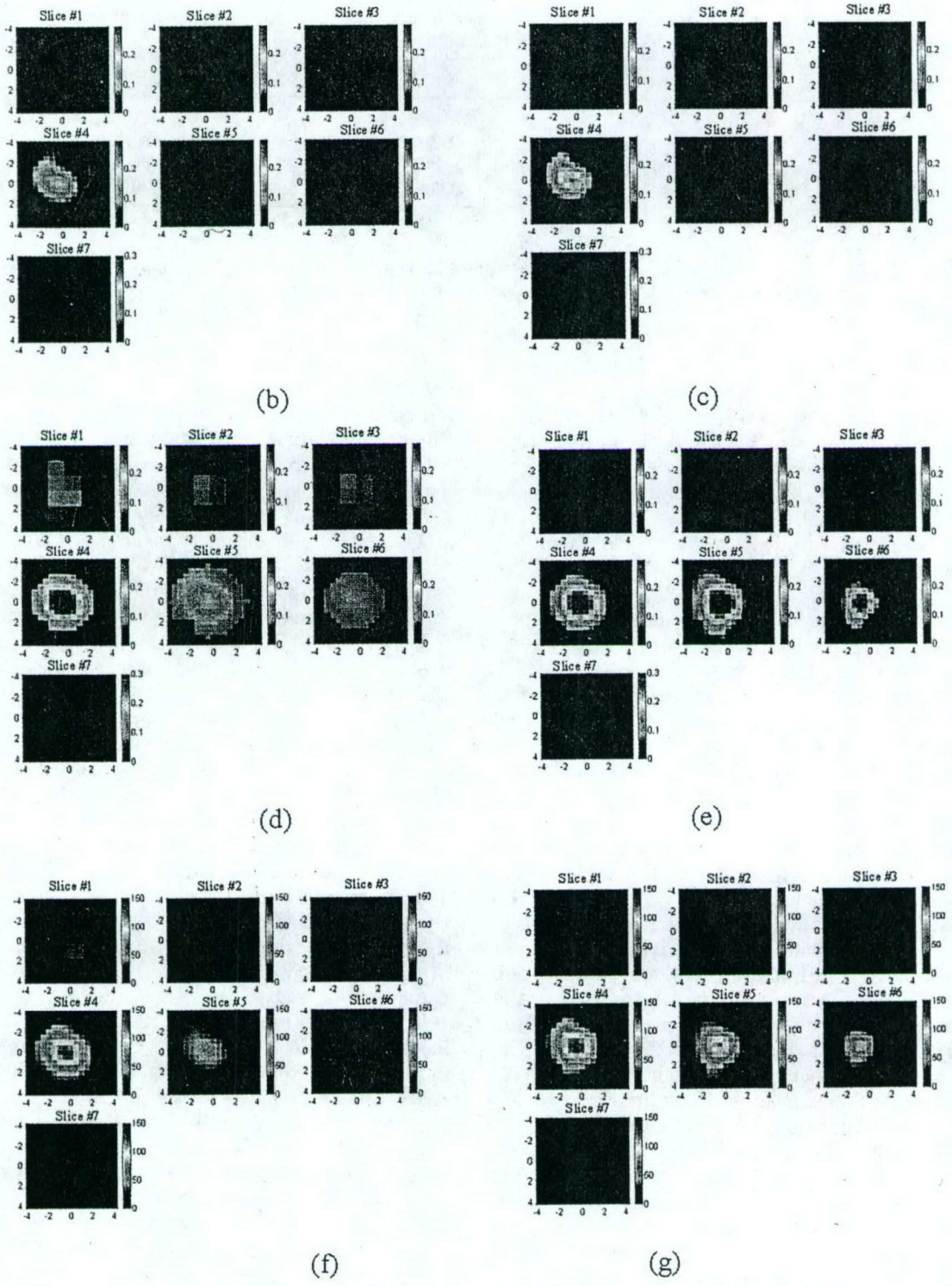

Fig. 4. (Continued)

hemoglobin distributions and the histological microvessel density counts for these two cancer cases.

The first example is a 33-year-old pregnant woman with a palpable 3 cm × 3 cm × 1.5 cm lump located at the twelve o'clock position on her left breast. The ultrasound image showed that the lesion had discrete nodularity [see Fig. 4(a)]. The center of the lump was ~2.5 cm beneath the skin surface. An ultrasound-guided core biopsy revealed that the lesion was both *in situ* and an invasive ductal carcinoma, as observed on multiple cores (histologic grade 3, nuclear grade 3). Optical absorption maps, as well as the total hemoglobin concentration distribution, were obtained without and with the depth correction. Figures 4(b) and 4(d) are the resulting optical absorption maps at 780 and 830 nm, respectively, obtained by the dual-mesh

Table 3. Comparison of the Reconstructed Results of the Two Cancer Cases without and with Depth Correction

Target Contrast	ID Number 21 (ROI: 8 × 8 × 1.3 cm)		ID Number 23 (ROI: 7 × 7 × 1.66 cm)	
	Without Norm	With Norm	Without Norm	With Norm
Reconstructed* ave. 6 dB μ_a (cm^{-1})				
780 nm	0.15/0.033/0.027	0.189/0.167/0.079	0.107/0.02/0.012	0.149/0.03/0.0135
830 nm	0.21/0.089/0.057	0.169/0.232/0.27	0.25/0.086/0.037	0.234/0.26/0.23
Reconstructed* ave. 6 dB Hb (μmol/l)	103.7/44.8/33	99.6/106.3/80.6	93.3/33/18.4	97/77.4/61.7

ID: Identification.
ROI: Region of interest, fine mesh.
*Mean values obtained within the target region for each target layer. The mean values of different target layers are calculated by averaging the reconstructed values of the voxels within the target region for corresponding layers.
Hb: Hemoglobin.

method without the depth correction, and Fig. 4(f) shows the corresponding total hemoglobin concentration. Figures 4(c) and 4(e) are the optical absorption maps of Figs. 4(b) and 4(d) with the depth correction, and Fig. 4(g) shows the resulting total hemoglobin concentration. The extinction coefficients used for calculating the oxygenated and deoxygenated hemoglobin (Hb) concentrations are $\varepsilon_{Hb}^{780} = 2.5448$, $\varepsilon_{HbO_2}^{780} = 1.6950$, $\varepsilon_{Hb}^{830} = 1.7973$, and $\varepsilon_{HbO_2}^{830} = 2.4198$ obtained from Ref. 24 in a natural logarithm scale in units of inverse millimoles times inverse centimeters. The details of the calculation can be found in Ref. 17. For each figure, slice 1 is the spatial x–y image of 8 cm × 8 cm obtained at 0.5 cm beneath the skin surface. Slice 7 is at a 3.5-cm depth, toward the chest wall, and the spacing between slices is 0.5 cm. Obviously, the uniformity of the absorption and the total hemoglobin distribution was improved with the depth correction. For quantitative comparison, the measured average absorption coefficients within 6 dB of the maximum value at two wavelengths, 780 and 830 nm, and the average total hemoglobin concentration within 6 dB of the maximum value were calculated for each target layer (see Table 3, ID number 23). For the absorption coefficient maps at 780 nm [Figs. 4(b) and 4(c)], the average values for three target layers were increased from 0.107, 0.022, and 0.0119 cm^{-1} to 0.149, 0.0296, and 0.0135 cm^{-1}, respectively. For the absorption coefficient maps at 830 nm [Figs. 4(d) and 4(e)], the average values for three target layers were increased from 0.247, 0.086, and 0.037 cm^{-1} to 0.234, 0.26, and 0.23 cm^{-1}, respectively. As a result, the average total hemoglobin concentrations for three target layers were increased from 93.3, 33, and 18.4 μmol/l to 97, 77.4, and 61.7 μmol/l, respectively. As reported in Ref. 19, the total histological microvessel counts were 60 (anterior/lateral), 88 (anterior/medial), and 152 (posterior), respectively, over 10 consecutive fields. The counts obtained from the anterior and the lateral samples correlated with the optical absorption and the total hemoglobin concentration shown in slice 3 of Figs. 4(b), 4(d), and 4(f). However, the high total counts obtained from a posterior sample did not correlate well with the low total hemoglobin distribution shown in slices 4 and 5 of Fig. 4(f), which was computed with the dual-mesh method. With the depth correction, the correlation of the high total counts with the hemoglobin concentration seen in the deeper slices 4 and 5 of Fig. 4(g) was dramatically improved.

The other example was obtained from a 53-year-old women with a palpable mass, but a normal mammogram. An ultrasound revealed an irregularly shaped lesion of 2 cm × 2 cm × 1.3 cm, and an ultrasound-guided surgical biopsy confirmed it to be an invasive and *in situ* ductal carcinoma (histological grade 2, nuclear grade 2). The lesion center was ~2.4 cm in depth relative to the skin. As in the previous case, the optical absorption maps, as well as the total hemoglobin concentration distribution, were obtained without and with the depth correction, and the measured average values within 6 dB of the maximum value for each target layer were calculated (Table 3, ID number 21). With the depth correction, the average total hemoglobin concentrations for three target layers were improved from 103.7, 44.8, and 33 μmol/l to 99.6, 106.3, and 80.6 μmol/l, respectively. The improved light absorption and hemoglobin concentration correlate well with the total number of microvessels, which were 83 (anterior), 121 (posterior/lateral), and 124 (posterior), respectively, over 10 consecutive fields, as reported in Ref. 19.

Table 3 summarizes the results of the two deeply located, large cancer cases. Similar to the phantom experimental results shown in Subsection 4.A, the reconstructed results from the modified dual-mesh method are less depth dependent. Dramatic improvement was obtained for the values at the bottom layers, with a small change in the reconstructed values at the first target layer. With the depth correction, both cases show improved correlation between the reconstructed total hemoglobin distributions and the histological microvessel density counts.

5. Discussion and Summary

The experiment results presented in Section 4 have shown that the modified dual-mesh algorithm with the depth correction alleviates the depth-dependent problem, which is related largely to the varying sensitivity with depth in a reflection geometry.[21] However, as we see from Tables 1 and 2, the reconstructed mean value in the target region can reach only 68%–75% of the expected value for large phantom targets,

which have a μ_a higher than 0.17 cm^{-1}. For large absorbers with a μ_a higher than 0.17 cm^{-1}, the reconstructed μ_a may be underestimated due to linear suppression.[25] In the reported two large cancer cases, the reconstructed μ_a values are higher than 0.17 cm^{-1}, which might be beyond the linear range. Fortunately, the tumor sizes are not as large as those of the bigger phantoms; therefore, the accuracy of the reconstructed absorption coefficients should be better than 68%–75%. Nonlinear forward models, such as the finite-element method, may avoid this problem by updating the weight matrix with the trade-off of increased computation time. We are currently pursuing investigations along these lines.

In conclusion, the dual-mesh algorithm with a depth correction can significantly improve the reconstructed absorption distributions in deeper-target layers. The experimental results of phantoms have shown that the reconstructed absorption maps are more uniform for phantom targets. The clinical results of two deeply located, large cancers have shown improved correlation between the reconstructed total hemoglobin concentrations and the histological microvessel density counts.

Scott Kurtzman and Poornima Hegde are thanked for their clinical consultations and microvessel density counting. NanGuang Chen, Daqing Piao, and graduate students Puyun Guo and Shikui Yan are acknowledged for their continuous help on NIR system and probe modifications. We thank the following funding agents for their support: U.S. Department of Defense Army Breast Cancer Program (DAMD17-00-1-0217, DAMD17-03-1-0690), Donaghue Foundation, and the National Institutes of Health (8R01EB002136-02).

References

1. B. Tromberg, N. Shah, R. Lanning, A. Cerussi, J. Espinoza, T. Pham, L. Svaasand, and J. Butler, "Non-invasive *in vivo* characterization of breast tumors using photon migration spectroscopy," Neoplasia **2,** 26–40 (2000).
2. R. M. Danen, Y. Wang, X. D. Li, W. S. Thayer, and A. G. Yodh, "Regional imager for low resolution functional imaging of the brain with diffusing near-infrared light," Photochem. Photobiol. **67,** 33–40 (1998).
3. M. A. Franceschini, K. T. Moesta, S. Fantini, G. Gaida, E. Gratton, H. Jess, M. Seeber, P. M. Schlag, and M. Kashke, "Frequency-domain techniques enhance optical mammography: initial clinical results," Proc. Natl. Acad. Sci. USA **94,** 6468–6473 (1997).
4. X. Li, T. Durduran, A. Yodh, B. Chance, and D. N. Pattanayak, "Diffraction tomography for biomedical imaging with diffuse-photon density waves," Opt. Lett. **22,** 573–575 (1998).
5. C. Matson and H. Liu, "Analysis of the forward problem with diffuse photon density waves in turbid media by use of a diffraction tomography model," J. Opt. Soc. Am. A **16,** 455–466 (1999).
6. K. Paulsen and H. Jiang, "Spatially varing optical property reconstruction using a finite element diffusion equation approximation," Med. Phys. **22,** 691–701 (1995).
7. S. Arridge and M. Schweiger, "Photon-measurement density functions, Part I: Analytical forms," Appl. Opt. **34,** 7395–7409 (1995).
8. S. Arridge and M. Schweiger, "Photon-measurement density functions, Part II: Finite-element-method calculations," Appl. Opt. **34,** 8026–8037 (1995).
9. H. Jiang, K. Paulsen, U. Osterberg, B. Pogue, and M. Patterson, "Optical image reconstruction using frequency-domain data: simulations and experiments," J. Opt. Soc. Am. A **2,** 253–266 (1995).
10. Y. Yao, Y. Wang, Y. Pei, W. Zhu, and R. L. Barbour, "Frequency-domain optical imaging of absorption and scattering distributions by a Born iterative method," J. Opt. Soc. Am. A **14,** 325–341 (1997).
11. Q. Zhu, T. Durduran, M. Holboke, V. Ntziachristos, and A. Yodh, "Imager that combines near infrared diffusive light and ultrasound," Opt. Lett. **24,** 1050–1052 (1999).
12. Q. Zhu, E. Conant, and B. Chance, "Optical imaging as an adjunct to sonograph in differentiating benign from malignant breast lesions," J. Biomed. Opt. **5,** 229–236 (2000).
13. Q. Zhu, N. G. Chen, D. Q. Piao, P. Y. Guo, and X. H. Ding, "Design of near infrared imaging probe with the assistance of ultrasound localization," Appl. Opt. **40,** 3288–3303 (2001).
14. N. G. Chen, P. Y. Guo, S. K. Yan, D. Q. Piao, and Q. Zhu, "Simultaneous near infrared diffusive light and ultrasound imaging," Appl. Opt. **40,** 6367–6380 (2001).
15. S. Carraresi, T. S. M. Shatir, F. Martelli, and G. Zaccanti, "Accuracy of a perturbation model to predict the effect of scattering and absorbing inhomogeneities on photon migration," Appl. Opt. **40,** 4622–4632 (2001).
16. V. Ntziachristos, X. H. Ma, and B. Chance, "Time-correlated single photon counting imager for simultaneous magnetic resonance and near-infrared mammography," Rev. Sci. Instrum. **69,** 4221–4233 (1998).
17. Q. Zhu, N. G. Chen, and S. Kurtzman, "Imaging tumor angiogenesis using combined near infrared diffusive light and ultrasound," Opt. Lett. **28,** 337–339 (2003).
18. Q. Zhu, M. Huang, N. G. Chen, K. Zarfos, B. Jagjivan, M. Kane, P. Hegde, and S. Kurtzman, "Ultrasound-guided optical tomographic imaging of malignant and benign breast lesions: initial clinical results of 19 cases," Neoplasia **5,** 379–388 (2003).
19. Q. Zhu, S. Kurtzman, P. Hegde, M. Huang, N. G. Chen, B. Jagjivan, M. Kane, and K. Zarfos, "Imaging heterogeneous tumor hemoglobin distributions of advanced breast cancers by optical tomography with ultrasound localization," Proc. Natl. Acad. Sci. (to be published).
20. M. Huang, N. G. Chen, B. Yuan, and Q. Zhu, "3D simultaneous absorption and scattering coefficient reconstruction for the reflection geometry," in *Optical Tomography and Spectroscopy of Tissue V,* B. Chance, R. R. Alfano, B. J. Tromberg, M. Tamura, and E. M. Sevick-Muraca, eds., Proc. SPIE **4955,** 52–58 (2003).
21. S. Fantini, M. Franceschini, S. A. Walker, J. S. Maier, and E. Gratton, "Photon path distributions in turbid media: applications for imaging in optical tomography," in *Photon Migration and Spectroscopy of Tissue and Model Media: Theory, Human Studies and Instrumentation,* B. Chance and R. R. Alfano, eds., Proc. SPIE **2389,** 340–349 (1995).
22. M. Huang, T. Q. Xie, N. G. Chen, and Q. Zhu, "Simultaneous reconstruction of absorption and scattering maps with ultrasound localization: feasibility study using transmission geometry," Appl. Opt. **42,** 4102–4114 (2003).
23. Q. Zhu, D. Sullivan, B. Chance, and T. Dambro, "Combined ultrasound and near infrared diffusive light imaging," IEEE Trans. Ultrason. Ferroelectr. Freq. Control **46,** 665–678 (1999).
24. M. Cope, "The application of near infrared spectroscopy to non invasive monitoring of cerebral oxygenation in the newborn infant," Ph.D. dissertation (University College London, UK, 1991).
25. S. Carraresi, T. S. M. Shatir, F. Martelli, and G. Zaccanti, "Accuracy of a perturbation model to predict the effect of scattering and absorbing inhomogeneities on photon migration," Appl. Opt. **40,** 4622–4632 (2001).

Neoplasia • Vol. 5, No. 5, September/October 2003, pp. 379–388 379

www.neoplasia.com

Appendix 8

Ultrasound-Guided Optical Tomographic Imaging of Malignant and Benign Breast Lesions: Initial Clinical Results of 19 Cases[1]

Quing Zhu, Minming Huang*, NanGuang Chen*, Kristen Zarfos†, Bipin Jagjivan†, Mark Kane†, Poornima Hedge† and Scott H. Kurtzman†*

*Bioengineering Program, Electrical and Computer Engineering Department, University of Connecticut, Storrs, CT 06269-2157, USA; †University of Connecticut Health Center, Farmington, CT 06030, USA

Abstract

The diagnosis of solid benign and malignant tumors presents a unique challenge to all noninvasive imaging modalities. Ultrasound is used in conjunction with mammography to differentiate simple cysts from solid lesions. However, the overlapping appearances of benign and malignant lesions make ultrasound less useful in differentiating solid lesions, resulting in a large number of benign biopsies. Optical tomography using near-infrared diffused light has great potential for imaging functional parameters of 1) tumor hemoglobin concentration, 2) oxygen saturation, and 3) metabolism, as well as other tumor distinguishing characteristics. These parameters can differentiate benign from malignant lesions. However, optical tomography, when used alone, suffers from low spatial resolution and target localization uncertainty due to intensive light scattering. Our aim is to combine diffused light imaging with ultrasound in a novel way for the detection and diagnosis of solid lesions. Initial findings of two early-stage invasive carcinomas, one combined fibroadenoma and fibrocystic change with scattered foci of lobular neoplasia/lobular carcinoma *in situ*, and 16 benign lesions are reported in this paper. The invasive cancer cases reveal about two-fold greater total hemoglobin concentration (mean 119 μmol) than benign cases (mean 67 μmol), and suggest that the discrimination of benign and malignant breast lesions might be enhanced by this type of achievable optical quantification with ultrasound localization. Furthermore, the small invasive cancers are well localized and have wavelength-dependent appearance in optical absorption maps, whereas the benign lesions appear diffused and relatively wavelength-independent.

Neoplasia (2003) **5,** 379–388

Keywords: breast cancer detection and diagnosis, optical tomography, ultrasound imaging, tumor angiogenesis, image reconstruction.

Introduction

Ultrasound imaging is a well-developed medical diagnostic tool that is used in conjunction with mammography for the differentiation of simple cysts from solid lesions in breast examinations [1]. When the criteria for a simple cyst are strictly adhered to, the accuracy of ultrasound is 96% to 100% [2]. Ultrasound specificity in breast cancer detection, however, is not high as a result of the overlapping characteristics of solid benign and malignant lesions [3,4]. The insufficient predictive value of ultrasound has prompted radiologists to recommend biopsies on most solid nodules, which result in a large number of biopsies yielding benign breast lesions. Currently, 70% to 80% percent of such biopsies yield benign findings [5]. In addition, the diagnostic accuracy of ultrasound depends largely on the experience of physicians.

Diffuse optical tomography in the near-infrared (NIR) is an emerging modality with potential applications in radiology and oncology [6–13]. Optical tomography with NIR light is made possible in a spectrum window that exists within tissues in the 700- to 900-nm NIR region, in which photon transport is dominated by scattering rather than absorption. Optical tomography offers several functional parameters to differentiate malignant cancers from benign lesions. It has been shown that breast cancers have higher blood volumes than nonmalignant tissues because of angiogenesis [14]. Tumor blood volume and microvascular density are parameters anatomically and functionally associated with tumor angiogenesis. If a single optical wavelength is used, optical absorption related to tumor angiogenesis and other normal blood vessels can be measured. If two or more optical wavelengths are used, both oxyhemoglobin (oxyHb) and deoxyhemoglobin (deoxyHb) concentrations can be measured simultaneously. However, optical tomography alone has not been widely used in clinical studies. The fundamental problem of intense light scattering remains, which makes the target localization difficult, especially for small lesions. In general, localization or imaging based on tomographic inverse scattering approaches suffers from low spatial resolution and location uncertainty, and the inversion problem

Address all correspondence to: Prof. Quing Zhu, Bioengineering Program, Electrical Engineering Department, University of Connecticut, Storrs, CT 06269, USA. E-mail: zhu@engr.uconn.edu

[1]We thank the following funding agents for their support: the DOD ARMY (DAMD17-00-1-0217, 17-01-1-0216), the Donaghue Foundation, and the National Institutes of Health (NIH; 1R01CA94044-01A1).

Received 31 March 2003; Revised 9 July 2003; Accepted 18 July 2003.

is, in general, underdetermined and ill posed. The image reconstruction results depend on many parameters, such as the system signal-to-noise ratio, regularization schemes used in inversion, and so on.

Due to the above described deficiencies, literature data on optical tomography have been limited to feasibility studies or case reports [7–13]. However, these deficiencies can be overcome by a novel technique using a combination of NIR diffusive light and ultrasound [15–18]. The combined imager consists of a hand-held probe housing a commercial ultrasound probe and NIR source and detectors for coregistration. Ultrasound is used to scan suspicious lesions, whereas coregistered optical measurements are used to image and characterize the functional parameters of the lesions. With the *a priori* knowledge of lesion structure initially obtained by ultrasound, the tissue volume can be approximately segmented into a lesion region and a background region; optical reconstruction from the optical measurements can be performed by using finer imaging voxel size corresponding to the lesion region and coarse voxel size corresponding to the background region [18]. Consequently, the image reconstruction is well defined because the total number of imaging voxels with unknown optical properties is reduced significantly. In addition, the reconstruction is less sensitive to noise because the weight matrix is appropriately scaled for inversion, and convergence can be achieved within a small number of iterations.

In this paper, we report our initial clinical results of using the combined technique to image and characterize ultrasonically detected breast lesions. A total of 18 patients (19 cases) of invasive breast carcinomas (2 cases), combined fibroadenoma and fibrocystic changes with scattered foci of lobular neoplasia/lobular carcinoma *in situ* (noninvasive carcinoma; 1 case), juvenile atypical ductal hyperplasia (1 case), and fibroadenomas and fibrocystic changes (15 cases) are reported here. The diameters of these lesions are on the order of 1 cm. For the first time, we report high sensitivity of optical tomography in diagnosing early-stage invasive cancers and in differentiating them from small benign lesions. We also show a highly localized pattern of angiogenesis distribution of small invasive cancers. Our initial results are very encouraging and suggest that the discrimination of benign and malignant breast masses could be enhanced by this type of achievable optical quantification coupled with ultrasound localization.

Materials and Methods

The major technical aspects of our combined imaging technique have been described in detail previously [16]. Briefly, the NIR system consists of 12 pairs of dual-wavelength (780 and 830 nm) laser diodes, which are used as light sources, and their outputs are amplitude-modulated at 140 MHz. For each source pair, the outputs from the two laser diodes at both wavelengths were coupled to the tissues through a 200-μm optical fiber. On the receiver side, eight photomultiplier tubes (PMTs) were used to detect diffusely scattered light from the tissues, and eight optical fibers (3 mm in diameter) were used to couple detected diffusive light from the tissues to the PMTs. The high-frequency radiofrequency (RF) signals were amplified and heterodyned to 20 kHz. The heterodyned signals were further amplified and band pass–filtered at 20 kHz. A reference signal of 20 kHz was also generated by directly mixing the detected RF signals with the RF signal generated from the oscillator. The reference signal was necessary for retrieving phase shifts. Eight detection signals and one reference were sampled and acquired into the PC simultaneously. The entire data acquisition took about 3 to 4 seconds, which was fast enough for acquiring data from patients.

A picture of our combined probe and imaging system used in the reported clinical studies is shown in Figure 1*a*, and the probe configuration and optical sensor distribution are shown in Figure 1*b*. Both amplitude and phase at each source–detector pair are obtained and the resulting total number of measurements is $12 \times 8 \times 2 = 192$. The combined probe is made of a black plastic plate 10 cm in diameter; therefore, a semi-infinite boundary condition can be used for NIR measurement geometry. The amplitudes and phases acquired at all source–detector pairs at the normal contralateral breast were used to calculate the

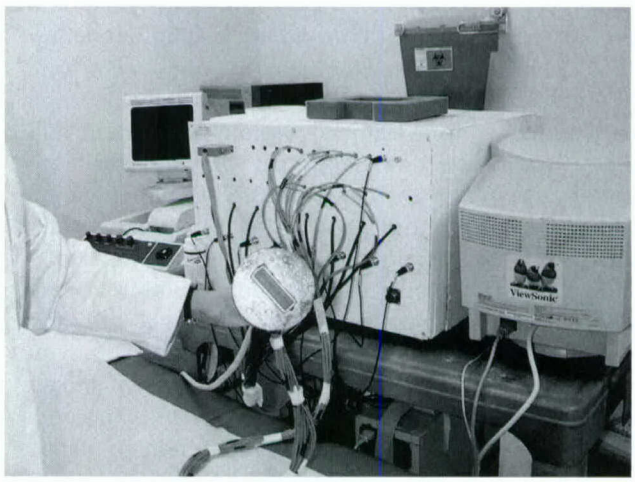

(a)

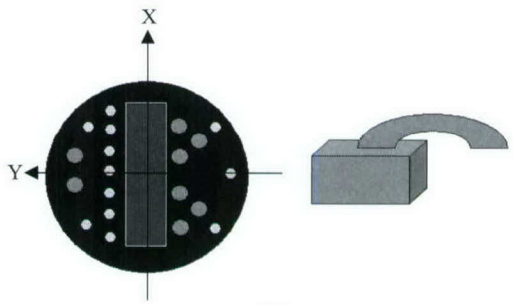

(b)

Figure 1. *(a) Picture of the combined probe and frequency domain imager. (b) Sensor distribution of the combined probe. Smaller circles in (b) are optical source fibers and big circles are detector fibers. A commercial ultrasound probe is located at the center of the combined probe, and the optical source and detector fibers are distributed at the periphery of the ultrasound probe.*

background absorption coefficient $\bar{\mu}_a$ and the reduced scattering coefficient $\bar{\mu}_s'$.

The details of our dual-mesh optical imaging reconstruction algorithm have been described in Ref. [18]. Briefly, the entire tissue volume is segmented based on initial coregistered ultrasound measurements into a lesion region *L* and a background region *B*. A modified Born approximation is used to relate the scattered field $U_{sd}(r_{su}, r_{dt}, \omega)$ measured at the source (s) and detector (d) pair *i* to absorption variations $\Delta\mu_a(r')$ in each volume element of two regions within the sample. The matrix form of image reconstruction is given by:

$$[U_{sd}]_{M\times I} = [W_L, W_B]_{M\times N}[M_L, M_B]^T_{N\times 1}$$

where W_L and W_B are weight matrices for lesion and background regions, respectively; and $[M_L] = [\int_{1_L} \Delta\mu_a(r')d^3r', \ldots \ldots \int_{N_L} \Delta\mu_a(r')d^3r'$ and $[M_B] = [\int_{1_B} \Delta\mu_a(r')d^3r', \ldots\ldots \int_{N_B} \Delta\mu_a(r')d^3r')$ are total absorption distributions of lesion and background regions, respectively. The weight matrices are calculated based on the background $\bar{\mu}_a$ and $\bar{\mu}_s'$ measurements obtained from the normal contralateral breast.

Instead of reconstructing the $\Delta\mu_a$ distribution directly, as is done in the standard Born approximation, the total absorption distribution *M* is reconstructed and the total is divided by different voxel sizes of lesions and background tissues to obtain the $\Delta\mu_a$ distribution. By choosing a finer grid for lesion and a coarse grid for background tissues, we can maintain the total number of voxels with unknown absorption on the same scale of the total measurements. As a result, the inverse problem is less underdetermined. In addition, because the lesion absorption coefficient is higher than that of background tissues, in general, the total absorption of the lesion over a smaller voxel is on the same scale as the total absorption of the background over a bigger voxel. Therefore, the matrix $[M_L, M_B]$ is appropriately scaled for inversion. In all experiments, a finer grid of $0.5 \times 0.5 \times 0.5$ (cm^3) and a coarse grid of $1.5 \times 1.5 \times 1.5$ (cm^3) were chosen for the lesion region and the background tissues, respectively. The total reconstruction volume was chosen to be $9 \times 9 \times 4$ cm^3. The reconstruction is formulated as a least square problem and the unknown distribution *M* is iteratively calculated using the standard conjugate gradient method.

The perturbations for both wavelengths used to calculate absorption maps were normalized as $U_{sd}(r_{si}, r_{di}, \omega) = \frac{U_L(r_{si}, r_{di}, \omega) - U_N(r_{si}, r_{di}, \omega)}{U_N(r_{si}, r_{di}, \omega)} U_B(r_{si}, r_{di}, \omega)$, where $U_L(r_{si}, r_{di}, \omega)$ and $U_N(r_{si}, r_{di}, \omega)$ were optical measurements obtained at the lesion region and the normal region of the contralateral breast, and $U_B(r_{si}, r_{di}, \omega)$ was the calculated incident field using the measured background. This procedure cancels the unknown system gains associated with different sources and detectors as well as electronic channels.

The commercial one-dimensional (1-D) ultrasound probe acquires two-dimensional (2-D) ultrasound images in the *x*–*z* plane (*z* is the propagation direction) and the 2-D NIR probe provides three-dimensional (3-D) optical measurements for 3-D image reconstruction. Therefore, at each location, a 2-D ultrasound image is coregistered with a corresponding set of 3-D optical measurements in the *x*–*z* plane. However, if we approximate a lesion as an ellipsoid, we are able to estimate its diameters from two orthogonal ultrasound images. The 3-D lesion center can be approximated from two orthogonal 2-D ultrasound images. However, two sources of error can affect accurate lesion location and volume estimation. First, the diameter measurements of large irregular lesions are inaccurate because lesion boundaries may not be well defined in ultrasound images. Second, the target boundaries seen by different modalities may be different due to different contrast mechanisms. To account for these errors, we use a lesion center estimated from the 2-D coregistered ultrasound image and use much larger diameters in both spatial dimensions than ultrasound-measured ones to highlight the lesion region for fine-mesh optical reconstruction. We have found from experiments that the abovementioned measurement inaccuracies have little effects on reconstructed optical properties as long as the lesion depth is measured correctly and the total number of unknown voxels is of the same order as the total number of measurements. The lesion depth *z* and the lesion boundaries in the *z* direction can be estimated reasonably well from 2-D coregistered ultrasound using normal tissue structure patterns.

Clinical studies were performed at the University of Connecticut Health Center (UCHC; Farmington, CT). The UCHC IRB committee approved the human subject protocol. Patients with palpable and nonpalpable masses that were visible on clinical ultrasound and who were scheduled for biopsy were enrolled as research subjects. These subjects were scanned with the combined probe, and ultrasound images and optical measurements were acquired at multiple locations including the lesion region scanned at two orthogonal positions, a normal region of the same breast if the breast was large, and a normal symmetric region of the contralateral breast also scanned at two orthogonal positions.

Results

Examples of Invasive Cancers

Figure 2*a* shows a gray scale ultrasound image of a nonpalpable lesion of a 55-year-old woman. The ultrasound showed a nodular mass with internal echoes and the lesion was considered suspicious. The estimated lesion diameter measured from two orthogonal ultrasound images was 8 mm. An ultrasound-guided core needle biopsy was recommended and the biopsy result revealed that the lesion was intraductal and infiltrating ductal carcinoma (nuclear grade II, histologic grade III). The cancer, once removed from the breast, measured 1 cm in greatest diameter, and was composed predominantly of invasive carcinoma (>95%), extending to surgical margins. Negative margins were achieved upon reexcision.

The average tissue background absorption coefficients $\bar{\mu}_a$ and the reduced scattering coefficients $\bar{\mu}_s'$ at 780 and 830 nm were measured as $\mu_a^{780} = 0.02$ cm^{-1}, $\mu_s'^{780} = 8.2$ cm^{-1}, $\mu_a^{830} = 0.04$ cm^{-1}, and $\mu_s'^{830} = 6.0$ cm^{-1}, respectively. The initial estimates of the lesion center and the

diameter from coregistered ultrasound were (0, 0.3, 2.3) cm and 8 mm. To account for errors in lesion geometry estimate and for differences in optical contrast, we used a 6-cm diameter in both *x* and *y* spatial dimensions at the center of (0, 0.3, 2.3) cm for fine-mesh optical reconstruction. The lesion diameter in depth is estimated as 1 cm by comparing the top and the bottom of lesion boundaries from normal tissue patterns. The white arrow arrays on the top and bottom of the lesion in Figure 2*a* point to normal tissue boundaries.

The optical absorption maps at both wavelengths are shown in Figure 2, *b* and *c*, respectively. In both Figure 2, *b* and *c*, the first slice is 0.7 cm deep into the breast tissue from the skin surface and the last slice is closer to the chest wall. The spacing of the slices is 0.5 cm. The horizontal and vertical axes of each slice are spatial *x* and *y* dimensions of 9 cm in size. The lesion is well resolved in slice 5 and has shown much larger spatial extension at 830 nm than that at 780 nm. The measured maximum absorption coefficients are $\mu_a^{780} = 0.24\ cm^{-1}$ and $\mu_a^{830} = 0.28\ cm^{-1}$, respectively, and the absorption maxima at both wavelengths are located at (0, 1.0, 2.3) cm, which is close to the lesion center measured by ultrasound.

By assuming that the major chromophores are oxygenated (oxyHb) and deoxygenated (deoxyHb) hemoglobin molecules in the wavelength range studied, we can estimate the distribution of total hemoglobin concentration as shown in Figure 2*d*. The extinction coefficients used for calculating oxyHb and deoxyHb concentrations were $\varepsilon_{Hb}^{780} = 2.54$, $\varepsilon_{HbO_2}^{780} = 1.70$, $\varepsilon_{Hb}^{830} = 1.80$, $\varepsilon_{HbO_2}^{830} = 2.42$, obtained from Ref. [19] in a natural logarithm scale with units of inverse millimoles times inverse centimeters. The measured maximum total hemoglobin concentration for lesions is 122 μmol, and the measured average background hemoglobin concentration is 14 μmol. The spatial extent of the lesion's angiogenesis is measured from the full width at half maximum (FWHM) of the total hemoglobin map and it is estimated to be 2.0 cm. This number is about two and half times larger than the 8 mm diameter measured by ultrasound and suggests that optical contrasts extend well beyond the cancer periphery due to angiogenesis.

Because our hand-held probe can be easily rotated or translated, we have acquired at least three coregistered ultrasound and NIR data sets at the lesion location for each patient and have reconstructed corresponding optical absorption maps as well as the total hemoglobin concentration distribution under the coregistered ultrasound guidance. The average maximum total hemoglobin concentration at the cancer region is 115 μmol (±27.6 μmol) and the average background total hemoglobin concentration is 13 μmol (±1.5 μmol). The large standard deviation at the cancer region is likely related to the probe compression at different spatial locations and elastic properties of the blood vessels in the cancer region.

Another example was obtained from a 56-year-old woman who had a solid mass with internal ultrasound echoes measuring 9 mm in size (Figure 3*a*). The lesion was considered suspicious, and ultrasound-guided core needle biopsy revealed that the lesion was *in situ* and invasive ductal carcinoma (nuclear grade II, histologic grade II). The tumor, once removed from the breast, measured 1.5 cm in greatest diameter, and was composed predominantly of invasive carcinoma (>80%), extending to the inferior/anterior surgical margin. Negative inferior margin was achieved upon reexcision.

The average tissue background absorption coefficient $\bar{\mu}_a$ and the reduced scattering coefficient $\bar{\mu}'_s$ at 780 and 830 nm were measured as $\mu_a^{780} = 0.04\ cm^{-1}$, $\mu_s'^{830} = 4.7\ cm^{-1}$, $\mu_a^{780} = 0.03\ cm^{-1}$, and $\mu_a'^{830} = 5.8\ cm^{-1}$, respectively. The initial estimate of the lesion center and diameters from coregistered ultrasound were (0, 0.6, 1.9) cm and 9 mm, respectively. Again, we used a 6-cm diameter in both *x* and *y* spatial dimensions at the center of (0, 0.6, 1.9) for fine-mesh optical reconstruction. The optical absorption maps at both wavelengths are shown in Figure 3, *b* and *c*, respectively. In Figure 3, *b* and *c*, the first slice is 0.4 cm deep into the breast tissues from the skin surface and the last slice is closer to the chest wall. The spacing between the slices is 0.5 cm. This lesion is well resolved in slice #4 and has shown much larger spatial extension at 780 nm than that at 830 nm. The measured maximum absorption coefficients are $\mu_a^{780} = 0\ .29\ cm^{-1}$ and $\mu_a^{830} = 0.25\ cm^{-1}$, respectively. The absorption maxima at both wavelengths are located at (0,1.0,1.9000) cm, which is very close to the lesion center measured by ultrasound. The calculated maximum total hemoglobin concentration of the lesion is 128 μmol, and the background concentration is 24 μmol. The measured FWHM of the total hemoglobin map is 3.5 cm, which is more than three times larger than the 9 mm diameter measured by ultrasound and again suggests that optical contrasts extend well beyond the cancer periphery due to angiogenesis. The average maximum total hemoglobin concentration calculated from three NIR data sets is 123 μmol (±6.2 μmol) and the average background hemoglobin concentration is 24 μmol (±0.5 μmol). The variation of total hemoglobin concentrations acquired at slightly different spatial probe positions is much smaller than that in the previous case.

An Example of Combined Fibroadenoma and Fibrocystic Changes with Scattered Foci of Lobular Neoplasia/Lobular Carcinoma In Situ (Noninvasive Carcinoma)

This patient had a solid lesion measuring 1.1 cm in diameter as shown in Figure 4*a* ultrasound image. The lesion was diagnosed as having a benign appearance; however, the biopsy result revealed combined fibrocystic changes associated with microcalcifications and scattered foci of lobular neoplasia/lobular carcinoma *in situ* with pagetoid extension along ducts, but no invasive carcinoma. Also present was a fibroadenoma involved by lobular neoplasia.

The average background tissue absorption coefficients and reduced scattering coefficients at both wavelengths were measured as $\mu_a^{780} = 0.04\ cm^{-1}$, $\mu_s'^{780} = 3.3\ cm^{-1}$, $\mu_a^{830} = 0.02\ cm^{-1}$, and $\mu_s'^{830} = 3.5\ cm^{-1}$, respectively. The initial estimate of the lesion center and the diameter from ultrasound were (0, 0.9, 1.4) and 1.1 cm. The reconstructed absorption maps as well as total hemoglobin concentration distribution are shown in Figure 4, *b*–*d*, respectively. The

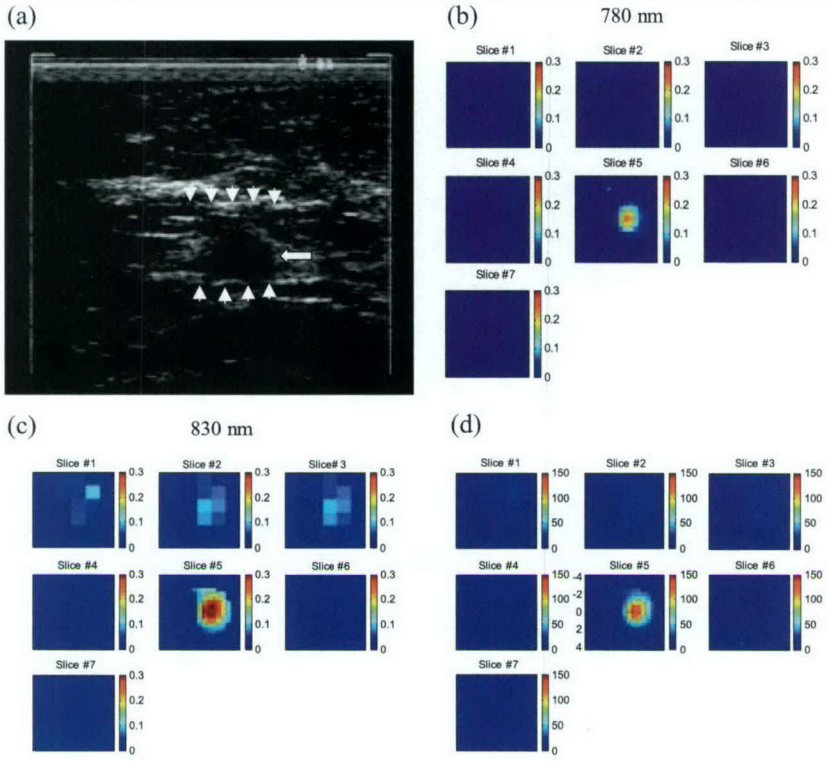

Figure 2. *(a) shows a gray scale ultrasound image of a nonpalpable lesion of a 55-year-old woman. The lesion pointed by the arrow was located at the 4 o'clock position of the right breast measuring 8 mm in diameter. Ultrasound showed nodular mass with internal echoes and the lesion was considered suspicious. (b) and (c) are optical absorption maps at 780 and 830 nm, respectively. x and y axes are spatial dimensions of 9 × 9 cm. The slices starting from left to right correspond to absorption maps from 0.7 cm underneath the skin surface to the chest wall in 0.5-cm spacing. (d) is the total hemoglobin concentration and the vertical scale is in micromoles.*

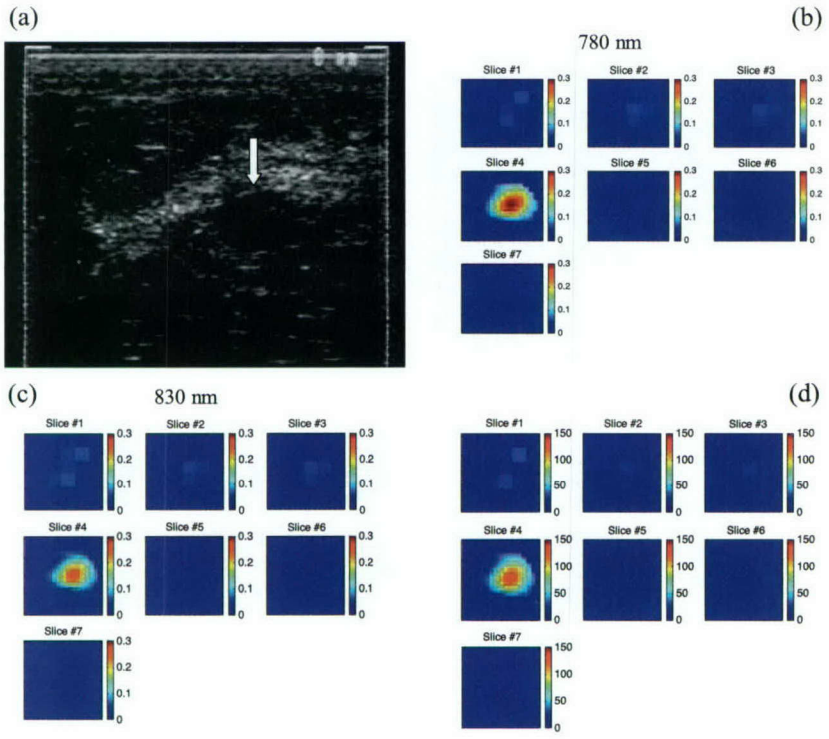

Figure 3. *This example was obtained from a 56-year-old woman who had nonpalpable lesion located at the 10 o'clock position of the left breast. Ultrasound showed a solid mass (a) with internal echoes measuring 9 mm in size and the lesion was considered suspicious. (b) and (c) are optical absorption maps at 780 and 830 nm, respectively. The slices start from 0.4 cm underneath the skin surface to the chest wall in 0.5-cm spacing. (d) is the total hemoglobin concentration.*

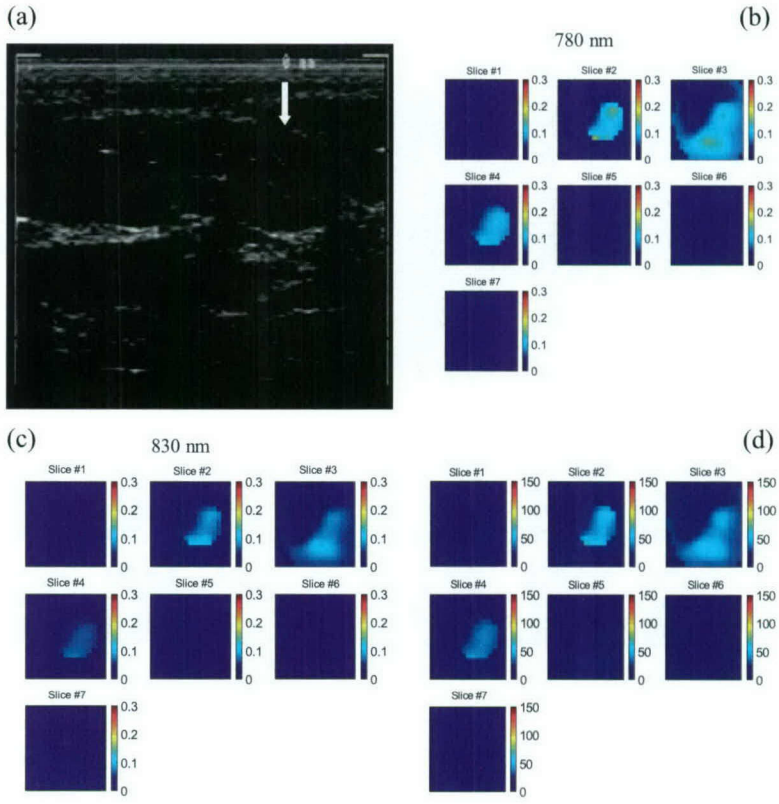

Figure 4. *(a) shows a solid lesion at the 2 o'clock position measuring 1.1 cm in diameter in ultrasound image. The lesion was diagnosed as having benign appearance because of well-defined boundaries. Ultrasound-guided core biopsy revealed scattered foci of lobular neoplasia, carcinoma in situ but not invasive, and fibroadenoma and fibrocystic changes with associated microcalcifications. (b) and (c) are optical absorption maps at 780 and 830 nm, respectively. The slices start from 0.5 cm underneath the skin surface to the chest wall in 0.5-cm spacing. (d) is the total hemoglobin concentration.*

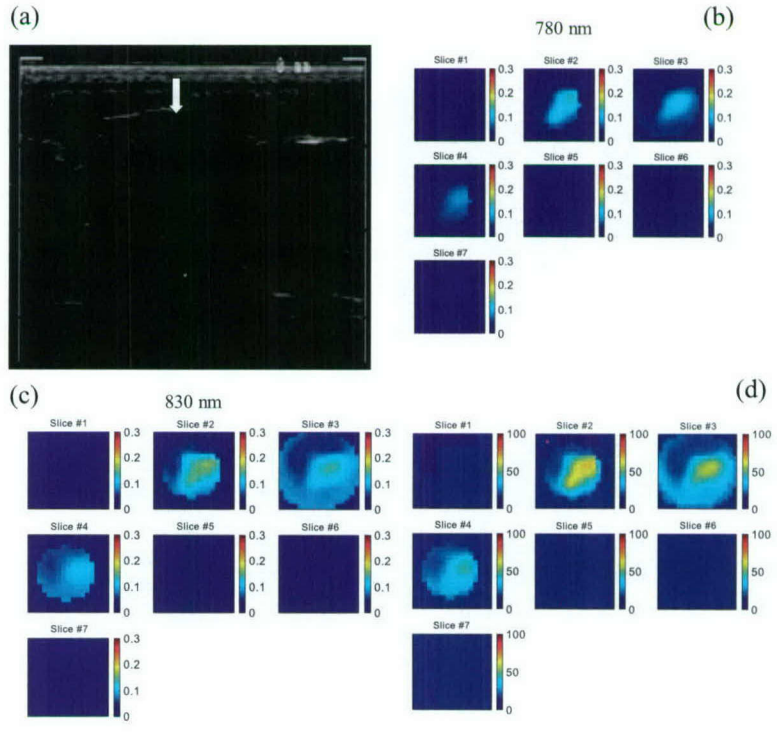

Figure 5. *(a) shows an ultrasound image of a solid hypoechogenic lesion located at 9 to 10 o'clock position of a 37-year-old woman's breast. The diagnosis was that the lesion could represent fibroadenoma; however, there was a chance that the lesion could be a carcinoma because of the irregular shape and posterior shadow seen by ultrasound. (b) and (c) are optical absorption maps at 780 and 830 nm, respectively. The slices start from 0.5 cm underneath the skin surface to the chest wall in 0.5-cm spacing. (d) is the total hemoglobin concentration.*

measured maximum absorption coefficients are μ_a^{780} = 0.13 cm^{-1} and μ_a^{830} = 0.09 cm^{-1}, respectively, which are about half of those measured in invasive cancer cases. In addition, the absorption coefficient distributions are diffused at both wavelengths and no resolvable or localized lesions are seen. The calculated maximum total hemoglobin concentration is 53 μmol, which is less than half of those in invasive cancer cases. The calculated background value is 13 μmol. The average maximum hemoglobin concentration calculated from four reconstructed NIR images at lesion location is 48 μmol (±2.8 μmol) and the value for the background is 12 μmol (±0.4 μmol). This example suggests that tumor vascularization may not be developed at the early noninvasive stage of combined fibrocystic change and neoplasia/carcinoma *in situ*.

Example of Fibroadenoma and Other Benign Lesions

Figure 5*a* shows an ultrasound image of a hypoechoic mass of a 37-year-old woman. The diagnosis was that the lesion likely was a fibroadenoma; however, there was concern that the lesion could be a carcinoma because of the irregular shape and the posterior shadowing seen by ultrasound. An ultrasound-guided core breast biopsy revealed that the lesion was simply a fibroadenoma.

Optical absorption maps are shown in Figure 5, *b* and *c*, as well as the total hemoglobin distribution in Figure 5*d*. Compared with the invasive cancer cases, the spatial distributions of the absorption coefficients as well as the total hemoglobin concentration are quite diffused, and a higher absorption region at 830 nm corresponds to lesion regions seen by ultrasound. The measured maximum lesion absorption coefficients at 780 and 830 nm are μ_a^{780}=0.10 cm^{-1} and μ_a^{830}=0.12 cm^{-1}, respectively, and these values are less than half of those small invasive cancer cases. The calculated maximum total hemoglobin concentration is 52 μmol and the background hemoglobin concentration is 14 μmol. The calculated average maximum total hemoglobin concentration from four NIR images acquired at lesion region is 59 μmol (±5.1 μmol) and the average background is 16 μmol (±1.0 μmol).

Table 1 lists all the measured parameters of the 19 cases [from left to right: biopsy result, lesion size measured by ultrasound in *x* and *z* dimensions (because lesions are small, the lesion size in *y* is similar to that measured in the *x* dimension), region of interest (ROI) used for fine-mesh NIR imaging, FWHM measured from NIR imaging, maximum absorption coefficients measured at both wavelengths, maximum and average total hemoglobin concentrations (the average is computed within FWHM)]. For the two invasive cancer cases, NIR parameters are given for two different ROIs and the results show that the choice of ROI has negligible effects on the absorption and hemoglobin measurements.

The statistics of maximum total hemoglobin concentration of three groups obtained from the 19 cases are shown in Figure 6. The benign group of fibroadenoma (15 cases) and hyperplasia (1 case) has an average of 67 μmol (±17.0 μmol), the combined fibroadenoma and fibrocystic change with noninvasive neoplasia/carcinoma *in situ* case has a maximum of 48 μmol, and the invasive cancer group of two cases has shown about two-fold greater average of 119 μmol (±1.6 μmol). If average total hemoglobin concentration is used, the values are 46 (±11.3), 30, and 86 (±2.12) μmol for the three corresponding groups, respectively. The malignant group also presents about two-fold greater average hemoglobin concentration than that of the benign group. The average sizes of lesions of the three groups measured by ultrasound are 1.05 (±0.3), 1.1, and 0.9 (±0.07) cm, respectively. The lesion size is the geometric mean of diameters measured in *x* and *z* dimensions.

Because our study is in its early clinical trial stage, we do not intend to provide the sensitivity and specificity of the combined method due to the limited sample size available. However, our initial findings are very encouraging and suggest that early-stage small invasive cancers have much higher optical contrast than benign lesions and could be diagnosed with high specificity possibly due to tumor angiogenesis.

Discussion

As described earlier, due to intense light scattering, optical tomography alone has not been widely used in clinical studies. Data in the published literature have been limited to feasibility studies or case reports. Pogue et al. [9] reported pilot results of one invasive ductal carcinoma 1 cm in size and one benign fibroadenoma 3 cm in size. The reported maximum total hemoglobin concentrations were 68 μmol for the cancer case and 55 μmol for the benign case. Although the invasive cancer size reported by this group is comparable to ours, the system they used can only acquire NIR data from a ring area with optical sources and detectors deployed around the breast (2-D imager). Therefore, incomplete information could lead to smaller reconstructed absorption coefficients and total hemoglobin concentrations than those reported here using our 3-D NIR imager. In addition, an investigation with phantoms has shown that NIR alone, in general, reconstructs lower absorption coefficients and therefore lower total hemoglobin concentrations than true values [20]. This can be seen from two studies of the same data reported in Refs. [7,13]. Authors in Ref. [7] reported an average of 35 μmol total hemoglobin concentration of a 2-cm ductal carcinoma *in situ* by using NIR measurements alone. After reprocessing the same NIR measurement data using an approximate lesion depth obtained from a separate ultrasound image, the authors reported that the calculated average total hemoglobin concentration was increased to 67 μmol [13].

The reported small early-stage invasive cancers appear isolated and are well resolved from background tissues in optical absorption maps as well as in total hemoglobin distributions. However, the combined fibroadenoma and fibrocystic change with scattered foci of lobular neoplasia/lobular carcinoma *in situ* case showed no difference in optical absorption and hemoglobin concentration than those

Table 1. Measured Parameters of 19 Cases.

Reference Number	Biopsy Results	Lesion Size (Ultrasound) [cm]	ROI	FWHM (NIR) [cm]	Max μ_a [cm^{-1}], 780 nm	Max μ_a [cm^{-1}], 830 nm	Max Total Hb [μM]	Average Total Hb [μM]
13	Invasive cancer	0.9 × 0.6	6 × 6 × 1	3.5	0.28	0.24	123	87
			10 × 10 × 1	3.5	0.27	0.24	122	88
25	Invasive cancer	0.8 × 0.5	6 × 6 × 1	2.0	0.22	0.26	115	84
			10 × 10 × 1	2.1	0.22	0.26	115	84
32	Fibrocystic and lobular neoplasia/carcinoma	1.1 × 1.1	10 × 10 × 1.2	6.1	0.12	0.08	48	30
11	Fibroadenoma	1.2 × 0.8	8 × 8 × 1	4.9	0.11	0.10	49	37
8	Fibroadenoma	2.2 × 1.3	8 × 8 × 1.6	2.7	0.07	0.03	24	16
9	Fibroadenoma	0.9 × 0.7	8 × 8 × 1	4.9	0.15	0.18	77	52
7	Fibroadenoma and sclerosing adenosis with extensive calcification	1.0 × 0.6	10 × 10 × 1	3.8	0.16	0.11	59	41
17	Fibrocystic changes	0.6 × 0.7	10 × 10 × 1	5.8	0.16	0.16	76	53
20	Fibroadenoma	1.2 × 0.6	10 × 10 × 1	5.7	0.14	0.14	67	45
30	1: Fibrocystic change	1.7 × 1.1	8 × 8 × 1.3	4.0	0.10	0.15	59	39
30	2: Sclerosing adenosis and epithelial hyperplasia without atypical	1.4 × 1.2	8 × 8 × 1.3	4.0	0.15	0.23	88	57
22	Fibroadenoma	1.0*	10 × 10 × 1.5	3.7	0.15	0.15	72	46
36	Fibroadenoma	1.9 × 0.9	9 × 9 × 1	4.7	0.13	0.18	73	50
28	Fibroadenoma	1.9 × 1.1	9 × 9 × 1.3	4.2	0.14	0.16	71	45
33	Fibroadenoma	1.2 × 0.7	10 × 10 × 1	7.0	0.13	0.13	61	44
37	Fibroadenoma	0.8 × 0.6	8 × 8 × 1	6.0	0.16	0.18	80	53
35	Fibroadenoma	1.3 × 1.3	9 × 9 × 2	4.3	0.14	0.15	59	41
38	Hyalinized fibroadenoma	0.8 × 0.4	6 × 6 × 1	2.5	0.17	0.22	90	67
29	Atypical ductal hyperplasia	1.1 × 0.8	9 × 9 × 1	3.7	0.10	0.17	64	44

*See by X-ray.

obtained from fibroadenoma cases. This suggests that optical tomography may not be sensitive to early-stage mixed benign changes and noninvasive neoplasia/carcinoma *in situ* because tumor neovascularization has not been developed. This result is consistent with magnetic resonance imaging (MRI) findings on the low detection sensitivity of carcinoma *in situ* [21–23]. However, optical imaging may be a valuable tool for monitoring the development or transition of lesions from noninvasive to early invasive stage. Certainly, more cases are needed to validate the observations reported here. For larger cancers, highly heterogeneous wavelength-dependent optical absorption distributions and total hemoglobin distribution have been observed in four cases [18], and these distributions could provide valuable information for monitoring and assessing cancer therapy under treatment. Currently, we are pursuing research along this line and more cases will be reported in the future.

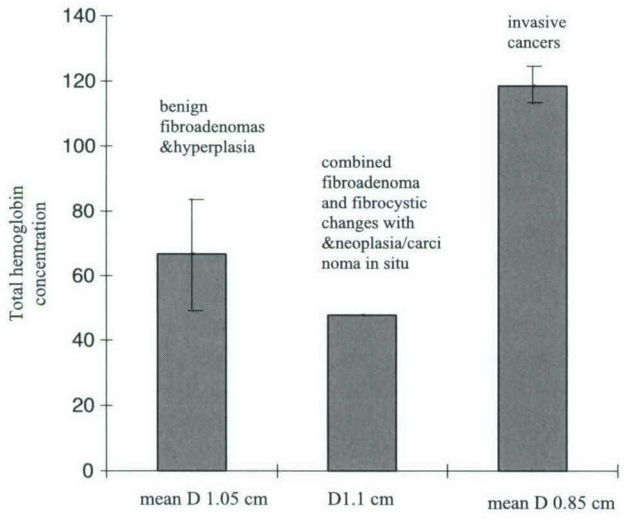

Figure 6. *The average maximum total hemoglobin concentration obtained from benign fibroadenomas and hyperplasia, and combined fibroadenoma and fibrocystic change with neoplasia/carcinoma in situ (noninvasive) and invasive cancer groups are shown in bars. The standard deviations of three groups are also provided. The average sizes of lesions of the three groups are 1.05 (0.3), 1.1, and 0.9 (0.07) cm, respectively.*

In principle, the distribution of oxygenation saturation can be estimated as S = oxyHb/(oxyHb+deoxyHb), with deoxyHb and oxyHb distributions calculated from absorption maps at the two wavelengths of 780 and 830 nm. However, because background tissues mainly consist of water and lipid and these two chromophores contribute to the total absorption estimate as well, we could not obtain reasonable background oxygenation saturation and compare it with lesion oxygenation saturation. Recently, we have improved our NIR system by adding another wavelength at 660 nm, which may allow us to accurately estimate the background oxygenation saturation and to compare it with lesion oxygenation saturation.

If we reconstruct the lesion area only, we could distribute partial perturbations caused by background to lesion and increase calculated lesion absorption and therefore hemoglobin concentration. However, with the dual-mesh scheme,

we reconstruct the entire imaging volume instead of the lesion area only, and distribute the perturbations to both lesion and background. We did phantom experiments using the dual-mesh scheme and obtained absorption coefficients, which were always within 10% of the true values depending on the phantom contrasts [24].

Two-dimensional ultrasound provides fine tissue layer structures in depth (z) direction (Figure 2, *arrow arrays*), and the 2-D ultrasound image is coregistered with optical data in z. Therefore, we only need to consider possible angiogenesis extensions in z and we have extended the lesions to the closest normal tissue lines in z. In spatial dimensions, we have some uncertainty in another dimension (y) based on 2-D $x-z$ ultrasound image, and we need to extend the lesion region to a larger area to account for this as well as for possible angiogenesis extension.

The reported optical tomography study was used to image and characterize ultrasonically detected lesions. However, in one benign fibroadenoma case, the lesion was not visible in ultrasound but was seen by conventional X-ray mammogram. By knowing the approximate lesion region with respect to the nipple location from the patient's mammogram, we used a fine mesh for optical reconstruction in a larger region of $9 \times 9 \times 1.5$ cm^3, and identified a possible lesion that showed slightly higher optical absorption than that of the background. We believe that optical tomography, assisted by conventional mammography and/or ultrasound localization, has potential as a screening tool to identify and characterize malignancy.

Our initial findings provide evidence that optical tomography, combined with ultrasound, could be used to differentiate early-stage small invasive breast cancers from benign lesions. Because of the limited sample size available, we are not able to provide sensitivity and specificity results in this paper. In addition, for the patients studied, four fibroadenoma cases and one intraductal hyperplasia were excluded from the statistics shown in Figure 6. The four fibroadenoma cases were scanned at the beginning of the study. One patient was scanned after core biopsy due to scheduling problem, and the possible blood distribution change due to biopsy procedure has to be considered. The other three young patients have small and dense breasts. For these three patients, the optical amplitude and phase data sets were highly scattered even in the normal contralateral breast. Therefore, no reliable background tissue absorption and scattering coefficients can be obtained. Three possible sources for these findings were identified. First, because these breasts were small and dense, the skin and probe contact was not always good. Second, a thick gel layer used for coupling the ultrasound transducer with the skin can serve as a light tunneling medium from sources to detectors. This portion of the light can saturate the detectors and give false readings. Caution was taken in the later studies by compressing the probe harder against the examined breast to ensure good probe–tissue contact, and by placing a very thin gel layer underneath the ultrasound transducer during scanning. The third source are tissue heterogeneities of the young dense breasts. However, by carefully removing outliers from normal breast data, we could obtain reasonably good reference data for imaging. One patient with intraductal hyperplasia data was excluded from the study. This patient had a solid lesion located at the nipple area and the nipple had a very dark color. Four NIR image data sets obtained at the lesion area had the same artifacts and the artifact consistently showed up with very high absorptions at both wavelengths. When the lesion locations were changed in different images with different probe positions, the artifact location changed very little. A similar artifact showed up in the two reference data sets acquired in the contralateral normal breast. We do not know the exact source of this artifact because there was no report that this patient had problems at the contralateral breast. Care was taken in the later studies by acquiring at least four reference data sets at the normal symmetric region of the contralateral breast, as well as at normal regions of the same lesion breast. Reference data sets were always checked for normal background absorption changes before imaging the lesions.

Summary

Initial clinical results from the use of optical tomography combined with conventional ultrasound demonstrate that there is a huge optical contrast between early-stage invasive cancers and benign solid lesions due to angiogenesis. An average of 52 μmol difference was obtained between two small invasive cancers and a group of 16 benign solid lesions. In addition, the small invasive cancers were localized well in absorption maps and have shown wavelength-dependent absorption changes, whereas the benign lesions appeared more diffused in absorption maps and have shown relatively wavelength-independent absorption changes. The combined fibrocystic changes and noninvasive neoplasia/carcinoma *in situ* case did not show a significant difference in optical absorption and total hemoglobin concentration than those of benign lesions. This suggests that the angiogenesis may not be developed at the early noninvasive stage of the mixed benign changes and fibroadenoma with neoplasia/carcinoma *in situ*. However, optical tomography may have a potential role in monitoring the development and/or transition of cancers from the noninvasive to the invasive stage.

Our reported initial results are very encouraging and demonstrate that our unique approach, which combines optical tomography with ultrasound, has great potential to detect and characterize breast lesions.

Acknowledgements

The authors thank Ellen Oliver, surgical nurse of the Cancer Center of the UCHC, for her continuous efforts on patient scheduling. Q. Zhu expresses her sincere thanks to Prof. Britton Chance of the University of Pennsylvania for his continuous encouragement and support on combined imaging and valuable discussions on cancer biology. Graduate students Puyun Guo, Shikui Yan, and Daqing Piao are

acknowledged for their continuous help on the NIR system construction and improvement.

References

[1] Stavros TA, Thickman D, and Rapp C (1995). Solid breast nodules: use of sonography to distinguish between benign and malignant lesions. *Radiology* **196,** 123–34.

[2] Sickles EA (1998). Detection and diagnosis of breast cancer with mammography. *Perspect Radiol* **1,** 36–65.

[3] Rahbar G, Sie AC, Hansen GC, Prince JS, Melany ML, Reynolds H, Jackson VP, Sayre JW, and Bassett LW (1999). Benign *versus* malignant solid breast masses: US differentiation. *Radiology* **213,** 889–94.

[4] Jackson VP (1995). The current role of ultrasonography in breast imaging. *Radiol Clin North Am* **33,** 1161–170.

[5] Sickles EA (1988). Detection and diagnosis of breast cancer with mammography. *Perspect Radiol* **1,** 36–65.

[6] Yodh A, and Chance B (1995). Spectroscopy and imaging with diffusing light. *Phys Today* **48,** 34–40.

[7] Tromberg B, Shah N, Lanning R, Cerussi A, Espinoza J, Pham T, Svaasand L, and Butler J (2000). Non-invasive *in vivo* characterization of breast tumors using photon migration spectroscopy. *Neoplasia* **2** (1:2), 26–40.

[8] Franceschini MA, Moesta KT, Fantini S, Gaida G, Gratton E, Jess H, Seeber M, Schlag PM, and Kashke M (1997). Frequency-domain techniques enhance optical mammography: initial clinical results. *Proc Natl Acad Sci* **94,** 6468–473.

[9] Pogue B, Poplack SP, McBride TO, Wells WA, Osterman K, Osterberg U, and Paulsen KD (2001). Quantitative hemoglobin tomography with diffuse near-infrared spectroscopy: pilot results in the breast. *Radiology* **218,** 261–66.

[10] Dehghani H, Pogue B, Poplack SP, and Paulsen KD (2003). Multiwavelength three-dimensional near-infrared tomography of the breast: initial simulation, phantom, and clinical results. *Appl Opt* **42** (1), 135–45.

[11] Ntziachristos V, Yodh A, Schnall M, and Chance B (2000). Concurrent MRI and diffuse optical tomography of breast after indocyanine green enhancement. *Proc Natl Acad Sci* **97** (6), 2267–772.

[12] Jiang H, Xu Y, Iftimia N, Eggert J, Klove K, Baron L, and Fajardo L (2001). Three-dimensional optical tomographic imaging of breast in a human subject. *IEEE Trans Med Imaging* **20** (12), 1334–340.

[13] Jholboke M, Tromberg B, Li X, Shah N, Fishkin J, Kidney D, Butler J, Chance B, and Yodh A (2000). Three-dimensional diffuse optical mammography with ultrasound localization in human subject. *J Biomed Opt* **5** (2), 237–47.

[14] Vaupel P, Kallinowski F, and Okunieff P (1989). Blood flow, oxygen and nutrient supply, and metabolic microenvironment of human tumors: a review. *Cancer Res* **49,** 6449–465.

[15] Zhu Q, Durduran T, Holboke M, Ntziachristos V, and Yodh A (1999). Imager that combines near infrared diffusive light and ultrasound. *Opt Lett* **24** (15), 1050–1052.

[16] Chen NG, Guo PY, Yan SK, Piao DQ, and Zhu Q (2001). Simultaneous near infrared diffusive light and ultrasound imaging. *Appl Opt* **40** (34), 6367–380.

[17] Zhu Q, Conant E, and Chance B (2000). Optical imaging as an adjunct to sonograph in differentiating benign from malignant breast lesions. *J Biomed Opt* **5** (2), 229–36.

[18] Zhu Q, Chen NG, and Kurtzman HS (2003). Imaging tumor angiogenesis by the use of combined near infrared diffusive light and ultrasound. *Opt Lett* **28** (5), 337–39.

[19] Cope M (1991). PhD Dissertation University of College London.

[20] Zhu Q, Chen NG, Piao DQ, Guo PY, and Ding XH (2001). Design of near infrared imaging probe with the assistance of ultrasound localization. *Appl Opt* **40** (19), 3288–303.

[21] Gilles R, Zafrani B, Guinebretiere JM, Meunier M, Lucidarme O, Tardivon AA, Rochard F, Vanel D, Neuenschwander S, and Arriagada R (1995). Ductal carcinoma *in situ*: MRI imaging–histopathologic correlation. *Radiology* **196,** 415–19.

[22] Fischer U, Westerhof JP, Brinck U, Korabiowska M, Schauer A, and Grabbe E (1996). The ductal carcinoma *in situ* in contrast-enhanced dynamic MR mammography. *RoFo* **164,** 290–94.

[23] Orel SG, Mendoca MH, Reynolds C, Schnall MD, Solin LJ, and Sullivan DC (1997). MR imaging of ductal carcinoma *in situ*. *Radiology* **202,** 413–20.

[24] Huang MM, Chen NG, Yuan BH, and Zhu Q (2003). 3D simultaneous absorption and scattering coefficients reconstruction for the reflection geometry. In *Optical Tomography and Spectroscopy of Tissue V*. B Chance, RR Alfano, BJ Tromberg, M Tamura, EM Sevick-Muraca (Eds). SPIE, Bellingham, WA. Vol. **4955,** pp. 52–58.

-Benign versus Malignant Breast Masses: Optical Differentiation using US to Guide Optical Imaging Reconstruction

Benign versus Malignant Breast Masses: Optical Differentiation using US to Guide Optical Imaging Reconstruction

Quing Zhu+, Edward B. Cronin*, Allen A. Currier*, Hugh S. Vine*, Minming Huang+, NanGuang Chen+, Chen Xu+

+ Bioengineering Program, Electrical and Computer Engineering Department, University of Connecticut, Storrs, CT 06269

*Department of Radiology, Hartford Hospital, Hartford, CT 06102

Original Research

Abstract

PURPOSE: To investigate the feasibility of optical tomography with ultrasound (US) localization in differentiating malignant from benign breast masses. To compare the optical tomography method with Doppler US in the assessment of tumor angiogenesis.

MATERIAL AND METHODS: Between May 2003 and March 2004, 73 patients underwent US-guided biopsy and were scanned with a combined imager consisting of a commercially available US system and a near infrared (NIR) imager. A hand-held probe with a centrally located US transducer and NIR sensors surrounding it was used to simultaneously acquire co-registered US images and optical data. The lesion location provided by US was used to guide optical imaging reconstruction. Light absorption was measured at two wavelengths. From this, tumor angiogenesis was assessed based on calculated total hemoglobin concentration.

RESULTS: There were 8 invasive carcinomas and 73 benign lesions. The mean maximum and average values of hemoglobin concentration of the malignant group were 122 μ mol/liter ($\pm$ 26.8) and 88 μ mol/liter ($\pm$ 24.5), respectively, and the mean maximum and average values of the benign group were 55 μ mol/liter ($\pm$ 24.8) and 38 μ mol/liter ($\pm$ 17.4), respectively. Both maximum and average of total hemoglobin level were statistically significantly higher in the malignant group than the benign group ($P<0.001$). Using a threshold value of 95 μ mol/liter, the sensitivity, specificity, positive predictive value, and negative predictive value were 100%, 96%, 73%, and 100%.

Conclusion: Optical tomography with US localization has a great potential to improve the sensitivity and specificity of gray scale US and Doppler US for breast cancer diagnosis.

Index terms: US, Optical tomography, Diagnosis, Breast Neoplasm

Introduction

Large numbers of breast biopsies are performed with benign results (1). The use of ultrasound (US) as an adjunct to x-ray mammography decreased the number of benign biopsies by enabling reliable differentiation of simple cysts (2-4) from solid lesions. However, the US features of a solid lesion alone are frequently not reliable enough to avoid the need for biopsy (5,6).

Tumor angiogenesis is known to be critical for the autonomous growth and spread of breast cancers (7,8). This is a complex process involving both the incorporation of existing host blood vessels into the tumor and the creation of tumor microvessels. This process is moderated by tumor angiogenesis factors (9). In principle, the altered hemodynamics that accompany tumor angiogenesis provide the basis for discrimination between malignant and benign masses of the breast by color Doppler sonography (10). However, the diagnostic value of Doppler US in avoiding the need for biopsy has been limited. (11,12).

Optical tomography, a new technique that employs diffused light in the near infrared (NIR) spectrum, provides functional images of tumor angiogenesis and tumor hypoxia. It has recently been under investigation in several pilot clinical studies (13-19). If a single optical wavelength is used, the optical absorption related to tumor angiogenesis can be measured. If appropriately selected multiple wavelengths are used, the optical absorptions at these wavelengths can be measured and proportions of oxyhemoglobin (oxyHb) and deoxyhemoglobin (deoxyHb) can be calculated. The total hemoglobin concentration and tumor hypoxia can be calculated from oxyHb and deoxyHb distributions; these functional parameters are highly correlated with lesion malignancy (20). Optical tomography has not been used because the intense scattering caused by tissue limits imaging resolution as well as lesion localization. Co-registration of optical

tomography with US or MRI, has shown promise in overcoming these problems (17,19,22). A flexible light guide using optical fibers makes optical imaging compatible with many other imaging modalities and allows for simultaneous imaging under identical geometric conditions. The lesion structure information provided by other modalities can be used to assist optical imaging reconstruction and therefore reduce the location uncertainty and improve the quantification accuracy of light.

A prior optical tomography study using *a priori* lesion structural information provided by co-registered US has shown that two early stage invasive cancers had a two-fold higher total hemoglobin concentration compared with a small group of benign lesions (19). In this study, we further evaluate the optical tomography using *a priori* US information in a separate group of biopsy patients recruited from a different clinical site. We also compare optical tomography with Doppler US on mapping tumor angiogenesis.

Materials and Methods

Patients

The study was performed at the Radiology Department of Hartford Hospital from May 2003 to March 2004. The study protocol was approved by local IRB committee and DOD Medical Research and Materiel Command. Signed informed consent was obtained from all patients. The eligible patients were initially referred for US-guided biopsy and their lesions were identified by US at the time of the study. Those patients with lesions not visible in US were not studied except three with lesion location well estimated from either x-ray mammography or MRI films by one of the authors (E. B. C, A.A. C, H.S.V). The final study group consisted of 73 patients aged from 24 to 88 (mean 51). Of the 73 patients in the study, eight were excluded from analysis. One patient did not have US visible lesion after careful examination and two patients' optical data were not recorded appropriately due to equipment failure. Two patients had lesions very close to dark nipples and optical images showed nipple artifacts located at nipple-shadowing positions seen by US. Three patients had small dense breasts and the poor probe-tissue contact produced image artifacts.

Ultrasound examinations were performed with spatial image compounding and a 15 MHz linear transducer (Acuson Sequoia, 15L8). Based on US, x-ray and or MRI findings, one of the authors (E.B. C, A.A. C, H.S.V) scored each lesion to be biopsied using the BIRADs classification as normal, benign, probably benign, suspicious, and highly suspicious for malignancy. For Doppler US measurements, any persistent color Doppler signals were taken to represent blood vessels. The location of the vessels with respect to the lesion was documented as peripheral to the lesion, inside the lesion, or both.

NIR system

A hand-held hybrid probe was used, consisting of the commercially available US transducer located in the middle and near-infrared source-detector light guides (optical fibers) distributed at the periphery (see Fig.1). The technical aspects of the NIR imager have been described in detail previously (21). Briefly, the imager consisted of 12 pairs of dual wavelength (780nm and 830nm) laser diodes, which were used as light sources, and their outputs were coupled to the probe through optical fibers. On the receiving side, 8 photomultiplier (PMT) tubes were used to detect diffusely scattered light from the tissue and 8 optical fibers were used to couple detected light to the PMTs. The laser diodes' outputs were amplitude modulated at 140 MHz and the detector outputs were demodulated to 20KHz. Eight detection signals and one reference were amplified, sampled and acquired into a PC simultaneously. The entire data acquisition took about 3 to 4 seconds, which was fast enough for acquiring data from patients. For each patient, US images and optical measurements were acquired simultaneously before biopsy procedures at multiple locations including the lesion region, a normal region of the same breast, and a normal symmetric region of the contralateral breast. The optical data acquired at normal regions were used as reference for calculating the scattered field caused by lesions. The best reference data set was selected based on linear fitting result of received amplitude and phase profiles.

Optical Imaging Method

The details of our dual-mesh optical imaging reconstruction algorithm have been described previously (22-23). Briefly, the NIR reconstruction takes advantages of US localization of lesions and segments the imaging volume into finer grid in US identified lesion region and coarser grid in non-lesion regions. To account for possible larger angiogenesis extension of

ultrasound-identified lesions, we have used a much larger region of interest for finer grid lesion mapping. In all images, 0.5cm $\times$ 0.5cm $\times$ 0.5 cm imaging grid was used for lesion and 1.5cm $\times$ 1.5cm $\times$ 1 cm was used for background region. A modified Born approximation is used to relate the scattered field $U_{sd}(r_{si}, r_{di}, \omega)$ measured at the optical source (s) and detector (d) pair i to light absorption variations $\Delta\mu_a^{\lambda}(r')$ at wavelength λ in each volume element of two regions within the sample. The matrix form of image reconstruction is given by

$$[U_{sd}]_{M\times 1} = [W_L, W_B]_{M\times N}[M_L, M_B]^T{}_{Nx1} \qquad (1)$$

where W_L and W_B are weight matrices for lesion and background regions, respectively; $[M_L] = [\int_{1_L} \Delta\mu_a^{\lambda}(r')d^3r', \ldots\ldots \int_{N_L} \Delta\mu_a^{\lambda}(r')d^3r']$ and $[M_B] = [\int_{1_B} \Delta\mu_a^{\lambda}(r')d^3r', \ldots\ldots \int_{N_B} \Delta\mu_a^{\lambda}(r')d^3r']$ are total absorption distributions of lesion and background regions, respectively. The weight matrices are calculated based on the background absorption $\overline{\mu}_a^{\lambda}$ and reduced scattering $\overline{\mu}'_s{}^{\lambda}$ measurements obtained from the normal contralateral breast. Instead of reconstructing $\Delta\mu_a^{\lambda}$ distribution directly, as is done in the standard Born approximation, the total absorption distribution M is reconstructed and the total is divided by different voxel sizes of lesion and background tissue to obtain $\Delta\mu_a^{\lambda}$ distribution. By choosing a finer grid for lesion and a coarse grid for background tissue, we can maintain the total number of voxels with unknown optical absorption on the same scale of the total measurements. As a result, the inverse problem is less underdetermined. In addition, since the lesion absorption coefficient is higher than that of background tissue, in general, the total absorption of the lesion over a smaller voxel is on the same scale as the total absorption of the background over a bigger voxel. Therefore, the matrix $[M_L, M_B]$ is appropriately scaled for inversion.

Since the major chromophores are deoxygenated (deoxyHb) and oxygenated (oxyHb) hemoglobin in the wavelength range studied, we can estimate deoxyHb and oxyHb concentrations at each imaging voxel by inverting the following equations voxel by voxel as:

$$\begin{bmatrix} \mu_a^{\lambda_1}(r') \\ \mu_a^{\lambda_2}(r') \end{bmatrix} = \begin{bmatrix} \varepsilon_{Hb}^{\lambda_1}, \varepsilon_{HbO_2}^{\lambda_1} \\ \varepsilon_{Hb}^{\lambda_2}, \varepsilon_{HbO_2}^{\lambda_2} \end{bmatrix} \times \begin{bmatrix} deoxyHb(r') \\ oxyHb(r') \end{bmatrix} \tag{2}$$

$$\begin{bmatrix} deoxyHb(r') \\ oxyHb(r') \end{bmatrix} = \frac{1}{\Delta} \begin{bmatrix} \varepsilon_{HbO_2}^{\lambda_2}, -\varepsilon_{HbO_2}^{\lambda_1} \\ -\varepsilon_{Hb}^{\lambda_2}, \varepsilon_{Hb}^{\lambda_1} \end{bmatrix} \times \begin{bmatrix} \mu_a^{\lambda_1}(r') \\ \mu_a^{\lambda_2}(r') \end{bmatrix}. \tag{3}$$

where $\mu_a^{\lambda_1}(r')$ and $\mu_a^{\lambda_2}(r')$ are absorption coefficients obtained at imaging voxel r', where wavelengths λ_1 and λ_2 correspond to 780 nm and 830 nm in our system, respectively. εs are extinction coefficients given in Ref. [24]. The total hemoglobin concentration $totalHb(r') = deoxyHb(r') + oxyHb(r')$ can be calculated as:

$$totalHb(r') = \frac{1}{\Delta}\left\{\{\varepsilon_{HbO_2}^{\lambda_2} - \varepsilon_{Hb}^{\lambda_2}\}\mu_a^{\lambda_1}(r') + \{\varepsilon_{Hb}^{\lambda_1} - \varepsilon_{HbO_2}^{\lambda_1}\}\mu_a^{\lambda_2}(r')\right\} \tag{4}$$

Maximum and average lesion total hemoglobin concentrations were measured and the average was computed inside the lesion with the total hemoglobin concentration within 50% of the maximum value (FWHM).

The perturbations at each wavelength used to calculate absorption maps were normalized as $U_{sd}(r_{si}, r_{di}, \omega) = \frac{U_L(r_{si}, r_{di}, \omega) - U_N(r_{si}, r_{di}, \omega)}{U_N(r_{si}, r_{di}, \omega)} U_B(r_{si}, r_{di}, \omega)$, where $U_L(r_{si}, r_{di}, \omega)$ and $U_N(r_{si}, r_{di}, \omega)$ were optical measurements obtained at the lesion region and the normal region of the contralateral breast, and $U_B(r_{si}, r_{di}, \omega)$ was the calculated incident field using the measured background. This procedure cancels the unknown system gains associated with different sources and detectors as well as electronic channels.

Since the hand-held probe can be easily rotated or translated, at least three co-registered US and NIR data sets were acquired at the lesion location and the corresponding optical absorption maps as well as the total hemoglobin concentration distribution were reconstructed using the co-registered US. The data given in Table I and II are average values obtained from at least three sets of NIR images.

Statistical Analysis

The following parameters were calculated by using these formulas: Sensitivity = TP x 100/(TP + FN); specificity = TN x 100/(TN + FP); positive predictive value = TP x 100/(TP + FP); and negative predictive value = TN x 100/(TN + FN), where TP is true-positive findings, TN is true-negative findings, FP is false-positive findings, and FN is false-negative findings. Student's t distribution was used to calculate statistical significance.

Results

Table I lists results of malignant cases (n=8), fibroadenomas (n=20), fibrocystic changes (n=15), fibrosis (n=8), other benign solid lesions (n=8), complex cysts (n=21), and hyperplasia (n=1). The lesion biopsy results are given in column 1, the number of patients in each category is in column 2, average US BIRADS score and Doppler US appearance are given in columns 3 and 4, respectively, maximum total hemoglobin concentration of the lesion and the average total hemoglobin measured within FWHM are given in columns 5 and 6, respectively. The group average is given at the end of each category and Fig. 2 is the graph representation of mean maximum total hemoglobin values and standard deviations. No significant difference was found among benign groups but a more than two-fold higher total hemoglobin concentration was found in malignant (mean maximum 122 μ mol/liter ($\pm$ 26.8), mean average 88 μ mol/liter ($\pm$ 24.5) measured within FWHM) versus benign groups (mean maximum 55 μ mol/liter($\pm$ 24.8), mean average 38 μ mol/liter ($\pm$ 17.4) measured within FWHM). Both maximum and average of total hemoglobin level were statistically significantly higher in the malignant group than the benign group ($P<0.001$). Figure 3 is the scattered plot of malignant group (square), fibroadenoma (diamond), fibrocystic changes (triangle), fibrosis (solid circle), other benign (short bar), complex cysts (longer bar), and hyperplasia (square, right end). If 95 μ mol/liter was chosen as a threshold to separate malignant and benign lesions, the NIR data of two fibroadenomas and one minimal non-atypical hyperplasia and fibrosis (classified as fibrosis) are above the threshold. The size, US diagnosis and NIR parameters of these three false positives are given in Table II. The sensitivity, specificity, positive predictive value, and negative predictive value were 100% (8 of 8), 96% (70 of 73), 73% (8 of 11), and 100% (70 of 70).

Optical tomography also provides higher sensitivity and specificity than Doppler US. Although Doppler US blood flow was demonstrated in five out of eight malignant cases, blood flow was also present in 30% of fibroadenomas, 46% of fibrocystic changes, 29% of fibrosis, 50% of other benign solid lesions and 19% of complex cysts. Since the diffused light probes microvessel density rather than relatively large blood vessels as the Doppler US does, the sensitivity and specificity of optical contrast are expected to be much higher than Doppler US.

Example 1

A 45-year old woman had a suspicious lesion located at 3 o' clock position shown on MRI. The lesion was identified sonographically at the time of biopsy as ill-defined slightly heterogeneous, mildly hypoechoic mass of 6 mm in diameter. Doppler US revealed large blood vessels both inside and at the periphery of the lesion (Fig.4 (a)). US images and optical measurements were obtained simultaneously before an US-guided biopsy procedure. Pathology revealed intraductal and invasive mammary duct carcinoma (nuclear grade III, histologic grade III).

Optical absorption maps of lesion region at both wavelengths 780nm and 830 nm were reconstructed as shown in Fig. 4(b) and (c). The first slice is the spatial x-y image of 0.5 cm deep from the skin surface and the last slice is 3.5 cm deep toward the chest wall. The dimensions of each slice are 9 cm by 9 cm. The spacing between the slices is 0.5 cm. The vertical scale is the absorption coefficient in unit of cm^{-1}. The lesion is well resolved in slice #2. The total hemoglobin concentration map is shown in Fig 4. (d) and the vertical scale is in μ mol/liter. The measured maximum value at lesion area is 162.0 μ mol/liter with the average value of 121.1 μ mol/liter calculated within FWHM. The average background total hemoglobin

outside of the FWHM region is 29.1 μmol/liter. The average maximum total hemoglobin concentration at the cancer region obtained at slightly different probe positions is 149.91 μmol/liter ($\pm$ 39.23 μmol/liter) and the average background total hemoglobin concentration is 29.03 μmol/liter ($\pm$ 0.18 μmol/liter). The large standard deviation obtained from slightly different probe positions is likely due to the probe compression at different positions and elastic properties of the blood vessels in the cancer region.

Example 2

A 37-year old woman had a known infiltrating lobular carcinoma (nuclear grade II-III) located at 12 o'clock position of the right breast and measuring 1 cm in size by US at the time of this study (Fig. 5(a)). No blood vessels or flow were identified by Doppler US. The total hemoglobin concentration map of the carcinoma is shown in Fig.5 (b). The cancer is well resolved in slices #3 and #4 and shown 110.4 μmol/liter maximum and 77.8 μmol/liter average total hemoglobin concentration within FWHM, respectively. The mean maximum hemoglobin concentration of three NIR scans at slightly different probe locations is 102.1 μmol/liter and the mean within FWHM of the three NIR scans is 68.7 μmol/liter. Two new lesions located at 7 o'clock of the same breast and 10 o'clock of the contralateral breast previously shown by MRI were identified sonographically at the time of the biopsy measuring 6 and 7 mm in diameter, respectively. Figure 6 (a) is the US image of the 7 o'clock right breast lesion and (b) is the total hemoglobin concentration map of the lesion. No blood vessels or flow were identified in new lesions by Doppler US. No resolvable lesion was found in the hemoglobin map and the maximum total hemoglobin concentration is only 24.2 μmol/liter. The biopsy result revealed benign non-proliferative fibroadipose breast tissue with focal microcystic alteration, apocrine

metaplasia and periductal chronic mastitis. No atypical cells were found. The 10 o'clock suspicious lesion of the contralateral breast had similar ultrasonic and optical characteristics. No resolvable lesion was found in the hemoglobin concentration map and the maximum total hemoglobin concentration is only 27.5 μ mol/liter. The biopsy result revealed benign proliferative fibroadipose breast tissue with focal aprocrine papillary epitheliosis. No atypical cells were found.

Example 3

A 75-year old woman had a suspicious lesion with solid component (pointed by the arrow in Fig. 7 (a)) adjacent to a cyst. The lesion was located at 9 o'clock of the right breast. Doppler US has shown several large blood vessels located at the peripheral of the lesion. The total hemoglobin concentration map is shown in Fig. 7(b) and the distributions are quite diffused as compared with the localized distributions of malignant cancer cases. The measured maximum total hemoglobin concentration is 38.18 μ mol/liter and the average measured within FWHM is 26.31 μ mol/liter. The lesion was an intraductuctal papilloma with no evidence of atypical cells or malignancy.

Example 4

A 59-year old woman had a simple cyst with adjacent complex cyst or solid nodule as pointed by the arrow shown in Fig. 8 (a). The lesion was measured as 1.3 cm $\times$ 1.0 cm and located at 3:30 o'clock of the left breast. The complex cyst was aspirated completely with no residual abnormality left. The light absorption maps (not shown) as well as the total hemoglobin map (see Fig. 8(b)) indicate low light absorption and therefore low hemoglobin concentration at the central location of the cyst (pointed by the arrow in (b)). An incomplete ring with higher light absorption and therefore high hemoglobin concentration surrounding the cyst is observed.

Although the measured total hemoglobin concentration is the highest in the complex cyst group due to the higher absorption ring (maximum 94 μ mol/liter and average 62.8 μ mol/liter measured within FWHM), the distribution is obviously different from the malignant cases. Cysts in general have very low light absorption due to low water absorption in the wavelength range studied and therefore low hemoglobin concentration. The higher absorption ring is likely caused by the cyst wall. This example suggests that both hemoglobin distribution and threshold level have to be evaluated for accurate diagnosis of suspicious lesions.

Discussion

With the increased public awareness of the potential benefits of early detection of breast cancer, more women are now practicing self-examination and undergo periodic screening (26). As a result, more lesions are being detected by palpation, screening mammography and screening MRI for high risk or dense breasts. Consequently, radiologists and surgeons are performing an increasing number of breast biopsies, 60-80% of these revealing benign findings (27). Accurate non- invasive methods of distinguishing malignant from benign lesions could help to reduce the number of biopsies for lesions that prove to be benign. US is frequently used as an adjunct tool to x-ray mammography in differentiating simple cysts from solid lesions and also plays an important role in guiding interventional procedures such as needle aspiration, core-needle biopsy, and prebiopsy needle localization (4, 25). Recently, screening US has also been recommended for the dense breast (28-29). Our technique of using optical tomography with US localization has demonstrated a great potential for non-invasively distinguishing malignant and benign masses and therefore a potential role for reducing benign biopsies. Earlier results obtained from two invasive early stage cancers and 17 benign lesions have shown that malignant cancers of 1 cm in size present an average of 119 μmol/liter maximum total hemoglobin concentration while the benign group has an average of 67 μmol/liter (19). A nearly two fold higher contrast has been obtained. This paper with 8 early stage cancer cases and a group of 52 benign solid lesions and 21 complex cysts obtained from different clinical site further demonstrates the diagnostic potential of this technique. Again, the invasive cancers reveal more than two-fold greater total hemoglobin concentration. No false negatives were present in the reported study. Since our samples are limited, we plan to undertake a larger, prospective clinical trial to validate these results.

One potential limitation of optical tomography could be imaging lesions very close to dark nipple-areolar tissue. Since the light absorption of the dark skin is high, the light perturbations attributed by lesions may be secondary to the perturbation cased by the nipple-areolar complex. Therefore, optical imaging reconstruction may not reconstruct lesions correctly. Two cases that were excluded from analysis were caused by this problem. Lighter-colored nipple-areolar complex skin did not appear to cause a problem. Lesions more than 2 cm away from a dark nipple did not cause artifacts.

Another potential problem is the poor probe-tissue contact when examining small dense breasts. Three cases that were excluded from the analysis were related to this problem. By developing probes of different sizes suitable for smaller breasts, good probe-tissue contact may be achieved. Currently, we have designed an optical switch, which will allow selection of different probes suitable for the size of the examined breast.

Three benign lesions, including two fibroadenomas and one minimally non-atypical duct hyperplaisa and fibrosis also showed high total hemoglobin concentration which suggested high microvessel density. The high total hemoglobin concentration of fibroadenoams may be explained by a pilot study on vascular features of fibroadenoma (30), where two different groups of fibroadenomas were recognized. The first group showed low microvascular permeability and high extracellular volume fraction. The low vascular permeability was shown histopathologically to have a lower density of small vessels. The second group showed higher

microvascular permeability and a lower extracellular volume fraction. The higher microvascular permeability was shown to have a higher density of small vessels than that of the first group. The patient with minimally non-atypical duct hyperplaisa and fibrosis (case 3 in Table II) showed significant enhancement on MRI, suggesting increased vascularity in that area.

We do not envision that our technique will be used as a screening tool since US visible lesions are needed to map out the target and background regions for dual-mesh optical imaging reconstruction. If lesion locations can be accurately estimated from other imaging modalities, for example MRI, our technique could be expanded for lesion characterization using those modalities as well. However, more precise depth information is required if data obtained from other modalities are not co-registered with the NIR data. The three reported cases with lesions seen by MRI or mammogram were reconstructed with accurate *a priori* knowledge of lesion location.

Due to intense light scattering, optical tomography alone has not been widely used in clinical studies. The data in the published literature have been limited to feasibility studies or case reports. In addition, systems used to acquire optical tomography data vary considerably. Most of the optical systems use transmission geometry, where the light sources and detectors are either deployed around the examined breast in a single or multiple rings (13,16) or light sources deployed on one side of the breast and detectors on the opposite side with the breast compressed in between (17,18). It is very clear that without *a priori* knowledge of lesion locations from other imaging modalities, no one has achieved significant and consistent improvements in accurate light quantification and therefore, differentiation between benign and malignant

processes. The only example found in the literature, which was related to our study, was reported in (15, 31). The authors reported an average of 35 μmol/liter total hemoglobin concentration in a 2 cm ductal carcinoma in situ by using NIR measurements alone. After re-processing the same NIR measurement data using an approximate lesion depth obtained from a separate US image, the calculated average total hemoglobin concentration was increased to 67 μmol/liter (31). This value is closer to average of 88 μmol/liter obtained from 8 malignant cases reported here.

In principle, the distribution of oxygenation saturation can be estimated as Y = oxyHb /(oxyHb+deoxyHb) with deoxyHb and oxyHb distributions calculated from absorption maps at the two wavelengths of 780 nm and 830 nm. However, since background tissue mainly consists of water and lipid and these two chromophores contribute to the total absorption estimate as well, we could not obtain reasonable background oxygenation saturation and compare it with lesion oxygenation saturation. Currently, we are in the process of adding more wavelengths to the NIR system. Nevertheless, initial experience with a small group of cancer cases suggests that the deoxyHb concentration of malignant lesions may not be as significant as stressed by previous investigators but the total hemoglobin concentration is highly specific in differentiating small invasive malignant cancers from benign lesions.

The reported malignant cases were generally early stage (approximately 1 cm in size except one with size of 2. 2 cm). For larger cancers, the angiogenesis distributions are complex and distorted (22). The value of optical tomography in larger tumors may be to map tumor angiognesis and evaluate vascular changes as well as tumor hypoxia during chemotherapy. This

type of information could prove invaluable in monitoring chemotherapy responses of breast cancer treatment and assessing treatment efficacy and will be evaluated in a planned future study.

Acknowledgements:

Roxanne P. Rotondaro, Coordinator of Partnership for Breast Care of Hartford Hospital, is greatly acknowledged for coordinating this research project. The US technologists Mariana Armandi, Elaine Potonec, Muna Buser, Mehdi Sedigh and Tom Samsel of Radiology Department of Hartford Hospital are extremely helpful in assisting US data acquisition and patent scanning. Dr. Frederick Conard of Radiology Department of Hartford Hospital is acknowledged for initiating the clinical study at Hartford Hospital. Martha Ahlquist, Coordinator of Clinical Research Office of Hartford Hospital, is thanked for consenting patients. Dr. Daqing Piao of ECE Dept of University of Connecticut is acknowledged for his continuous help on NIR probe improvements. The clinical study is funded by DOD ARMY Breast Cancer Program (DAMD17-00-1-0217). We also thank the following funding agents for the partial support: Donaghue Foundation and NIH (5R01EB002136).

References:

1. Howard J. Using mammography for cancer control: an unrealized potential. Cancer 1987; 33:33-48.
2. Hilton SW, Leopold GR, Olson LK, Willson SA. Real-time breast sonography: application in 300 consecutive patients. AJR 1986; 147:479-486.
3. Rubin E, Miller VE, Berland LL, Han SY, Koehler RE, Stanley RJ. Hand-held real-time breast sonography. AJR 1985; 144:623-627.
4. Jackson VP. The current role of ultrasonography in breast imaging. Radiol Clin North Am 1995; 33: 1161-1170.
5. Sickles EA, Filly FA, Callen PW. Breast cancer detection with ultrasonography and mammography: comparison using state-of-the-art equipment. AJR 1983; 140:843-845.
6. Rahbar G, Sie AC, Hansen GC, Prince JS. Melany ML, Reynolds HE. Jackson VP, Sayre JW and Bassett LW. Benign versus malignant solid masses: US differentiation. Radiology 1999; 213:889-894.
7. Schor AM, Schor SL. Tumour angiogenesis. J Pathol 1983; 141:385-413.
8. Folkman J, Watson K, Ingber D, Hanahan D. Induction of angiogenesis during the transition from hyperplasia to neoplasia. Nature 1989; 339:58-61.
9. Vaupel P, Kallinowski F, Okunieff P. Blood flow, oxygen and nutrient supply, and metabolic microenvironment of human tumors: a review. Cancer Research 1989; 49: 6449-6465.
10. Taylor KJW, Ramos I, Carter D. et al. Correlation of Doppler US tumor signals with neovascular morphologic features. Radiology 1988; 166-57.

11. Wilkens TH, Burke BJ, Cancelada DA, Jatoi I. Evaluation of palpable breast masses with color Doppler sonography and gray scale imaging. J Ultrasound Med 1998; 17:109-115.

12. Reinukainen H, Rissanen, T, Paivansalo, M, Paakko, E, jauhiainen, J, and Suramo, I. B-mode, power Doppler and contrast-enhanced power Doppler ultrasonography in the diagnosis of breast tumors. Acta Radiologica 2001; 42 (1): 106-113.

13. Pogue B, Poplack SP, McBride TO, Wells WA, Osterman K, Osterberg U, and Paulsen KD. Quantitative hemoglobin tomography with diffuse near-infrared spectroscopy: pilot results in the breast. Radiology 2001; 218: 261-266.

14. Franceschini MA, Moesta KT, Fantini S, Gaida G, Gratton E, Jess H, Seeber M, Schlag PM, Kashke M. Frequency-domain techniques enhance optical mammography: initial clinical results. Proc. of Nat. Ac. of Sci., 1997; 94: 6468-6473.

15. Tromberg B, Shah N, Lanning R, Cerussi A, Espinoza J, Pham T, Svaasand L, and Butler J. Non-Invasive in vivo characterization of breast tumors using photon migration spectroscopy. Neoplasia 2000; 2(1:2): 26-40.

16. Jiang H, Xu Y, Iftimia N, Eggert J, Klove K, Baron L and Fajardo L (2001). Three-dimensional optical tomographic imaging of breast in a human subject. IEEE Trans on Medical Imaging, **20**(12), 1334-1340.

17. Ntziachristos V, Yodh A, Schnall M., and Chance B. Concurrent MRI and diffuse optical tomography of breast after indocyanine green enhancement. Proc. of Nat. Ac. of Sci. 2000; **97** (6): 2267-2772.

18. Grosenick D., Moesta KT., Wabnitz H., Mucke J., Stroszczynski C., Macdonald R., Schlg P, and Rinneberg H . Time-domain optical mammography: initial clinical results on detection and characterization of breast tumors. Applied Optics 2003; 42(16): 3170-3186.

19. Zhu Q., Huang, MM, Chen, NG, Zarfos, K, Jagjivan, B, Kane, M, Hegde P, Kurtzman, SH. Ultrasound-guided optical tomographic imaging of malignant and benign breast lesions. Neoplasia 2003; 5(5): 379-388.

20. Brown J.M. The Hypoxic cell. Cancer Research 1999; 59(23):5863-5870.

21. Chen NG, Guo PY, Yan SK, Piao DQ, and Zhu Q. Simultaneous near infrared diffusive light and ultrasound imaging. Applied Optics 2001; **40** (34): 6367-6380.

22. Zhu Q, Chen NG, Kurtzman HS. Imaging tumor angiogenesis by the use of combined near infrared diffusive light and ultrasound. Optics Letters 2003; **28** (5): 337-339.

23. Huang, MM and Zhu, Q. A Dual-mesh optical tomography reconstruction method with depth correction using a priori ultrasound information. Applied Optics 2003; 43(8):1654-1662.

24. Cope M, Ph.D Dissertation, University of College London, 1991.

25. Fornage BD, Coan JD, David CL. Ultrasound-guided needle biopsy of the breast and other interventional procedures. Radiol Clin North Am 1992; 30:167-185.

26. Baines CJ, Miller AB, Bassett AA. Physical examination: its role as a single screening modality in the Canadian National Breast Screening Study. Cancer 1989; 63:1816-1822.

27. Selzer MH. The significance of breast complaints as correlated with age and breast cancer. Am Surg 1992; 58:413-417.

28. Bassett LW, Ysrael M, Gold RH, Ysrael C. Usefulness of mammography and sonography in women less than 35 years of age. Radiology 1991; 180:831-835.

29. T.M. Kolb, J. Lichy and J. H. Newhouse. Occult cancer in women with dense breast: detection with screening US - diagnostic yield and tumor characteristics. Radiology 1998; **207**: 191-199.

30. Weinstein D, Strano S, Cohen, P., Fields S., J. Gomori, HM and Hadassa Degani H., Breast Fibroadenoma: Mapping of Pathophysiologic Features with Three-Time-Point, Contrast-enhanced MR Imaging—Pilot Study. Radiology 1999; 210: 233-240.

31. Jholboke M, Tromberg B, Li X, Shah N, Fishkin J, Kidney D, Butler J, Chance B, and Yodh A. Three-dimentional diffuse optical mammography with ultrasound localization in human subject. Journal of Biomedical Optics 2000; **5**(2), 237-247.

Figure Captions

Fig. 1. Picture of the combined probe and frequency domain NIR imager. A commercial US probe is located at the center of the combined probe and the optical source and detector fibers are distributed at the periphery of the US probe. Since the diffused photons launched from a source and received by a detector travel a "banana" path, lesions underneath the US probe can be imaged with high sensitivity.

Fig.2. The average maximum total hemoglobin concentration obtained from 7 groups of carcinoma (121.6 μmol/liter ($\pm$26.8)), fibroadenomas (65.9 μmol/liter ($\pm$25.5), fibrocystic changes (55.6 μmol/liter ($\pm$16.6), fibrosis (66.2 μmol/liter ($\pm$31.2), other solid benign (55.2 μmol/liter ($\pm$25.2), complex cysts(40.7 μmol/liter ($\pm$21.3), hyperplasia (56.2 μmol/liter).

Fig.3. Scattered plot of carcinoma (square), fibroadenomas (diamond), fibrocystic changes (triangle), fibrosis(circle), other solid benign (short bar), complex cysts(longer bar), hyperplasia (circle, right end).

Fig. 4. (ID41P2). (a) US image of a suspicious lesion located at 3 o'clock of the left breast of a 45-year old woman. Doppler US revealed large blood vessels both inside and at peripheral of the lesion. Pathology revealed intraductal and invasive mammary duct carcinoma (nuclear grade III, histologic grade III). (b) and (c) are optical absorption maps obtained at 780 nm and 830 nm, respectively. The unit of optical absorption is cm^{-1} ranging from 0.0 to 0.3 cm^{-1}. The first slice is the spatial x-y image of 0.5 cm deep from the skin surface and the last slice is 3.5 cm toward the chest wall. The spacing between the

slices is 0.5 cm. The lesion is well resolved in slice #2. (d) The total hemoglobin concentration map computed from absorption maps of (b) and (c). The vertical scale is the total hemoglobin concentration in μ mol ranging from 0 to 150 μ mol/liter.

Fig. 5. (ID52P7). (a) US image of an infiltrating lobular carcinoma located at 12 o'clock position of the right breast of a 37-year old woman. The lesion was measured 1 cm in size by US at the time of this study. No blood vessels or flow were seen by Doppler US. (b) The total hemoglobin concentration map computed from absorption maps obtained at 780nm and 830nm (not shown). The lesion is well resolved in slices #3 and #4. The vertical scale is the total hemoglobin concentration in μ mol ranging from 0 to 150 μ mol/liter.

Fig. 6. (ID52P17). (a) US image of a suspicious lesion located at 7 o'clock of the right breast of the same patient with an infiltrating lobular carcinoma shown in Fig.5. No blood vessels or flow were seen by Doppler US. The biopsy result revealed benign non-proliferative fibroadipose breast tissue. (b) The total hemoglobin concentration map computed from absorption maps of 780nm and 820nm (not shown). The vertical scale is the total hemoglobin concentration in μ mol ranging from 0 to 150 μ mol/liter.

Fig. 7. (ID54P3). (a) US image of a suspicious lesion located at 9 o'clock of the right breast of a 75-year old woman. Large blood vessels were seen by Doppler US at the peripheral of the lesion. The biopsy result revealed that the lesion was intraductuctal papilloma with no evidence of atypical cells or malignancy. (b) The total hemoglobin concentration map computed from absorption maps of 780nm and 830nm (not shown).

The vertical scale is the total hemoglobin concentration in μmol ranging from 0 to 150 μmol/liter.

Fig. 8 ((D39P2). A 59-year old woman had a simple cyst with adjacent complex cyst or solid nodule as pointed by the arrow shown in (a). The lesion was located at 3:30 o'clock of the left breast. The complex cyst was aspirated completely with no residual abnormality left. The light absorption maps (not shown) as well as the total hemoglobin map in (b) indicate low light absorption and therefore low hemoglobin concentration at the central location of the cyst close to origin in slice 2. An incomplete ring with higher light absorption and therefore high hemoglobin concentration surrounding the cyst is observed.

Table Captions

Table I: Biopsy results, US findings and NIR parameters of lesions.

Table II: Biopsy results, US and NIR parameters of three false positives.

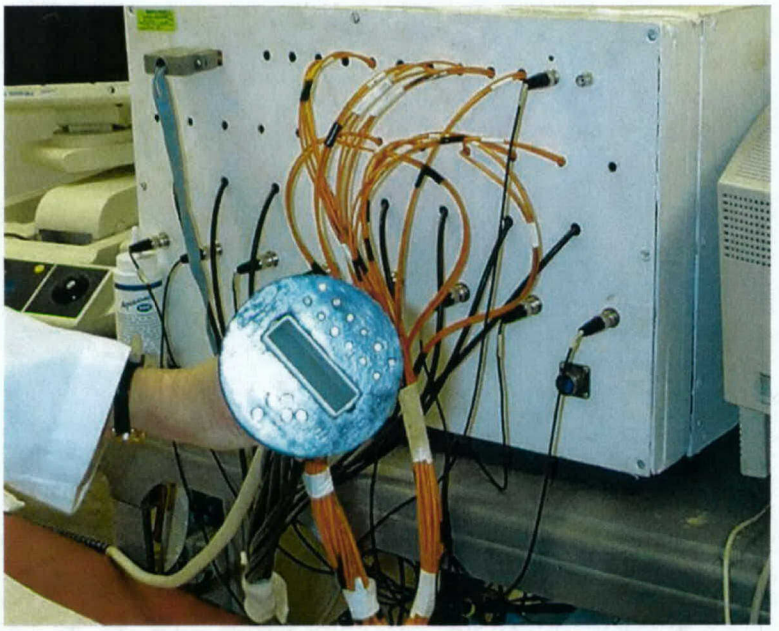

Fig.1. Picture of the combined probe and frequency domain NIR imager. A commercial US probe is located at the center of the combined probe and the optical source and detector fibers are distributed at the periphery of the US probe. Since the diffused photons launched from a source and received by a detector travel a "banana" path, lesions underneath the US probe can be imaged with high sensitivity.

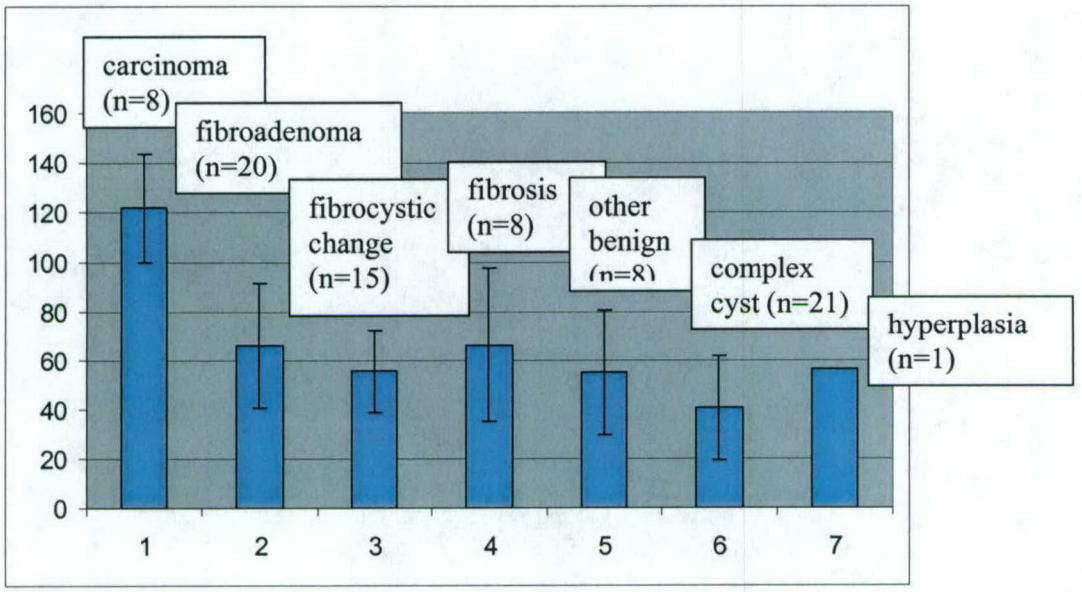

Fig. 2. Graph indicates mean value of maximum total hemoglobin concentration of each group and standard deviation (bar). Horizontal: group numbers. Vertical: total hemoglobin concentration in μ mol/liter

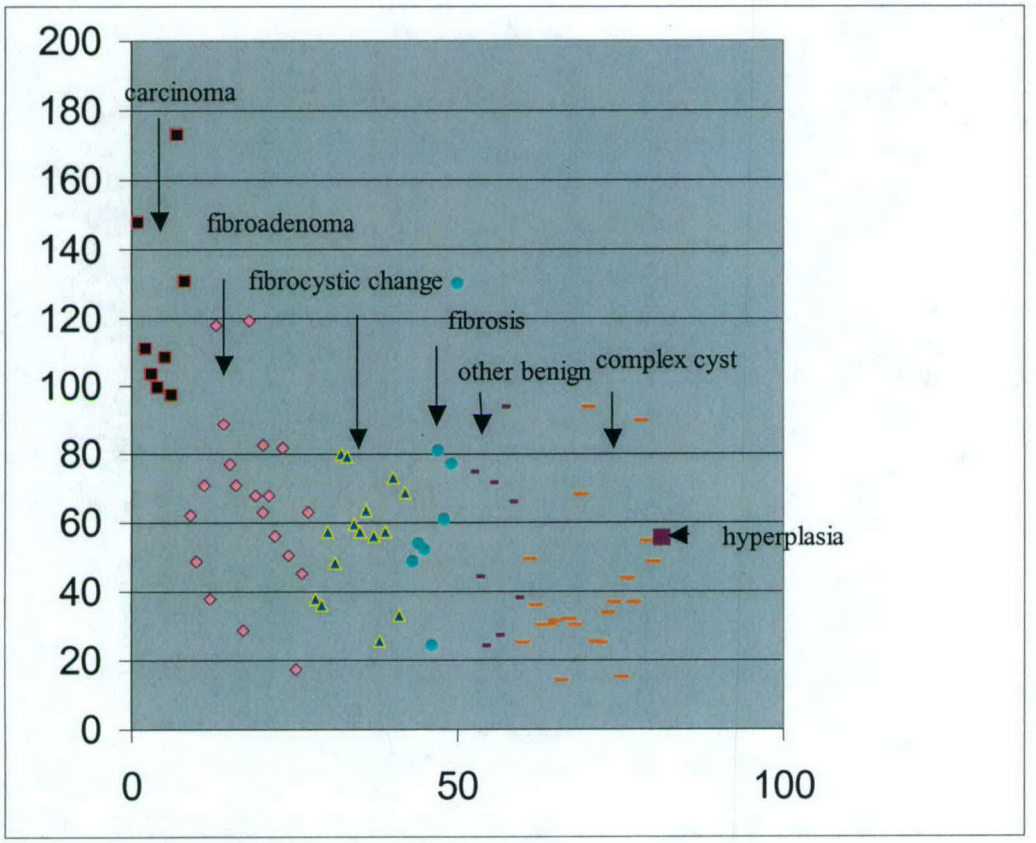

Fig.3. Scatter plot of carcinoma (square), fibroadenoma (diamond), fibrocystic changes (triangle), fibrosis (solid circle), other solid benign (short bar), complex cysts (longer bar), hyperplasia (square, right end). Horizontal: patient numbers. Vertical: maximum total hemoglobin concentration in μ mol/liter.

(color print)

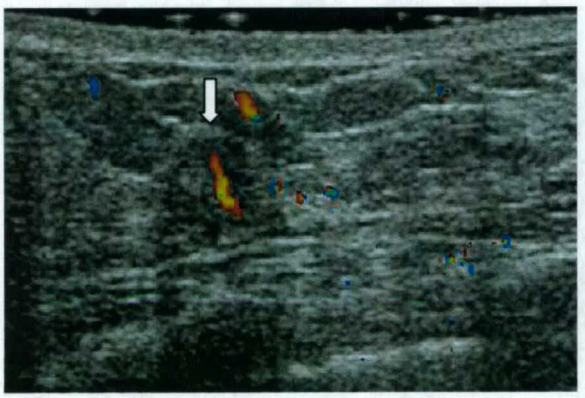

(a)

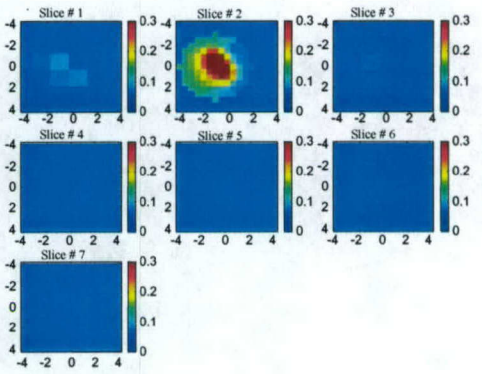

(b)

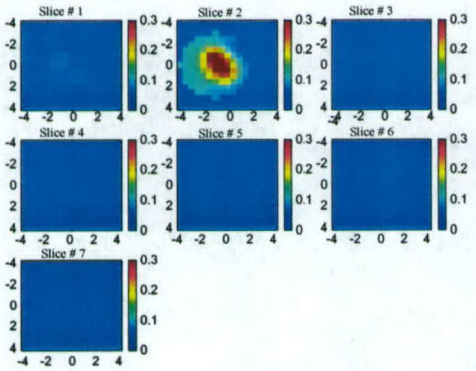

(c)

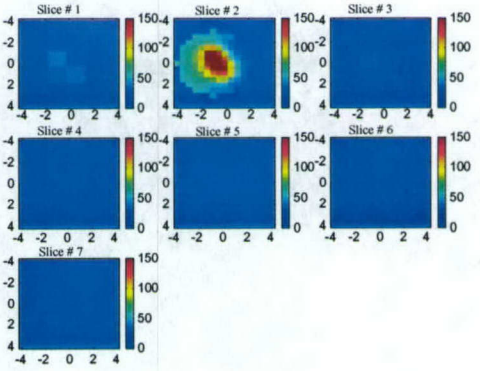

(d)

Fig. 4. (ID41P2). (a) US image of a suspicious lesion located at 3 o'clock of the left breast of a 45-year old woman. Doppler US revealed large blood vessels both inside and at peripheral of the lesion. Pathology revealed intraductal and invasive mammary duct carcinoma (nuclear grade III, histologic grade III). (b) and (c) are optical absorption maps obtained at 780 nm and 830 nm, respectively. The unit of optical absorption is cm^{-1} ranging from 0.0 to 0.3 cm^{-1}. The first slice is the spatial x-y image of 0.5 cm deep from the skin surface and the last slice is 3.5 cm toward the chest wall. The spacing between the slices is 0.5 cm. The lesion is well resolved in slice #2. (d) The total hemoglobin concentration map computed from absorption maps of (b) and (c). The vertical scale is the total hemoglobin concentration in μ mol/liter ranging from 0 to 150 μ mol/liter.

(Fig. 5 (b): color print)

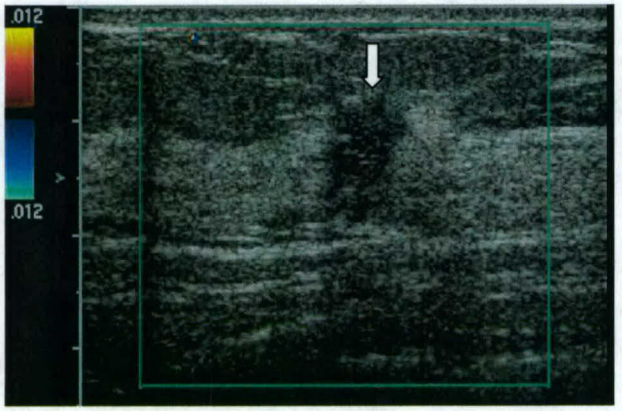

(a)

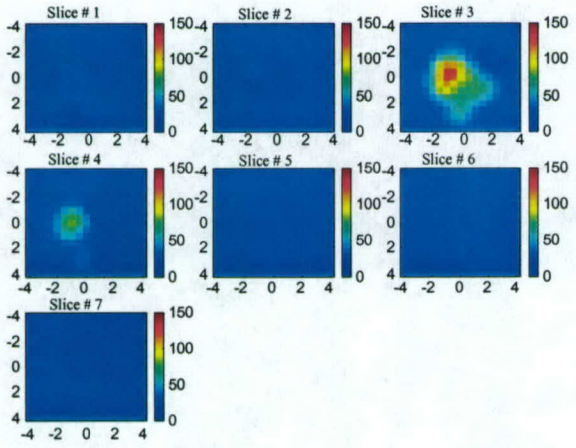

(b)

Fig. 5. (ID52P7). (a) US image of an infiltrating lobular carcinoma located at 12 o'clock position of the right breast of a 37-year old woman. The lesion was measured 1 cm in size by US at the time of this study. No blood vessels or flow were seen by Doppler US. (b) The total hemoglobin concentration map computed from absorption maps of 780nm and 830nm. The lesion is resolved in slices #3 and #4. The vertical scale is the total hemoglobin concentration in μ mol/liter ranging from 0 to 150 μ mol/liter.

(Fig. 6 (b): color print)

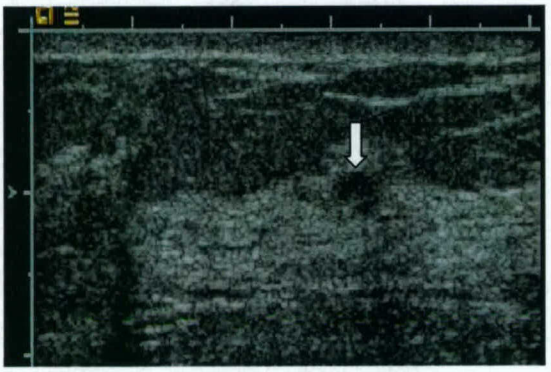

(a)

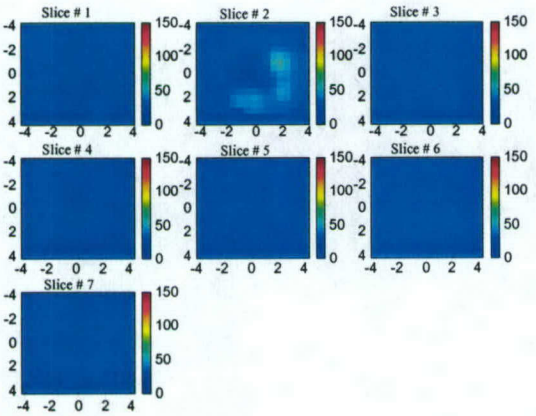

(b)

Fig. 6. (ID52). (a) US image of a suspicious lesion located at 7 o'clock of the right breast of the same patient with an infiltrating lobular carcinoma shown in Fig.5. No blood vessels or flow were seen by Doppler US. The biopsy result revealed benign non-proliferative fibroadipose breast tissue. (b) The total hemoglobin concentration map computed from absorption maps of 780nm and 830 nm (not shown). The vertical scale is the total hemoglobin concentration in μ mol/liter ranging from 0 to 150 μ mol/liter.

(color print)

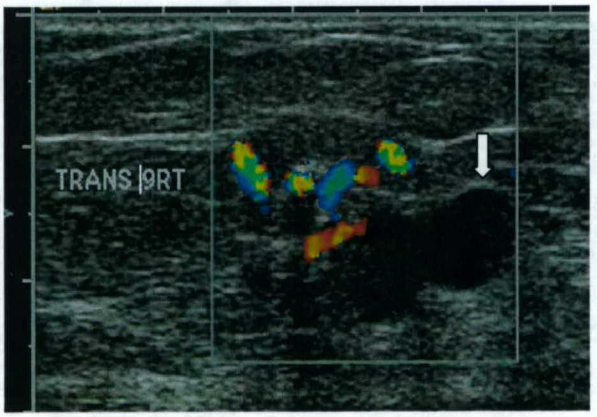

(a)

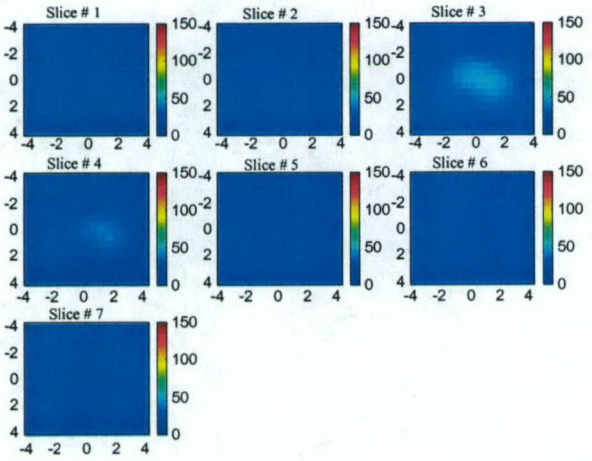

(b)

Fig. 7. (ID54P3). (a) US image of a suspicious lesion located at 9 o'clock of the right breast of a 75-year old woman. Large blood vessels were seen by Doppler US at the peripheral of the lesion. The biopsy result revealed that the lesion was intraductuctal papilloma with no evidence of atypical cells or malignancy. (b) The total hemoglobin concentration map computed from absorption maps of 780nm and 830 nm (not shown). The vertical scale is the total hemoglobin concentration in μ mol/liter ranging from 0 to 150 μ mol/liter.

(Fig. 8 (b): color print)

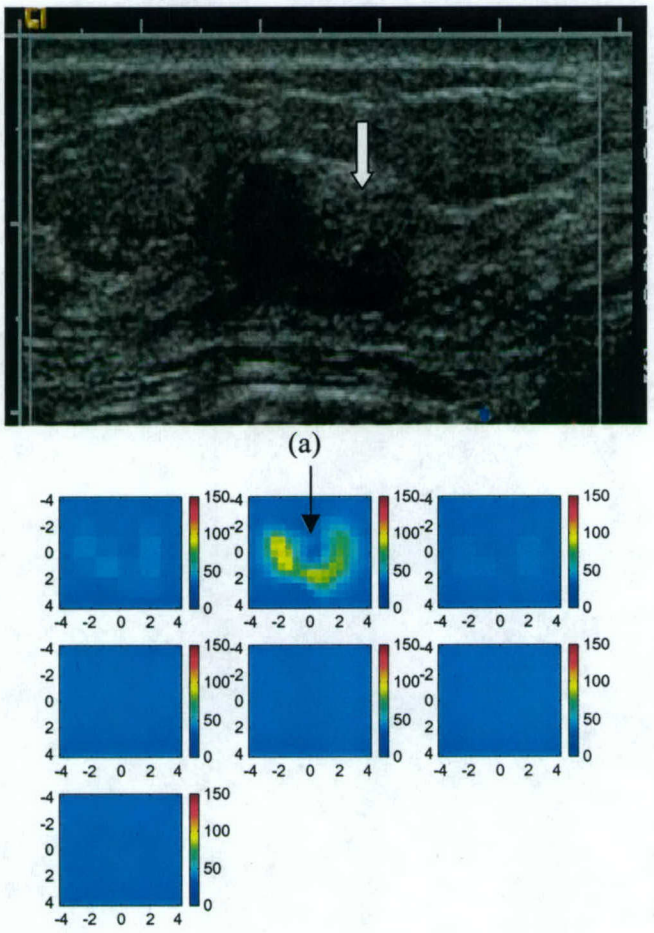

Fig. 8 (D39P2). A 59-year old woman had a simple cyst with adjacent complex cyst or solid nodule as pointed by the arrow shown in (a). The lesion was located at 3:30 o'clock of the left breast. The complex cyst was aspirated completely with no residual abnormality left. The light absorption maps (not shown) as well as the total hemoglobin map in (b) indicate low light absorption and therefore low hemoglobin concentration at the central location of the cyst close to origin in slice 2. An incomplete ring with higher light absorption and therefore high hemoglobin concentration surrounding the cyst is observed.

Table I: Lesion characteristics, US findings and optical tomography parameters

Lesion Characteristics (biopsy results, lesion size)	Patient number	US & Doppler BIRADS	Doppler	Total Hb in μmol/liter maximum	average in FWHM
Intraductal and invasive mammary duct carcinoma (0.6 cm)	1	4	both	147.9	109.5
Intraductal and invasive mammary Duct carcinoma (2.2 cm)	1	known	peripheral	103.8	69.7
Invasive ductual carcinoma ($\leq$1cm)	2	5	peripheral	151.8($\pm$29.7)	116.4($\pm$11.7)
Infiltrating lobular carcinoma (0.9cm)	1	known	no flow	102.1	68.7
Invasive mammary duct carcinoma &DCIS (1.1 cm)	1	5	peripheral	97.5	67.7
Infiltrating ductal carcinoma &DCIS (1 cm)	1	4	no flow	100.0	68.4
Infiltrating mammary ductal carcinoma (0.9cm)	1	5	no flow	108.5	78.7
Group Average	**(n=8)**	**4.6($\pm$0.5)**		**121.6($\pm$26.8)**	**88.4($\pm$24.5)**
Fibroadenoma(1.0cm ($\pm$ 0.6cm))	2	4($\pm$0.0)	both	55.7 ($\pm$38.2)	37.7($\pm$28.4)
Fibroadenoma (0.9cm ($\pm$ 0.3cm))	4	4 ($\pm$0.0)	peripheral	54.9 ($\pm$9.6)	38.7($\pm$7.4)
Fibroadenoma (0.8cm ($\pm$ 0.4cm))	14	3.8($\pm$0.6)	no flow	70.5 ($\pm$27.2)	49.5($\pm$19.4)
Group Average	**(n=20)**	**3.9 ($\pm$0.5)**		**65.9($\pm$ 25.5)**	**46.1($\pm$18.3)**
Fibrocystic change(0.6cm ($\pm$ 0.2cm))	5	3.8 ($\pm$0.4)	peripheral	43.3 ($\pm$ 14.5)	29.6($\pm$9.7)
Fibrocystic change (0.8cm ($\pm$ 0.5cm))	7	3.9($\pm$0.38)	no flow	56.5 ($\pm$14.0)	40.3($\pm$10.4)
Fibrocystic change (0.8cm ($\pm$ 0.3cm))	2	4($\pm$0.0)	x-ray or MRI visible	76.7 ($\pm$ 4.9)	51.1($\pm$ 11.4)
Fibrocystic change(0.6cm)	1	4	inside	68.7	48.5
Group Average	**(n=15)**	**3.9($\pm$0.4)**		**55.6($\pm$ 16.6)**	**38.9($\pm$ 11.9)**
Fibrosis (0.8cm)	1	4	both	81.2	57.8
Fibrosis (0.4cm)	1	4	peripheral	49.0	31.0
Fibrosis (1.0cm ($\pm$ 0.8cm))	5	4 ($\pm$0.0)	no flow	68.4($\pm$37.9)	47.3($\pm$26.1)
Fibrosis	1	4	x-ray visible	54.0	36.3
Group Average	**(n=8)**	**4($\pm$0.0)**		**66.2($\pm$31.2)**	**45.2($\pm$21.3)**
Other Benign					
Tubular adenoma (0.4cm)	1	4	both	94.1	65.2
Intraductal papilloma (1.5cm)	1	4	peripheral	38.3	26.6
Tubular adenoma(0.4cm)	1	4	peripheral	66.2	45.8
Normal tissue (1.0cm ($\pm$ 0.4cm))	4	3.5($\pm$0.6)	no flow	42.8($\pm$ 23.2)	29.3($\pm$ 14.2)
Ductual and stromal cells (0.3cm)	1	4	inside	72.0	53.1
Group Average	**(n=8)**	**3.8($\pm$0.5)**		**55.2($\pm$ 25.2)**	**38.5($\pm$ 17.2)**
Complex cyst (0.6cm)	1	4	both	37.0	23.9
Complex cyst	3	2.7($\pm$0.6)	peripheral	46.9($\pm$9.6)	**32.5**($\pm$7.8)
Complex cyst	17	2.9($\pm$0.6)	no flow	39.8($\pm$23.3)	27.5($\pm$15.9)
Group Average	**(n=21)**	**3.0($\pm$0.7)**		**40.7($\pm$21.3)**	**28.0($\pm$14.6)**
Hyperplasia (high risk) (0.6cm)	1	3	no flow	56.2	38.0

Table II: Parameters of three false positive lesions

Lesion characteristics (biopsy results)	size	US findings BIRADS	Doppler	Total HB in μ mol/liter maximum	average in FWHM
fibroadenoma	1.91×0.85	4	no flow	117.8	81.3
fibroadenoma	1.50×0.70	4	no flow	119.0	85.2
minimally duct hyperplasia and fibrosis	3.4×1.56	4	no flow	129.9	89.2

Imaging heterogeneous tumor hemoglobin distributions of larger breast cancers by optical tomography with ultrasound localization

Quing Zhu*, Scott H. Kurtzman+, Poornima Hegde+, Susan Tannenbaum+, Minming Huang*, NanGuang Chen*, Bipin Jagjivan+, Mark Kane+, Kristen Zarfos+

*University of Connecticut
371 Fairfield Rd, U1157
Storrs, CT 06269

+University of Connecticut Health Center
263 Farmington, CT 06030

Correspondence: Prof. Quing Zhu; zhu@engr.uconn.edu;

Key words, tumor angiogenesis, optical tomography, ultrasound, breast disease

Abstract

Angiogenesis distribution in advanced breast cancers is highly distorted and heterogeneous. Non-invasive imaging and monitoring of angiogenesis is invaluable for initial diagnosis and for assessing tumor response to treatment. By combining ultrasound and near infrared optical imaging, a reliable new technique has emerged for localizing and characterizing tumor angiogenesis within the breast. This new technique employs a commercial ultrasound transducer coupled with an array of near-infrared optical fibers mounted on the hand-held probe. The ultrasound image is used for lesion localization and guiding optical imaging reconstruction. Optical sensors are used for imaging tumor total hemoglobin distribution, which is directly related to tumor angiogenesis. Six large breast carcinomas were studied and microvessel density count was then performed on tissue samples obtained from these cancers. Two patients had locally advanced breast cancers and received neoadjuvant chemotherapy for three months. In one patient, the total hemoglobin distribution before chemotherapy showed high concentration distributed at the cancer periphery, and the distribution was confined to the core area after three months treatment. In another patient, the maximum hemoglobin concentration has significantly reduced from 255.3, 147.5 to 76.9 in unit of μmol/liter and also in spatial extension from the beginning to the end of the treatment. The other four patients had large cancers of 2.0 cm to 3.0 cm in size and were imaged either at the time of core biopsy or at the definitive surgery. The histological microvessel density counts from these tumor samples correlate to the hemoglobin distributions with correlation coefficient of 0.64. These initial results suggest that this new imaging technique has a great potential to image heterogeneous angiogenesis distribution of larger cancers *in vivo* and monitor angiogenesis changes during chemotherapy.

Introduction

Noninvasive functional imaging of breast cancer presents a unique and worthwhile challenge. Optical tomography using near infrared (NIR) diffused light offers great potential as a non-invasive method for monitoring tumor hemoglobin distribution (1,2), which is directly related to tumor angiogenesis development. Tumor angiogenesis is a key factor required for tumor growth and metastasis. The use of this NIR method also provides direct insight into tumor metabolism and tumor hypoxia (3), important indicators of response to therapy. These functional parameters are potentially highly relavant for initial diagnosis and for assessing tumor response to treatment when given in the pre-operative setting. Intense light scattering using NIR in tissue makes lesion localization difficult. Thus to date, optical tomography has been limited to laboratory tests and feasibility studies (3-7). In this report, we further describe our experience using a novel combination of ultrasound (US) and NIR to overcome the scattering obstacle. Ultrasound imaging is frequently used as an adjunct tool to mammography in differentiating cysts from solid lesions. US also plays an important role in guiding interventional procedures such as needle aspiration, core-needle biopsy, and pre-biopsy needle localization (8). However, ultrasound features that occur in solid breast masses are not reliable enough to determine whether invasive evaluation is needed or non-invasive follow-up is indicated (9). The lack of specificity of ultrasound has prompted radiologists to recommend biopsies on most solid nodules, resulting in a 70 to 90 percent negative biopsy rate (10).

By combining ultrasound and optical imaging, a reliable technique has emerged for localizing and characterizing lesions within the breast (11-14). The technique is implemented by

simultaneously deploying optical sensors and a commercial ultrasound transducer mounted on a hand-held probe, and utilizing co-registered lesion structure information provided by ultrasound to improve the inverse optical imaging reconstruction. Results have shown that early stage invasive breast cancers can be separated from benign lesions by their significantly higher total hemoglobin concentration (14).

Angiogenesis distribution in advanced cancers is highly distorted and heterogeneous (15). This distorted distribution is related to the complex angiogenesis process involving both the incorporation of existing host blood vessels into tumor and the creation of tumor microvessels. This process is regulated by angiogenesis factors (16). Blood flow through these tumor vessels is heterogeneous. Some areas have high flow, others have slower flow and develop necrosis (17). Tumors with relatively poor blood perfusion may not receive adequate delivery of systemic therapy. This lack of perfusion may be a factor in poor response to intravenous chemotherapy treatment in some patients (18). Current clinical practice that is used to assess tumor response to chemotherapy relies on crude measurements such as clinical measurements of tumor size and changes in US or mammography. New imaging techniques include ^{15}O-water contrast-enhanced positron emission tomography (PET) (19), dynamic contrast-enhanced MRI (20-21), ^{99}m Tc-sestamibi contrast-enhanced single-photon emission tomography (22-23), and Doppler sonography (24). The first three techniques require rather expensive systems and may only be used at the beginning and the end of chemotherapy leaving the entire treatment period completely unmonitored. The Doppler sonography is limited to imaging large blood vessels. Compared with Doppler sonography that visualizes larger blood vessels, optical tomography images tumor microvessel density, which is directly related to tumor angiogenesis distributions.

Furthermore, near-infrared systems are cost-effective, portable and can be easily coupled to clinical ultrasound systems for repeated imaging.

Although pilot studies of imaging tumor hemoglobin distributions have been conducted with optical tomography, no one has obtained heterogeneous hemoglobin distributions in advanced cancers and demonstrated the correlation of the hemoglobin distributions with histological microvessel density counts. In this paper, we report, to the best of our knowledge, the first heterogeneous hemoglobin distributions of large cancers imaged by optical tomography, and we show that the hemoglobin distribution correlates to histological microvessel density counts. We also demonstrate the potential of optical tomography on monitoring pre-operative neo-adjuvant chemotherapy response and assessing treatment efficacy.

2. Materials and Methods

A hand-held hybrid probe consists of a commercial ultrasound transducer located in the center and our near-infrared source-detector fibers mounted in a housing, distributed at the periphery (14). The technical aspects of the NIR imager have been described in detail previously (12). Briefly, the imager consists of 12 pairs of dual wavelength (780nm and 830nm) laser diodes, which are used as light sources, and their outputs are coupled to the probe through optical fibers. An additional wavelength (660nm) is added to the system, which allows reliable estimation of tumor oxygenation saturation. On the receiving side, 8 photomultiplier tubes (PMTs) were used to detect diffusely scattered light from the tissue and 8 optical fibers were used to couple detected light to the PMTs. The laser diodes' outputs were amplitude modulated at 140 MHz and the detector outputs were demodulated to 20KHz. The demodulated signals were further

amplified and band pass filtered at 20 KHz. A reference signal of 20 KHz was also generated by directly mixing the detected RF signals with the RF signal generated from the oscillator. The reference signal was necessary for retrieving phase shifts. Eight detection signals and one reference were sampled and acquired into a computer simultaneously. The entire data acquisition took about 3 to 4 seconds, which was fast enough for acquiring data from patients.

The details of our dual-mesh optical imaging reconstruction algorithm have been described in Ref (13). Briefly, the NIR reconstruction takes advantages of ultrasound localization of lesions and segments the imaging volume into finer grid in lesion region L and coarser grid in non-lesion background regions B. In all images, 0.5cm $\times$ 0.5cm $\times$ 0.5 cm imaging grid was used for lesion and 1.5cm $\times$ 1.5cm $\times$ 1 cm was used for background region. A modified Born approximation is used to relate the scattered field U_{sd} measured at each source (s) and detector pair (d) to total absorption variations at wavelength λ in each volume element of two regions within the sample. The matrix form of image reconstruction is given by

$$[U_{sd}]_{M\times 1} = [W_L, W_B]_{M\times N}[M_L, M_B]^T{}_{Nx1} \qquad (1)$$

where W_L and W_B are weight matrices for lesion and background regions, respectively, and are calculated from the background absorption and reduced scattering measurements acquired at the normal contralateral breast. M_L and M_B are total absorption distributions of lesion and background regions, respectively. The absorption distribution at each wavelength is obtained by dividing M_L and M_B with different voxel sizes in lesion and background tissue regions. With this dual-mesh scheme, the inversion is well conditioned and the image reconstruction converges in a few iterations.

Since the major chromophores are deoxygenated (deoxyHb) and oxygenated (oxyHb) hemoglobin in the wavelength range studied, we can estimate deoxyHb and oxyHb concentrations at each imaging voxel by inverting the following equations voxel by voxel as:

$$\begin{bmatrix} \mu_a^{\lambda_1}(r') \\ \mu_a^{\lambda_2}(r') \end{bmatrix} = \begin{bmatrix} \varepsilon_{Hb}^{\lambda_1}, \varepsilon_{HbO_2}^{\lambda_1} \\ \varepsilon_{Hb}^{\lambda_2}, \varepsilon_{HbO_2}^{\lambda_2} \end{bmatrix} \times \begin{bmatrix} deoxyHb(r') \\ oxyHb(r') \end{bmatrix} \tag{2}$$

$$\begin{bmatrix} deoxyHb(r') \\ oxyHb(r') \end{bmatrix} = \frac{1}{\Delta} \begin{bmatrix} \varepsilon_{HbO_2}^{\lambda_2}, -\varepsilon_{HbO_2}^{\lambda_1} \\ -\varepsilon_{Hb}^{\lambda_2}, \varepsilon_{Hb}^{\lambda_1} \end{bmatrix} \times \begin{bmatrix} \mu_a^{\lambda_1}(r') \\ \mu_a^{\lambda_2}(r') \end{bmatrix}. \tag{3}$$

where $\mu_a^{\lambda_1}(r')$ and $\mu_a^{\lambda_2}(r')$ are absorption coefficients obtained at imaging voxel r', where wavelengths λ_1 and λ_2 correspond to 780 nm and 830 nm in our system, respectively. ε s are extinction coefficients given in Ref. (25). The total hemoglobin concentration $totalHb(r') = deoxyHb(r') + oxyHb(r')$ and oxygenation saturation $Y\% = \dfrac{oxyHb(r')}{oxyHb(r') + deoxy(r')} 100\%$ can be calculated as:

$$totalHb(r') = \frac{1}{\Delta} \left\{ \{\varepsilon_{HbO_2}^{\lambda_2} - \varepsilon_{Hb}^{\lambda_2}\} \mu_a^{\lambda_1}(r') + \{\varepsilon_{Hb}^{\lambda_1} - \varepsilon_{HbO_2}^{\lambda_1}\} \mu_a^{\lambda_2}(r') \right\} \tag{4}$$

and

$$Y\% = \frac{-\varepsilon_{Hb}^{\lambda_2} \dfrac{\mu_a^{\lambda_1}(r')}{\mu_a^{\lambda_2}(r')} + \varepsilon_{Hb}^{\lambda_1}}{(\varepsilon_{HbO_2}^{\lambda_2} - \varepsilon_{Hb}^{\lambda_2}) \dfrac{\mu_a^{\lambda_1}(r')}{\mu_a^{\lambda_2}(r')} - (\varepsilon_{HbO_2}^{\lambda_1} - \varepsilon_{Hb}^{\lambda_1})} 100\% , \tag{5}$$

We have found that the best two wavelengths for total hemoglobin calculation are 780nm and 830nm, and the best two wavelengths for oxygen saturation calculation are 660 nm and 830nm. These wavelength pairs were used in computing total hemoglobin concentration and oxygen saturation distributions reported in result section.

Since ultrasound resolution is less than one millimeter in depth for a typical 7.5 MHz ultrasound transducer such as the one we used, the boundaries between cancers and normal tissue structures can be visualized well. However, the spatial extensions of larger cancers in general are not well resolved in ultrasound. In addition, the NIR three dimensional data is co-registered with one of the two spatial dimensions and depth dimension of ultrasound. Another spatial dimension is estimated by assuming symmetry of the lesion. Furthermore, the optical contrast may well extend beyond the tumor periphery due to angiogenesis development. Therefore, a larger region of interest (ROI) particularly in spatial dimensions than that visualized by ultrasound is used for finer grid lesion region in the image reconstruction. The ROI used for each patient is listed in Table I.

Clinical studies were performed at the University of Connecticut Health Center (UCHC). The UCHC IRB committee approved the human subject protocol. Written consents were obtained from all patients. Patients with palpable and non-palpable masses that were visible on clinical ultrasound and who were scheduled for biopsy or neo-adjuvant chemotherapy were enrolled as research subjects. Six patients with cancer sizes ranged from 2.5 to 4 centimeters were studied. One patient had infiltrating papillary cancer and the cancer was metastasized to lymph nodes and spinal code. Positron emission tomography (PET) was obtained at the beginning and the end of her neo-adjuvant chemotherapy. This patient was imaged with the modified system of three wavelengths and the oxygen saturation maps were obtained. For each patient, ultrasound images and optical measurements were acquired simultaneously at multiple locations including the lesion region, a normal region of the same breast if the breast was large, and a normal symmetric region of the contralateral breast. The optical data acquired at normal region with the best linear

amplitude and phase profiles were used as reference for calculating the scattered field caused by lesions. The total hemoglobin concentration maps are quantified by measuring the maximum value at each depth (layer) and the average within 50% of the maximum value. Since the hand-held probe can be easily rotated or translated, at least three co-registered ultrasound and NIR data sets were acquired at the lesion location and the corresponding optical absorption maps as well as the total hemoglobin concentration distribution were reconstructed using the co-registered ultrasound. The data given in Table column 5 (left column) are average values obtained from at least three sets of NIR images.

To correlate the imaged hemoglobin distribution with histology microvessel density, we have performed microvessel density counts. Samples obtained at surgical biopsy or breast-conservation surgery were used for counting. For each sample, sections 3 to 5 micrometer thick were stained on an immunohistochemistry slide staining system (DAKO autostainer) with factor 8/86 mouse monoclonal antibody (anti-human von Willebrand factor, DAKO Corp, Carpinteria, Calif) at 1:100 dilution digested by proteinase K for 3 minutes, by labeled polymers (DAKO EnVision plus) immunoperoxidase method. Histological microvessel density count was assessed by immunohistochemistry as initially proposed by Weidner et al (18). The microvessel density counts were performed in ten consecutive fields with the use of an ocular grid at X200 magnification. The first field chosen was a hotspot (area of maximum vascular density either within the infiltrating tumor mass or at the tumor-stromal interface). Since the cancers were large, two to three separate sample blocks were selected for microvessel counts as per the specimen orientation in the surgical pathology report.

The excised specimen is always oriented by the surgeon with sutures designating the resection margins. Tumor sampling for histologic studies demonstrates the relationship of the tumor to the designated resection margins. Since the patients were imaged from the anterior approach with the patient in supine position, orientation of the anterior and deep (posterior) location within the optical and ultrasound images could be easily linked to the orientation of the surgical material.

3. Results

The first patient was a 44-year-old woman, who had a 4 cm x 4 cm x 1.5 cm palpable mass (Fig.1 (a)) located at the 6 to 8 o'clock position of the left breast that was considered as highly suspicious for malignancy. An ultrasound guided needle biopsy confirmed that the lesion was a high-grade invasive carcinoma with necrosis. The total hemoglobin concentration map shown in Fig.1 (b) reveals that the distribution is highly heterogeneous. The image reveals a high concentration of hemoglobin distributed at the cancer periphery. Slice 1 is the spatial x-y image of 9 cm x 9 cm obtained at a depth of 0.2 cm deep from the skin surface. Slice 7 is 3.2 cm deep toward the chest wall and the spacing between slices is 0.5 cm. The vertical scale is μ mol/liter ranging from 0 to 100 μ mol/liter. The maximum and average hemoglobin concentrations of three layers (slice 3,4 and 5) are 90.7/56.2,50.2/31.6 and 27.4 /25.2 in the unit of μ mol/liter, respectively. Since this cancer was considered too large for breast conserving surgery with an acceptable cosmetic result, the patient was treated with chemotherapy in the neo-adjuvant setting for three months. At the time the patient completed the chemotherapy, we imaged her tumor again. Figure 1 (c) is the ultrasound image of the cancer three months later. The cancer contrast is poor and cancer boundaries are completely unclear, probably due to treatment. Figure 1 (d) is the total hemoglobin distribution. The maximum and

average hemoglobin concentrations of three layers (slice 3, 4 and 5) are 73.6/50.4, 23.0/28.6, and 19.0/21.0 in the unit of μmol/liter, respectively. Compared with the images acquired before treatment, the spatial extension of the hemoglobin concentration is much smaller and more confined to the core area. The maximum total hemoglobin concentration is reduced by about 15 μmol/liter. This example demonstrates the feasibility of monitoring the angiogenesis changes during the treatment using the combined technique of US and NIR light analysis.

To correlate the NIR images with microvessel densities, we selected two block samples obtained at breast-conservation surgery marked as anterior and posterior (see Fig. 1(c) insertion) for microvessel counting. The total number of microvessels were 114 (anterior) and 48 (posterior and inferior) per 10 consecutive fields at 200 magnification, respectively (see table I: case 1). The high counts obtained at anterior correlate with the high hemoglobin concentration shown in slice 3 of Fig.1 (d). A representative section demonstrating high microvessel density is shown in Fig.1 (e). Immunohistochemical staining with antibody to Factor -VIII highlights the endothelial cells (stained brown) lining the vessels within the section. The low counts obtained at posterior and inferior block sample correlate with the low hemoglobin concentration seen in deeper slice 5 of Fig.1(d).

The second patient was a 47-year-old woman who had a 3 cm x 3 cm x 2 cm dominant mass at the 2 o'clock position in her left breast. Ultrasound showed a hypoechoic mass with irregular margins (see Fig. 2(a)) and the lesion was considered as highly suspicious for malignancy. Resection of the mass revealed an infiltrating carcinoma (histological grade II, nuclear grade II) with low mitotic activity. Figure 2 (b) shows the total hemoglobin map and the hemoglobin

concentration is low and the distribution is heterogeneous. The measured maximum total hemoglobin concentration and average of three layers (slices 4, 5, and 6) are 48.0/33.7, 48.4 /33.9 and 44.4/31.8 in the unit of μmol/liter, respectively. The total counts of microvessels obtained from anterior and posterior core biopsy samples were 61 and 40, respectively (see Table I: case 2). The total counts measured from anterior and posterior tumor samples obtained at definitive surgery were 52 and 29, respectively. These low counts correlate well with the low hemoglobin concentration shown in Fig. 2(b) and indicate that the tumor was poorly perfused. A representative section demonstrating low microvessel density is shown in Fig.2 (c).

The third example was obtained from 46 year-old woman who had a swollen left breast of two months duration with mild erythema of the skin overlying the lower inner quadrant. No discrete mass was palpable. A fine needle aspiration biopsy of the left breast followed by an incisional biopsy from the lower inner quadrant showed infiltrating ductal carcinoma of cellularity, defined as the percentage of invasive tumor comprised of tumor cells, ranging from 30 to 60% of tumor bed. PET imaging obtained before her chemotherapy treatment (see Fig.3 (a)) revealed that the cancer had metastasized to lymph nodes and spinal code. The cancer was quite diffuse occupying the entire breast. The patient was treated with adriamycin-based chemotherapy. We identified the upper quadrant mass from ultrasound and monitored the angiogenesis and oxygen saturation changes with the hybrid technique during her chemotherapy treatment. Figure 4(a), (b) and (c) are ultrasound images acquired at the beginning, during the fourth cycle of chemotherapy, and before definitive surgery, (d), (e) and (f) are corresponding total hemoglobin changes, and (g), (h) (i) are corresponding oxygen saturation maps. The

maximum hemoglobin concentration has significantly reduced from 255.3, 147.5 to 76.9 in unit of μmol/liter and also in spatial extension from the beginning to the end of the treatment. High oxygen saturation was noted in the tumor initially near chest-wall region (slice 6 &7 of Fig.4(g)) and fell to deoxygenated levels at the time of the second scan (Fig. 4(h) and (i)). Microvessel count obtained from core biopsy sample at inner low quadrant was 190, which could be related to the high hemoglobin concentration seen in Fig. 4(d) since the cancer was diffused throughout the entire breast. The low inner quadrant did not have visible ultrasound mass and therefore, we could not monitor this area. Microvessel counts of surgical samples obtained from anterior and posterior of the upper quadrant mass we imaged were 111 and 68 which correlate with higher and lower hemoglobin images seen in slice 4 and 6 of Fig.4(f). PET imaging showed a complete response to chemotherapy (see Fig.3(b)). Upon completion of neo-adjuvant chemotherapy, the patient underwent left modified radical mastectomy. Residual tumor was noted diffusely infiltrating all the quadrants as well as beneath the nipple. However, there was marked reduction in tumor cellularity to 5% throughout the fibrotic bed of the residual tumor.

Table I summarizes the results of six cases with biopsy results given in column 1. Column 2 and column 3 list the location of core biopsy samples and the corresponding microvessel counts. Four cases were diagnosed with fine needle biopsy and no tumor sample was available for microvessel density counting. Columns 4 and 5 (left) provide the location of the surgical sample obtained at the definitive surgery and the corresponding microvessel counts. The maximum and average hemoglobin concentrations at the corresponding depth (layer) were given

in column 5 (right). The ultrasound measured cancer size (right) at the time of the study or at the beginning of the chemotherapy, and the ROI used for finer mesh (left) for each case are given in the last column. The data of microvessel density count (column 5 left) versus measured maximum total hemoglobin concentration (column 5 right) are shown in Fig. 5. The linear regression curve is also given in the figure and the correlation coefficient is 0.64, which is statistically significant ($P<0.05$). One data point obtained at the posterior/inferior location of case 4 was removed as an outlier in obtaining the linear regression curve.

4. Discussion:

For the large cancers presented here, ultrasound can accurately diagnose the malignancy. The value of optical tomography in this setting is to map tumor angiognesis and evaluate vascular changes as well as tumor hypoxia during chemotherapy. Tumor hypoxia is related to tumor growth rate and drug response (26). This type of information could prove invaluable in understanding the chemosensitivity of tumors.

For each individual patient except case 4, the maximum and average total hemoglobin concentrations measured at top and bottom layers correlate to the histological microvessel density counts obtained at anterior and posterior samples, respectively. Case 4 was a 33-year-old pregnant woman and the NIR data was obtained 8 days after biopsy at the time of the patient visit. The larger variation in total counts at different tumor locations may partially relate to the inherent heterogeneity of breast tumors and the differential distribution of angiogenesis in the viable and schirrous regions. Nevertheless, the relatively higher counts obtained from the three sample blocks correlate to a large extent to the high hemoglobin distribution.

In the reported studies, we have used bulk absorption and reduced scattering coefficients obtained from the fitting results of normal breasts to compute the weight matrices. We reconstructed the absorption variations of both lesion and background and then compute the total hemoglobin distribution from the absorption changes. Optical scattering changes also contribute to the measured perturbations. We have attempted to reconstruct both absorption and reduced scattering changes simultaneously, but have not been successful with the modified Born approximation. The main reason is that the weight matrices of absorption and scattering coefficients are not on the same order. By appropriately scaling the weight matrices as reported in Ref. 27, we can improve the simultaneous reconstruction for phantom targets but not reliably for all clinical cases. Currently, we are investigating simultaneous reconstruction using the finite element method. We are also investigating the time resolved method (28) because scattering inhomogeneities mainly influence photons with rather short propagation paths (29, 30). However, a study of 13 optically visible cancers using the time resolved method has shown that 12 cases have presented 10% to 175% relative changes in absorption between tumor and surrounding tissue (6). Only two cases have shown relative scattering heterogeneity changes from 10% to 15% and one case has shown changes of 25% from the bulk value. Therefore, we believe the results reported here mainly represent the changes of lesion absorption and the correlation between the total hemoglobin concentration and the microvessel counts provides further evidence of this.

In this paper, we have reported initial results of heterogeneous total hemoglobin distributions of six large breast cancer cases imaged by optical tomography with ultrasound localization. The measured total hemoglobin concentration correlates, to a large extent, to the histological

microvessel density counts. These initial results suggest that optical tomography with ultrasound localization has a great potential to image tumor angiogenesis *in vivo*, monitor angiogenesis and oxygen changes within tumors during chemotherapy.

Acknowledgements:

Authors would like to thank Ellen Oliver, surgical nurse of the Cancer Center at the University of Connecticut Health Center, and Deborah McMahon, coordinator of Radiology Department at the University of Connecticut Health Center for their continuous efforts in patient scheduling. Radiology ultrasound technologists are extremely helpful in assisting US data acquisition and patent scanning. We thank the following funding agents for their support: National Institute of Health (R01EB002136), Donaghue Foundation and Department of Defense ARMY Medical Research and Materiel Command (DAMD17-00-1-0217, 17-01-1-0216).

References:

(1) Yodh A and Chance B . Spectroscopy and imaging with diffusing light. Phys Today 1995; **48**, 34-40.

(2) Tromberg B, Shah N, Lanning R, Cerussi A, Espinoza J, Pham T, Svaasand L, and Butler J. Non-Invasive in vivo characterization of breast tumors using photon migration spectroscopy. Neoplasia 2000; 2(1:2): 26-40.

(3) Ntziachristos V, Yodh A, Schnall M., and Chance B. Concurrent MRI and diffuse optical tomography of breast after indocyanine green enhancement. Proc. of Nat. Ac. of Sci 2000; **97** (6): 2267-2772.

(4) Franceschini MA, Moesta KT, Fantini S, Gaida G, Gratton E, Jess H, Seeber M, Schlag PM, Kashke M. Frequency-domain techniques enhance optical mammography: initial clinical results. Proc. of Nat. Ac. of Sci 1997; 94: 6468-6473.

(5) Pogue B, Poplack SP, McBride TO, Wells WA, Osterman K, Osterberg U, and Paulsen KD . Quantitative hemoglobin tomography with diffuse near-infrared spectroscopy: pilot results in the breast. Radiology 2001; 218: 261-266.

(6) Grosenick D., Moesta KT., Wabnitz H., Mucke J., Stroszczynski C., Macdonald R., Schlg P, and Rinneberg H . Time-domain optical mammography: initial clinical results on detection and characterization of breast tumors. Applied Optics 2003; 42(16): 3170-3186.

(7) Jiang H, Xu Y, Iftimia N, Eggert J, Klove K, Baron L and Fajardo L. Three-dimensional optical tomographic imaging of breast in a human subject. IEEE Trans on Medical Imaging, 2001; 20(12), 1334-1340.

(8) Fornage BD, Coan JD, David CL. Ultrasound-guided needle biopsy of the breast and other interventional procedures. Radiol Clin North Am 1992; 30:167-185.

(9) V. P. Jackson , The current role of ultrasonography in breast imaging. Radiol Clin North Am **33** 1995; 1161-1170.

(10) Hall, F. M, Storella, J. M., Silverstone, D. Z., et al. Non-palpable breast lesions: recommendations for biopsy based on suspicious carcinoma of mammography. Radiology 1988; 167; 353-358.

(11) Zhu Q, Durduran T, Holboke M, Ntziachristos V and Yodh A. Imager that combines near infrared diffusive light and ultrasound. Optics Letters. 1999; **24**(15): 1050-1052.

(12) Chen, NG, Guo, PY, Yan, SK, Piao DQ, and Zhu, Q. Simultaneous near infrared diffusive light and ultrasound imaging. Applied Optics 2001; **40**(34): 6367-6380.

(13) Zhu, Q, Chen NG, Kurtzman, S. Imaging tumor angiogenesis using combined near infrared diffusive light and ultrasound. Optics Letters 2003; 28(5): 337-339.

(14) Zhu, Q., Huang, MM, Chen, NG, Zarfos, K, Jagjivan, B, Kane, M, Hegde P, Kurtzman, SH . Ultrasound-guided optical tomographic imaging of malignant and benign breast lesions. Neoplasia. 2003; 5(5): 379-388.

(15) Mankoff DA, Dunnwald LK, Gralow JR, Ellis GK, Charlop A, Lawton TJ, Schubert EK, Tseng J, Livington RB. Blood Flow and Metabolism in Locally Advanced Breast Cancer: Relationship to Response to Therapy. Journal of Nuclear Medicine 2002; 43(4): 500-509.

(16) Vaupel P, Kallinowski F, Okunieff P . Blood flow, oxygen and nutrient supply, and metabolic microenvironment of human tumors: a review. Cancer Research 1989; 49: 6449-6465.

(17) Jain RK. Hemodynamic and transport barriers to the treatment of solid tumors. Int J Radiat Biol. 1991; 60:85–100.

(18) Weidner N, Semple JP, Welch WR, Folkman J. Tumor angiogenesis and metastasis – correlation in invasive breast carcinoma. N Engl J Med. 1991; 324(1):1-8.

(19) Wilson CBJH, Lammertsma AA, McKenzie CG, Sikora K, Jones T. Measurements of blood flow and exchanging water space in breast tumors using positron emission tomography: a rapid and non-invasive dynamic method. Cancer Res 1992; 52:1592–1597.

(20) Abraham DC, Jones RC, Jones SE, et al. Evaluation of neoadjuvant chemotherapeutic response of locally advanced breast cancer by magnetic resonance imaging. Cancer 1996; 78:91–100.

(21). Gilles R., Guinebretiere JM, Shapeero LG, Lesnik A, Contesso G, Sarrazin D., Assessment of breast cancer recurrence with contrast-enhanced subtraction MR imaging: preliminary results in 26 patients. Radiology 1993; 188:473-478.

(22). Maini CL, Tofani A, Sciuto R, et al. Technetium-99m-MIBI scintigraphy in the assessment of neoadjuvant chemotherapy in breast carcinoma. J Nucl Med 1997; 38:1546–1550.

(23). Mankoff DA, Dunnwald LK, Gralow JR, Ellis GK, Drucker MJ, Livingston RB. Monitoring the response of patients with locally advanced breast carcinoma to neoadjuvant chemotherapy using [technetium-99m]-sestamibi scintimammography. Cancer 1999; 85:2410–2423.

(24). Kedar RP, Cosgrove DO, Smith IE, Mansi JL, Bamber JC. Breast carcinoma: measurement of tumor response to primary medical therapy with color flow Doppler imaging. Radiology 1994; 190:825–830.

(25) Cope M, Ph.D Dissertation, University of College London, 1991.

(26) Vaupel P, Schlenger K, Knoop C, Hockel M (1991). Oxygenation of human tumors: evaluation of tissue oxygen distribution in breast cancers by computerized O2 tension measurements. Cancer Research, 51:3316-3322.

(27) Huang, MM, Xie, TQ, Chen, NG, and Zhu, Q . Simultaneous reconstruction of absorption and scattering maps with ultrasound localization. Applied Optics 2003; 42(19):4102-4114.

(28) Chen, NG and Zhu, Q. Time-resolved optical measurements with spread spectrum excitations. Optics Letters 2002; 127(20): 1806-1808.

(29) Gandjbakhche AH, Chernomordik V., Hebden JC, and Nossal R. Time-dependent contrast functions for quantitative imaging in time-resolved Tranillumination experiments. Applied Optics 1998; 37:1973-1981.

(30) Hall DJ, Hebden JC., Delpy DT. Imaging very-low-contrast object in breastlike scattering media with a time-resolved method. Applied Optics 1997; 36: 7270-7276.

Figure Captions:

Figure 1 (case 1). (a) Ultrasound image of a 44-year-old woman who had a 4 cm by 4 cm palpable left breast mass. An ultrasound guided needle biopsy revealed that the lesion was a high-grade invasive carcinoma with necrosis. (b) Total hemoglobin concentration of the lesion. Slice 1 is x-y image of 9 cm by 9 cm obtained at 0.2 cm depth from the skin surface and slice 7 is 3.2 cm deep toward the chest wall. The order of slices is from left to right and top to bottom. The spacing between the slices is 0.5 cm. The vertical scale is μmol/liter ranging from 0 to 100 μmol/liter. (c) Ultrasound image of the same cancer treated with chemotherapy for three months. (d) Total hemoglobin concentration of the lesion and the vertical scale is μmol/liter ranging from 0 to 100 μmol/liter. (e) Representative section of the infiltrating ductal carcinoma of breast demonstrating high microvessel density (original magnification X200; anti-human von Willebrand factor, DAKO EnVision plus).

Figure 2(case 2). (a) Ultrasound image of a 47-year-old woman with a highly suspicious lesion located at 2'oclock position of her left breast. Surgical pathology report revealed that the mass was an infiltrating carcinoma with low mitotic activity. (b) Total hemoglobin concentration of the lesion in μmol/liter ranging from 0 to 100 μmol/liter. Slice 1 is x-y image of 9 cm by 9 cm obtained at 0.5 cm depth from the skin surface and slice 7 is 3.5 cm deep toward the chest wall. (c) Representative section of infiltrating ductal carcinoma of breast demonstrating low microvessel density (original magnification X200; anti-human von Willebrand factor, DAKO EnVision plus).

Figure 3 (case 5). Positron emission tomography images of 46 year-old woman who had a swollen left breast. Core biopsy revealed a locally advanced infiltrating papillary cancer. (a) Image acquired before chemotherapy. The ductal carcinoma in the left breast is pointed by the small black arrow and positive lymph notes (black dots) are pointed by the longer black arrow. The positive spinal code is pointed by the white arrow. (b) Image acquired after 6 cycles of chemotherapy before the definitive surgery. The activities of carcinoma in the left breast, positive lymph notes, and positive spinal code are no-longer visible.

Figure 4 (case 5). Corresponding US images acquired at the beginning (a), 4^{th} cycle (b) and end (c) of chemotherapy. (d), (e) and (f) are corresponding NIR hemoglobin concentrations, while (g), (h) and (i) are oxygen saturation maps. Slice 1 is x-y image of 9 cm by 9 cm obtained at 0.5 cm depth from the skin surface and slice 7 is 3.5 cm deep toward the chest wall. The slices in (d)-(i) are numbered from left to right and top to bottom.

Figure 5. Microvessel density counts obtained at anterior and posterior surgical samples versus measured maximum total hemoglobin concentration at the corresponding layers. Linear regression analysis obtained 0.64 correlation coefficient, which is statistically significant ($P<0.05$).

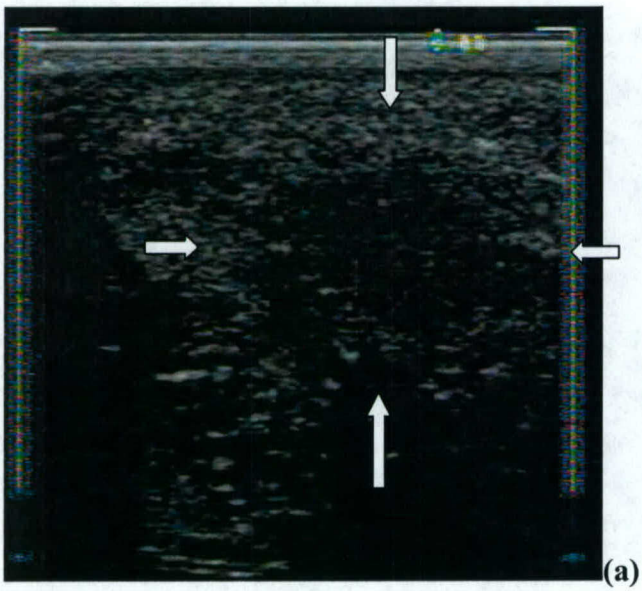

(a)

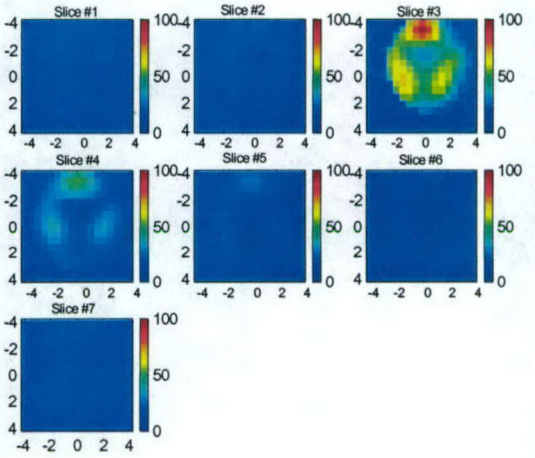

(b)

anterior (skin)

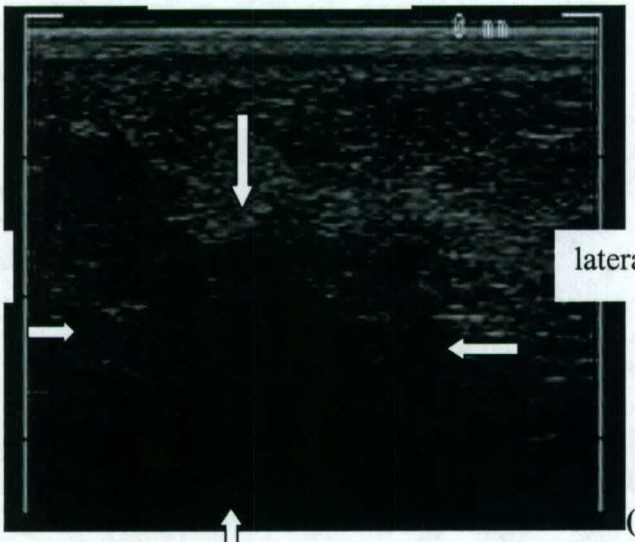

medial

lateral

(c)

posterior (chest wall)

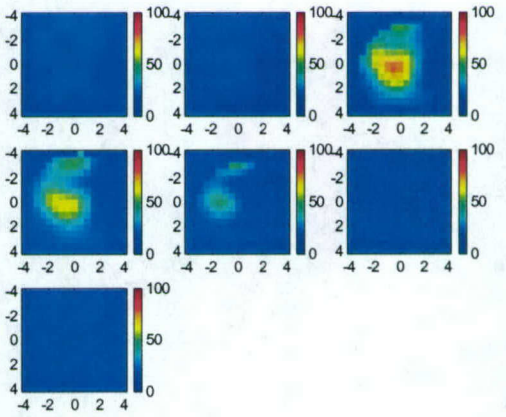

(d)

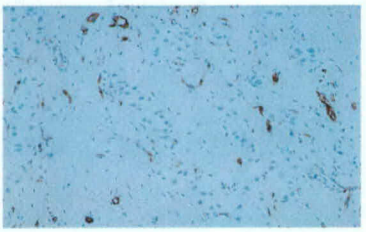

(e) Figure 1.

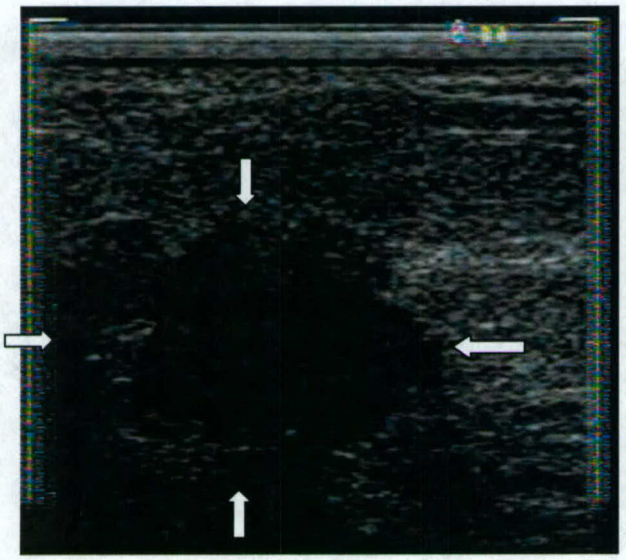

(a)

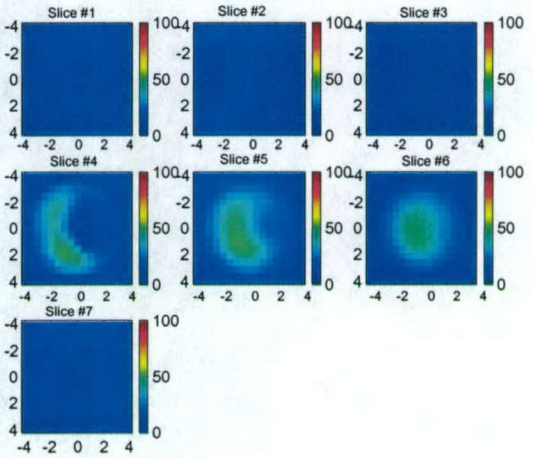

(b)

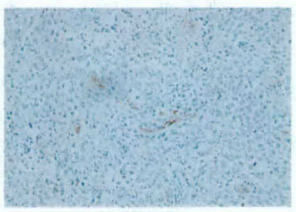

(c)

Figure 2.

Fig. 3.

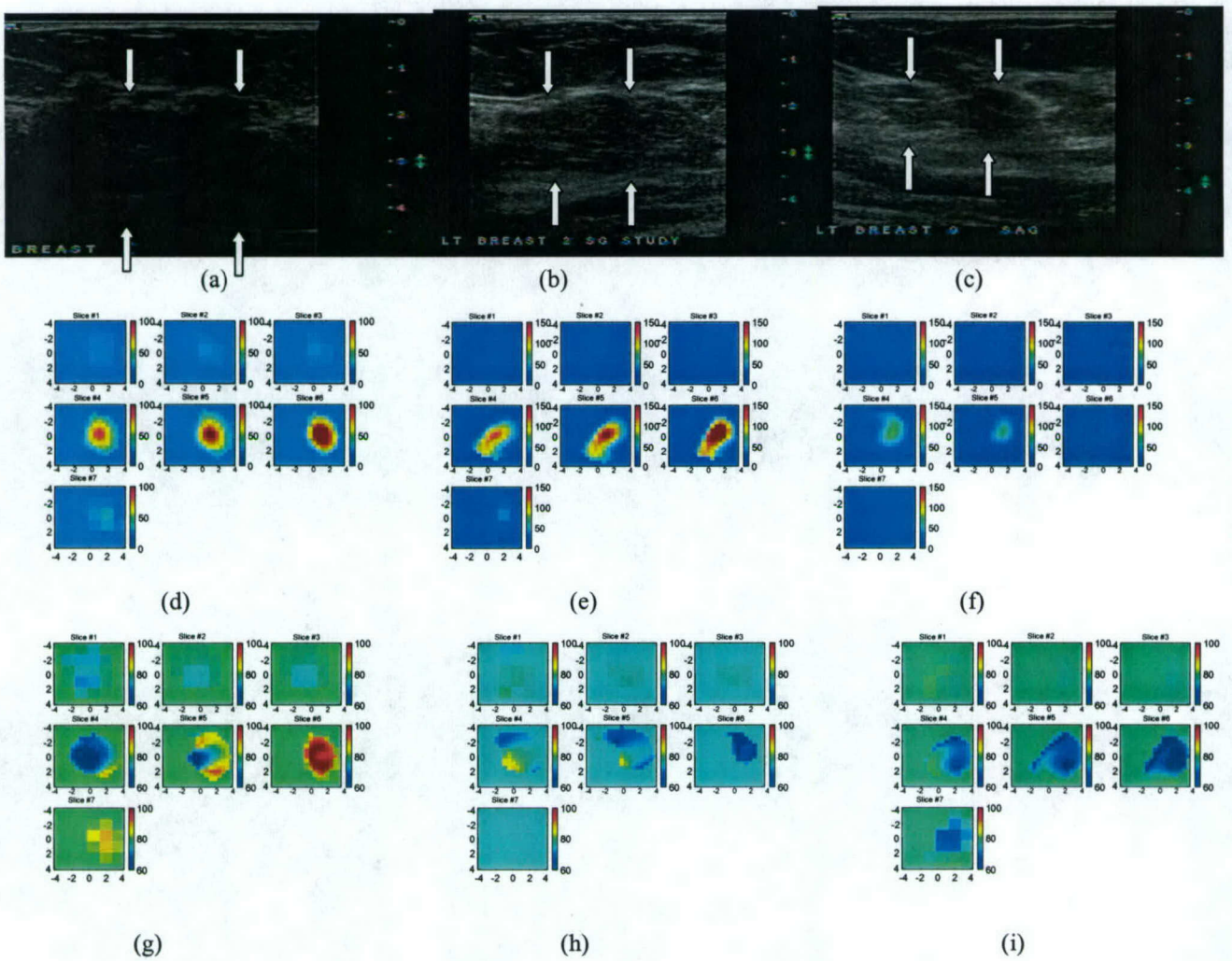

Fig.4.

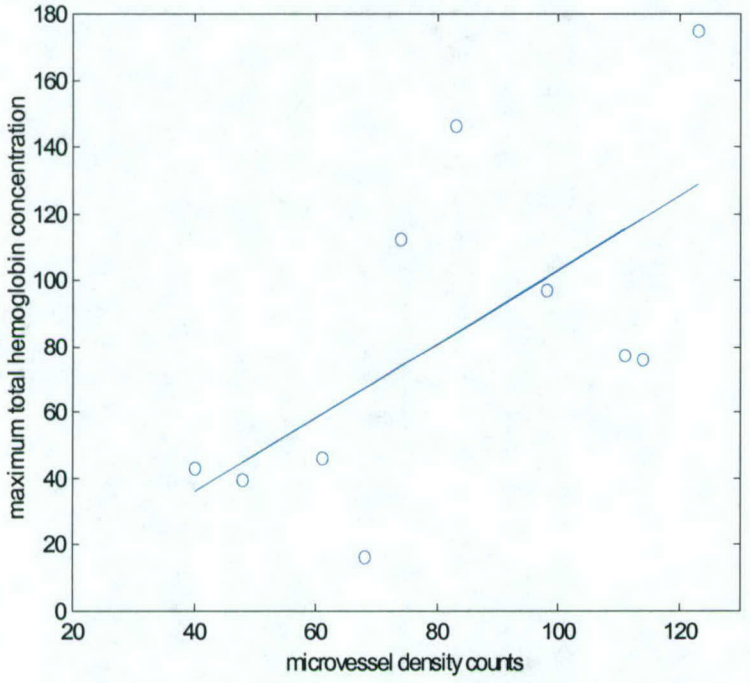
maximum total hemoglobin concentration
microvessel density counts
0
20
40
60
80
100
120
140
160
180
20
40
60
80
100
120

Fig.5.

Table I. Histological microvessel density counts and total hemoglobin measurements

Cases	location	mvd per 10 fields at x200	location	mvd per 10 fields at x 200	total Hb (maximum /ave)	Size measured by US (cm)	ROI for NIR imaging (cm)
Case 1	NA	NA	ANT	114	(75.9/54.0)	4×4×1.5; 8.4×8.4 ×1.9	
High-grade Invasive Carcinoma	NA	NA	POST/INF	48	(39.5/26.6)		
Case 2	ANT	61 **	ANT	52	(45.9/31.6)	3×3×2.0; 9 × 9 ×2.0	
infiltrating carcinoma	POST	40**	POST	29	(42.9/30.8)		
Case 3	NA	NA	ANT	83	(146.4/106.0)	2.5×2.5×1.3; 8×8×1.6	
	NA	NA	POST	124 *	(174.9/122.3)		
invasive and *in situ* ductal carcinoma	NA	NA	POST/LAT	121			
Case 4	NA	NA	ANT/LAT	60 *	(112.5/81.1)	3 ×3 × 1.5; 7×7 ×1.7	
	NA	NA	ANT/MED	88			
invasive and *in situ* ductal carcinoma	NA	NA	POST/INF	152	(88.4/65.8)		
Case 5	NA	NA	ANT	111	(77.2/55.6)	4×4×2.0; 8×8 ×2.0	
	NA	NA	POST	68	(16.1/12.9)		
infiltrating ductal carcinoma	ANT(LIQ)+	190	ANT(LIQ)	61			
Case 6	NA	NA	ANT	86 *	(97/66.5)	2×2×1.0; 7×7×1.0	
Infiltrating ductal carcinoma	NA	NA	POST	109			

ANT: anterior; POST: posterior; LAT: lateral. MED: medial. INF: inferior
mvd per 10 fields at x200x: total microvessels per 10 consecutive fields at 200 magnifications
+LIQ: Low inner quadrant
*average is used in obtaining Fig.5.
**For case 2, NIR/US data are acquired at core biopsy and therefore the microvessel density counts obtained at the time of core US were used in Fig.5.